Study on the influence of different error sources on sky radiance measurements and inversion-derived aerosol products in the frame of AERONET

TESIS DOCTORAL

Benjamín Torres Rodríguez

Grupo de Óptica Atmosférica

Departamento de Física Teórica, Atómica y Óptica

Universidad de Valladolid

February 2012

Study on the influence of different error sources on sky radiance measurements and inversion-derived aerosol products in the frame of AERONET

Tesis Doctoral

Dirigida por Dr. Alberto Jesús Berjón Arroyo y Dr. Carlos Toledano Olmeda.

Ponente Dra. Mª Inmaculada de la Rosa García

Grupo de Óptica Atmosférica

Departamento de Física Teórica, Atómica y Óptica

Universidad de Valladolid

February 2012

A mis padres

Acknowledgement

Que nadie tema que su causa sea olvidada; que nadie espere una ventaja o un privilegio. Juntos podremos hacerlo todo, si a todos damos su justa oportunidad...

Discurso de proclamación del Rey Juan Carlos I el 22 de Noviembre de 1975 tras la muerte de Franco.

Sí has venido hasta esta página esperando encontrar tu nombre, puedes sentir mi agradecimiento. Seguro que ha habido un momento en estos últimos cuatro años en el que hayamos soltado juntos un buena carcajada; espero estas líneas te sirvan como pago. Aunque si eres de los que crees que este agradecimiento es demasiado pequeño, estoy de acuerdo contigo. Lamentablemente el tiempo apremia y hay cosas en las que uno puede correr (traduciones, resumenes...) pero en otras no, y darte las gracias a ti como te lo mereces, es algo que me voy a tomar muy en serio. Por eso te emplazo a esperar unos días, tal vez semanas, para cuando la versión definitiva para el tribunal esta terminada; espero que para entonces tu curiosidad sea recompensada.

Contents

Índice

List of Figures

List of Tables

Introduction (English)

We build too many walls and not enough bridges.

Isaac Newton

Context

The atmospheric aerosol is defined as the ensemble of solid and liquid particles suspended in the atmosphere. The aerosol particles can be natural (marine aerosols, desert dust or volcanic aerosols, etc.) or anthropogenic (nitrates, sulfates, organics, carbonaceous, etc.), or even a combination of both components, with particle sizes ranging from a few nanometers to hundreds of micrometers, thus leading to a complex and heterogeneous system with different physical, chemical and optical properties (Willeke and Baron (1993); D'Almeida et al. (1991)).

Atmospheric aerosol particles have an impact on the Earth's climate by scattering and absorption of solar radiation and by modification of cloud properties. These effects remain the largest source of uncertainty in our current understanding of the Earth's climate system, as stated by the last IPCC report (Solomon et al., 2007). Atmospheric aerosol particles are also known to cause adverse health effects (e.g. EU Directive 2008/50/EC). Measurement and modeling of aerosol effects remain a challenge due to the complexity of the processes and the heterogeneity of aerosols in terms of chemical composition, physical and optical properties, as well as spatial and temporal distribution.

The remote sensing of the atmospheric aerosol is a well-established technique that is currently used for routine monitoring of this atmospheric component, both ground-based and from satellite. Due to the large spatial and temporal variability of the aerosol there was a need for the implementation of global ground-based observations. The AERONET Network (Holben et al., 1998) program, initiated by NASA and LOA in the 90's, is the most extended network and the data provided are currently used by a wide community for aerosol characterization, satellite and model validation and synergetic use with other instrumentation (lidar, in-situ, radiation, etc.).

AERONET is currently a federation of networks (AERONET, PHOTONS, RIMA, AEROCAN, CSIRO) and there exist three calibration facilities: NASA-Goddard, PHOTONS-Lille and RIMA-Valladolid. The RIMA Network for Sun photometer Aerosol Measurements started in 2004 and is managed by the University of Valladolid, in collaboration with AEMET and PHOTONS. The calibration facility operates since 2006 and it is currently in charge of 30 AERONET sites located in Spain, Portugal and other European and non-European countries.

The calibration activity of our group as federated network within AERONET is very relevant for this PhD work. We have acquired the necessary knowledge with the instrumentation, in particular the calibration process and the operational issues during field deployment. This knowledge, combined with the wide experience in aerosol research of the group, is an privileged starting point. The second great support is the long term collaboration of our group with LOA-University of Lille, especially with Dr. Philippe Goulub, NASA-Goddard, and, finally, with Cimel Electronique, the company manufacturing the Cimel-318 sun/sky radiometer utilized in AERONET.

Motivation

Even though ground based remote sensing of aerosols is a common technique in aerosol research, there are still open questions and inconsistencies in the modeling of the aerosol optical properties, for example regarding complex shapes, as in the case of desert dust (Dubovik et al., 2006). There are known limitations in the inversion of sky radiances, for instance, the accuracy assessment of AERONET version 1 inversion algorithm (Dubovik et al., 2000) notes that there are large uncertainties in the retrieved products from almucantar scans at low solar zenith angles (SZA) and/or at low aerosol optical thickness conditions. Furthermore, no assessment has been published for version 2 which presents some novelties as the spheroid model in the retrieval algorithm (Dubovik et al., 2006).

The radiance measurements, which are the inputs in the mentioned retrieval algorithm together with the aerosol optical thickness, are obtained following two geometries within AERONET: principal plane and almucantar. The first one provides more stable inversion results around noon (due to the observation of larger scattering angle range) minimizing the problem presented in the accuracy assessment analysis (as it will be commented further on in this PhD report, chapter 2).

After the release of AERONET version 2 in 2007, both principal plane and almucantar inversions were provided. However, few months later the principal plane retrievals were removed. Nevertheless, in the period of coexistence, some discrepancies between them were observed. Albeit the assessment study was only done for version 1, problems related to almucantar retrievals for low SZA were found for real data in version 2. For example in Dubovik (2009), the desert dust retrievals in Hamim site (August 2004) presented an unrealistic diurnal variability (up to 10%) of

parameters such as the single scattering albedo in almucantar retrievals due to the limitation of scattering angle range at low SZA.

The consequence of this is the lack of information on the inversion-derived properties such as size distribution, refractive index and single scattering albedo in the middle of the day (except at high latitudes), which are necessary for the evaluation of the aerosol.

Possible explanations of the discrepancies between the retrievals from principal plane and the almucantar are the measurement accuracy and/or the model. Many authors have concentrated on the modeling issue, trying to find out whether the discrepancy between modeled and measured sky radiances is a result of incorrect phase function, shape assumptions, etc. (Gasteiger et al., 2011). Given the above-mentioned experience of our group, the analysis here tries to shed some light on the question if measurement errors could be the source of this inconsistency in the retrievals.

In order to analyze the effect of radiance measurement errors on the derived aerosol properties, it was necessary to run the Dubovik AERONET inversion algorithm in research mode. This was possible thanks to the collaboration with Dr. Oleg Dubovik in the frame of the present PhD research work.

Objectives

The main goal of this PhD is to contribute to the investigation of the causes behind the discrepancies between almucantar and principal plane retrievals, specifically, to examine if they can be associated with the errors in the radiance measurements.

From the all possible sources of error (e.g. temperature dependencies, direct sun errors, clock errors, surface reflectance...) we focus on the analysis of sky radiance errors that may lead to such discrepancies: calibration, pointing and finite field of view.

It is important to remark that all three constitute systematic errors that cannot be reduced by averaging or other statistical procedures. If possible they should be corrected, in a similar way as it was shown for the direct sun channel calibration with the KCICLO method (Cachorro et al., 2008). However, correcting the systematic uncertainties not always possible and a quantitative evaluation of such errors is therefore necessary.

These errors will be analyzed in terms of their effect on the radiance as well as their qualitative and quantitative impact on the aerosol properties that are retrieved by means of the AERONET inversion algorithm. We will focus on the size distribution, complex refractive index and single scattering albedo.

Thesis layout

To fulfill the objectives, this PhD-thesis is structured as follows: in chapter 1, the context and background regarding AERONET and the inversion of sky radiances is provided.

Chapter 2 provides an insight on the sky radiance and the aerosol properties of the four main aerosol types considered further on to make the simulations. Their characteristics are derived from the AERONET climatology by Dubovik et al. (2002): marine (coarse mode predominant, non-absorbing), dust (coarse, absorbing), urban (fine mode predominant, non-absorbing) and biomass burning (fine, absorbing).

In chapter 3, we describe the nature and provide quantification of the three error sources that we have considered for analysis. The estimated uncertainties for each error have been obtained from various sources:

- The radiance calibration, performed with calibrated integrating spheres, was described by Holben et al. (1998). This procedure is now one step more complicated, since the calibration standard must be transferred from NASA-Goddard to the other calibration facilities. However, the improvements in NASA primary calibration (better than 3%) makes possible to keep the estimated 5% accuracy throughout the network.
- The typical pointing error of AERONET field photometers has been investigated in collaboration with Cimel company. A full sun scan developed by Cimel was introduced in the routine measurement sequence. We developed a procedure to evaluate the pointing error from these measurements. Currently the AERONET sites calibrated by RIMA-Valladolid are equipped with this capability and the pointing error can be monitored together with a larger set of quality checks that are routinely performed.
- Two methods have been used to estimate the field of view of the Cimel sun photometers: the first one using the sun as a source and the second one in the laboratory with the help of a laser source.

Then, chapters 4, 5 and 6 describe the impact of each error: calibration, pointing and field of view, respectively on the radiances and the retrieved aerosol properties. The study basically consists on simulating sky radiances, to which we will add the estimated uncertainties to be able to quantify the effects separately. In this way the study could be considered as a theoretical study. However, there is a close relationship with the experimental measurements, because those inspired the set of systematic errors to be analyzed as well as the thresholds and typical values employed throughout the simulations.

The last part of the PhD-thesis contains the conclusions and outlook of the whole work.

Introducción (Spanish)

Mi corazón espera
también, hacia la luz y hacia la vida,
otro milagro de la primavera.

Antonio Machado
"A un olmo viejo"
Hablando de la España de ayer (y de hoy).

Contexto

El aerosol atmosférico se define como el conjunto de partículas sólidas o líquidas en suspensión en la atmósfera. Los aerosoles pueden ser de origen natural (aerosol marino, polvo del desierto, aerosol volcánico...) o antropogénico (nitratos, sulfatos, orgánicos, carbonáceos, etc.) o también combinación de ambos, con tamaños que van desde los pocos nanómetros hasta los cientos de micras, características que hacen que sea un sistema complejo y heterogéneo con diferentes propiedades físicas, químicas y ópticas (Willeke and Baron (1993); D'Almeida et al. (1991)).

El aerosol atmosférico produce un impacto sobre el clima de la Tierra mediante la absorción y el scattering de la radiación solar, así como modificando las propiedades de las nubes. Estos efectos son aún la mayor fuente de incertidumbre en nuestro actual conocimiento del sistema climático terrestre, como quedo establecido en el último informe del IPCC (Solomon et al., 2007). Diversos problemas de salud también son atribuidos a las partículas del aerosol atmosférico (ver por ejemplo la directiva europea de calidad del aire 2008/50/EC). La modelización y medida de los efectos de los aerosoles se presenta todavía como un desafío debido a la complejidad de su formación y a su heterogeneidad en términos de composición química, física, propiedades ópticas, así como a su distribución espacial y temporal.

La detección remota de aerosoles es una técnica bien establecida que es usada normalmente para monitorizar de manera rutinaria este componente atmosférico, usando tanto medidas desde suelo como medidas de satélite. Debido a la gran variabilidad espacial y temporal del aerosol, había la necesidad

de una implementación global de observaciones desde tierra. La red AERONET (Holben et al., 1998), iniciada por NASA y LOA en los años noventa, es la red más extendida y los datos proporcionados son utilizados actualmente por una amplia comunidad científica para la caracterización de aerosoles, así como para la validación de satélite y para aprovechar las sinergias con otra instrumentación (lidar, in situ, radiación, etc.)

AERONET es actualmente una federación de redes (AERONET, PHOTONS, RIMA, AEROCAN, CSIRO), donde existen tres instalaciones de calibración: NASA-Goddard, PHOTONS-Lille y RIMA-Valladolid. La red RIMA se inició en 2004 y es administrada por la Universidad de Valladolid, en colaboración con la AEMET y PHOTONS. La estación de calibración opera desde 2006 *y actualmente está a cargo de* 30 *estaciones de AERONET ubicadas en España, Portugal y otros países europeos y no europeos.*

La actividad de calibración de nuestro grupo como red federada dentro de AERONET es muy relevante para este trabajo de tesis doctoral, ya que hemos adquirido el conocimiento necesario con la instrumentación, en particular, con el proceso de calibración y con los problemas operativos durante las medidas de los equipos en las estaciones. Este conocimiento, combinado con la amplia experiencia en la investigación de aerosoles del grupo, es un punto de salida privilegiado. El segundo gran soporte es la extrecha colaboración de nuestro grupo con el LOA de la Universidad de Lille, en especial con el Dr. Philippe Goulub, así como con NASA-Goddard, y con Cimel Electronique, que es la empresa encargada de la fabricación del Cimel-318, instrumento estándar dentro de la red AERONET.

Motivación

A pesar de que las medidas ópticas desde suelo para la detección de aerosoles es una técnica común en la investigación de aerosoles, todavía hay preguntas abiertas y ciertas inconsistencias en la modelización de las propiedades ópticas del aerosol, por ejemplo el efecto de la formas complejas, como en el caso del aerosol desértico (Dubovik et al., 2006). Existen limitaciones conocidas en la inversión de la radiancia de cielo, por ejemplo, la evaluación de la exactitud del algoritmo de inversión AERONET versión 1 *(Dubovik et al., 2000) señala que existen ciertas incertidumbres en los productos obtenidos de los análisis almucantar a bajos ángulos cenitales solares (*SZA*) o en condiciones de bajo espesor óptico de aerosol. Sin embargo, aún no se ha publicado la evaluación de la versión* 2*, la cual presenta ciertas novedades como el modelo de esferoides en el algoritmo de inversión (Dubovik et al., 2006).*

Las medidas de radiancia de cielo, las cuales conforman junto con el espesor óptico de aerosoles la entrada del algoritmo de inversión mencionado, se obtienen usando dos geometrías distintas dentro de la red AERONET: plano principal y almucantar. La primera de ellas ofrece resultados de la inversión más estables alrededor del mediodía (debido a la observación de mayor rango de ángulo de scattering) minimizando el problema presentado en el análisis de evaluación de la exactitud del modelo (como se

comentará más adelante en este trabajo, concretamente en el capítulo 2).

Tanto las inversiones de plano principal como de almucantar eran ofrecidas por AERONET poco después del lanzamiento de la versión 2. Sin embargo, unos meses más tarde, las inversiones de plano principal fueron retiradas. No obstante, en el período de coexistencia de ambas, se observaron ciertas discrepancias entre dichos procedimientos. Si bien el estudio de evaluación se llevó a cabo sólo para la versión 1, los mismos problemas relacionados con la inversión de datos de almucantar para bajos SZA fueron encontraron para los datos reales en la versión 2. Por ejemplo, en Dubovik (2009), las inversiones de intrusiones desérticas en la estación de Hamim (Agosto de 2004) presentaban una variabilidad diurna que no era realista (hasta del $10\,\%$) de parámetros tales como el albedo de scattering simple en las inversiones de almucantar debido a la limitación de ángulos de scattering con SZA bajos.

Como fruto de estas limitaciones aparece una falta de información sobre las propiedades derivadas de la inversión, tales como la distribución de tamaño, el índice de refracción y albedo de scattering simple en el mediodía (excepto a altas latitudes), y que son necesarias para una correcta evaluación del aerosol.

Entre las posibles explicaciones de las discrepancias entre los productos de inversión obtenidos mediante plano principal y almucantar son la exactitud de la medición y/o el modelo. Muchos autores se han concentrado en el tema de modelado, tratando de averiguar si las discrepancias entre los modelos y las medidas de radiancias cielo son el resultado de suposiciones incorrectas sobre la función de fase, forma, etc. (Gasteiger et al., 2011). Dada la experiencia antes mencionada de nuestro grupo, el presente análisis trata de arrojar algo de luz sobre la cuestión acerca de si los errores de en la medida pueden ser las causas de esta falta de coherencia en las inversiones.

Con el fin de analizar el efecto de los errores de la medida de radiancia sobre las propiedades de los aerosoles derivados, era necesario correr el algoritmo de Dubovik, utilizado dentro de la red AERONET. Esto fue posible gracias a la colaboración con el Dr. Oleg Dubovik en el marco del presente trabajo de investigación doctoral.

Objectivos

El objetivo principal de esta tesis es contribuir a la investigación de las causas que hay detrás de las discrepancias entre los productos de inversión obtenidos de plano principal y de almucantar, en concreto, examinar si pueden estar asociados con los errores en la medida de la radiancia.

De todas las fuentes posibles de error (por ejemplo, dependencias con la temperatura, los errores de reloj, reflectancia de la superficie ...) nos hemos centramos en el análisis de los errores de radiancia que están asociados a la calibración, al apuntamiento de los fotómetros y a la existencia de un campo de visión (FOV) finito en los fotómetros.

Es importante resaltar que los tres constituyen errores sistemáticos que no pueden ser eliminados mediante promedios u otros procedimientos estadísticos. si es posible, deben ser corregidos, de forma similar a como se mostró para los errores de calibración en las medidas directas al Sol mediante el método KCICLO (Cachorro et al., 2008). Sin embargo, no siempre es posible corregir los errores sistemáticos, por lo que se hace necesaria una evaluación cuantitativa de los mismos.

Estos errores se analizarán primero en términos de su efecto sobre la medida de radiancia, de manera cualitativa y cuantitativa, para después estudiar su impacto sobre las propiedades de los aerosoles que se obtienen por medio del algoritmo de inversión de AERONET; de entre todas las propiedades nos centraremos en la distribución del tamaño, el índice de refracción y el albedo de scattering simple.

Esquema de la tesis

Para cumplir con los objetivos, esta tesis está estructurada de la siguiente manera: en el capítulo 1, se exponen el contexto y los antecedentes relacionados con AERONET y la inversión de las medidas de radiancia de cielo.

El capítulo 2 ofrece una visión sobre las medidas de radiancia de cielo y las propiedades de los aerosoles para cuatro tipos principales considerados más adelante para hacer las simulaciones. Las características de estos aerosoles "tipo" derivan del análisis de climatología de AERONET, (Dubovik et al., 2002), en concreto para esta trabajo se han escogido: oceánico (modo grueso predominante, no absorbente), desértico (predominancia de modo grueso, absorbente), urbano (modo fino predominante, no absorbente) y la quema de biomasa (predominancia de modo fino, absorbente).

En el capítulo 3, se describe la naturaleza y la cuantificación de las tres fuentes de error que hemos considerado para el análisis. Las incertidumbres estimadas para cada error se han obtenido de la manera siguiente:

- *La calibración de radiancia, realizada con esferas integradoras calibradas, fue descrita en Holben et al. (1998). Este procedimiento es actualmente un poco más complicado, ya que el estándar de calibración se debe transferir de la NASA-Goddard a las otras instalaciones de calibración. Sin embargo, las mejoras en la calibración primaria de la NASA (por debajo del $3\,\%$) hace posible mantener el $5\,\%$ estimado de precisión en toda la red.*
- *El error típico de apuntamiento de los fotómetros de campo AERONET ha sido investigado en colaboración con la empresa Cimel. Dicha empresa ha desarrollado un nuevo tipo de medida que hemos introducido en la secuencia de medida rutinaria. Dentro de la tesis, hemos desarrollado un procedimiento para evaluar el error de apuntamiento de estas medidas. En la actualidad todas las estaciones de AERONET calibradas por RIMA-Valladolid están equipados con esta medida y el error de apuntamiento puede ser monitorizado junto con un conjunto más amplio de controles de*

calidad que se realizan rutinariamente.

- *Dos métodos se han utilizado para estimar el campo de visión de los fotómetros solares Cimel: el primero utilizando el sol como fuente y el segundo en el laboratorio con la ayuda de una fuente de láser.*

  Posteriormente, los capítulos 4, 5 y 6 describen el impacto de cada error: calibración, apuntamiento y campo de visión finito, respectivamente, primero sobre las medidas de radiancia de cielo, para después ver su efecto sobre las propiedades de los aerosoles obtenidos como productos de la inversión. El estudio consiste básicamente en la simulación de medidas de radiancia de cielo, a las que después se añaden las incertidumbres estimadas, siendo capaces así de cuantificar los efectos por separado. De esta manera el estudio podría ser considerado como un estudio teórico. Sin embargo, existe una estrecha relación con las medidas experimentales, debido a que son el conjunto de errores sistemáticos los que inspiran los umbrales y los valores típicos empleados a lo largo de las simulaciones.

La última parte de esta tesis doctoral contiene las conclusiones y las perspectivas que arroja el trabajo.

Chapter 1

Measurement and inversion of the sky radiance in the frame of AERONET

In this house we obey the laws of thermodynamics!

Homer Simpson

Resumen en español del capítulo:

Este primer capítulo tiene un marcado carácter descriptivo y está dividido en dos partes bien diferenciadas. La primera parte versa sobre la red AERONET, dentro de la cual se enmarca el presente trabajo; por otro lado, la segunda parte describe de manera más teórica y a partir de modelos históricos, en qué consiste el procedimiento actual de inversión de medidas fotométricas para la obtención de propiedades ópticas y microfísicas de los aerosoles utilizado por la red AERONET.

De este modo, la primera parte comienza con una descripción del contexto en el que se se creó y desarrolló AERONET, para dar posteriormente una visión general sobre en qué consiste la red, qué medidas realiza y qué productos ofrece. En este punto, se presenta la red RIMA (Red Ibérica de Medida de Aerosoles) federada dentro de la propia AERONET. Esta red posee una estación de calibración propia. El procedimiento de calibración para las medidas de irradiancia y de radiancia (éstandar dentro de AERONET) queda descrito también en esta primera parte del capítulo. El Grupo de Óptica Atmosférica de la Universidad de Valladolid es el encargado de dicho proceso en la red RIMA. Este grupo es responsable también de la administración general de la red, para lo cual ha desarrollado la herramienta CAELIS que es un software encargado de tratar todos los datos (y meta-datos) generados por los fotómetros de la red RIMA.

La parte que recoge los modelos de inversión comienza describiendo el procedimiento presentado en King et al. (1978) que deriva la distribución de tamaños, mediante valores de extinción de aerosoles obtenidas de medidas de irradiancia solar directa. En segundo lugar, se presenta la inversión descrita en Nakajima et al. (1996), la cual incorpora las medidas de radiancia de cielo al procedimiento de inversión. Por último, se muestra la inversión pormenorizada en Dubovik and King (2000) y actualmente utilizada en AERONET para obtener productos como la distribución de tamaños, el índice de refracción o el albedo de scattering simple, a partir de medidas de irradiancia solar directa y de radiancia de cielo.

1.1 The AErosol RObotic NETwork (AERONET)

1.1.1 Context

In the past decades, the study and knowledge of the atmospheric aerosol has demonstrated to have a great relevance, not only for its importance as atmospheric constituent, but also for its impact in many different aspects of the life on Earth (Solomon et al. (2007), IPCC, 2007). Indeed, aside from its importance as a pollutant (generated by industrialization and fossil fuel combustion), that has direct impact on ecosystems and human health, it has also been recognized for its influence on the global climate system. This effect is denoted as "aerosol radiative forcing" and includes the so-called direct effects, basically scattering and absorption of solar radiation, as well as indirect effects, by the modification of cloud properties (cloud lifetime, cloud albedo, precipitation, chemistry, etc.).

As explained in the introduction, the aerosol particles can be natural (sea salt, desert dust, volcanic ash) or anthropogenic (nitrates, sulfates, organics, carbonaceous, etc), or a mixture of both, with particle sizes ranging from few nanometers to hundreds of micrometers, thus leading to a complex and heterogeneous system with different physical, chemical and optical properties (Willeke and Baron (1993); D'Almeida et al. (1991)). This complexity makes necessary a multidisciplinary approach in the study of the aerosol, that implies integrating the use of very different methods and techniques.

In this wide context of the aerosol studies, we are focused on the measurement and study of the aerosol columnar properties using spectroradiometric techniques. These techniques are based on the interaction of the radiation with the physical material represented by the particles suspended in the atmosphere. The spatial and temporal variability of the aerosol concentration leaded to the establishment and development of measurement networks of different kind. In particular, there are several ground-based global remote sensing networks devoted to the aerosol monitoring. The most important are AERONET (Holben et al., 1998); PFR-GAW (Wehrli, 2005); and SKYNET (Takamura and Nakajima, 2004). The present PhD research work has been developed within RIMA (Toledano et al., 2011), which is part of AERONET.

1.1.1.1 General description.

The AErosol RObotic NETwork (AERONET, Holben et al. (1998)) program was started by the National Aeronautics and Space Administration (NASA) in the 90's, in collaboration with PHOTONS (Laboratoire d'Optique Atmosphérique-LOA, University of Lille), as a federation of networks with regional or national extent deployed on ground in the form of stations for monitoring atmospheric aerosols. AERONET aims at providing reliable monitoring of global aerosol optical and microphysical properties, to facilitate the characterization of the aerosol properties, the validation of satellite

products related to the aerosol as well the synergy with other instrumentation (lidar, surface radiation, in situ aerosol, etc.). The AERONET Synergy Tool, available at the AERONET website, is an example of integration of the AERONET observations with satellite data (MODIS, MISR, OMI, AIRS) lidar data from MPLNET, incoming solar radiation (SolRAD), back-trajectories, aerosol models (GOCART, NOGAPS), etc.

According to the AERONET website, "the program provides a long-term, continuous and readily accessible public domain database of aerosol optical, microphysical and radiative properties for aerosol research and characterization". For this purpose, the network imposes standardization of instruments, measurements, calibration, processing and data distribution. The standardization is a key characteristic of AERONET, that allowed its great expansion and wide usage in the scientific community.

The standard AERONET instrument is the Cimel Electronique 318. This is an automatic sun and sky radiometer, equipped with 8 or 9 spectral channels covering the spectral range 340-1640 nm. It performs both direct Sun measurements and sky radiance observations in the almucantar and principal plane configurations. There exist different versions within the network: old analog photometers (standard and polarized versions with 8 channels), digital 8-channel photometers (standard and polarized) and finally the Short Wave Infrared (SWIR, also called "extended" instruments, with 9 channels) and the dual polar photometers. It is not intended here to provide an exhaustive description of each model. We will just remark that, independently of the version, all instruments operating within AERONET are equipped at least with the spectral channels 440, 670, 870, 936 nm and 1020 nm. Apart from these, each version may have additional channels, such as 500 nm, 1640 nm, ultraviolet (340, 380 nm) or polarized channels. However the four common channels are the core of the measurement protocol.

The measurement sequence is standardized within AERONET. The preprogrammed sequence of measurements starts at an air mass of 7 in the morning and ends at an air mass of 7 in the evening (approximately 8° solar elevation). It consists of a series of direct sun and sky radiance measurements at fix solar elevations during sunrise and sunset (called "Langley sequence"). For solar zenith angles below 60° (air mass of 2), direct Sun measurements are performed every 15 minutes and sky radiances are acquired every hour in the almucantar and principal plane configurations. A sequence of three such direct Sun measurements are taken 30 seconds apart creating a triplet observation per wavelength. The time variation of clouds is usually greater than that of aerosols causing an observable variation in the triplets that can be used to screen clouds in many cases. Additionally the 15 minute interval allows a longer temporal frequency check for cloud contamination. There is an operational cloud-screening algorithm in AERONET, fully described by Smirnov et al. (2000).

The calibration is carried according to a strict protocol, which is the base of the data quality

assurance in the network. The instruments are calibrated before and after deployment in the field. The operation period is approximately 1 year. The field instruments are calibrated by comparison with master instruments, which are instruments that meet high operating standards and are calibrated at high altitude stations (Mauna Loa Observatory in Hawai (USA), Izaña in Canary Islands (Spain)). AERONET has distributed calibration facilities, that include both the intercalibration for the direct Sun channels and the radiance sphere calibration for sky channels. Intercalibration sites are: GSFC, Carpentras and Autilla. More details about the calibration procedure are provided below.

All AERONET data are automatically sent to GSFC (via satellite or internet) to be processed by a common algorithm. A preprocessing converts data from the different sources in a unique format and stores them in a database, producing reports about the instrument status that are posted in the webpage. Then, the data are processed and uploaded to the website in near real time. Level 1.0 data are unscreened and level 1.5 are cloud-screened, although these may not have the final calibration applied and therefore they are not quality assured. After the calibration post-deployment, the data are reprocessed (assuming linear change rate in the calibration coefficients) and manually inspected, following a set of criteria (`http://aeronet.gsfc.nasa.gov/new_web/PDF/AERONETcriteria_final1.pdf`). If the data fulfill the crieria, they are raised to the level 2.0 (quality assured data). Since 2006 the Version 2 Direct Sun and Inversion Algorithm is operational. Details and the corresponding references are provided in the AERONET website (`http://aeronet.gsfc.nasa.gov/new_web/data.html`).

The data are distributed through the AERONET website, with a clear data policy that must be accepted by the user before downloading data. The unique source of data ensures that the latest version of the data processing is used. It must be noted that AERONET remarks that only level 2.0 data are quality assured for scientific research. However this data level is only available when the instrument is returned to the calibration facility after an operation period, therefore it may take months to have it available. Applications that need near-real time data may use level 1.0 or level 1.5 data, but those need to be handled with care.

After several years of continuous measurements, to provide information about aerosol climatologies at key sites is now possible (Eck et al. (1999), Holben et al. (2001); Smirnov et al. (2002a); Dubovik et al. (2002)). There is great interest within the AERONET managers that the sites provide long-term high quality datasets, so that an increasing number of sites can provide consistent local climatologies, that may help in satellite and model validation. As for January 2012, only 13 out of more than 750 AERONET sites listed in the webpage have more than 7 years of level 2.0 data.

1.1.1.2 RIMA & CAELIS.

The Iberian network for Sun photometer aerosol measurements (RIMA, Red Ibérica de Medida fotométrica de Aerosoles, Toledano et al. (2011)) is a scientific network, that was created in 2004 with the aim of promoting the collaboration among several Spanish institutions devoted to the measurement and analysis of the aerosol properties. The scientific objectives of RIMA are the same as those described for AERONET. Since 2006, RIMA has a calibration facility for Cimel sun photometers, located in Valladolid, Spain. The calibration process and network management are carried out by the Group of Atmospheric Optics of the University of Valladolid (GOA-UVa) in collaboration with the Izaña Atmospheric Research Center (AEMET). This calibration work is possible thanks to the large support that is provided by GSFC-NASA and PHOTONS. The RIMA master instruments are calibrated at Izaña in collaboration with PHOTONS.

The GOA-UVa group has developed in the last years a set of tools that are needed for the operation and management of RIMA subnetwork. The CAELIS system (`www.caelis.uva.es`) is a software developed for managing all data and meta-data generated by RIMA sun photometers. The software is designed with a core to which are connected a set of different tools for data acquisition real time processing, that are driven by a task manager capable to set their priority and organize them. The system is also provided with a relational database in which the data are stored and classified. The database allows powerful search and extraction of data for multiple applications. The two main purposes of CAELIS are the automated control of RIMA instruments and sites; and the provision of data for research purposes. All the information generated by the system is offered to the users through a web interface.

In this web interface the users can access multiple information related with radiometric measurements. The first service provided through this system is a tool for site managers and researchers in the frame of AERONET: site description; real-time information to track the status of the photometers (e.g. location, measurement periods, calibration coefficients, instrumental issues, etc.); access AERONET data (via AERONET site); and documentation about instruments, failures and troubleshooting.

Currently, RIMA includes 30 instruments and 20 sites located in the Iberian Peninsula, the Canary Islands, North Africa, Norway, Finland, Germany, Italy and Cuba. In the frame of the cooperation with PHOTONS, several stations and instruments are under the shared responsibility of both networks (e.g. Huelva). This cooperation has been even stronger since the approval of the European Infrastructure project ACTRIS (`www.actris.net`) belonging to the 7 th European Framework Programme, that unifies PHOTONS-RIMA-IZAÑA in a unique calibration platform named AERONET-EUROPE.

During 2011, the CAELIS system has been enhanced to integrate data from other sources

apart from RIMA. For example, water vapor from GPS and meteorological information are now assimilated and stored in the database. This has largely enhanced the research capabilities, by combining multiple datasets in the fashion of the AERONET synergy tool.

1.1.2 Direct Sun measurements

The direct sun measurements at each spectral channel $F(\lambda)$ allow the determination of the total optical depth of the atmosphere (τ); this magnitude can be understood as the attenuation of sunlight passing through the atmosphere containing aerosol particles, molecules, and absorbing gases and is described by the well-known Lambert-Beer Law, which states that the monochromatic direct solar flux density F ($Wm^{-2}\mu m^{-1}$) in the Earth's surface can be expressed as:

$$F(\lambda) = F_0(\lambda)e^{-m_s\tau} \tag{1.1}$$

where F_0 is the flux at the upper limit of the atmosphere, τ is the total optical thickness and m_s is the optical air mass that can be approximated as $m_s = 1/\cos\theta_s$ while $\theta_s \leq 75^o$ (exact formulation can be found in Kasten and Young (1989)).

Under cloud-free conditions, the total optical thickness can be separated into the gaseous absorption τ_g, the molecular scattering or Rayleigh scattering τ_R, and the aerosol scattering and absorption τ_a. Therefore, the aerosol optical depth (AOD or τ_a) can be derived from the total optical depth discounting the Rayleigh optical thickness (τ_R), which is known for a standard atmosphere and can be corrected by local pressure (P), and the gaseous absorptions (τ_g):

$$\tau_a = \tau - \tau_R\frac{P}{P_0} - \tau_g \tag{1.2}$$

However, the atmospheric components are not equally distributed in the atmospheric profile, so the air mass is different for each one. This is especially true at large SZA. Thus, considering different air masses for each element, we obtain:

$$F(\lambda) = F_0(\lambda)e^{(-\tau_a m_a - \tau_R\frac{P}{P_0}m_R - \tau_g m_g)} \tag{1.3}$$

This is the expression used in AERONET version 2 direct sun algorithm.

The AOD data at different wavelengths allow the determination of the Ångström exponent (α) (Angstrom, 1961), according to:

$$\tau_a(\lambda) = \beta \cdot \lambda^{-\alpha} \tag{1.4}$$

The water vapor column abundance is retrieved by means of a channel centered in the 936 nm-absorption band. The rest of the channels are used for retrieval of the aerosol optical depth, therefore centered at wavelengths with few or no absorption by atmospheric gases (see table 1.1).

Table 1.1: Observation wavelengths of Cimel-318 sun photometers. All channels are used for direct Sun observations. Channels denoted with asterisk (*) are used for sky radiance measurements (almucantar and principal plane).

Instrument type	Spectral channels (nm)
Standard (analog. and digital)	340, 380, 440*, 500, 670*, 870*, 936, 1020*
Extended	340, 380, 440*, 500*, 670*, 870*, 936, 1020*, 1640*

1.1.2.1 Calibration of direct Sun channels

The extraterrestrial signal $F_0(\lambda)$ is the calibration coefficient for each spectral channel. As explained above, field instruments are calibrated by comparison (inter-calibration) with master instruments previously calibrated at high altitude stations. The accuracy of the master calibration is about 0.5%, whereas for field instruments the calibration uncertainty is $1-2\%$ (larger for shorter wavelengths) due to uncertainty in the calibration transfer (Holben et al., 2006)).

The inter-calibration procedure is based on the realization of simultaneous co-located measurements of the master and the instruments to calibrate under certain atmospheric conditions. These restrictions are established to ensure enough stability in the atmosphere to minimize the uncertainty of the inter-calibration procedure: clear sky and aerosol optical depth (440 nm) stable at noon and below 0.3. Other restrictions are imposed, such as the availability of enough co-located measurements to ensure the stability of the ratios between master and field instrument over a wide range of air masses. When this conditions are fulfilled the field instrument can be calibrated just by a ratio of raw signals of each channel ($F_{field}(\lambda)$) with the master raw signal ($F_{master}(\lambda)$):

$$F_{0_{field}}(\lambda) = F_{0_{master}}(\lambda)\frac{F_{field}(\lambda)}{F_{master}(\lambda)} \tag{1.5}$$

The calibration of the master instruments is carried out by the Langley plot method (Shaw, 1983). This method, based on the Beer-Bouguer-Lambert law is used to derive the extraterrestrial signal of the instrument by means of a set of direct sun observations performed over a range of air masses (typically from 7 to 2):

$$\ln F(\lambda) = \ln F_0(\lambda) - \tau m_s \tag{1.6}$$

The measurements provide a straight line ($\ln F$ vs. m_s), from whose intercept ($\ln F_0(\lambda)$) the extraterrestrial signal (F_0) can be extracted. The main requirement for this method to provide accurate calibration is that the total optical thickness of the atmosphere (τ) remains constant

during the set of measurements. The components with more rapid changes are water vapor and the aerosol particles, once we restrict our observations to cloud-free conditions. Therefore high altitude stations, located high above the boundary layer, are very adequate for this Langley absolute calibrations, because both the aerosol and the water vapor content are low and may be often considered constant. Another characteristic of a good location for Langley calibration is the low latitude, preferably close to the tropics. This reduces the time of the sunrise (change of air mass from 7 to 2) or sunset, facilitating the assumption of constant total optical thickness.

With these apparently simple restrictions (frequent clear sky, clean atmosphere, high altitude, low latitude and the necessary infrastructure), very few locations worldwide are available for routine Langley calibration. AERONET calibrates its masters in the Mauna Loa Observatory (19.5° N-155.6° W, 3397 msl), whereas PHOTONS and RIMA calibrate their masters at Izaña Observatory (18.3° N-16.5° W, 2373 msl).

The water vapor channel (936 nm) suffers from larger atmospheric variations than the pure aerosol channels. Furthermore, the strong absorption of solar radiation by this component requires a special treatment: the so-called "Modified Langley Method" (Michalsky et al., 1995).

1.1.2.2 Data products.

The primary product derived from the direct Sun observations is the spectral aerosol optical depth or thickness (AOD). Together with that, column water vapor abundances are also provided, as well as the Ångström exponents in various wavelength ranges.

In version 2, the total optical depth and the various components and obtained correcting the data of Rayleigh, O_3, NO_2, etc. are also provided.

Finally, the Spectral Deconvolution Algorithm (O'Neill et al., 2003) provides separation of the fine and coarse mode optical depths, thus the fine mode fraction of the AOD.

A description of all products is provided in the AERONET website (`http://aeronet.gsfc.nasa.gov/new_web/data_description_AOD_V2.html`). Column header and data units for all data products are given too (`http://aeronet.gsfc.nasa.gov/new_web/units.html`).

1.1.3 Sky radiance measurements

The acquisition of multi-wavelength and multi-angle sky radiances is the base for the retrieval of optical and microphysical properties of the aerosol particles, such as size distribution, single scattering albedo, refractive index and phase function. The retrieval of such properties is complex and requires the application of inversion algorithms (see section 1.2). The accuracy and quality

control of the radiance measurements is basic for the quality of the inversion-retrieved properties. This issue is the main topic of this PhD research, and will be developed along this report.

1.1.3.1 Measurement protocol

There are two geometries followed within AERONET to carry out the sky radiance measurements: almucantar and principal plane. As mentioned, all instruments within the network utilize at least the four standard spectral channels: 440, 670, 870 and 1020 nm. Apart from these, each version of the photometers may measure with additional channels, such as 500 or 1640 nm (see table 1.1), or polarized channels at 870 nm.

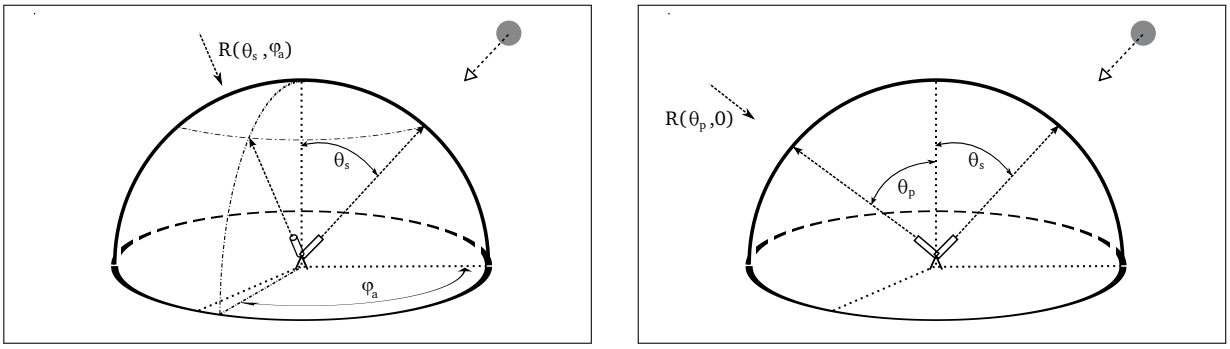

Figure 1.1: Figures describing the two geometries used within AERONET network for the measurements of the sky radiances: on the left, the almucantar is represented while the principal plane appears on the right.

In the almucantar configuration, figure 1.1 on the left, the sun-photometers keep the zenith angle constant (equal to the solar zenith angle θ_s). The measurement sequence previously executes a direct Sun measurement, and then the instrument covers the whole range of azimuth angle, starting at 3° and finishing at 180°. The movement is done first towards right (taking the sun as reference) and then, after pointing the Sun again, is repeated towards the left. The observation angles are the same for both branches and are contained in table 1.2 in the row addressed for almucantar description. The sequence is repeated for each of the channels and the entire measurement takes about 5 minutes, depending on the instrument version.

Assuming an homogeneous atmosphere, the measurements taken in both branches right and left can be considered symmetrical and the final radiance values used in the AERONET inversion algorithm for the almucantar are obtained making the average between them. This operation procedure is exclusive for almucantar geometry, and theoretically, confers higher quality on the data. For instance, this process allows to eliminate those data contaminated by clouds: those measurements with radiances differences higher than 20% between right and left branches are eliminated (this and other criteria are described in `http://aeronet.gsfc.nasa.gov/new_web/Documents/AERONETcriteria_final1_excerpt.pdf`)

Table 1.2: Observation angles for sky radiance measurements in the almucantar and principal plane geometries. In the almucantar, angles are azimuth positions relative to the azimuth solar position (with 2 branches, right and left from the Sun). In the principal plane, angles are zenith angles relative to the zenith solar position (negative means below the Sun). Note the double observation at 6°, indicating the change from Aureole to Sky channels.

Measurement type	Observation angles
Almucantar	0° 2.0°, 2.5°, 3.0°, 3.5°, 4.0°, 4.5°, 5.0°, 6.0°, 6.0°, 8.0°, 10.0°, 12.0°, 14.0°, 16.0°, 18.0°, 20.0°, 25.0°, 30.0°, 35.0°, 40.0°, 45.0°, 50.0°, 60.0°, 70.0°, 80.0°, 90.0°, 100.0°, 110.0°, 120.0°, 130.0°, 140.0°, 160.0°, 180.0°
Principal plane	0° -6.0°, -5.0°, -4.5°, -4.0°, -3.5°, -2.5°, -2.0°, 2.0°, 2.5°, 3.0°, 3.5°, 4.0°, 4.5°, 5.0°, 6.0°, 6.0°, 8.0°, 10.0°, 12.0°, 14.0°, 16.0°, 18.0°, 20.0°, 25.0°, 30.0°, 35.0°, 40.0°, 45.0°, 50.0°, 60.0°, 70.0°, 80.0°, 90.0°, 100.0°, 110.0°, 120.0°, 130.0°, 140.0°

In the principal plane geometry, figure 1.1 on the right, the azimuth angle is the one that remains constant (and equal to the solar azimuth) and the instruments, after a direct Sun measurement again, take the sky radiance measurements from the different zenith angles depicted in table 1.2. There is not possibility in this case of applying any criterion of symmetry because the different airmass and variable contribution of the surface albedo make the principal plane not to be symmetric with respect to the solar position. Even though the current AERONET database does not offer any retrieval data from the principal plane measurements, all the approaches to the study have been made using only the data obtained from "positive" angular values of table 1.2. This positive sign is given to the movement of the instrument from the Sun towards the zenith.

It is interesting to mention here the relation between the scattering angle (Θ), the solar zenith and azimuth[1] angles (θ_s,φ_s) and the observation angles θ_v and φ_v (Nakajima et al., 1996):

- In the case of almucantar geometry: $\cos(\Theta) = \cos^2(\theta_s) + \sin^2(\theta_s)\cos(\varphi_v - \varphi_s)$
- In the case of principal plane geometry: $\cos(\Theta) = \cos(\theta_v \mp \theta_s)$ The signs: $(-)$ in the case of $(\varphi_v - \varphi_s = 0°)$ and $(+)$ for the case of $(\varphi_v - \varphi_s = 180°)$.

As a consequence, the observation angle in the principal plane coincides with the scattering angle, whereas in the almucantar the scattering angle depends on both the solar zenith angle and the azimuth (observation) angle. The scattering angle observed with the almucantar geometry is limited by $0^o \leq \Theta \leq 2\theta_s$ reaching its maximum ($2\theta_s$) at $\varphi_s = 180°$. On the other hand, the maximum value of the scattering angle in the principal plane measurement is the maximum angle (θ_M) from the principal plane set of values (see table 1.2) which fulfills that $\theta_M - SZA < 90°$[2]. This fact has important consequences in the retrievals, and it will be further analyze in chapter 2.

To end up, we just briefly indicate that the almucantar and principal plane measurements are acquired each hour. In former times, these sequence was maintained throughout the day. However

[1] Normally, the azimuth origin is taken in the sun position and therefore $\varphi_s = 0$. Note that this assumption was made in figure 1.1

[2] More than 90° would mean to measure the ground

the new models do not perform almucantar scans in the middle of the day if the SZA is below 40° (the reasons will be clearly shown in the next chapters).

1.1.3.2 Calibration of sky radiance channels

The sky radiance observations are acquired with two different gains (or amplification). Low gain is used close to the Sun, due to the higher radiance in the aureole region. Those are called "Aureole" channels. After 6° observation angle (azimuth in the almucantar or zenith in the principal plane), the instrument changes to the high gain channels, called "Sky" channels. At 6° the observation is made with both channels, allowing to perform consistency checks, since aureole and sky channels have independent calibration coefficients.

Actually, standard instruments measure aureole and sky radiances with different physical channels (collimator, optics, detector). The ratio Aureole/Sky (or A/K ratio) at 6° can be therefore used to detect obstructions in one of the collimators or front windows (which are unfortunately very frequent, due to insects, spider webs, humidity, etc.). Conversely, extended instruments measure aureole and sky with the same physical channel (thus they are called "monochannel sun photometers"). For these instruments, the A/K ratio cannot be used to detect obstructions because some obstruction would affect the aureole and the sky channel equally (although differently in general for each wavelength).

The radiance calibration is made with an integrating sphere (uniform radiance source). This sphere is in turn calibrated with a traveling master instrument, which is calibrated at GSFC Calibration Facility to a NIST standard. Field instruments are calibrated in radiance before and after a deployment period (same as the sun channel calibration). The integrating sphere is calibrated with the traveling master every 3 months. Several spheres are operational at the three calibration facilities (GSFC, Lille, Valladolid), with diameters in the range $8 - 20$ inch, 2 to 4 lamps and different port sizes and output radiances.

In the calibration procedure, the photometer is placed in front of the sphere port and radiances are acquired in all aureole and sky channels. Then the calibration coefficients are calculated as the ratio between the raw signal at each channel (4 aureole and 4 sky in the standard instruments; 6 aur+6 sky in extended instruments) and the output radiance at the given wavelength. The main precaution in this procedure is that the sphere output must be stable, therefore it is necessary to wait some minutes for the lamps to stabilize. The aging of the lamps must be controlled to avoid miscalibration due to degradation.

1.1.3.3 Data products.

There is a large set of optical and microphysical parameters that are derived with the version 2 operational inversion algorithm. They are presented in table 1.3. The complete list of radiance and inversion products is given in the AERONET website (`http://aeronet.gsfc.nasa.gov/new_web/units.html`). As mentioned, only almucantar measurements are used in the operational inversion algorithm.

Table 1.3: Aerosol Inversion Retrievals from Sun-Sky Radiance Measurements. List of products and data units.

Magnitude	Units
Size Distribution dV(r)/dln r	$\mu m^3/\mu m^2$
Single Scattering Albedo	None
Refractive Index (real part)	None
Refractive Index (imaginary part)	None
Volume Concentration	$\mu m^3/\mu m^2$
Volume Median Radius	μm
Effective Radius	μm
AOD Extinction	None
AOD Absorption	None
Phase Functions	None
Asymmetry Factor	None
Broadband Flux (Downward/Upward at BOA and TOA)	W/m^2
Spectral Flux (Downward/Upward/Diffuse)	W/m^2
Radiative Forcing (BOA and TOA)	W/m^2
Radiative Forcing Efficiency (BOA and TOA)	W/m^2
Sphericity Parameter	%

Besides these products, the file containing data also includes several quality control parameters, such as the number of symmetrical angles in the almucantars, the retrieval error, the solar zenith angle and the measured optical depth in the coincident direct sun observation.

The level 2.0 inversion products must fulfill a set of requirements that are described by Holben et al. (2006) and `http://aeronet.gsfc.nasa.gov/new_web/Documents/AERONETcriteria_final1_excerpt.pdf`.

1.1.4 Present issues within AERONET

Several issues related with the inversion data are currently investigated within the AERONET community. As indicated in the introduction to the thesis, almucantar and principal plane retrievals present differences that may be attributed to measurement errors or model inaccuracies. As also commented in the introduction the principal plane retrievals, initially included in version 2, were removed from the AERONET database. Therefore, the principal plane retrieval can not be used to fill the gap between morning and evening almucantar retrievals, which are robust only at large SZA.

There are also known limitations in the inversion of sky radiances, especially related to the large uncertainty of the retrieved products from almucantar scans at low solar zenith angles (SZA) and/or at low aerosol optical thickness conditions. The retrieval of quality assured (level 2.0) optical parameters such as single scattering albedo is limited to moderate optical depths ($AOD_{440nm} > 0.4$. Therefore this and other key parameters for aerosol radiative forcing calculation are not provided at SZA smaller than 50° or $AOD_{440nm} < 0.4$. This means, for instance, that sites in Spain only provide single scattering albedos during occasional desert dust or biomass burning events, but no information from these parameters is provided for the typical background aerosol.

The case shown in figure 1.2 is an example of inconsistent almucantar retrievals in AERONET. It was detected in the Hamim site (Saudi Arabia) (Dubovik, 2009). Basically it consists in the unexpected change obtained in the inversion derived properties during the day (e.g. diurnal variability of the single scattering albedo) while the aerosol optical thickness and Angstrom parameter remain constant along the day, indicating no significant change in the aerosol amount or type.

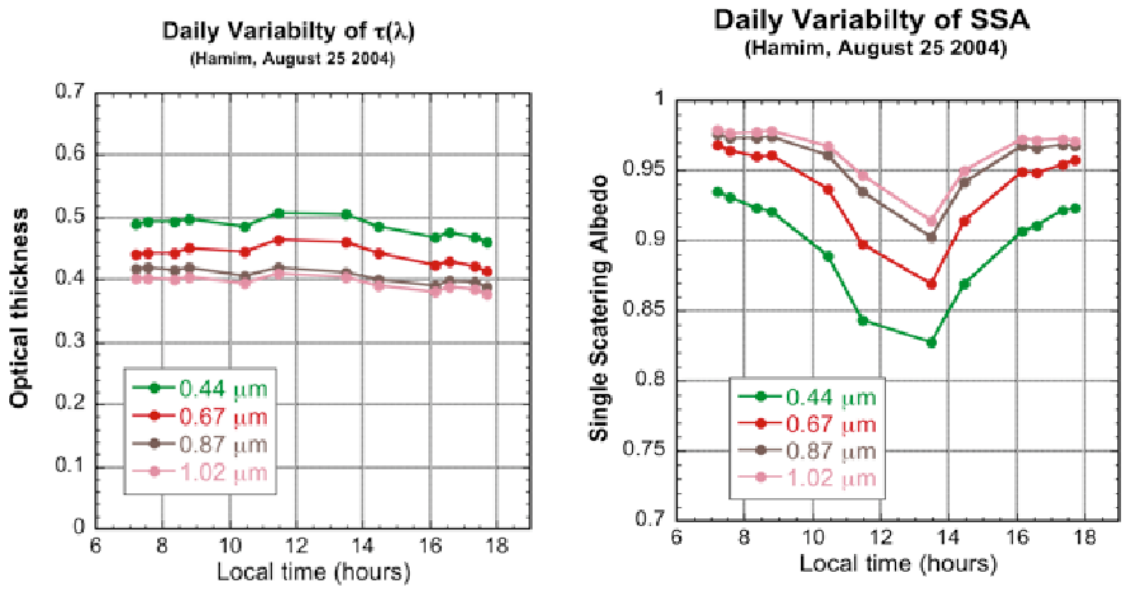

Figure 1.2: Figures extracted from Dubovik (2009). The AOD (left) and the ω_o (right) at four wavelengths channels from Hamim site during 25th August of 2004 are represented.

Figure 1.2 shows the AOD (left) and the single scattering albedo (right) of Hamim station (Saudi Arabia) on August 25th, 2004. It can be observed that the AOD for the channels keeps almost a constant value during the day whereas the $omega_o$ has a decrease of 10%. The reason behind this variation is the limited range of observed scattering angles in the almucantar at short SZA, as it will be shown in chapter 2 (self-consistency studies). However other hypotheses that could amplify the effect need to be considered as well (calibration, pointing, aureole/sky discrepancy).

Currently, the errors associated to AERONET products are based on the analysis of Dubovik and King (2000), which was realized for the first version of the algorithm. There is no specific

documentation concerning the errors for the second version of the algorithm. To these difficulties (technical difficulties of the measurements on one hand, and complexity of scientific models on the other hand) concerning radiometric measurements, it must be added the occasional discrepancies with aerosol observations based on more direct techniques (e.g. in situ and sampling). All these facts support the crucial need to establish the quality of inversion products, by carrying out an analysis of the error sources affecting the original measurements, such as the quantification of the sensitivity of the models that are used to derive these errors estimations.

With these purposes some works have been conducted. Olmo et al. (2008) used the analysis of principal plane with a different inversion algorithm to compare with AERONET retrievals of the same radiance measurements. Other groups, such as the participants in the SAMUM project (Mueller et al., 2010a,b) have found agreements but also important discrepancies between optical and microphysical properties of aerosols observed using in situ techniques in comparison to those obtained with inversion methods.

The GSFC-NASA has recently accomplished the Distributed Regional Aerosol Gridded Observational Network (DRAGON) campaign. In it, a gridded network of approximately 50 sun photometers between Washington DC and Baltimore was established in July 2011. Other lidar and ground based spectrometers participated, as well as three aircraft instrumented with in situ airborne aerosol samplers, overflying the ground-based network. This experiment was also conducted with the purpose of comparing sun photometer retrievals with other sources of measurements, including satellite, aircraft and ground-based in situ, and was a unique opportunity to carefully compare in situ to remote sensing instruments and provide state of the art validation.

1.2 Inversion methods

Light scattering by the atmospheric aerosols modifies the diffuse and direct solar radiation observed at the Earth's surface. If the atmospheric characteristics were known, including the vertical distribution of aerosols and their optical and microphysical properties, the radiation measured by the sun-photometers could be simulated with a high degree of accuracy (in the absence of clouds), using any of the so-called forward (or direct) methods (Kokhanovsky et al., 2010).

However, the problem arises because we need to infer the size distribution and optical properties of aerosol particles from the ground-based measurements of diffuse and direct solar radiation. This problem is tackled by the so-called "inversion" procedure that utilizes an inverse transformation by recovering unknown input parameters of the forward model (aerosol properties) from known output of the forward model (the set of base-ground measurements, normally given for different wavelengths and scattering angles as we saw for the AERONET-network).

Theoretically, the best solution of the problem is given by the best fitting set of aerosol parameters through the continuous space of all possible solutions. Unfortunately, often several different combinations of aerosol parameters produce the same, or nearly the same, radiation distribution. Therefore, the general solution is fundamentally nonunique or becomes nonunique in the presence of minor measurement noise.

Nevertheless, most of the possible solutions are often disastrously poor, in the sense that the solution oscillates or displays some other features which conflict with a priori knowledge of the aerosol properties (Phillips, 1962). Using this idea, we can try to solve the multiple solution problem by introducing, in an appropriate way, the a priori information at our disposal.

For example, the inversion procedure presented by Dubovik and King (2000) proposes adding a priori assumptions on smoothness of the size distribution or spectral smoothness of the optical properties in the inversion procedure to constrain the solution while reproducing the measurement field within the error bars established for the measurements. This method is the one used in AERONET network to retrieve the aerosol properties from the measurements of the ground-based CIMEL sun-photometers. As this PhD-thesis is framed in the AERONET scope, all the tests that will be presented to investigate the effects of the sky-radiance errors in the aerosol retrievals will be made using this inversion code.

As a consequence, the subsection 1.2.3 will be entirely dedicated to a better description of this methodology. But before, we will present two previous inversion methods in subsections 1.2.1 and 1.2.2, mainly for two reasons: first, they inspire some of the assumptions used later by Dubovik and King (2000). Second, their study allows us to introduce some useful concepts of the aerosol science.

The inversion proposed by King et al. (1978), presented in subsections 1.2.1, utilizes direct measurements, so apart of commenting the inversion, some of the aerosol optical properties related to the direct measurements which were not presented in subsection 1.1.2 will be in parallel described. On the other hand, the inversion presented by Nakajima et al. (1996), discussed in subsection 1.2.2, uses the sky radiances and thus gives us a chance to describe new properties related to the diffuse radiation.

1.2.1 King's inversion

1.2.1.1 Defining the problem

In this subsection we present the inversion proposed by King et al. (1978) which uses the aerosol optical thickness to derive the aerosol size distribution. As we commented in subsection 1.1.2, the aerosol optical thickness is obtained by means of the comparison of the direct sun measurements

and the extraterrestrial radiation Eq. (1.1). The aim here is to obtain the aerosol size distribution from this parameter. The integral equation which relates the aerosol optical depth and the aerosol size distribution, can be written as:

$$\tau_a(\lambda) = \int_0^\infty \int_0^\infty \pi r^2 Q_{ext}(\chi, m) n(r, z) dz dr \tag{1.7}$$

This relation is obtained after applying Mie scattering theory, where the aerosol is considered to consist of homogeneous spherical particles which are non-dispersive over the wavelength range of observations. In the Eq. (1.7), $n(r, z)dr$ is the height-dependent aerosol number density in the radius range $r + dr$, m is the refractive index of the aerosol particles and Q_{ext} is the extinction efficiency factor from Mie theory which depends on the refractive index, the wavelength of the incident illumination (λ) and the aerosol radius. Normally, these last two parameters are grouped together and known as Mie's parameter defined as $\chi := \frac{2\pi r}{\lambda}$.

If we define the columnar aerosol size distribution n_c as the number of particles per unit area per unit radius interval in a vertical column through the atmosphere, we can rewrite Eq. (1.7) as follows:

$$\tau_a(\lambda) = \int_0^\infty \pi r^2 Q_{ext}(\chi, m) n_c(r) dr \tag{1.8}$$

Since an expression for $n_c(r)$ cannot be written analytically as a function of the $\tau_a(\lambda)$ values (solving Eq. (1.8)) a numerical approach must developed. Therefore we need to make some transformations to Eq. (1.8):

1. Replace the integral by a summation over coarse intervals in r, as it is described in Herman et al. (1971). In this case, we will take q intervals.
2. Establish finite limits of integration with $r_1 = r_a$ and $r_{q+1} = r_b$.

With these two approximation we obtain:

$$\tau_a(\lambda) \simeq \int_{r_a}^{r_b} \pi r^2 Q_{ext}(\chi, m) n_c(r) dr \simeq \sum_{j=1}^{q} \int_{r_j}^{r_{j+1}} \pi r^2 Q_{ext}(\chi, m) n_c(r) dr \tag{1.9}$$

where the kernel function of optical thickness can be defined as $K_\tau := \pi r^2 Q_{ext}(\chi, m)$, and computed from Mie theory (if we know the refractive index) in every interval (r_j,r_{j+1}). Hence, if the columnar aerosol size distribution is known and the refractive index estimated with reasonable accuracy, the aerosol optical thickness can readily be computed. This is the forward problem and generally poses no difficulty using modern computers.

Because K_τ increases monotonically with radius, but the size distribution generally decreases rapidly with radius, it is convenient to rewrite Eq. (1.9) in terms of a volume size distribution $\nu_c(lnr) = dV_c(r)/dlnr$ representing the volume of particles per unit area per unit log radius interval in a vertical column through the atmosphere. Thus we obtain

$$\tau_a(\lambda) = \sum_{j=1}^{q} \int_{\ln r_j + \frac{\Delta \ln r}{2}}^{\ln r_j - \frac{\Delta \ln r}{2}} \frac{3}{4\pi r^3} K_\tau(\chi, m)\ \nu_c(\ln r) dr \tag{1.10}$$

where we have rearranged the q intervals giving them the same longitude in terms of $\ln r$.

If, now, we have p measurements of the aerosol optical depth, $\tau_a(\lambda_i) = g_i$ with $i = 1 : p$, and we assume, $\nu_c(\ln r) = f_j$, constant within each interval, a system of linear equations can be established as:

$$\mathbf{g{=}Af} \tag{1.11}$$

This last equation would represent the mathematical formulation of the spectral aerosol optical thickness as a function of aerosol size distribution for a measurement with no error. Evidently, we need to consider an error for τ_a at each wavelength defined as $\epsilon_i = \epsilon(\lambda)$, and the Eq. (1.11) gets the form:

$$\mathbf{g{=}Af{+}\boldsymbol{\epsilon}}$$

$$\begin{pmatrix} g_1 \\ g_2 \\ ... \\ g_i \\ ... \\ g_p \end{pmatrix} = \begin{pmatrix} A_{11} & A_{12} & ... & ... & A_{1q} \\ A_{21} & A_{22} & ... & ... & A_{2q} \\ ... & ... & A_{ij} & ... & ... \\ A_{p1} & A_{p2} & ... & ... & A_{pq} \end{pmatrix} \begin{pmatrix} f_1 \\ f_2 \\ ... \\ f_j \\ ... \\ f_q \end{pmatrix} + \begin{pmatrix} \epsilon_1 \\ \epsilon_2 \\ ... \\ \epsilon_i \\ ... \\ \epsilon_p \end{pmatrix} \tag{1.12}$$

where we have stabled A_{ij} as,

$$A_{ij} = \int_{\ln r_j + \frac{\Delta \ln r}{2}}^{\ln r_j - \frac{\Delta \ln r}{2}} \frac{3}{4\pi r^3} K_\tau(r_j, \lambda_i, m) dr \tag{1.13}$$

1.2.1.2 Minimization of the errors. Inversion procedure

Before starting the discussion, let us go back to Eq. (1.11) where the errors in the measurement were not assumed. If now we choose q equal to the number of the measurements p, we obtain a system of linear equations with unique solutions if the rows of matrix A are linearly independent and different from zero (Rouche-Capelli theorem). The solution is derived inverting the matrix A:

$$\mathbf{f}=\mathbf{A^{-1}g} \tag{1.14}$$

Observe at this point, that applying this methodology to real cases with errors in the measurements (or/and the errors derived from the discretization process) the uncertainty in the products will be given by:

$$\mathbf{\Delta f}=\mathbf{A^{-1}}\boldsymbol{\epsilon} \tag{1.15}$$

The last comment about this idealized inversion refers to the independent linearity of matrix A. Note that an stable form of A^{-1}, and therefore of the solution f, is acquired if the rows of the A matrix are linearly independent and very different. However, the kernel function an individual measurement using the standard wavelengths (e.g. AERONET from 440 nm to 1020 nm) is broad and overlapping, and as a consequence the rows of the A matrix differ little from one another and being nearly linearly dependent. Using the aerosol optical thickness derived from AERONET, the integral over radius for discrete radii intervals (that produces rows of A), leads to tremendous overlap, especially when $r > 1.5\mu m$.

Recovering the expression with errors, it seems obvious that to solve the problem, we will need to minimize the error vector $\boldsymbol{\epsilon}$. In study presented by King et al. (1978), the author refers to the works by Phillips (1962) and Twomey (1965) where is discussed the instability in the solution vector $\boldsymbol{f}$ which results if Eq. (1.12) is directly solved by minimizing $\sum_i \epsilon_i^2$. For this problem, the inversion presented by King et al. (1978) uses the suggestion previously proposed in the work of Phillips (1962) where the author introduces a constraint to discriminate against such instability. This constrain is related to the smoothness of the derived size distribution and establishes that the sum of the squares of the second derivatives of the solution points should be minimized. With all this information, the solution vector $\boldsymbol{f}$ is presented in King et al. (1978) as the vector who minimizes a performance function Q, define as:

$$Q = \sum_{i=1}^{p} \epsilon_i^2 + \gamma \sum_{j=2}^{q-1} (f_{j-1} - 2f_j + f_{j+1})^2 \tag{1.16}$$

where γ is some non-negative lagrange multiplier. In the case that we know that there are some

measurements $\tau_a(\lambda_i)$ which are more precise than others, the Gauss-Markov theorem should be considered and the Eq. (1.16) replaced for the expression:

$$Q = \sum_{i=1}^{p}\sum_{j=1}^{p} C_{ij}^{-1}\epsilon_i\epsilon_j + \gamma\sum_{j=2}^{q-1}(f_{j-1} - 2f_j + f_{j+1})^2 \tag{1.17}$$

where C_{ij} is an element of the covariance matrix C whose elements are given by $C_{ij} = \sigma^2_{g_i g_j}$.

Now following the methodology suggested by Twomey (1963), the function Q is derived respect to each of the f_k coefficients.

$$\begin{aligned}\frac{\partial Q}{\partial f_k} &= \sum_{i=1}^{p}\sum_{j=1}^{p} C_{ij}^{-1}\frac{\partial}{\partial f_k}(\epsilon_i\epsilon_j) + \gamma\sum_{j=2}^{q-1}\frac{\partial}{\partial f_k}(f_{j-1} - 2f_j + f_{j+1})^2 \\ &= \sum_{i=1}^{p}\sum_{j=1}^{p} C_{ij}^{-1}(-A_{ik})\epsilon_j + \sum_{i=1}^{p}\sum_{j=1}^{p} C_{ij}^{-1}\epsilon_i(-A_{kj}) + \gamma\sum_{j=2}^{q-1}\frac{\partial}{\partial f_k}(f_{j-1} - 2f_j + f_{j+1})^2\end{aligned} \tag{1.18}$$

If we solve the third member of the last equation for each f_k, and we make $\sum_k \frac{\partial Q}{\partial f_k} = 0$; we obtained the following relation:

$$\mathbf{-A^T C^{-1}\epsilon + \gamma H f = 0 \Rightarrow -A^T C^{-1} g + A^T C^{-1} A f + \gamma H f = 0} \tag{1.19}$$

with the H-matrix defined by Twomey (1963) as:

$$H = \begin{pmatrix} 1 & -2 & 1 & 0 & ... & ... & ... & ... & 0 \\ -2 & 5 & -4 & 1 & 0 & ... & ... & ... & 0 \\ 1 & -4 & 6 & -4 & 1 & 0 & ... & ... & 0 \\ 0 & 1 & -4 & 6 & -4 & 1 & 0 & ... & 0 \\ ... & ... & ... & ... & ... & ... & ... & ... & ... \\ 0 & ... & ... & 0 & 1 & -4 & 6 & -4 & 1 \\ 0 & ... & ... & ... & ... & 0 & 1 & -2 & 1 \end{pmatrix} \tag{1.20}$$

Working out the value of f, we obtained:

$$\mathbf{f = (A^T C^{-1} A + \gamma H)^{-1} A^T C^{-1} g} \tag{1.21}$$

Some considerations should be made to properly use the equation Eq. (1.21):

1. If the errors are assumed to be equal and non correlated, the matrix C is simplified as $C = s^2 I$ with $s = rms$ and I the identity matrix.

2. If the errors are non correlated but they are different, we need to define the elements of C-matrix as $C_{ij} = \sigma^2_{\tau_a}(\lambda_i)\delta_{ij}$ (where δ_{ij} is the Kronecker delta function)

3. With C defined in this manner, Eq. (1.21) is equivalent to making a weighted least-squares fit to the data subject to a constraint.

1.2.1.3 Iterative process in King inversion

Instead of working with $\nu_c(lnr)$, the volume size distribution. King works with n_c, the numerical aerosol size distribution n_c. As the size distribution in this form can not be considered as constant in the intervals, he subdivides it as $n_c(r) = h(r)f(r)$, where $h(r)$ varies rapidly with r, and $f(r)$ is more slowly varying, and susceptible to be considered as constant in the intervals.

The function $h(r)$ is established as the size distribution given by Junge (1955):

$$h(r) = r^{(-v^*+1)} \rightarrow h(\log r) = 10^{(-v^*+1)\log r} \tag{1.22}$$

With all these changes, the equation Eq. (1.21) is still valid if the values A_{ij} are define as,

$$A_{ij} = \int_{r_j}^{r_j+1} \pi r^2 Q_{ext}(r, \lambda_i, m)h(r)dr \tag{1.23}$$

After these preliminaries, let us study the iterative process proposed by King et al. (1978). Initially a zeroth-order weighting function $h^{(0)}(r)$ is assumed in Eq. (1.23) (doing $v^* \simeq 3$) from which first order $f^{(1)}(\bar{r}_j)$ values are computed with the aid of Eq. (1.21). Since the solution vector $\mathbf{f^{(1)}}$ represents a modifying factor to the assumed form of $h^{(0)}(r)$, the $f^{(1)}(\bar{r}_j)$ values are then used to calculate a first order weighting function $h^{(1)}(r)$ which better represents the size distribution than the initially assumed weighting function. The first-order weighting function is then substituted back into Eq. (1.23) from which a second-order $\mathbf{f^{(2)}}$ is obtained through Eq. (1.21). This iterative procedure is continued until a stable result is obtained (Herman et al., 1971).

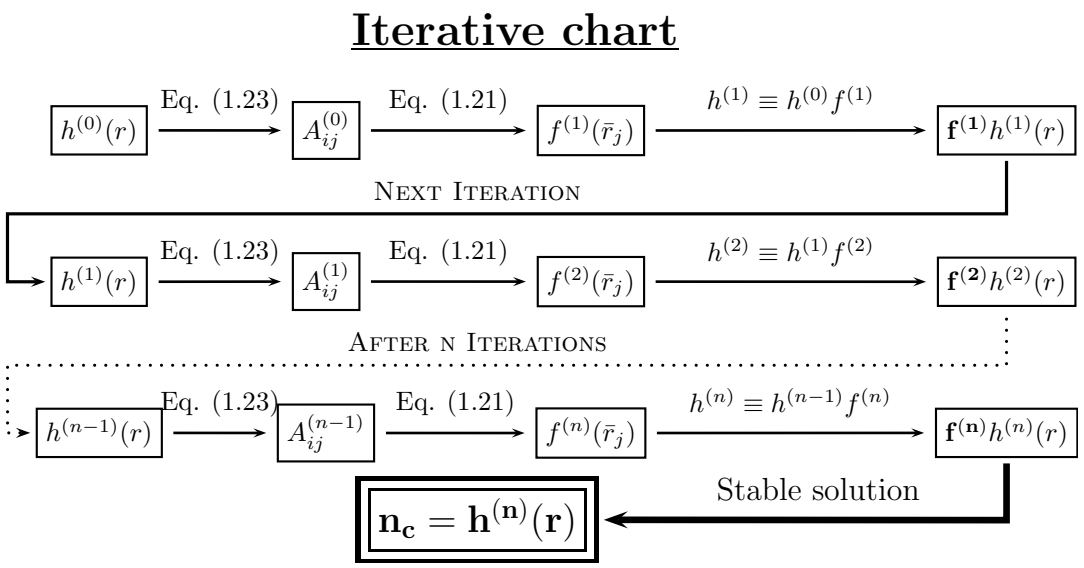

The author describes two advantages in this method:

- The most obvious is that the quadrature error which results from Eq. (1.12), when $f(r)$ is assumed constant in each coarse interval, will be smaller the closer $h(r)$ comes to describing the size distribution. In fact, $\mathbf{f}$ will tend to the vector unit.

- The smoothing constraint minimizes the second derivatives of $f(r)$, which allows the function $n_c(r)$ to vary freely. That is very important because these functions, as Junge distribution, have a large curvature.

However, during the process there are three parameters that are not calculated yet: Q_{ext}, γ and v^*.

- The extinction efficiency factor, Q_{ext}, is determined by the method described by King and Byrne (1976), with a fixed value of $m = 1.45 - 0.00i$.

- The γ value has not a significant meaning alone, whereas the $\gamma_{rel} = \frac{\gamma H_{kj}}{(A^T C^{-1} A)_{kj}}$ is the important parameter, since γ enters in a manner such a that elements of γH are to be added to $A^T C^{-1} A$. The parameter γ is selected between the minimum of the values $\gamma_{rel} = \frac{\gamma H_{11}}{(A^T C^{-1} A)_{11}}$ (with γ_{rel} varying from 10^{-3} until 1), which keeps all the $f(r)$ positive.

- The value of v^* is definitely established as $v^* = \alpha + 2$, but in the inversion is varying from the value $v^* - 0.5$ to $v^* + 0.5$.

1.2.2 Nakajima's inversion

The inversion proposed by Nakajima et al. (1996) looks for deriving the aerosol properties including sky radiance measurements as inputs, apart from the sun direct measurements already presented in the King inversion. In the first part of the subsection, we will briefly describe the important definitions regarding the diffuse radiation, then, in a second step we will study the inversion procedure.

1.2.2.1 Defining the problem

Diffuse radiation

The monochromatic diffuse radiation solar flux density E ($Wm^{-2}\mu m^{-1}$) is determined as the solution of the radiative transfer equation (RTE, Liou (1980)):

$$\begin{aligned} E(\Theta,\lambda) =& \frac{F_o}{4\pi}\frac{\mu_s}{\mu_v-\mu_s}\left[\frac{\omega_o\tau_a P_a(\Theta,\lambda)+\tau_R P_R(\Theta,)}{\tau_a+\tau_R}+q(\Theta,\lambda)\right][e^{-\frac{\tau_a+\tau_R}{\mu_v}}-e^{-\frac{\tau_a+\tau_R}{\mu_s}}], \quad \mu_s\neq\mu_v \\ E(\Theta,\lambda) =& \frac{F_o}{4\pi}\frac{1}{\mu_s}\left[\omega_o\tau_a P_a(\Theta,\lambda)+\tau_R P_R(\Theta,)+q(\Theta,\lambda)\right][e^{-\frac{\tau_a+\tau_R}{\mu_s}}], \quad \mu_s=\mu_v \end{aligned} \tag{1.24}$$

where, $P_a(\Theta,\lambda)$ and τ_a are aerosol phase function and aerosol optical depth, while $P_R(\Theta,\lambda)$ and τ_R are the Rayleight components, and ω_o is the aerosol single scattering albedo. These parameters will be described later. In the equation $q(\Theta,\lambda)$ represents the multiple scattering (MS) contribution. On the other hand, μ_s and μ_v are respectively the inverses of the solar and vision air masses, which can be approximated as $cos(\theta_s)$ and $cos(\theta_v)$, as commented in subsection 1.1.2, if $\theta_s \leq 75^o$ and $\theta_v \leq 75^o$ respectively. Comparing these equations with the two geometries presented in subsection 1.1.3, the principal plane would be included in the first expression as $\mu_s \neq \mu_v$. The almucantar is defined in the second expression since $\mu_s = \mu_v$.

Since Nakajima et al. (1996) focus the analysis on the almucantar, we will develop the following study in this geometry. Using the Eq. (1.1), we can rewrite the second equation of Eq. (1.24) (valid for the almucantar) as:

$$E(\Theta,\lambda) = \frac{Fm_s}{4\pi}\left[\omega_o\tau_a P_a(\Theta,\lambda)+\tau_R P_R(\Theta)+q(\Theta,\lambda)\right] \tag{1.25}$$

The aerosol phase function, $P_a(\Theta,\lambda)$, is a normalized function which describes the angular distribution of scattered radiation produced by the aerosol and, therefore, depends on the aerosol type. In the same way, the Rayleigh phase function, $P_R(\Theta)$, defines the angular distribution of the

scattered light produced by the air molecules. This magnitude is known and can be expressed as:

$$P_R(\Theta) = \frac{3}{4}\left(1 + \cos^2(\Theta)\right); \tag{1.26}$$

The concept of the single scattering albedo represents the ratio between the scattered light and the extinction (scattered plus absorbed light). For the Rayleigh scattering, this magnitude is 1. On the other hand, for the aerosol case it depends on the aerosol type and mathematically can be written as:

$$\omega_o = \frac{\tau_{a_s}}{\tau_a} = \frac{\tau_{a_s}}{\tau_{a_a} + \tau_{a_s}} \tag{1.27}$$

Finishing with the definitions, and equally to Eq. (1.9), from Mie analysis we can express the scattering part of the aerosol optical depth as:

$$\tau_{a_s}(\lambda) = \int_{r_a}^{r_b} \pi r^2 Q_{scat}(\chi, m) n_c(r) dr \tag{1.28}$$

After these definitions, we go back to Eq. (1.25), where we left the analysis presented by Nakajima et al. (1996). The author at this point, instead of $E(\Theta, \lambda)$, considers the diffuse sky flux normalized by the direct flux, which is the one obtained in their measurements and defined as:

$$R(\Theta, \lambda) \equiv \frac{E(\Theta, \lambda)}{F m_0 \Delta\Omega} = \omega_o \tau_a P_a(\Theta, \lambda) + \tau_R P_R(\Theta) + q(\Theta, \lambda) \equiv \beta_A(\Theta, \lambda) + q(\Theta, \lambda) \tag{1.29}$$

The Eq. (1.29) is strictly monochromatic and can be used only in the regions where there is not strong absorption by gases. Its single-scattering (SS) part equals the total differential scattering coefficient, $\beta_A(\Theta, \lambda) = \omega_o \tau_a P_a(\Theta, \lambda) + \tau_R P_R(\Theta)$.

It is important to emphasize the contribution of MS term, $q(\Theta, \lambda)$. As the authors clearly state, for instance, at $\Theta = 60°$ and $\lambda = \ 0.500\ \mu m$ this contribution is 41% when $SZA = 30°$ and $\tau_{500} = 0.2$. Therefore, an accurate scheme for the MS treatment of radiative transfer is needed within the inversion code.

From the $R(\Theta, \lambda)$ data, the differential scattering coefficient $\beta_A(\Theta, \lambda)$ is obtained by an iterative regression incorporating a MS algorithm; from $\beta_A(\Theta, \lambda)$, and possibly τ data, the volume size distribution of the atmospheric aerosol is finally derived, $\beta_A(\Theta, \lambda) = \omega_o \tau_a P_a(\Theta, \lambda)$. As the ratio R is approximately proportional to τ, the inversion procedure is very stable even for small optical thicknesses of the order of 0.01, as those found in polar regions or high altitude locations.

In this second case, apart from the integral expression for the aerosol optical thickness for the direct measurements (Eq. (1.8)), we will need to define the aerosol differential scattering coefficient of the whole atmospheric column for the diffuse radiation:

$$\begin{aligned} \tau_a(\lambda) &= \int_{r_a}^{r_b} \pi r^2 Q_{ext}(\chi, m) n_c(r) dr \\ \beta_A(\Theta, \lambda) = \omega_o \tau_a P_a(\Theta, \lambda) &= \omega_o \int_{r_a}^{r_b} \pi r^2 Q_{ext} P_a(\Theta, \lambda) n_c(r) dr = \int_{r_a}^{r_b} K_{scat}(\Theta, \chi, m) n_c(r) dr \end{aligned} \tag{1.30}$$

We should insist again that we are considering that the particles are spherical, and therefore, we are following the Mie scattering theory. On the other hand, in Nakajima code (the SKYRAD.pack code), instead of the numerical aerosol size distribution, the volume size distribution is used. As a consequence, the two quantities in Eq. (1.30) are rewritten as:

$$\begin{aligned} \tau_a(\lambda) &= \int_{r_a}^{r_b} \frac{3}{4\pi r^3} K_\tau(\chi, m)\ \nu_c(\ln r) dr \\ \beta_A(\Theta, \lambda) &= \int_{r_a}^{r_b} \frac{3}{4\pi r^3} K_{scat}(\Theta, \chi, m)\ \nu_c(\ln r) dr \end{aligned} \tag{1.31}$$

where K_{scat} and K_τ are kernel functions.

Observe here, with the same aim as in Eq. (1.13) we could define a new set of A_{ij} as:

$$A_{ij} = \int_{\ln r_j + \frac{\Delta \ln r}{2}}^{\ln r_j - \frac{\Delta \ln r}{2}} \frac{3}{4\pi r^3} K_{scat}(\Theta, \chi, m)\ \nu_c(\ln r) dr \tag{1.32}$$

were we assume again $\nu_c(\ln r) = f_j$, and we incorporate new g_i as $g_i = \beta_A(\Theta, \lambda)$.

The authors, at this point of the discussion, noticed that the behavior of K_τ and K_{scat} determines the radius interval of reliable information content for the aerosol optical and physical features, and that after inspecting several kernels at the refractive indexes typical of the atmospheric aerosol, the radius interval is found to be indicative for $0.03 - 3\mu m$ when there is only extinction data, while is significant in the interval $0.06 - 10\mu m$ for the sky radiance data; combining both data, the radius interval is indicatively from $0.03 - 10\mu m$.

1.2.2.2 SKYRAD.pack (Nakajima Code)

The SKYRAD consist in two programs; the first one (MKDATA) is for computing simulated data of direct and diffuse solar radiation from aerosol properties and the second (REDML) is for retrieving (inversion) aerosol properties from solar radiation data.

MKDTA (Forward code.)

The first part of the code, MKDTA, is the part in charge of solving the expressions presented in Eq. (1.24) and modeling the direct and diffuse radiation for different wavelengths, from the aerosol size distribution, the solar zenith angle, the aerosol complex refractive index at each wavelength ($m_i(\lambda_i)$), the ground albedo ($A_i(\lambda_i)$) for each wavelength and the aerosol optical thickness at 500 μm. In other words, it is the part solving the radiative transfer equation presented in Eq. (1.24). The function of MKDTA is summarized in the figure 1.3.

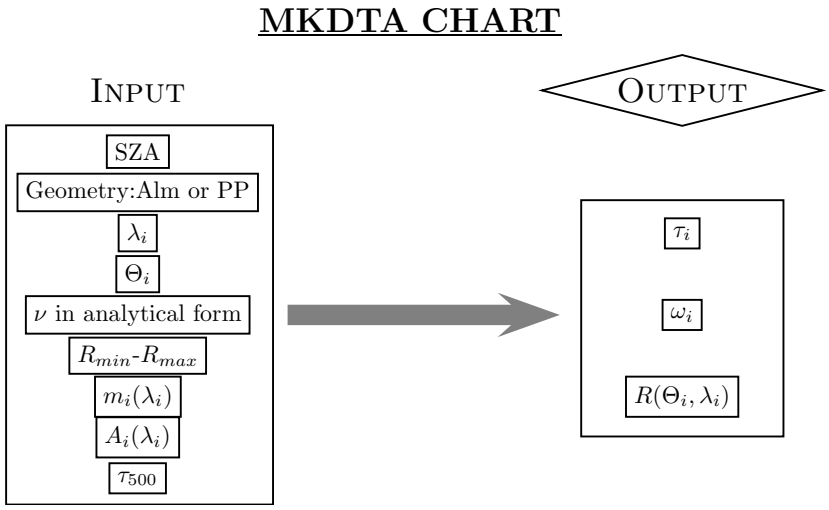

Figure 1.3: Scheme of the MKDTA program.

The treatment of the radiative transfer problem concerning the optical quantities that MKDTA does, is mainly based on the IMS (improved multiple and single scattering) method which uses the delta-M approximation for the truncation of the aerosol phase function (Wiscombe, 1977) (as a delta function plus a 2M-term series of Legendre polynomials which depends on Θ) and corrects the solution for the first and second order of scattering (Stamnes and Dale, 1981).

REDML (Backward code.)

The second part of the Nakajima code is the REDML program, which retrieves the aerosol features from the data of direct and normalized diffuse radiation, so it is the part including the inversion procedure. There are four different modes of operation selected by an index called as $INDM$. The main differences between the indexes are related to the use of the aerosol optical thickness and the way of performing the inversion. Thus, in $INDM = 2$, the aerosol optical thickness is not used, and only the data from R is considered; also, selecting this index, the code applies a non-linear inversion as will be explained later. In $INDM = 0, 1, -1$ the aerosol optical thickness is used and the inversion procedure is the same used in 1.21, but introducing the A_{ij} coming from the sky measurements (Eq. (1.13)).

The other differences are minor, for instance, in $INDM = 1$, the aerosol optical depth is fixed

in the first iteration and is varied in the next iterations while for $INDM = 0, -1$, it is kept fixed during all the process. More information about the other differences can be gained in Nakajima et al. (1996).

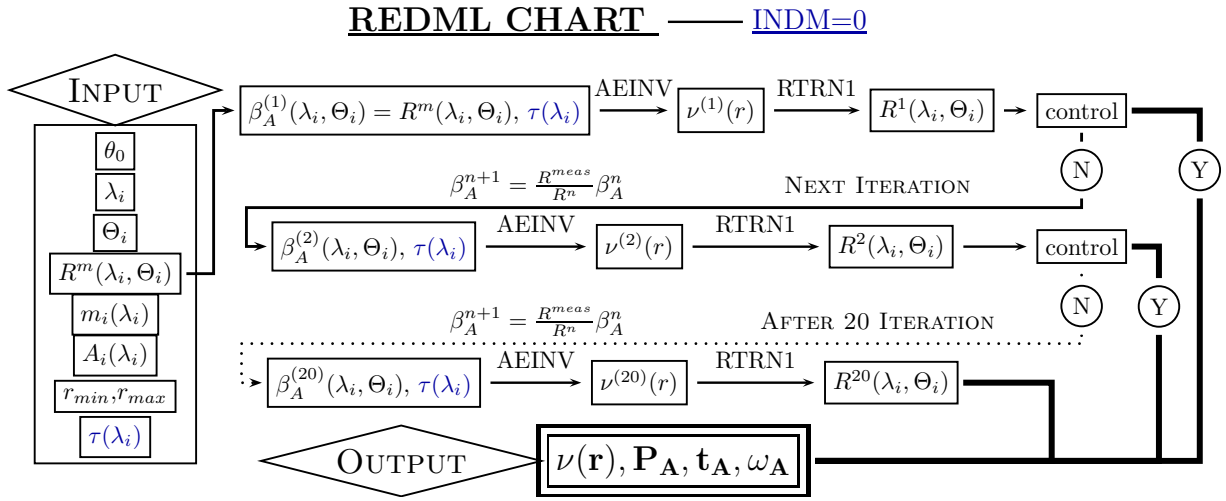

Figure 1.4: Scheme of the REDML program for $INDM$=0.

A general idea of the inversion process can be acquired from figure 1.4, which is the chart representing the case for $INDM = 0$. The process starts from the initial values of $\beta_A(\Theta)$ and τ_a or at the nth iteration from the values of $\beta_A^n(\Theta)$ and τ_a^n, for $INDM = 0, 1, -1$, and only $\beta_A(\Theta)$ or $\beta_A^n(\Theta)$ for $INDM = 2$. With these values the subroutine AEINV computes $\nu^{(n)}(r)$.

From these values of $\nu^{(n)}(r)$ thought the subroutine RTRN1, which is basically the module MKDTA, the code computes the value of $R^{(n)}(\Theta)$ (for all the $INDM$) and τ^n (for $INDM = 1, 2$). Finally, it is obtained $\beta_A^{n+1}(\Theta)$ by comparing $R^{(n)}(\Theta)$ with the corresponding experimental data, and then it iterates until a stop condition is reached.

The output data are common in all of them and consist of the aerosol volume spectrum, the aerosol optical thickness and the aerosol phase function and the reconstructed radiance data, at the selected wavelengths and scattering angles.

In short, there are three defined process: a first process, AEINV which obtains the optical properties from the inversion of the $\beta_A(\Theta)$ and τ_a, a second step which computes $R^n(\Theta)$ from the optical properties (RTRN1-MKDTA), and the third step which consists of eliminating the multiple scattering part to obtain again $\beta_A^n(\Theta)$. We will describe this two inversion parts starting from this last one.

Obtaining SS from MS

Within the SKYRAD.pack code, the part used to derive differential scattering coefficient $\beta_A(\Theta)$ from measurements of normalized sky flux $R(\Theta)$ is the same for all the $INDM$ indexes and consists of a nonlinear iterative method:

Let us recall that a nonlinear iterative method of inversion starts with the assumption of a first-guess solution, which is updated at each iteration until the difference between experimental and computed data is within a prescribed value. The total differential scattering coefficient at the nth iteration is updated through the simple formula:

$$\beta_A^{n+1} = \frac{R^{meas}}{R^n}\beta_A^n \tag{1.33}$$

And then the initial guess for $\beta_A(\Theta)$ is obtained as $\beta_A^1(\Theta) = R^{meas}(\Theta)$.

AEINV

Before starting the explanation of the routines, it should be indicated that the inversion code counts with the a set of kernels K_{scat} obtained from the Mie intensity functions and efficiency factors for spherical particles which were previously computed at 55 grid points for Θ from 0^o to 180^o, and at 59 grid points for size parameters, χ (in logarithmic spaced). On the other hand, the volume size distribution, the output of the code, is given for 20 radius subintervals within the interval from 0.01 to $10\mu m^3$

The AEINV process works as follows: for $INDM = 2$, the inputs are the values of β_A^n and uses a nonlinear method[4] executed by several iterations. At the mth iteration and at the ith grid point, r_i, will update $\nu^{n,m}(r_i)$ with the equation:

$$\nu^{n,m+1}(r_i) = \nu^{n,m}(r_i)\prod_{j=1}^{NM}(1+\epsilon_j^m K_{ji}^*), \qquad (i = 1, ..., NS), \tag{1.34}$$

where $K_{ji}^* = K_{ji}/K_{max}$ is the normalized kernel, K_{max} is the maximum value of K_{ji}, and NM is the number of measurements angles. The quantity ϵ_j^m is the residual of the aerosol differential scattering coefficient for the jth angle and at the mth iteration, defined by $\epsilon_j^m = [\beta_{A_j}^n/\beta_{A_j}^m - 1]$, with $\beta_{A_j}^m$ computed by the use of $\nu^{n,m+1}(r_i)$ with $(i = 1, ..., NS)$. The estimation of the first-guess solution is particularly important, as it allows to speed up the convergence of the solution; for the first-guess spectrum the sum of three log normals is assumed, whose parameters are fixed according to the situation.

The other option, for $INDM = 0, 1, -1$, is the linear constrained method presented in the previous subsection based on solving Eq. (1.21). Apart from introducing τ_a, the β_A are part of the vector f, with the pertinent K_{scat} as A_{ij}.

[3]More recent studies have recalculated these Kernels for spheroids giving satisfactory results (Olmo et al., 2008).

[4]Twomey-Chahine method described in Twomey (1977) and also used by Hitzenberger and Rizzi (1986) and Trakhovsky and Shettle (1985)

1.2.3 Dubovik's inversion

The analyses in the two previous subsections, apart from describing the respective inversions, had an objective of leading the way towards presenting Dubovik's inversion. For instance, introducing King's inversion we introduced the concept of ν_c and defined its relation with τ_a by means of the A_{ij} in Eq. (1.13). However, the inversion presented in King et al. (1978) only uses the concept of n_c, and that is why, we redefined the A_{ij} in the discussion of the iterative process (subsection 1.2.1.3) again.

The reason behind this additional loop resides in the fact, that at the bottom, we tried to obtain the Eq. (1.21), first with the expressions valid for Dubovik's inversion procedure, with the A_{ij} (regarding absorption) defined in terms of ν_c. On the other hand, the study of Nakajima's inversion allowed us to introduce the A_{ij} regarding the scattering in Eq. (1.32) and also to consolidate some useful ideas regarding the a priori defined constrains in King's inversion.

Precisely, these useful ideas are also the starting point of Dubovik's algorithm though the procedure presents some novelties (Dubovik and King, 2000; Dubovik et al., 2000); the principal one is that in this new approach the constrains are applied over the logarithmic derivatives (Dubovik et al., 1995) rather than restricting the absolute derivatives.

Moreover, Dubovik's inversion also restricts the components of the refractive index, $n(\lambda)$ and $k(\lambda)$, since they appear as products in the retrieval. The constrains of these magnitudes are related to λ instead of $\ln r$ as for the size distribution. Nevertheless, the inversion assumes that the variations admitted in the size distribution are expected to be much stronger than for the spectral variations of the real ($n(\lambda)$) and the imaginary part ($k(\lambda)$) of the refractive index. That is why the constrains are imposed in higher derivative order for the size distribution than for the refractive index.

1.2.3.1 Probability density function and Maximum Likelihood method

The mathematical approach followed by Dubovik and King (2000) presents some variations respect to the ones analyzed until here (even though the philosophy is quite similar). Apart from the cited reference, a further insight of the inversion procedure analyzed here can be gained in Videen (2004), specifically, in the chapter "Optimization of numerical inversion in photopolarimetic remote sensing" by Dr. Oleg Dubovik (available also in `www.giss.nasa.gov/staff/mmishchenko/2004_kluwer_dubovik.pdf`).

As the starting point of the code description we should go back to Eq. (1.11), where we find a system of equations in which the number of equations, or measurements (p), is higher than the unknowns (q). Unluckily, the presence of the noise does not allow the elimination of the "extra"

information (where the extra equations could be canceled) and as a consequence no a unique solution can provide exact equality of the right part (Af) to the left part (g).

Therefore small differences ("fitting errors") between the left and right parts of the linear equation are always present. If the characteristics of the noise in the observations f are known (how the errors look like), the best solution of overdetermined system of equations would be the one reproducing the known statistical properties of measurement errors as closely as possible.

The agreement of the "fitting" errors Δg with a known error distribution can be evaluated using the probability density function (PDF) as a function of modeled errors $P(\Delta g)$: the higher the $P(\Delta g)$ the closer the modeled Δg is to the known statistical properties. Thus, the best solution $\hat{a}^{best}$ should result in modeled errors corresponding to the most probable error realization, i.e., to the PDF maximum:

$$P(\Delta g) = P(g^*(\hat{a}) - g) = P(g^*(\hat{a}|g)) = max \tag{1.35}$$

where $g*(\hat{a})$ is the vector of "retrieved measurements" using the derived aerosol properties $\hat{a}$ (aerosol size distribution, spectral real and imaginary refractive indices).

In essence, this principle is the well-known Maximum Likelihood Method (MLM). The PDF written as a function of measurements $P(g*(\hat{a})|g)$ is called the Likelihood Function. The MLM is one of the strategic principles of statistical estimation that provides statistically the best solution in many senses.

If the error PDF is described by a normal distribution, then the MLM is reduced to a particular case widely known as the "least-square solution". The basic principle of this method hinges on the fact that the normal (or Gaussian) distribution is the expected and most appropriate function for describing random noise. Hence the normal PDF for each vector g of measurements can be written in the form:

$$P(g^*(\hat{a})|g) = ((2\pi)^m det(S_\epsilon))^{-\frac{1}{2}} \exp(-\frac{1}{2}(g^*(\hat{a}) - g)^T) S_\epsilon^{-1}(g^*(\hat{a}) - g)) \tag{1.36}$$

where T denotes matrix transposition, S_ϵ is the covariance matrix of the vector g, $det(S_\epsilon)$ denotes the determinant of S_ϵ, and p is the dimension of vectors g and $g^*(\hat{a})$.

In the simplest case of only one source of data (e.g., spectral aerosol optical thickness as in King inversion), the principle of maximum likelihood dictates that the best estimate for the solution for the aerosol properties $\hat{a}$ corresponds to the maximum value of Eq. (1.36), which in turn is equivalent to minimizing the term in the exponential. Thus we seek to minimize the square norm Q_1 defined

by:

$$Q_1 = \epsilon^T S_\epsilon^{-1} \epsilon = \sum_{i=1}^{p} \sum_{j=1}^{p} (g_i^*(\hat{a}) - g_i)^T) S_{\epsilon\ ij}^{-1} (g_j^*(\hat{a}) - g_j) \tag{1.37}$$

where ϵ is the error vector denoting deviations from the measurements and our forward model, and defined in the same way as in Eq. (1.12).

Dubovik and King (2000) refer to the introduction of constraints as adding virtual measurements, where the constraints are treated mathematically in an identical way to real measurements. This is an obvious way of reducing the ambiguity associated with an ill-posed problem, but the introduction of erroneous constraints is itself equivalent to adding, along with more information, additional error. That error would have a non-random nature and would result in solution systematic errors, or biases. Thus it is important to add only valid and physically plausible constraints to the possible solutions. It is, after all, possible for a constraint to be too loose, too tight, or simply incorrect.

As an example, the constraint in the second derivative term of the size distribution can be introduced in the similar way that in Eq. (1.16):

$$Q_2 = \sum_{i=1}^{q} \sum_{j=1}^{q} f_i H_{ij} f_j \tag{1.38}$$

where H_{ij} is the same as the one defined in Eq. (1.20).The minimization process, now, should be applied over the new function Q defined as,

$$Q = Q_1 + \gamma Q_2 \tag{1.39}$$

where γ as in the description of King's inversion is a non-negative Lagrange multiplier, which serves to weight the contribution of the smoothness constraint, relative to the contribution of the measurements.

Note here, that applying the methodology of MLM to the direct Sun measurements and using the same constrain as in King's inversion, we recover the same expressions obtained there and the solution that comes out is again (making $\sum_k \frac{\partial Q}{\partial f_k} = 0$):

$$\boldsymbol{f} = (\mathbf{A^T S_\epsilon^{-1} A} + \boldsymbol{\gamma} \mathbf{H})^{-1} \mathbf{A^T S_\epsilon^{-1} g} \tag{1.40}$$

As we commented the inversion presented in Dubovik and King (2000) proposes different constrains (logarithmic derivatives) and also retrieves the refractive index. After this introduction of

the MLM theory, we can now formulate that the solution of the Dubovik's inversion will be given by the minimum of the function:

$$Q = \sum_{k=1}^{5} \gamma_k [f_k^* - f_k(a)]^T (W_k)^{-1} [f_k^* - f_k(a)] \tag{1.41}$$

where the vector $\mathbf{f_1}$ correspond to the logarithms of $\tau(\lambda)$ at the selected wavelengths, the vector $\mathbf{f_2}$ correspond to the logarithms of the normalized radiance (see next subsection) at the selected wavelengths and angles, the vector $\mathbf{f_3}$ includes the values of the size distribution smoothing function, and $\mathbf{f_4}$ and $\mathbf{f_5}$ include the values of $n(\lambda)$ and $k(\lambda)$ smoothing functions. The matrix W_k are the weight matrices of random error in the input data sets. The vector a includes the logarithm of the retrieved values of the size distribution in the grid points and the values of the real and the imaginary part of the refractive index at the selected wavelengths. Finally, the Lagrange coefficients γ_k are defined from statistical considerations as the ratios of the error variances $\Delta_k : \gamma_k = \epsilon_1^2/\epsilon_k^2$. The multivariable search for the minimum of Eq. (1.41) is implemented by a stable numerical procedure combining matrix inversion and univariant relaxation according to Dubovik et al. (1998)

1.2.3.2 Forward model

The forward model used in Dubovik's inversion is the same as the one utilized by Nakajima et al. (1996). However, while describing Nakajima's code (subsection 1.2.2), the values introduced as inputs in the code were the sky radiances divided by the direct flux received, which were defined as normalized radiances. Dubovik's normalization is different as radiances are divided by the extraterrestrial flux and not by the direct flux. In fact, the extraterrestrial flux is just a constant number for each wavelength and does not contain any extra information as the direct flux does, for example information about the absorption.

The definition of this other "normalized" radiance is very simple:

$$R^*(\Theta, \lambda) = \frac{E(\theta, \varphi)}{F_o 4\pi} \tag{1.42}$$

where F_o is the extraterrestrial flux. Actually, this magnitude is corrected by Earth-Sun distance, which allows us to forget about the date in this discussion, highlighting again that it does not introduce additional information to the absolute value of the radiance. To reproduce exact values of radiance, it would be enough to multiply the normalized radiance derived by the code by values of the extraterrestrial flux (for each wavelength) and the Earth-Sun distance correction depending on the simulation day.

This difference in the input (radiances normalized to direct flux in Nakajima's code vs. absolute radiances, although divided by extraterrestrial flux in Dubovik's code) is relevant, as noted by

Mueller et al. (2010a), "The normalized sky brightness removes calibration uncertainties, but in this way we lose the information on particle absorption. The absolute sky radiance requires a very accurate radiometric calibration."

1.2.3.3 Spheroids model

The non-sphericity of the aerosol particles poses severe problems in the adequate retrieval of the aerosol properties by inversion of sky radiances. In the AERONET version 1 (Dubovik and King, 2000) two output possibilities were offered: either a spherical model was assumed or a pure non-spherical (spheroids) in case of dust. The spheroids are ellipsoids of revolution, that are described uniquely by 2 parameters (instead of 1 used for spheres). The ratio between the largest and the smallest particle dimension is called aspect ratio.

The use of spheroids for modelling desert dust relies on two facts. First, Mishchenko et al. (1997) showed that it is possible to reproduce the phase functions measured for desert dust assuming the same axis ratio distribution for all particle sizes. In situ studies of Saharan dust confirmed that aspect ratios do not have pronounced size dependence (Reid et al., 2003).

In order to account for aerosol non-sphericity, the atmospheric aerosol is modeled as an ensemble of randomly oriented spheroids. Specifically, AERONET operational retrieval uses the concept by (Dubovik et al., 2006) and models the particles for each size bin as mixture of spherical and non-spherical aerosol components. The non-spherical component was modeled by ensemble of randomly oriented spheroids

Chapter 2

Description of the selected aerosol types. Analysis of simulated radiances

Él que no va hasta la puerta, no aparca en la puerta.

Carlos Oliva (amigo e ingeniero de profesión)

Resumen en español del capítulo:

En este capítulo se describen las propiedades ópticas y microfísicas de los aerosoles "tipo" que hemos utilizado en los capítulos 4, 5 y 6, para estimar mediante radiancias simuladas, cuánto afectan los errores descritos en la introducción sobre las medidas, y sobre los productos obtenidos mediante el procedimiento de inversión, que realizamos a posteriori sobre las medidas simuladas.

La simulación de estas radiancias se ha hecho utilizando el modelo "forward" del código de Dubovik. En este capítulo se realizan las primeras simulaciones, aunque sin introducir ningún error. Con esta manera de proceder, podemos, por un lado, ver qué forma tienen las radiancias y además establecer cuáles son los patrones característicos de las mismas en función de cada tipo de aerosol. Por otro lado, nos permite realizar un test de auto-consistencia del modelo si aplicamos a estas radiancias el módulo de inversión del código y comparamos la salida con los valores de las propiedades de los aerosoles introducidas originariamente. Por último, hemos realizado un análisis de sensibilidad de las medidas simuladas frente a variaciones del índice de refracción y de la distribución de tamaños.

En el análisis de auto-consistencia se han constatado las inconsistencias en el almucantar cuando el ángulo solar cenital es bajo comentadas en la introducción. Dichas inconsistencias se manifiestan en las propiedades ópticas para todos los tipos de aerosol, así como en el modo grueso de la distribución de tamaños, aunque sólo para el caso del aerosol desértico. Para el plano principal, el análisis de auto-consistencia muestra una gran concordancia entre las entradas y las salidas. Sólo en el caso del aerosol procedente de la quema de biomasa aparecen ciertos desajustes en la distribución de tamaños para radios superiores a $3\mu m$.

Los test de sensibilidad del modelo nos ha permitido ver que para estos radios mayores que $3\mu m$, las variaciones en la distribución de tamaño no tienen trascendencia en las medidas de radiancia, donde las diferencias generadas son inferiores al $1{,}5\,\%$, justificando, por tanto, los problemas observados en la distribución de tamaños derivada para estos radios.

2.1 Introduction

The analysis of the different errors, in chapters 4, 5 and 6, will be carried out with simulated radiances using several typical and optically distinct aerosol types. Specifically, four aerosols have been considered with the intention of extending the error analysis to a wide range of different situations. The cases considered have been: desert dust, oceanic, clean urban, and absorbing biomass-burning aerosol.

Aerosol optical properties are gathered and discussed in numerous characterization studies. From of all these studies, we have selected the article of Dubovik et al. (2002) to parametrize the aerosols used in the present thesis. That work established the characteristics of different aerosol types as retrieved by the AERONET network, and therefore with Dubovik's inversion, from data acquired by ground-based radiometers at several key locations.

The chapter has been structured as follows. In the first place, section 2.2 will analyze the optical properties for each selected aerosol type (from Dubovik et al. (2002)) comparing them with values obtained in other studies. On the other hand, the section will also contain a self-consistency study of Dubovik's inversion for all the selected aerosols. This consistency test is explained in detail in the next section.

A brief radiance analysis will be made in section 2.3 using the forward code of Dubovik's inversion. It will compare radiance measurements simulated with different aerosols and in different conditions: changes in the geometry (almucantar vs principal plane); changes in the SZA, etc.

Finally, in section 2.4 several tests will be made to check how small modifications of the aerosol properties, such as the refractive index or the size distribution, change radiance simulations. The variations caused in other parameters, such as the aerosol optical depth and the single scattering albedo, will also be discussed.

2.2 Aerosol types selected for the simulations

Aerosol properties used to make the simulations in the present thesis are taken from the article Dubovik et al. (2002), where an analysis of the aerosol absorption and other optical properties is done at several key locations. The figure 2.1 is an extract of the table 1 of Dubovik et al. (2002) where values for parameterizing the size distribution (as bimodal log-normal) and the optical properties are given for these key locations.

In particular, the extract of the table contains information about two examples of Urban-industrial, two examples of biomass burning and another two of desert dust aerosol. But there are another six examples described in the other parts of the table. From all these twelve examples,

TABLE 1. Summary of aerosol optical properties retrieved from worldwide AERONET network of ground-based radiometers.

Urban–industrial and mixed	GSFC, Greenbelt, MD (1993–2000)	Crete–Paris, France (1999)
Number of measurements (total)	2400	300
Number of measurements (for ω_0, n, k)	200 (Jun–Sep)	40 (Jun–Sep)
Range of optical thickness; $\langle\tau\rangle$	$0.1 \le \tau(440) \le 1.0$; $\langle\tau(440)\rangle = 0.24$	$0.1 \le \tau(440) \le 0.9$; $\langle\tau(440)\rangle = 0.26$
Range of Ångström parameter	$1.2 \le \alpha \le 2.5$	$1.2 \le \alpha \le 2.3$
$\langle g\rangle$ (440/670/870/1020)	0.68/0.59/0.54/0.53 ± 0.08	0.68/0.61/0.58/0.57 ± 0.07
n; k	1.41 − 0.03τ(440) ± 0.01; 0.003 ± 0.003	1.40 ± 0.03; 0.009 ± 0.004
ω_0(440/670/870/1020)	0.98/0.97/0.96/0.95 ± 0.02	0.94/0.93/0.92/0.91 ± 0.03
r_{Vf} (μm); σ_f	0.12 + 0.11 τ(440) ± 0.03; 0.38 ± 0.01	0.11 + 0.13 τ(440) ± 0.03; 0.43 ± 0.05
r_{Vc} (μm); σ_c	3.03 + 0.49 τ(440) ± 0.21; 0.75 ± 0.03	2.76 + 0.48 τ(440) ± 0.30; 0.79 ± 0.05
C_{Vf}(μm³/μm²)	0.15 τ(440) ± 0.03	0.01 + 0.12 τ(440) ± 0.04
C_{Vc}(μm³/μm²)	0.01 + 0.04 τ(440) ± 0.01	0.01 + 0.05 τ(440) ± 0.02
Biomass burning	**Amazonian forest, Brazil (1993–1994); Bolivia (1998–1999)**	**South American cerrado, Brazil (1993–1995)**
Number of measurements (total)	700	550
Number of measurements (for ω_0, n, k)	250 (Aug–Oct)	350 (Aug–Oct)
Range of optical thickness; $\langle\tau\rangle$	$0.1 \le \tau(440) \le 3.0$; $\langle\tau(440)\rangle = 0.74$	$0.1 \le \tau(440) \le 2.1$; $\langle\tau(440)\rangle = 0.80$
Range of Ångström parameter	$1.2 \le \alpha \le 2.1$	$1.2 \le \alpha \le 2.1$
$\langle g\rangle$ (440/670/870/1020)	0.69/0.58/0.51/0.48 ± 0.06	0.67/0.59/0.55/0.53 ± 0.03
n; k	1.47 ± 0.03; 0.00093 ± 0.003	1.52 ± 0.01; 0.015 ± 0.004
ω_0(440/670/870/1020)	0.94/0.93/0.91/0.90 ± 0.02	0.91/0.89/0.87/0.85 ± 0.03
r_{Vf} (μm); σ_f	0.14 + 0.013τ(440) ± 0.01; 0.40 ± 0.04	0.14 + 0.01τ(440) ± 0.01; 0.47 ± 0.03
r_{Vc} (μm); σ_c	3.27 + 0.58τ(440) ± 0.45; 0.79 ± 0.06	3.27 + 0.51τ(440) ± 0.39; 0.79 ± 0.04
C_{Vf} (μm³/μm²)	0.12 τ(440) ± 0.05	0.1 τ(440) ± 0.06
C_{Vc} (μm³/μm²)	0.05 τ(440) ± 0.02	0.04 + 0.03 τ(440) ± 0.03
Desert dust and oceanic	**Bahrain–Persian Gulf (1998–2000)**	**Solar-Vil.–Saudi Arabia (1998–2000)**
Number of measurements (total)	1800	1500
Number of measurements (for ω_0, n, k)	100	250
Range of optical thickness; $\langle\tau\rangle$	$0.1 \le \tau(1020) \le 1.2$, $\langle\tau(1020)\rangle = 0.22$	$0.1 \le \tau(1020) \le 1.5$; $\langle\tau(1020)\rangle = 0.17$
Range of Ångström parameter	$0 \le \alpha \le 1.6$	$0.1 \le \alpha \le 0.9$
$\langle g\rangle$ (440/670/870/1020)	0.68/0.66/0.66/0.66 ± 0.04	0.69/0.66/0.65/0.65 ± 0.04
n	1.55 ± 0.03	1.56 ± 0.03
k(440/670/870/1020)	0.0025/0.0014/0.001/0.001 ± 0.001	0.0029/0.0013/0.001/0.001 ± 0.001
ω_0(440/670/870/1020)	0.92/0.95/0.96/0.97 ± 0.03	0.92/0.96/0.97/0.97 ± 0.02
r_{Vf} (μm); σ_f	0.15 ± 0.04; 0.42 ± 0.04	0.12 ± 0.05; 0.40 ± 0.05
r_{Vc} (μm); σ_c	2.54 ± 0.04; 0.61 ± 0.02	2.32 ± 0.03; 0.60 ± 0.03
C_{Vf} (μm³/μm²)	0.02 + 0.1 τ(1020) ± 0.05	0.02 + 0.02 τ(1020) ± 0.03
C_{Vc} (μm³/μm²)	−0.02 + 0.92 τ(1020) ± 0.04	−0.02 + 0.98 τ(1020) ± 0.04

Figure 2.1: Extract of the table 1 from Dubovik et al. (2002) where values for parameterizing the size distribution (as bimodal log-normal) and the optical properties such as the refractive index or single scattering albedo are given for several key locations. In the extract: urban aerosol in GSFC (Maryland-USA) and Paris (France), biomass burning aerosol in Amazonian forest (Brazil and Bolivia) and in Cerrado (Brazil) and desert dust aerosol in Bahrain (Bahrain) and in Solar Village (Saudi Arabia).

we have been selected for the simulations within the thesis: Solar Village site (Saudi Arabia) for desert dust, Lanai site (Hawaii-USA) for oceanic aerosol, Goddard Space Flight Center site (Maryland-USA) for clean urban and Mongu site (Zambia) for biomass burning.

The article proposes that the optical properties and the parameters of the size distribution can be derived as a function of the aerosol optical depth (see figure 2.1). The regressions of these optical parameters are more robust with the aerosol optical depth at 440 nm when fine mode dominates the size distribution (urban and biomass burning aerosols) whereas in coarse mode domination (oceanic and desert dust) they are better described using the 1020 nm wavelength.

In our four selected aerosols, two possibilities for the aerosol load have been considered: the first one around the averaged value of the aerosol optical depth, and the second one with more aerosol load so as to see if errors affect less when the aerosol load increases. For instance, in the urban aerosol example, GSFC (which can be seen at the top of figure 2.1), the reference values used for its aerosol optical depth (in this case at 440 nm) have been $\tau_{a_{ref}}(440) = 0.2$ (as $< \tau_a(440) >= 0.24$) and $\tau_{a_{ref}}(440) = 0.5$. Using these values and the expressions in figure 2.1 the rest of the parameters

are derived.

Along the section, there will be one subsection devoted to each selected aerosol type. These subsections will be divided in two different analysis: the first one will contain a description of the optical properties and size distribution parameters taken from Dubovik et al. (2002); in this description values obtained in other studies will be also referenced and compared with the ones used here. The second analysis will be a self-consistency test of Dubovik's code for each aerosol type: basically, the idea is to simulate radiance measurements with the forward module of Dubovik's code introducing in every case the pertinent size distribution and refractive index. These radiances are afterwards inverted with the backward module. The results of this inversion, the size distribution and the refractive index, will be compared with the original ones. A scheme of this idea is drawn in figure 2.2. The different "conditions", which are the solar zenith angles (5 cases) and the measurement geometry (almucantar or principal plane), are also included in the diagram.

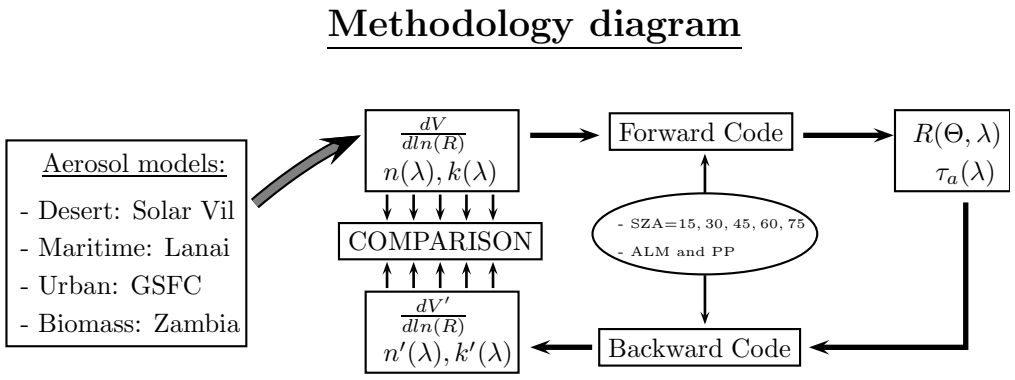

Figure 2.2: Methodology diagram followed to carry out the self-consistency test of Dubovik's code for different aerosol types, solar zenith angles and geometries for measuring the sky radiance.

The same procedure was used in Dubovik et al. (2000), even though, in that article the aerosol models were not obtained from a climatology analysis and the spheroid module (commented in subsection 1.2.3) was not included yet. In future chapters, the inverted radiances will contain the errors to study; but before introducing errors, to check if the inversion code and its forward and backward modules are self-consistent and in which conditions, is necessary in order to discount the discrepancies later on.

2.2.1 Desert Dust (Solar Village)

2.2.1.1 General characteristics

From all the desert dust examples described in Dubovik et al. (2002), aerosol properties obtained in Solar Village site (Saudi Arabia) are the ones chosen for this analysis. Solar Village (24.90° N-46.40° E, 790 msl) is an important solar powered electricity generating system situated approximately 50 km northwest of Riyadh, and therefore, inside the Arabian desert; these conditions make

that the aerosol registered in this site present optical properties representative of the so-called pure desert dust, without signs of urban pollution.

The size distribution (considered as bi-modal lognormal) is described in table 1 of Dubovik et al. (2002) as function of the aerosol optical depth at 1020 nm. Values of the representative parameters for the fine and the coarse mode are computed using the expressions given in table 1. Only two examples of the size distribution are used along this sensitivity error analysis. They are calculated taking as reference values: $\tau_{a_{ref1}}(1020) = 0.3$ and $\tau_{a_{ref2}}(1020) = 0.5$. Since they will be mentioned constantly, hereafter both examples will be denoted more simply as SolV1 and SolV2 respectively.

On the other hand, values of the refractive index do not depend on the aerosol optical depth. For the real part, they are set as as 1.56 regardless of the wavelength, while for the imaginary part the values vary with wavelength as follows: 0.0029 for 440 nm, 0.0013 for 670 nm and 0.001 for both 870 nm and 1020 nm.

The forward module of Dubovik's inversion code (section 1.2.3) uses the refractive index and the absolute values of the size distribution as inputs. The aerosol optical depth and the single scattering albedo of the considered examples (SolV1 and SolV2) are derived using the code[1].

Table 2.1 summarizes the aerosol properties of the two examples. Input and output sectors refer respectively to the inputs used and the products obtained with the forward module of the Dubovik's code. In the input part, the first parameter is the aerosol optical depth from which the values of the parameters defining the size distribution are obtained. These parameters, for both the fine and coarse mode, are situated in the table just after the AOD: particle volume concentration ($C_{Vi}[\mu m^3/\mu m^2]$), volume median radius ($R_{Vi}[\mu m]$) and mode width (σ_{Vi}). Note that the ratio of the coarse to the fine mode volume concentration is C_{Vc}/C_{Vf} 10, i.e. there is a clear coarse mode predominance. The refractive index is also located in the inputs, and as it was commented, presents the same values for both examples. The last parameter used as input is the sphericity (section 1.2.3), which for desert dust is 0, because all the particles are considered to be spheroids.

The output part is occupied by the calculated aerosol optical depth and the single scattering albedo. The discrepancies between the reference values $\tau_{a_{ref1}}(1020) = 0.3$ and $\tau_{a_{ref1}}(1020) = 0.5$ from which the size distribution is derived and the outputs $\tau_a(1020) = 0.332$ (SolV1) and $\tau_a(1020) = 0.557$ (SolV2) can be surprising at a first glance. But it should be noted that the parametrization of the size distribution comes from a regression and it is an approximation, therefore the output spectral aerosol optical depth will not exactly coincide with the input provided as reference. Nevertheless, we will typically denote the aerosol examples with the values used as reference for simplicity.

[1]Note that these values contrary to the radiance measurements do not depend on the "conditions", such as the measurement geometry or the solar zenith angle.

Table 2.1: Description of aerosol properties of the two examples considered from the desert dust aerosol in Solar Village site: SolV1 and SolV2 with $\tau_{a_{ref1}}(1020) = 0.3$ and $\tau_{a_{ref1}}(1020) = 0.5$ as reference values. The first row specifies the parameters describing the size distribution which is modeled as a bimodal lognormal function: $C_{Vi}[\mu m^3/\mu m^2]$, $R_{Vi}[\mu m]$ and σ_{Vi}. Refractive index and the sphericity parameter are also parts of the input. Single scattering albedo and aerosol optical depth, for each wavelength, are shown as the output after applying the forward model.

Desert Dust (Solar Village)								
INPUT	$\tau_{a_{ref}}(1020)$	R_{V_f}	σ_{V_f}	C_{V_f}	R_{V_c}	σ_{V_c}	C_{V_c}	*Sph.*
- SolV1 -	0.300	0.120	0.400	0.026	2.320	0.600	0.274	0
- SolV2 -	0.500	0.120	0.400	0.030	2.320	0.600	0.470	0
	$n(440)$	$n(670)$	$n(870)$	$n(1020)$	$k(440)$	$k(670)$	$k(870)$	$k(1020)$
- SolV1 -	1.5600	1.5600	1.5600	1.5600	0.0029	0.0013	0.0010	0.0010
- SolV2 -	1.5600	1.5600	1.5600	1.5600	0.0029	0.0013	0.0010	0.0010
OUTPUT	$\tau_a(440)$	$\tau_a(670)$	$\tau_a(870)$	$\tau_a(1020)$	$\omega_o(440)$	$\omega_o(670)$	$\omega_o(870)$	$\omega_o(1020)$
- SolV1 -	0.483	0.371	0.344	0.332	0.9300	0.9664	0.9772	0.9794
- SolV2 -	0.707	0.591	0.568	0.557	0.9209	0.9647	0.9768	0.9793

In addition, for the desert dust type there is another important element regarding the explanation of these discrepancies: The software package including the spheroids was developed later (Dubovik et al. (2006)) (described in subsection 1.2.3.3) than the variability analysis considered as reference here (Dubovik et al. (2002)). The assumption of non-sphericity rises the aerosol optical depth as a consequence of the increase in scattering. In particular, if we avoided the spheroids model in the forward module, the values for the aerosol optical depth at 1020 nm for SolV1 and SolV2 would be $\tau_a(1020) = 0.294$ and $\tau_a(1020) = 0.493$. These values are in a better agreement with the reference values and the differences could only be related to the inaccuracies in the regressions.

There is a general agreement comparing the values obtained for the size distribution, in table 2.1, with other existing works. Particularly for R_{V_c}, some in-situ studies suggest that its value is around 2.0 μm which is in agreement with the 2.32 μm obtained for Solar Village: Tanaka et al. (1989), dust originated in China and measured in Japan, Levin et al. (1980), dust storm over Israel desert and, Patterson and Gillette (1977), dust storm over Texas. More recent studies using AERONET data also registered a similar value: Prats et al. (2008) indicates that the value of R_{V_c} is equal to 2.09 μm for the Saharan dust intrusions in the south of the Iberian Peninsula. This value is consistent with models too. For example, the volume median radius of the coarse mode is about 2 μm, in Koepke et al. (1997) and Tegen and Lacis (1996).

The real part of the refractive index shows good agreement with several models which suggest a value of 1.53 (Koepke et al. (1997),Shettle and Fenn (1979)). Moreover, in situ values present deviations up to ± 0.05 which are attributed to differences in the dust composition and in the

measurements techniques (Patterson and Gillette (1977) and Sokolik and Toon (1999)), therefore a value of 1.56 can be considered adequate. However, the imaginary part of the refractive index used is relatively lower than 0.008, suggested in some models (Shettle and Fenn (1979)). This issue is directly related to the discussion about desert dust absorption between in-situ/models and remote sensing observations. As it will be commented in the next paragraph for single scattering albedo, remote sensing observations obtain lower absorption values than what the models suggest. On the other hand, the imaginary part dependence on λ is a distinctive feature of the desert dust; concretely, $k(\lambda)$ is 3-4 times higher at 440 nm than at the longer wavelengths, while it remains constant in the others aerosol types. This spectral dependence has been reported in many studies about models (Sokolik and Toon (1999)) and measurements (Kandler et al. (2007)).

The single scattering albedo increases or is constant with λ due to the domination of large particles. The high values obtained are similar to those retrieved with satellite data (Kaufman et al. (2001) and Tanre et al. (2001)). However, some differences appear while comparing with in situ results, which suggest lower values and therefore a higher absorption as it was commented for the real part of the refractive index (Sokolik and Toon (1999), Patterson and Gillette (1977)). Mineralogical studies tried to contribute in this discussion (Claquin et al. (1998) and Sokolik and Toon (1999)). Results indicated that the absorption is highly predetermined by the presence of hematite (iron oxide) in the dust. Furthermore, the way this component is mixed with quartz or clay makes giving an accurate value of the absorption very difficult.

2.2.1.2 Self-consistency test with Dubovik inversion code

The results of the self consistency test for desert dust are presented in figure 2.3. The study is made following the scheme presented in figure 2.2. Beside the size distribution and the refractive index, the single scattering albedo is illustrated due to its great significance. Results obtained with almucantar geometry are shown in the upper part, while results from simulations with principal plane are placed at the bottom. In all the representations, the results obtained for the case $\tau_{a_{ref}}(1020) = 0.3$ are plotted with a solid line and for the case $\tau_{a_{ref}}(1020) = 0.5$ with a dashed line. By now it should be noted that this study intends to help in the analysis by highlighting those differences arising from the forward-backward procedure, and help separate them from those associated to radiance errors.

Original size distribution is represented in black while those obtained after the forward and backward processes are plotted in different colors, depending on the solar zenith angle used for the simulations: dark blue for $SZA = 15°$, light blue for $SZA = 30°$, green for $SZA = 45°$, orange for $SZA = 60°$ and brown for $SZA = 75°$. There is a good agreement between original and derivate size distributions as can be seen in the figure 2.3, where to distinguish among the lines is difficult.

Single scattering albedo is plotted as a function of the solar zenith angle. Different colors have

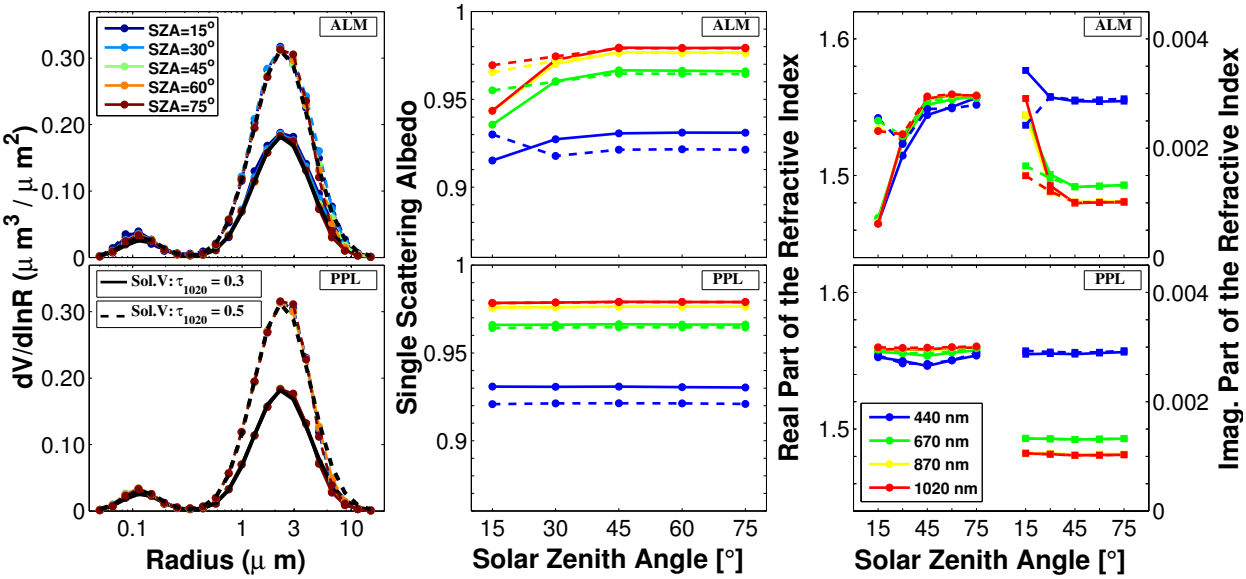

Figure 2.3: Summary of aerosol products obtained using Dubovik inversion for simulated radiance using desert dust aerosol type (Solar Village site) with two different AOD as reference: $\tau_{a_{ref}}(1020) = 0.3$ (solid line) and $\tau_{a_{ref}}(1020) = 0.5$ (dashed line): in the upper part almucantar results are shown whereas principal plane results are presented in the bottom part. Figures on the left correspond to size distribution results. Figures in the center illustrate the results for the single scattering albedo, and figures on the right describe the results for the refractive index.

been chosen for different wavelengths, thus, blue for 440 nm, green for 670 nm, yellow for 870 nm and red for 1020 nm. The expected result for the single scattering albedo is not shown in order to make the interpretation of the figure easier and they can be consulted in table 2.1. For principal plane, the expected and obtained values match for all the wavelengths and for both aerosol loads regardless of the SZA. Now it can be graphically seen how the highest values of the single scattering albedo are reached for the longest wavelength due to the predominance of the coarse mode as it was commented.

All the wavelengths present the same values for the single scattering albedo between the two aerosol loads except for the 440 nm case, where a small disagreement of 0.01 is found (from 0.92 to 0.93 in accordance with table 2.1). However, the most significant result is obtained with the almucantar analysis. The single scattering albedo for solar zenith angles smaller than 45° do not match with their expected values. While for large SZA, values are as good as for principal plane retrievals, when the SZA decreases some instabilities appear. In a nutshell, it can be explained by the fact that the information for retrieving the single scattering albedo is contained in short and large scattering angles. As for almucantar measurements the maximum scattering angle is twice the SZA, the measurements made with short SZA do not contain enough information to adequately retrieve the single scattering albedo. This was partially described for simulations in Dubovik et al. (2000), and for real AERONET data commented in the subsection 1.1.4 (extension of the work Dubovik (2009)).

About the refractive index, the retrievals for principal plane simulations are quite good again.

Introduced inputs (table 2.1) are exactly reproduced in the self-consistent process, as it can be observed in the left bottom part of figure 2.3. For the real part, the input value of 1.56 is only reached for the long wavelengths (870 nm and 1020 nm) and results for short wavelengths are slightly lower. In almucantars retrievals, both parts of the refractive index suffer instabilities when the SZA is smaller than 45°, as it happened with the single scattering albedo. Discrepancies are higher for the case with low aerosol load, particularly, for $SZA = 15°$, where the real part of refractive index is only 1.46, while the imaginary part is much higher than the inputs, specially for long wavelengths where values are three times larger.

2.2.2 Oceanic (Lanai)

2.2.2.1 General characteristics

A 5 year observation period in Lanai has been chosen to represent the characteristics of the oceanic aerosol from the examples in in Dubovik et al. (2002). The site is situated in Lanai island (20.74° N-156.92° W, 20 msl) closed to the coast and approximately 100 km away from Honolulu.

The principal distinct factor between this aerosol and the other three cases is its substantially lower optical thickness. Low aerosol optical thickness has been associated with high uncertainty to correctly retrieve the aerosol absorption and the refractive index (Dubovik et al. (2000)). The criteria of AERONET Version 2.0 establish that optical parameters are quality-assured when $\tau_a(440) > 0.4$ (apart from other set of quality criteria), level far away from the typical features of this aerosol. Nevertheless, the refractive index and the single scattering albedo retrieved will be used in the analysis, keeping always in mind the limitations.

According to table 1 of Dubovik et al. (2002), the values obtained for aerosol optical at 1020 nm vary from 0.01 to 0.2 with a mean value of $< \tau_a(1020) >= 0.04$. Therefore the reference values used for the two example of this aerosol are $\tau_{a_{ref}}(1020) = 0.05$ (Lana1) and $\tau_{a_{ref}}(1020) = 0.1$ (Lana2). With these values and using the expressions in table 1 of Dubovik et al. (2002) the parameters of the size distributions are calculated. Afterwards, the aerosol optical depth and the single scattering albedo are calculated running the forward module of Dubovik's code with these size distributions and the values of the refractive index also given in the same table. Table 2.2 summarizes all the values obtained in both examples. It is important to mention that the outputs for $\tau_a(1020)$ have almost the same values as the reference inputs in this case.

The coarse mode of this aerosol is smaller than for the desert dust: $C_{V_c}/C_{V_f} \sim 2$, but much higher than for urban and biomass burning which will be analyzed in the next sections as examples of fine mode predominance. The prevalence of a coarse mode in the oceanic aerosol is related with the presence of coarse sea salt particles. Properties of the size distribution, described in table 2.2, agree with the other studies: Shettle and Fenn (1979), Tanre et al. (1999), Gathman (1983).

Table 2.2: Description of aerosol properties of the two examples considered from oceanic aerosol in Lanai site: Lana1 and Lana2 with $\tau_{a_{ref1}}(1020) = 0.05$ and $\tau_{a_{ref1}}(1020) = 0.1$ as reference values. The first row specifies the parameters describing the size distribution which is modeled as a bimodal lognormal function: $C_{Vi}[\mu m^3/\mu m^2]$, $R_{Vi}[\mu m]$ and σ_{Vi}. Refractive index and the sphericity parameter are also parts of the input. Single scattering albedo and aerosol optical depth, for each wavelength, are shown as the output after applying the forward model.

Oceanic (Lanai)								
INPUT	$\tau_{a_{ref}}(1020)$	R_{V_f}	σ_{V_f}	C_{V_f}	R_{V_c}	σ_{V_c}	C_{V_c}	*Sph.*
- Lana1 -	0.050	0.160	0.480	0.020	2.700	0.680	0.040	100
- Lana2 -	0.100	0.160	0.480	0.040	2.700	0.680	0.080	100
	$n(440)$	$n(670)$	$n(870)$	$n(1020)$	$k(440)$	$k(670)$	$k(870)$	$k(1020)$
- Lana1 -	1.3600	1.3600	1.3600	1.3600	0.0015	0.0015	0.0015	0.0015
- Lana2 -	1.3600	1.3600	1.3600	1.3600	0.0015	0.0015	0.0015	0.0015
OUTPUT	$\tau_a(440)$	$\tau_a(670)$	$\tau_a(870)$	$\tau_a(1020)$	$\omega_o(440)$	$\omega_o(670)$	$\omega_o(870)$	$\omega_o(1020)$
- Lana1 -	0.137	0.079	0.059	0.052	0.9743	0.9700	0.9693	0.9698
- Lana2 -	0.274	0.157	0.119	0.103	0.9743	0.9700	0.9693	0.9698

The low absorption ($\omega_o > 0.97$ and $k(\lambda) = 0.0015$) was expected minding that the oceanic aerosol is basically composed of sea salt and water soluble particles with high relative humidity (Hess et al. (1998), Smirnov et al. (2002b)).

2.2.2.2 Self-consistency test with Dubovik inversion code

Same as described for the desert dust, results of the self-consistency test for oceanic aerosol are shown in figure 2.4. As for the desert dust, retrievals for the size distribution present good agreement with the original ones. Only very small discrepancies can be observed for radii larger than $5\mu m$, specially for principal plane simulations. These differences could be explained by the low influence of this part of the size distribution on the radiance measurements for the wavelengths used in AERONET (440 nm to 1020 nm); this idea will be further analyzed subsection 2.4.3.

Single scattering albedo values match with the ones in table 2.2. Contrary to desert dust case, the single scattering albedo decreases with the wavelength. The significant reduction of coarse mode against the fine mode together with the non-dependency of the imaginary refractive index on the wavelength, provokes this change. This is easy to see looking at the color (wavelength) distributions of figure 2.4, which are inverted compared to those in figure 2.3. Still, values are very close each other and the change of trend will be better observed in the study of the next aerosols types where the fine mode strongly predominates.

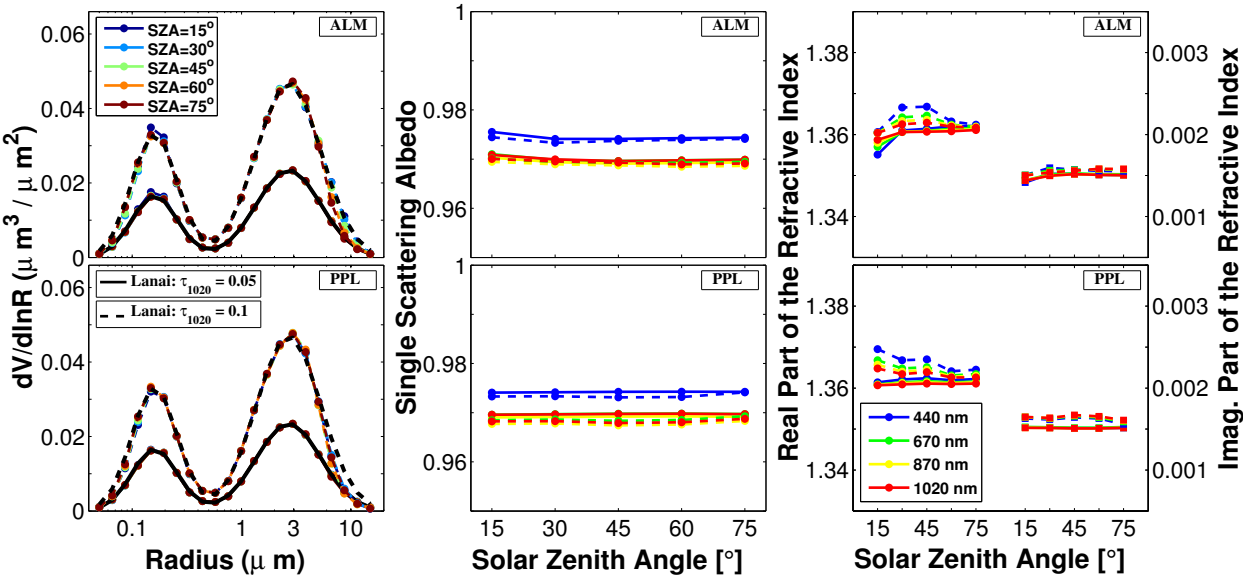

Figure 2.4: Summary of aerosol products obtained using Dubovik inversion for simulated radiance using oceanic aerosol type (Lanai site) with two different AOD: $\tau_a(1020) = 0.05$ (solid line) and $\tau_a(1020) = 0.1$ (dashed line): in the upper part almucantar results are shown whereas principal plane results are presented in the bottom part. Figures on the left correspond to size distribution results. Figures in the center illustrate the results for the single scattering albedo, and figures on the right describe the results for the refractive index.

Instability problems associated with the short SZA in almucantar measurements can be seen only for 15° and they are smaller than for the desert dust case. They are also noticeable for the real part of the refractive index; nevertheless, these instabilities were much larger in the previous case.

2.2.3 Urban (GSFC)

2.2.3.1 General characteristics

From the different examples which can be found in Dubovik et al. (2002) (Paris, GSFC, Mexico City and Maldives), the AERONET calibration center at NASA's Goddard Space Flight Center in Greenbelt, Maryland (38.99° N-76.84° W, 87 msl) is the one chosen for representing the urban aerosol. The place is located 20 km northeast of Washington inside the Boston-Washington megalopolis which is the second most heavily urbanized area in the United States supporting 50 million people. Nevertheless, GSFC site was selected in the analysis because it has the lowest absorption values of the urban aerosol (see table 1 in Dubovik et al. (2002)).

The case of fine particles with high absorption would be covered tackling the biomass burning in the next subsection, so here selecting the case with the lowest absorption seems more reasonable. To be more precise, we should refer to the aerosol found in GSFC as a clean-urban aerosol, but for simplicity, here we will refer to it as urban aerosol. Same as the previous cases two examples

of the urban aerosol are selected and their properties are given as function of $\tau_a(440)$. As it was commented in the introduction the reference values chosen are $\tau_{a_{ref}}(440) = 0.2$ (GSFC1) and $\tau_{a_{ref}}(440) = 0.5$ (GSFC2).

Table 2.3: Description of aerosol properties of the two examples considered from urban aerosol in GSFC site: GSFC1 and GSFC2 with $\tau_{a_{ref}}(440) = 0.2$ and $\tau_{a_{ref}}(440) = 0.5$ as reference values. The first row specifies the parameters describing the size distribution which is modeled as a bimodal lognormal function: $C_{Vi}[\mu m^3/\mu m^2]$, $R_{Vi}[\mu m]$ and σ_{Vi}. Refractive index and the sphericity parameter are also parts of the input. Single scattering albedo and aerosol optical depth, for each wavelength, are shown as the output after applying the forward model.

Urban (GSFC)								
INPUT	$\tau_{a_{ref}}(440)$	R_{V_f}	σ_{V_f}	C_{V_f}	R_{V_c}	σ_{V_c}	C_{V_c}	*Sph.*
- GSFC1 -	0.200	0.142	0.380	0.030	3.128	0.790	0.018	100
- GSFC2 -	0.500	0.175	0.380	0.075	3.275	0.790	0.030	100
	$n(440)$	$n(670)$	$n(870)$	$n(1020)$	$k(440)$	$k(670)$	$k(870)$	$k(1020)$
- GSFC1 -	1.4100	1.4100	1.4100	1.4100	0.0030	0.0030	0.0030	0.0030
- GSFC2 -	1.4100	1.4100	1.4100	1.4100	0.0030	0.0030	0.0030	0.0030
OUTPUT	$\tau_a(440)$	$\tau_a(670)$	$\tau_a(870)$	$\tau_a(1020)$	$\omega_o(440)$	$\omega_o(670)$	$\omega_o(870)$	$\omega_o(1020)$
- GSFC1 -	0.195	0.083	0.048	0.036	0.9718	0.9588	0.9476	0.9404
- GSFC2 -	0.559	0.254	0.145	0.102	0.9771	0.9691	0.9604	0.9535

Table 2.3 contains the aerosol properties of the two examples considered for urban aerosol. The aerosol optical thickness (at 440 nm) of the output is a little bit lower than the references for GSFC1 and around 10% higher for GSFC2. For this case, the justification of non-sphericity can not be used, because the particles are supposed to be 100% spheres. Nevertheless, we should not forget that the expression relating aerosol optical depth to the aerosol microphysical properties in Dubovik et al. (2002) is obtained from a regression and some tolerance should be admitted.

The high values of the single scattering albedo (estimated by Dubovik's code, AERONET retrievals) in GSFC are in a reasonable agreement with in-situ aircraft measurements, concretely for the experiments SCAR-America (Remer et al. (1997)) and the Tropospheric Aerosol Radiative Forcing Observational Experiment (TARFOX) (Hartley et al. (2000),Russell et al. (1999)). The first experiment showed $\omega_o(450) \sim 0.98-0.99$. The analysis made by (Hartley et al. (2000)) for TARFOX estimated values of the single scattering albedo for hydrated aerosol as $\omega_o(550) = 0.95 \pm 0.03$. Comparing with the models, these absorption values observed at GSFC site are close to the values expected for water-soluble aerosol (Koepke et al. (1997) and Shettle and Fenn (1979)).

The fine mode volume concentration is larger than the coarse mode for GSFC. For instance, in the example GSFC2, the ratio between volume concentration is $C_{V_f}/C_{V_c} = 2.5$. The volume median radius for the fine mode is $R_{V_f} \sim 0.15 - 0.17$ which coincides with in situ aerosol measurements

(Hartley et al. (2000)). There is also a good agreement in the coarse mode where volume median radius is $R_{V_C} \sim 3.0$. As in the case of oceanic aerosol, the highest values of the single scattering albedo are reached for the shortest wavelengths. However, the strong dominance of fine mode makes the dependence on the wavelength becomes larger (see values in table 2.3 compared to those table 2.2).

The real part of the refractive index is assumed to be constant, regardless of the wavelength, and equal to 1.41. This value is within the range $1.33 - 1.45$ which is the estimation of TARFOX experiment. On the other hand, this experiment estimates the imaginary part to be between 0.001 and 0.008; so the value of 0.003, retrieved by AERONET and used in table 2.3, also agrees with the in situ aircraft results.

2.2.3.2 Self-consistency test with Dubovik inversion code.

Self-consistency test, besides its primary objective, allows us to graphically see the properties commented in the previous subsection. Looking at the subfigures related to the size distribution in figure 2.5, the fine mode appears much higher than the coarse mode. Even though the ratio between fine and coarse volume concentrations is just 2.5, the fact that the width of the fine mode is half of the one in the coarse mode, makes the difference between the modes seem larger. Regarding the size distribution, it can be also observed how retrieved and original size distributions perfectly match for both almucantar and principal plane simulations.

The single scattering albedo presents stability problems for almucantar retrievals when the SZA is short. On the contrary, for principal plane retrievals the single scattering albedo remains constant. Same observations are valid for the refractive index too.

Several properties which went unnoticed in table 2.3 can be easier observed in the figure 2.5. For instance, the single scattering albedo is different for the two analyzed cases, GSFC1 and GSFC2. There is an increase of this parameter as the aerosol load grows, about 1%. This increase can not be justified with a variation in the refractive index, because it is the same for both cases[2]. However, contrary to the previous cases, there is a strong change in the shape of the size distribution for GSFC depending on the τ_a. Thus, the variability study reflects an increase in the fine mode with respect to the coarse mode as the aerosol optical depth grows (Dubovik et al. (2002)), which is reproduced in the study of GSFC1 and GSFC2. The maximum in the fine mode is also shifted towards larger radii (easier to see in figure 2.5). Both factors rise the number of particles in sizes where scattering has larger efficiency compared to the absorption. So, even though the absorption does not change, due to the changes in the size distribution, the scattering component increases,

[2]In the input (table 2.3). Even though there are some differences in the real part for the retrievals, they are very small and indicate smaller values for GSFC2. Following Bohren and Huffman (1983), that should mean a decrease of the ω_o and not the opposite, as in our case.

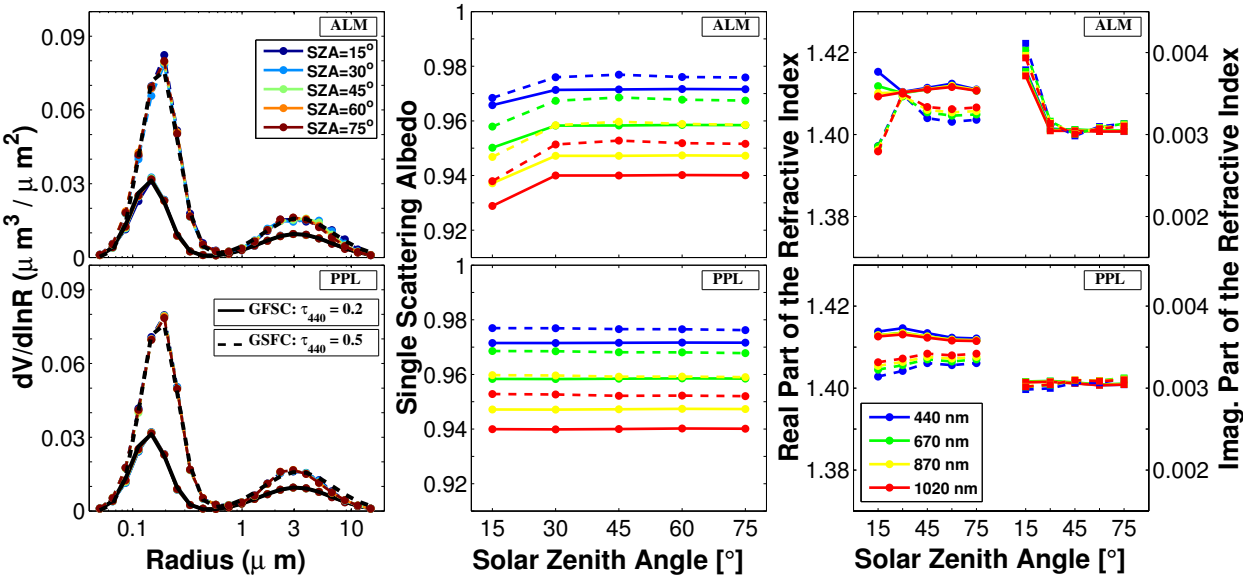

Figure 2.5: Summary of aerosol products obtained using Dubovik inversion for simulated radiance using urban aerosol type (GSFC site) with two different AOD: $\tau_a(440) = 0.2$ (solid line) and $\tau_a(440) = 0.5$ (dashed line): in the upper part almucantar results are shown whereas principal plane results are presented in the bottom part(almucantar results are shown in the upper and principal plane results in the bottom part). Figures on the left correspond to size distribution results. Figures in the center illustrate the results for the single scattering albedo, and figures on the right describe the results for the refractive index.

and consequently, the single scattering albedo.

2.2.4 Biomass burning (Mongu-Zambia)

2.2.4.1 General characteristics

The last case is devoted to the biomass burning aerosol. Biomass burning, or more simply smoke, is predominantly composed by fine particles and is known to be absorbing due to its high concentration of black carbon, which causes low values of ω_o. However, ω_o varies significantly for smoke of different origin and correlates with the presence of black carbon in combustion products. From the different environments characterized in the reference paper (North American boreal forest, Amazonian tropical forest and African savanna regions) we have chosen the site with the largest absorption, since for Urban aerosol we chose GSFC (the less absorbing), in order to enlarge the study range. The site with the largest absorption, and consequently the one chosen, is Mongu in Zambia.

Mongu (15.25° S-23.15° E, 1107.0 msl) is mainly sandy with a seasonal flood plain that is burned to the west annually from July through November. It is the capital of the western region in Zambia and it has an airport where, precisely, the AERONET-site is located.

In this case, the two aerosol loads considered as references are: $\tau_{a_{ref}}(440) = 0.4$ (Zamb1) and $\tau_{a_{ref}}(440) = 0.8$ (Zamb2). In table 2.4, values related to the size distribution and refractive index

for both examples are shown as inputs. The generated values, the aerosol optical depth and the single scattering albedo, appear in the output part.

Table 2.4: Description of aerosol properties of the two examples considered for biomass burning aerosol in Mongu site in Zambia.: Zamb1 and Zamb2 with $\tau_{a_{ref}}(440) = 0.4$ and $\tau_{a_{ref}}(440) = 0.8$ as reference values. The first row specifies the parameters describing the size distribution which is modeled as a bimodal lognormal function: $C_{Vi}[\mu m^3/\mu m^2]$, $R_{Vi}[\mu m]$ and σ_{Vi}. Refractive index and the sphericity parameter are also parts of the input. Single scattering albedo and aerosol optical depth, for each wavelength, are shown as the output after applying the forward model.

Biomass Burning (Zambia)								
INPUT	$\tau_{a_{ref}}(440)$	R_{V_f}	σ_{V_f}	C_{V_f}	R_{V_c}	σ_{V_c}	C_{V_c}	*Sph.*
- Zamb1 -	0.400	0.130	0.400	0.048	3.504	0.730	0.004	100
- Zamb2 -	0.800	0.140	0.400	0.096	3.788	0.730	0.007	100
	$n(440)$	$n(670)$	$n(870)$	$n(1020)$	$k(440)$	$k(670)$	$k(870)$	$k(1020)$
- Zamb1 -	1.5100	1.5100	1.5100	1.5100	0.0210	0.0210	0.0210	0.0210
- Zamb2 -	1.5100	1.5100	1.5100	1.5100	0.0210	0.0210	0.0210	0.0210
OUTPUT	$\tau_a(440)$	$\tau_a(670)$	$\tau_a(870)$	$\tau_a(1020)$	$\omega_o(440)$	$\omega_o(670)$	$\omega_o(870)$	$\omega_o(1020)$
- Zamb1 -	0.416	0.184	0.107	0.078	0.8778	0.8290	0.7811	0.7467
- Zamb2 -	0.872	0.397	0.232	0.167	0.8827	0.8402	0.7958	0.7620

The variations of the ω_o for the biomass burning depending on the location are attributed to differences in the relative percentage of combustion occurring in the flaming versus the smoldering phases[3]. There are other reasons though, as the degree of aging of the particles, ambient temperature, relative humidity and fire intensity (Reid et al., 1999). Values for the single scattering albedo in the sites analyzed in Dubovik et al. (2002) range from $\omega_o(1020) = 0.78$ in Africa savanna (Zambia) to $\omega_o(1020) = 0.91$ in the Boreal Forest (United States and Canada).

The fine mode dominates the particle size distribution for smoke from all regions reported in Dubovik et al. (2002). Particularly, the case selected for the biomass burning simulations, Mongu site (Zambia), has the smallest volume median radius (for the fine mode) and the largest for the coarse from all the regions (Amazonian and Boreal). Table 2.4 shows that R_{V_f} and R_{V_c} depend on the aerosol load, both of them being larger as the aerosol optical depth increases. The ratio between C_{V_f} and C_{V_c} is about 10, which is much larger than for the GSFC case.

The values of the refractive index do not depend on the aerosol optical depth and the high value of the imaginary part calls the attention. Due to the important absorption of this aerosol, the imaginary part (constant with wavelength and equal to 0.021) is one order of magnitude higher

[3]The more biomass is consumed during a flaming phase, the smaller the single scattering albedo, Ward et al. (1992) and Ward et al. (1996). While in savanna ecosystems 85% of the biomass is consumed by flaming, this percentage descends to 50% or even less in deforestation fires.

than in the other aerosol types. Finally, it can be observed that the value for the real part, 1.51 for all wavelengths, is a bit smaller than for desert dust (1.56) but much higher than the other two cases.

2.2.4.2 Self-consistency test with Dubovik inversion code.

Figure 2.6 illustrates the results of the self-consistency test for the biomass burning aerosol in Zambia. Considering only the example with less aerosol load, Zamb1 with $\tau_{a_{ref}}(440) = 0.4$, results have similarities with previous aerosol cases: good agreement for the size distribution between original and retrieved size distribution, reasonable accordance between expected and retrieved values for the single scattering albedo (except for short SZA in almucantar) and also satisfactory results for the refractive index. On the other hand, the low values of ω_o are quite notable, as well as the high values of the imaginary part of the refractive index.

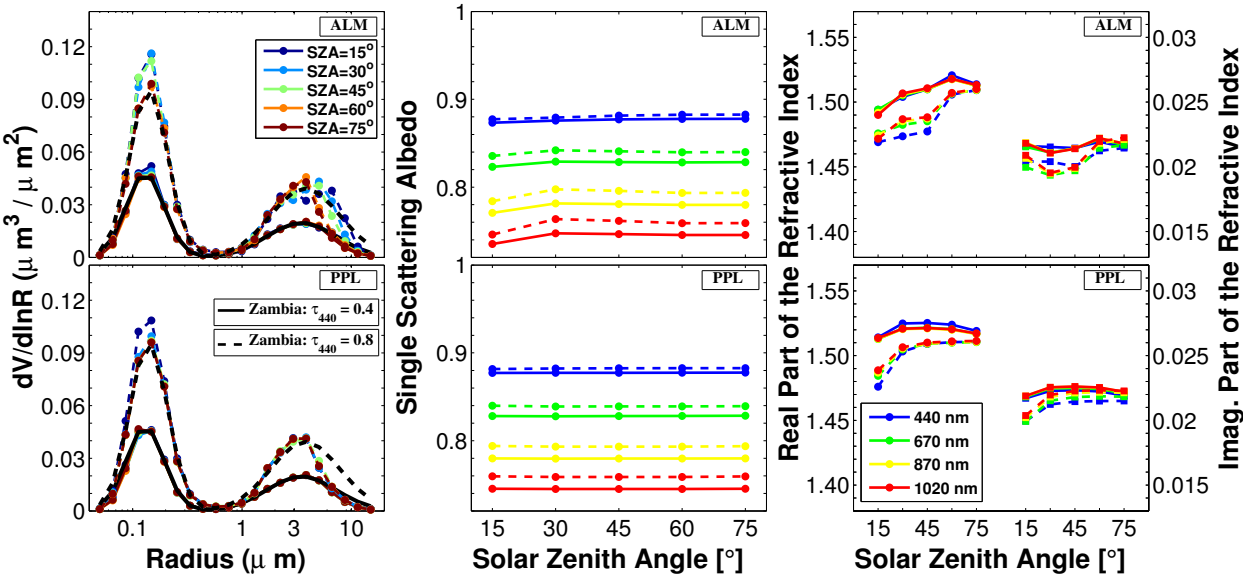

Figure 2.6: Summary of aerosol products obtained using Dubovik inversion for simulated radiance using the biomass burning aerosol climatic model (Mongu site in Zambia) with two different AOD: $\tau_a(440) = 0.4$ (solid line) and $\tau_a(440) = 0.8$ (dashed line): almucantar results are shown in the upper and principal plane results in the bottom part. Figures on the left correspond to size distribution results. Figures in the center illustrate the results for the single scattering albedo, and figures on the right describe the results for the refractive index.

However, the good concordance in the self consistency test for the Zamb2 example seems to vanish if we look at the size distribution. For the fine mode, when the maximum scattering angle is smaller than 120° ($SZA = 15°, 30°, 45°$ for almucantar and $SZA = 15°$ for the principal plane simulations), the values of the size distribution get unexpectedly higher than the original size distribution (up to 20%). This effect is accompanied by a sharp decline in the real refractive index (from 1.51 to $1.47 - 1.48$). Both effects compensate each other for the calculation of optical thickness: there are more particles but they scatter less light.

The disagreements are more striking in the coarse mode. For principal plane, all the size distributions are separated from the original one when the radius is higher than $3\mu m$. They all have the same values and decrease faster than the input for radii above $3\mu m$.

For the almucantar, nonetheless, the size distributions also get away from the original but they do not have a defined direction. The explanation of these issues resides in the low influence of the size distribution on the simulated measurements when the radius is larger than $3\mu m$ for the wavelengths used in the simulations; A similar effect was commented in the oceanic aerosol section and it will be discussed in more detail in the subsection 2.4.3.

Furthermore, in this case the predominance of the fine mode, which influences the simulated radiances more than in the oceanic case, and the fact that the coarse mode is displaced towards larger radius[4] make this effect more important.

2.3 Simulated radiance for each aerosol type

After describing the four aerosol types, the next step in this chapter is to analyze the corresponding simulated radiances: radiances for almucantar and principal plane geometries will be illustrated for the different examples in this section, while in the next one their sensitivity to several parameters will be studied, as for instance, the refractive index. The sensitivity study does not pretend to be quantitative as in Berjon (2007), where parameters are classified in order of their importance following the methodology described by Saltelli (2002). It should be remembered, that this work does not intend to make a validation of the AERONET inversion methodology and its products; we are interested in evaluating the origin of radiance error and quantifying them (chapter 3), and to analyze their repercussions on the inversion products (chapters 4, 5 and 6). Therefore, radiance sensitivity study will be specifically more orientated to a better understanding of the discussion in the following chapters and will have a pronounced descriptive character.

2.3.1 General aspects

Simulated normalized spectral radiances are plotted in figure 2.7 for almucantar configuration and in figure 2.8 for principal plane geometry, using the forward code of Dubovik inversion[5] (subsection 1.2.3.2) for the four aerosol types. Both figures are subdivided horizontally in three parts regarding the solar zenith angle; the one at the top represents simulations for $SZA = 15°$, the one in the middle for $SZA = 45°$ and the one at the bottom for $SZA = 75°$. Then each of these figures is subdivided for each aerosol type: top-left for desert dust (SolV2), top-right for oceanic (Lana2),

[4] R_{V_c} for Zambia cases are the largest among the selected sites.

[5] Following the normalization giving for Dubovik's code in subsection 1.2.3.2

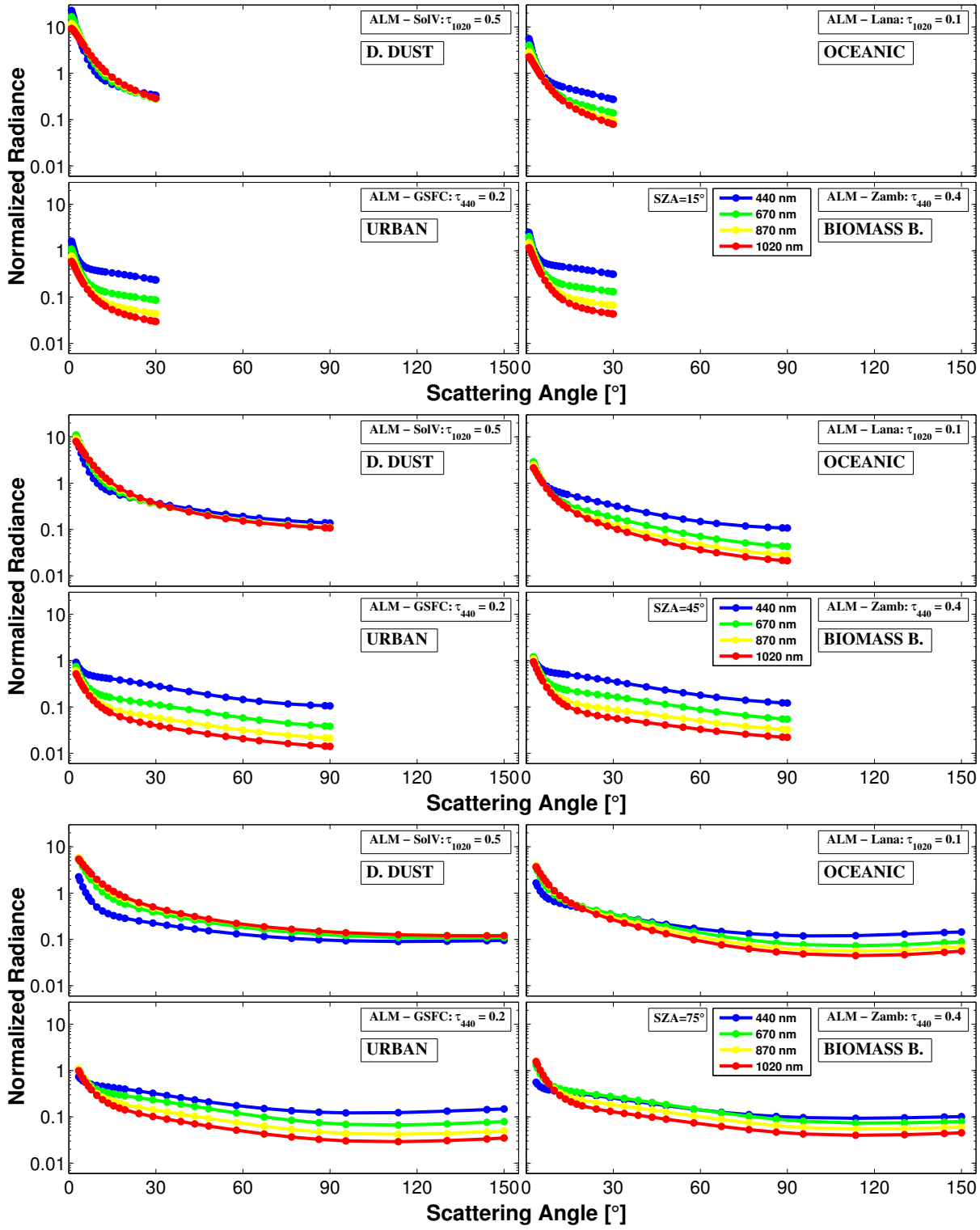

Figure 2.7: Simulated normalized spectral radiances obtained using the forward code of Dubovik inversion in an almucantar geometry. The figure at the top represents simulations for $SZA = 15°$, the figure in the middle for $SZA = 45°$ and the figure at the bottom for $SZA = 75°$. In each of the figures there is a subdivision for each aerosol type: top-left for desert dust (SolV2), top-right for oceanic (Lana2), bottom left for urban (GSFC1) and bottom right for biomass burning (Zamb1). In all of them, different colors have been used to represent the (Dubovik) normalized radiance values for different wavelengths: blue for 440 nm, green for 670 nm, yellow for 870 nm and red for 1020 nm.

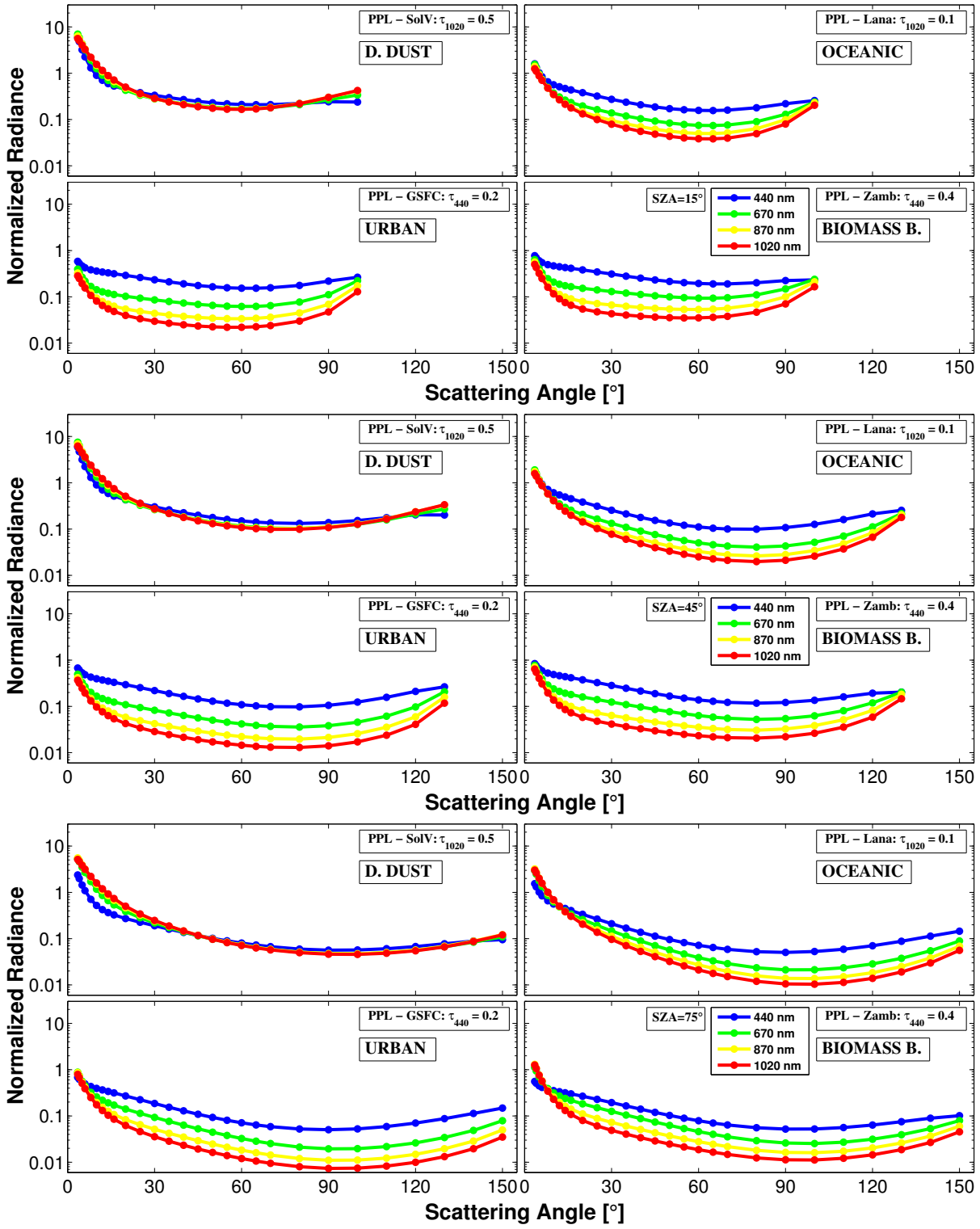

Figure 2.8: Simulated normalized spectral radiances obtained using the forward code of Dubovik inversion in a principal plane geometry. The figure at the top represents simulations for $SZA = 15°$, the figure in the middle for $SZA = 45°$ and the figure at the bottom for $SZA = 75°$. In each of the figures there is a subdivision for each aerosol type: top-left for desert dust (SolV2), top-right for oceanic (Lana2), bottom left for urban (GSFC1) and bottom right for biomass burning (Zamb1). In all of them, different colors have been used to represent the (Dubovik) normalized radiance values for different wavelengths: blue for 440 nm, green for 670 nm, yellow for 870 nm and red for 1020 nm.

bottom left for urban (GSFC1) and bottom right for biomass burning (Zamb1). Different colors have been used for different wavelengths: blue for 440 nm, green for 670 nm, yellow for 870 nm and red for 1020 nm.

In the figures, the dependence of the maximum scattering angle with the SZA excels in both figures compared to other aspects. This fact is even more notable for the almucantar geometry in which, as it was indicated in subsection 1.1.3, the maximum scattering angle is twice the SZA. In this way, the maximum scattering angle in figure 2.7 is 30° for the figure at the top where $SZA = 15°$, 90° for the figure in the middle where $SZA = 45°$ and 150° for the figure at the bottom where $SZA = 75°$. In subsection 1.1.3 we also commented that in the principal plane measurements, the scattering angle for each measurement is directly the corresponding measurement angle and that the maximum value of the scattering angle in a CIMEL-318 principal plane measurement is the maximum angle (θ_M) from the principal plane set of values which fulfills that $\theta_M - SZA < 90°$ (see values in table 1.2). For this reason, in figure 2.8, the maximum scattering angle is 100° (maximum in principal plane set of angles smaller than 105°) for the figure at the top where $SZA = 15°$, 130° (maximum in principal plane set of angles smaller than 135°) for figure in the middle where $SZA = 45°$ and 150° (maximum in principal plane set of angles smaller than 165°) for the figure at the bottom where $SZA = 75°$. The lack of information regarding scattering angles of almucantar vs. principal plane has been commented many times in the present thesis, and here, this issue is graphically shown.

2.3.2 Principal plane vs. almucantar

The first property that is observed comparing the principal plane vs almucantar measurements, (figure 2.7 and figure 2.8), is that the observation for principal plane corresponding to a scattering angles of $2SZA$ is the same as the almucantar one done at $\varphi_a = 180°$. Therefore, the two figures at the top have the same values at 30° of the scattering angle, the ones in the middle at 90° and the ones at the bottom at 150°.

For the rest of the scattering angles, the reasoning is not so easy. Looking at the figures, principal plane radiance measurements seems generally smaller than the almucantar ones (if they exist). To get an idea of the veracity of the last affirmation, let us compare the expressions of the single scattering radiance which were defined for principal plane and almucantar in Eq. (1.24), though here using the normalized radiance defined in Eq. (1.42):

$$\begin{aligned} R^*(\Theta,\lambda)^{(1)}_{\text{PPL}} =& \frac{\mu_s}{\mu_v - \mu_s}\left[\frac{\omega_o\tau_a P_a(\Theta) + \tau_R P_R(\Theta)}{\tau_a + \tau_R}\right][e^{-\frac{\tau_a+\tau_R}{\mu_v}} - e^{-\frac{\tau_a+\tau_R}{\mu_s}}] \\ R^*(\Theta,\lambda)^{(1)}_{\text{ALM}} =& \frac{1}{\mu_s}\left[\omega_o\tau_a P_a(\Theta) + \tau_R P_R(\Theta)\right][e^{-\frac{\tau_a+\tau_R}{\mu_s}}] \end{aligned} \tag{2.1}$$

If now we divide the expression for principal plane between the one for almucantar, and we do $\tau := \tau_a + \tau_R$, we obtain:

$$\frac{R(\Theta,\lambda)^{(1)}_{\text{PPL}}}{R(\Theta,\lambda)^{(1)}_{\text{ALM}}} = \frac{1}{\tau}\frac{\mu_s^2}{\mu_v - \mu_s}\left[e^{\tau\left(\frac{\mu_v-\mu_s}{\mu_v\mu_s}\right)} - 1\right] \tag{2.2}$$

If this expression was smaller than 1, it would mean that radiance measurement at θ_v for principal plane is smaller than the one made for almucantar at the same scattering angle. Unluckily the expression depends on μ_v, μ_s and τ and, in general, is not subject to simplifications. Nevertheless, for those cases where the exponential is close to one (exponent close to zero) we can do:

$$\left[e^{\tau\left(\frac{\mu_v-\mu_s}{\mu_v\mu_s}\right)} - 1\right] \sim \tau\left(\frac{\mu_v - \mu_s}{\mu_v\mu_s}\right) \tag{2.3}$$

and then,

$$\begin{aligned}\frac{R(\Theta,\lambda)^{(1)}_{\text{PPL}}}{R(\Theta,\lambda)^{(1)}_{\text{ALM}}} = \frac{1}{\tau}\frac{\mu_s^2}{\mu_v - \mu_s}\left[e^{\tau\left(\frac{\mu_v-\mu_s}{\mu_v\mu_s}\right)} - 1\right] \sim \frac{1}{\tau}\frac{\mu_s^2}{\mu_v - \mu_s}\tau\left(\frac{\mu_v - \mu_s}{\mu_v\mu_s}\right) \Rightarrow \\ \Rightarrow \frac{R(\Theta,\lambda)^{(1)}_{\text{PPL}}}{R(\Theta,\lambda)^{(1)}_{\text{ALM}}} \sim \frac{\mu_s}{\mu_v}\end{aligned} \tag{2.4}$$

which is easier to interpret. Actually, as we are limiting the principal plane to those scattering angles with almucantar measurements, we have that $\mu_v \in [\mu_s,\ 1]$, obtaining that the relation between principal plane and almucantar is always smaller than 1 regardless of the scattering angle.

However, we should not forget that the approximation requires a very small exponent. In other words: μ_s close to 1 or τ small enough to compensate for it. For instance, in the cases represented in figure 2.8, when the $SZA = 15°$ ($\mu_s = \cos(15°) = 0.966$), the approximation is valid always that $\tau < 1.5$, what happens for all the considered aerosols. In the second case with $SZA = 45°$ ($\mu_s = \cos(45°) = 0.707$), the approximation is valid only if $\tau < 0.8$ which is true for all the cases but for $\lambda = 440\ nm$ in the desert dust. The last plot with $SZA = 75°$ ($\mu_s = \cos(75°) = 0.259$) is much more restrictive and the approximation can be done only if $\tau < 0.1$ which reduces the validity for 870 nm and 1020 nm channels of all the aerosol except the desert dust, where it is never possible to do the approximation.

Nevertheless, the fact that the approximation is not valid does not mean that the relation principal plane vs almucantar is higher than one. Solving Eq. (2.2) numerically, it can be seen that the relation is smaller than one regardless of the scattering angles for all the cases and all the wavelengths except for the desert dust at 440 nm and $SZA = 75°$.

To end up the discussion, let us consider only those cases when the approximation in Eq. (2.4) is

true. For them, as the distance between μ_v and μ_s increases the differences between principal plane and almucantar rise as well. Then, the smaller is μ_s the higher the difference with μ_v can be. For all SZA, the ratio principal plane vs almucantar (in first scattering terms) will be the highest in the zenith where $\mu_v = 1$, this relation is about 95% when $SZA = 15°$, around 70% when $SZA = 45°$, and only 30% when $SZA = 75°$. The fact that radiance from principal plane is only about the 30% of the one for almucantar at zenith could explain the bending suffered by the principal plane (figure 2.8) compared to almucantar representation which is much flatter (figure 2.7), even though, the terms of multiple scattering were eliminated in the deduction.

2.3.3 Differences between the aerosol types

Normalized radiance values for 440 nm channel decrease with the SZA for all the aerosol types in both configurations. In other words, the intensity of the blue (440 nm) in the sky is higher at midday than when the sun is lower. However, for 670 nm, displayed as green (although spectrally in the red), radiance intensity keeps more or less constant throughout the day. As the wavelength increases, at 870 nm and 1020 nm channels, the radiance values even rise with the SZA.

So far, no distinction has been made for each aerosol type, and the abovementioned characteristics were common to all types. It is now time, therefore, to point out the most general differences for each aerosol type. Approximately, these differences provide the fingertip to each aerosol type, allowing not only the inversion algorithms but also the human eye to identify them. Before starting the discussion, it is worth noting the existence of a parallel study to the present thesis (Torres et al. (2011)), which examines experimental values of radiance measurements for various aerosols types (desert dust, biomass burning and continental aerosol) in Autilla del Pino site (Palencia, Spain). This study has not been added at this point due to the theoretical nature of the whole thesis regarding radiance measurements.

Looking at the data individually, the main difference that can be found is that the 4 channels appear close together for the desert dust and they are spread for the rest of the cases. For the oceanic, urban and biomass burning aerosol the four spectral lines can be easily recognized and they follow the sequence blue, green, yellow and red (more radiance for shorter wavelengths). However, for desert dust the lines are together, and for large SZA, the spectral sequence, commented above, is reversed. This is easily understood by those people living in areas with desert dust events, where the sky turns into whitish appearance during dust events. Another significant difference between the desert dust and the other cases is the strong decline of the radiance values after the aureole: the desert dust presents the highest values in the aureole region, visually noticeable due to the high sky radiance around the sun, but as the scattering angle grows the radiance values become the smallest, specially at 440 nm. For the rest of the aerosol types, the radiances do not decrease so strongly with increasing scattering angle, specially for the types dominated by the fine mode.

Also in these three types, in the almucantar configuration there is a local minimum between 100° and 120° which is not noticeable in the desert dust. This minimum is related to a minimum in the aerosol phase function, and the fact of keeping constant the optical mass in the almucantar allows to establish this association which is not so evident in the case of the principal plane.

Further details on other properties could have been discussed, especially related to the radiance values or multiple scattering, but a deep radiate transfer analysis is not within the scope of this study. Further insight can be gained in Coulson (1988) or Liou (1980) and the references therein.

2.4 Sensitivity of the simulated radiance to several factors

In order to better analyze the consequences that errors in radiance have on the inversion-retrieved products (chapter 4, 5 and 6), this section will qualitatively describe how small differences in the input parameters (complex refractive index and size distribution) affect the simulated radiances. As an example, if a certain pointing error can make the radiance to drop in a similar way that would arise from a decrease in the real part of the refractive index, it could be expected that the inversion code will diminish the real part of the refractive index in case such pointing error occurs.

2.4.1 Real refractive index

The real part of refractive index is the first parameter that has been analyzed regarding its impact over radiance measurements. An increase of the refractive index reduces the intensity of the phase function for short scattering angles, increasing the intensity for the large ones (Vermeulen (1996)). Therefore, its influence over the radiance is expected to be as a transfer of light towards higher scattering angles. Other parameters, such as the τ_a or ω_o, would be affected by the change of this parameter too. Both are expected to rise with an increase in the real part of the refractive index: τ_a because, theoretically, more light is scattered and therefore the direct beam is reduced; and ω_o because the absorption (associated with the imaginary part) does not vary (Bohren and Huffman (1983)) whereas the scattering increases. These implications are discussed below.

The working scheme consists of simulating measurements using the properties of the aerosol types described in section 2.2, but varying the real part of refractive index. More concretely, these tests are made modeling almucantars at $SZA = 75°$ for desert dust (SolV2), oceanic (Lana2), urban (GSFC2) and biomass burning (Zamb1), modifying their values of the real part of refractive index. For each wavelength, these increments are: -0.03, $+0.03$ and $+0.06$.

Figure 2.9 and Figure 2.10 represent radiance relative differences between simulated almucantars with and without modifications of the real part of the refractive index. Top panel in figure 2.9 shows the differences obtained by the simulations done with desert dust aerosol type (SolV2), while the

figure at the bottom illustrates the study done with oceanic aerosol (Lana2). In the figure 2.10, results for urban (GSFC2) and biomass burning (Zamb1) are plotted at the top and at the bottom respectively. The four representations are further divided into 4 subfigures, each one for each wavelength. Solid line is used for radiance relative differences obtained with an increment of -0.03, dashed line is used for $+0.03$ and dashed-dotted for $+0.06$.

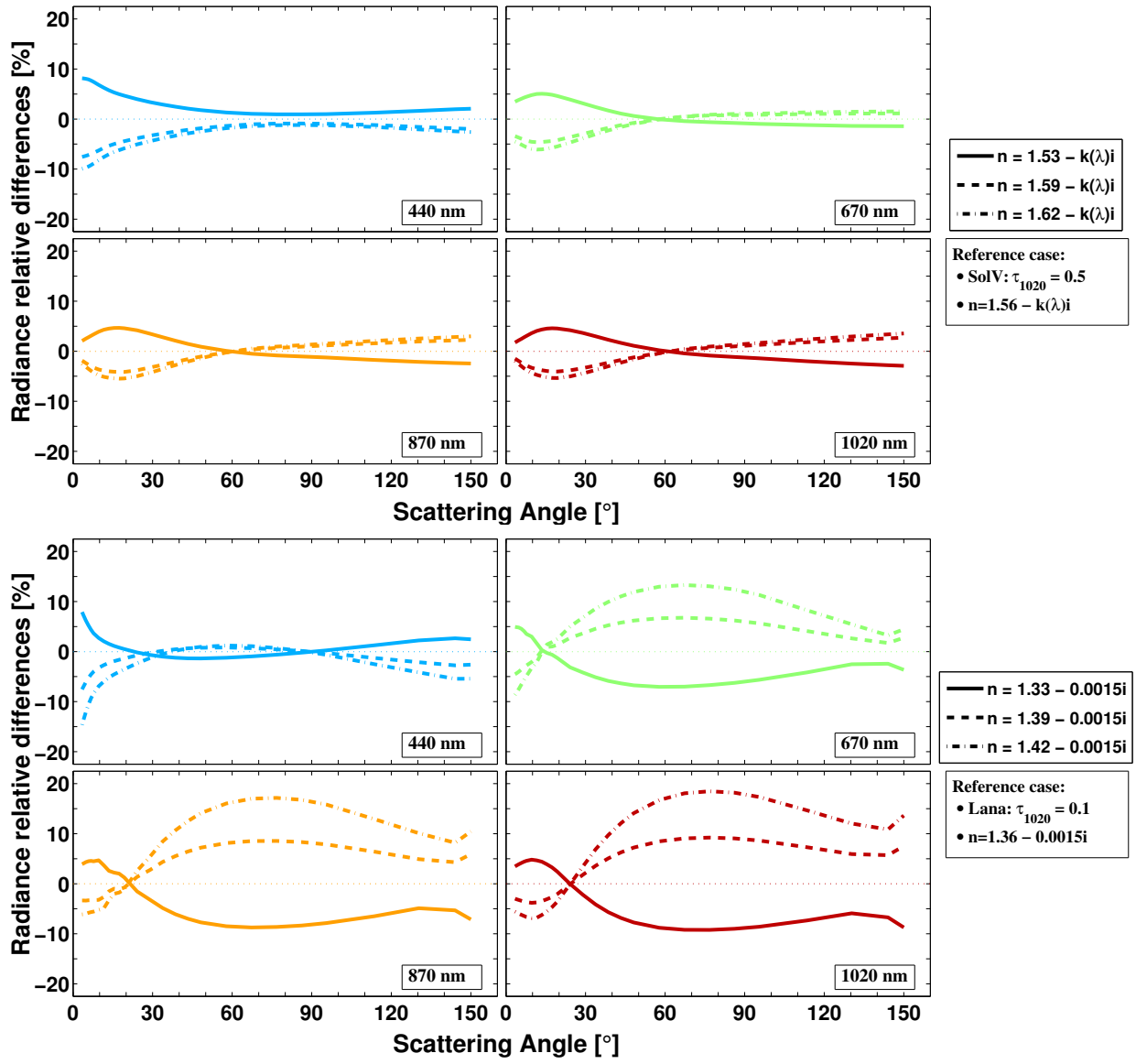

Figure 2.9: Radiance relative differences for desert dust (SolV2 - $\tau_{1020} = 0.5$, at the top) and oceanic (Lana2 - $\tau_{1020} = 0.1$, at the bottom) aerosols between almucantars with and without modifications of the real part of the refractive index. Different wavelengths are represented in different subfigures and with different colors (blue and top left for 440 nm, green and top right for 670 nm, orange and bottom left for 870 nm and red and bottom right for 1020 nm). In every subfigure, solid line is used for radiance relative differences obtained with an increment of -0.03, dashed line is used for $+0.03$ and dashed-dotted for $+0.06$.

Results show a symmetry between the increments -0.03 and $+0.03$ for the four aerosol types which means that there is a certain linearity in the radiance response against the change in the real refractive index. Radiance response to the increment $+0.06$ is twice as much as for $+0.03$ in most of the cases, but there are some exceptions, specially for the desert dust case. The largest relative

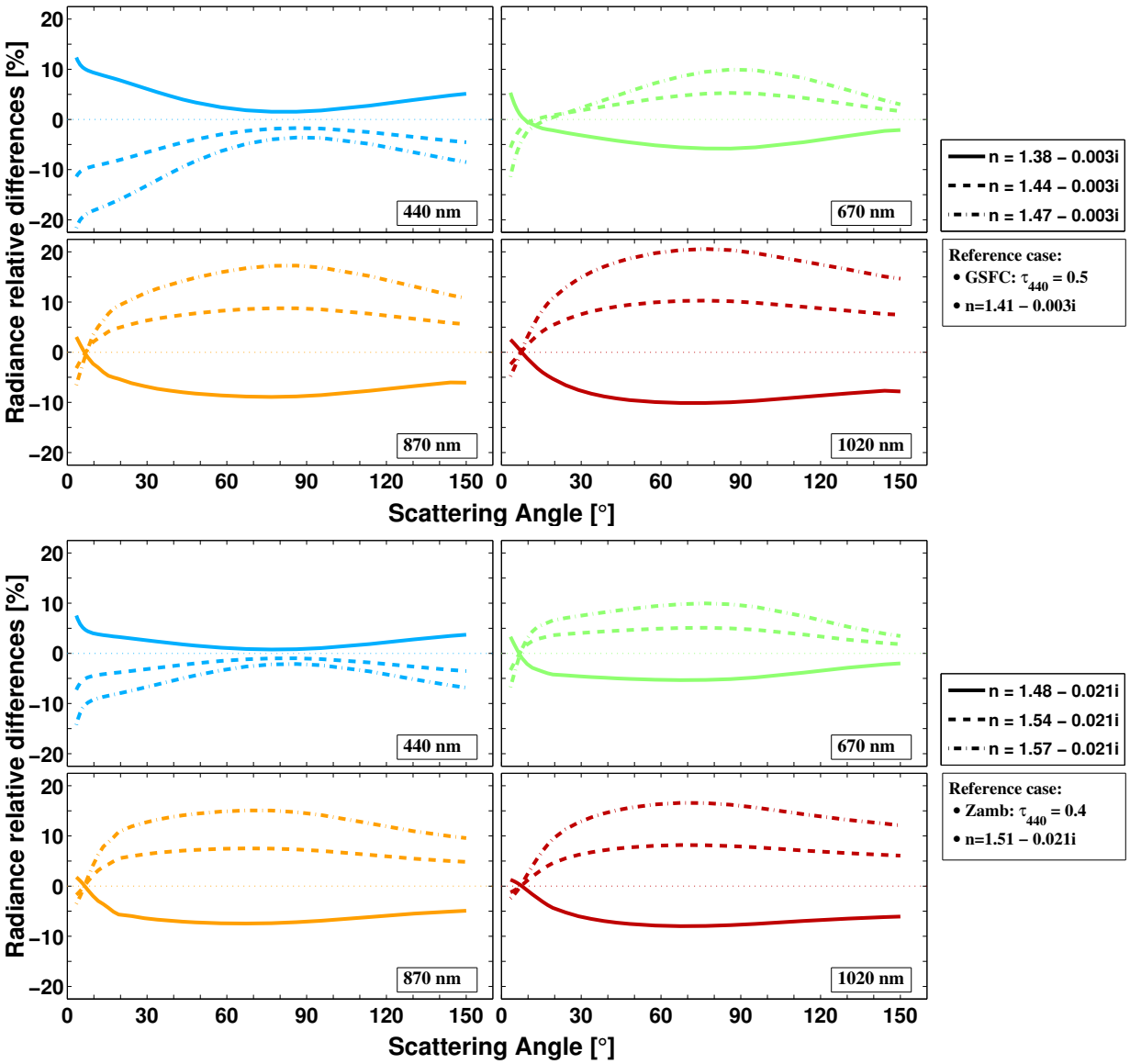

Figure 2.10: Radiance relative differences for urban (GSFC2 - $\tau_{440} = 0.5$, at the top) and biomass burning (Zamb1 - $\tau_{440} = 0.4$, at the bottom) aerosols between almucantars with and without modifications of the real part of the refractive index. Different wavelengths are represented in different subfigures and with different colors (blue and top left for 440 nm, green and top right for 670 nm, orange and bottom left for 870 nm and red and bottom right for 1020 nm). In every subfigure, solid line is used for radiance relative differences obtained with an increment of -0.03, dashed line is used for $+0.03$ and dashed-dotted for $+0.06$.

differences have been found for oceanic and urban aerosol. In relative terms, the increments are bigger in these two cases due to the smaller value of the refractive index; this fact could explain why relative differences are larger.

Looking at the figures, the shape of the differences matches the expectations: Negative increments in the refractive index produces a slope in the differences being higher at shorter angles. When the increments are positive the slope is rearranged in the opposite direction to larger scattering angles. We can approach to interpret these results in terms of the single scattering. As it

was commented, an increment in the real part of the refractive index reduces the intensity of the phase function for short scattering angles, increasing the intensity for larger ones. However, the phase function is a normalized function and the variations in τ_a and ω_o will fix the height[6] of the differences, and therefore, should be taken into the account in the analysis. In a descriptive way, the shape of the radiance differences will be given by the variations on the phase function but the high of these differences will depend on τ_a and ω_o.

Actually, for the aerosols selected, differences in τ_a are stronger, in general, than for ω_o as we will comment later (Table 2.5 and Table 2.6), so radiance differences are mostly affected by the change in τ_a. For small particles, an increase in n will produce an increase in τ_a and therefore in the total radiance (Eq. (2.1)). So rising n, apart from transferring light to larger angles, raises the total radiance. For negative increments of n the effects are just the opposite. Regarding the wavelength, τ_a variations at 440 nm are much stronger than for the rest of the channels (Table 2.5), and consequently, total variations in radiance are greater for this wavelength. This fact could explain that contrary to the rest of the channels, differences obtained at 440 nm for positive and negative increments of n do not cross (except for the oceanic aerosol). Crossing angle for the other wavelengths depends on the type of aerosol: for the desert dust this angle is around 60°, for oceanic is around 20° and for urban and biomass burning is only 10°. After the change of sign there are also diverse behaviors among the different aerosol types: while for oceanic and urban and biomass burning there is a maximum in the relative differences around 70°, for desert dust the differences grow constantly with the scattering angle.

Two brief comments to end up this discussion: consequences in τ_a due to an increase of n are not evident for large particles, i.e. for size parameters ($\chi = 2\pi r/\lambda$) larger than 4 (beyond the maximum of scattering efficiency, see Fig. 3.7 in Coulson (1988)). So in general the arguments provided before may not be valid for the desert dust due to its larger mean size. Finally, though the single scattering justifies the general characteristics of the differences in radiance, multiple scattering terms would need to be added if we wanted to carry out a more detailed analysis since its effects are far from negligible. As we commented in subsection 1.2.2, the multiple scattering (MS) contribution for $\Theta = 60°$ is as large as 40% for 500 nm wavelength, when $SZA = 30°$ and $\tau_{500} = 0.2$.

Table 2.5 shows the variations in the aerosol optical depth provoked by the increments of the real part of the refractive index. As we commented the variations have the same sign as the increments. The only exception is the desert dust for 1020 nm where the variations have opposite sign to the increments (note the comment above regarding the Mie theory, Fig. 3.7 in Coulson (1988)); although, the values for this particular case are practically insignificant compared to most of the values in the table. As in the study of the radiance relative differences, there is also a symmetry

[6]Following Eq. (2.1) for almucantar, the impact of τ_a and ω_o over the radiance does not depend on the scattering angle.

of the values obtained for -0.03 and $+0.03$. The values obtained for $+0.06$ are practically twice as large as the ones obtained for $+0.03$, indicating, that there is also a linearity between the increments in the real part of the refractive index and the variations in the aerosol optical depth. Once more, the desert dust case is an exception to this property.

Looking at the aerosol optical depth variations in the table 2.5, the highest values are found for shortest wavelengths and for those cases with a predominance of the fine mode. Then, maximum variations are obtained for urban aerosol at 440 nm. Differences are smaller for the biomass burning, but as it was commented, due to its higher value of the refractive index, the increments are smaller than for urban aerosol in relative terms. The fine mode has larger influence in the aerosol optical depth for the wavelength considered, as it will be seen in next sections, and also, it seems to be more affected by changes in the refractive index.

Table 2.5: Absolute differences in the **aerosol optical depth** between simulated almucantars with and without modifications of the real part of the refractive index for desert dust (SolV2), oceanic (Lana2), urban (GSFC2) and biomass burning (Zamb1).

	D. Dust (SolV2)			Oceanic (Lanai2)			Urban (GSFC2)			Biom. B. (Zamb1)		
Δn	-0.03	$+0.03$	$+0.06$	-0.03	$+0.03$	$+0.06$	-0.03	$+0.03$	$+0.06$	-0.03	$+0.03$	$+0.06$
λ [nm]	$\Delta\tau_a$											
440	-0.020	0.021	0.028	-0.028	0.028	0.057	-0.061	0.061	0.120	-0.035	0.036	0.071
670	-0.006	0.007	0.009	-0.013	0.014	0.028	-0.031	0.032	0.066	-0.015	0.016	0.033
870	-0.001	0.000	0.001	-0.007	0.007	0.015	-0.017	0.018	0.037	-0.008	0.008	0.017
1020	0.001	-0.002	-0.003	-0.005	0.005	0.010	-0.011	0.012	0.024	-0.005	0.005	0.010

On the other hand, variations of the single scattering albedo are presented in table 2.6. Changes of this parameter have also the same sign as the increments in the refractive index. As the imaginary part remains constant, the increase of the aerosol optical depth, for positive variations, is justified mostly by the increase of radiances observed in figure 2.9 and specially in figure 2.10. Therefore, the extinction grows due to a higher scattering which raises the value of the single scattering albedo. Again the desert dust case is the exception, but as explained in previous discussions, the values are considerably smaller than for the other aerosol types.

The highest variations are observed for the biomass burning. Due to its high absorption, the single scattering albedo for biomass burning has considerably smaller values than in the other three cases, specially at 1020 nm (about 0.75 versus the $0.96 - 0.97$ of the other three cases). For this reason, the variations in the scattering part of the extinction (changes in the real part of the refractive index) have more impact on the single scattering albedo. In more detail, deriving the

single scattering albedo against the scattering, in equation 1.27, we obtain:

$$\omega_o = \frac{\tau_{a_s}}{\tau_a} = \frac{\tau_{a_s}}{\tau_{a_a} + \tau_{a_s}} \Longrightarrow \frac{\partial \omega_o}{\partial \tau_{a_s}} = \frac{\tau_{a_a}}{(\tau_{a_a} + \tau_{a_s})^2} \Longrightarrow$$
$$\Longrightarrow \Delta\omega_o \simeq \frac{\tau_{a_a}}{(\tau_a)^2} \Delta\tau_{a_s} \tag{2.5}$$

where it can be seen that variations in the scattering part are transmitted to the single scattering albedo proportionally to the absorption part. The higher the absorption is, the stronger the impact on the single scattering albedo.

Table 2.6: Absolute differences in the **single scattering albedo** between simulated almucantars with and without modifications of the real part of the refractive index for desert dust (SolV2), oceanic (Lana2), urban (GSFC2) and biomass burning (Zamb1).

	D. Dust (SolV2)			Oceanic (Lanai2)			Urban (GSFC2)			Biom. B. (Zamb1)		
Δn	−0.03	+0.03	+0.06	−0.03	+0.03	+0.06	−0.03	+0.03	+0.06	−0.03	+0.03	+0.06
λ [nm]	$\Delta\omega_o$											
440	−0.001	0.001	0.002	−0.002	0.002	0.004	−0.002	0.002	0.003	−0.008	0.007	0.013
670	0.000	0.000	0.000	−0.002	0.002	0.004	−0.004	0.003	0.005	−0.013	0.012	0.022
870	0.001	−0.001	−0.001	−0.001	0.001	0.002	−0.004	0.004	0.007	−0.015	0.014	0.027
1020	0.001	−0.001	−0.001	−0.001	0.001	0.002	−0.005	0.004	0.008	−0.015	0.014	0.028

In a similar way, higher variations for longer wavelengths in urban aerosol (table 2.6) can be justified because the single scattering albedo is significantly shorter for longer wavelengths (table 2.3).

However, for oceanic aerosol, the variations in the single scattering albedo are higher for smaller wavelengths (same as the aerosol optical depth). It should be remembered here that for this aerosol the single scattering albedo almost does not depend on the wavelength (table 2.2). So, increments in the scattering part are transmitted in the same way for all channels. Thus, increments in single scattering albedo of shorter wavelengths are higher due to the higher increments in the scattering part.

2.4.2 Imaginary refractive index

The second parameter in the analysis is the imaginary part of the refractive index. This parameter is introduced in optics related to the absorption, i.e. it is responsible of the loss of light during a scattering process. That is why, an increment of this parameter is expected to reduce the quantity of light, not only in the direct beam (rising the aerosol optical depth) but also reducing the quantity

of the scattered light (radiance).

Again the working scheme consists of simulating measurements varying the imaginary part of refractive index and compare to those made without any modifications of the aerosol properties described in 2.2. All tests are made using almucantars at $SZA = 75°$ and with the same aerosols as in the previous section: desert dust (SolV2), oceanic (Lana2), urban (GSFC2) and biomass burning (Zamb1).

The increments for this parameter are different depending on the aerosol type: for desert dust, oceanic and urban, the values are -0.001, $+0.001$ and $+0.002$, while for biomass burning they are -0.01, $+0.01$ and $+0.02$. It would not have sense to apply the same increments to the biomass burning due to its larger absorption. So, these increments are one order of magnitude higher than for the other aerosol types as its imaginary part of the refractive index. Before the discussion, it is appropriated to remember that for the desert dust, the imaginary part of the refractive index depends on the wavelength while it is assumed constant for the other aerosol types (Dubovik et al., 2002). Figure 2.11 and Figure 2.12 represent radiance relative differences between simulated almucantars with and without modifications of the imaginary part of the refractive index.

The top panel in figure 2.11 illustrates the differences obtained by the simulations done with desert dust aerosol model (SolV2) and the figure at the bottom shows the analysis done with oceanic aerosol (Lana2). In the figure 2.12, results for urban (GSFC2) and biomass burning (Zamb1) are plotted at the top and at the bottom respectively. Following the same scheme as in figure 2.9 and figure 2.10, the figures are further divided into 4 subfigures, each one for each wavelength. Solid line is used for radiance relative differences obtained with an increment of -0.001, dashed line is used for $+0.001$ and dashed-dotted for $+0.002$ in all the subfigures (except for the ones for biomass burning, whose values are -0.01, $+0.01$ and $+0.02$).

The general characteristics observed in the radiance differences can be understood using again the single scattering approximation, Eq. (2.1). Contrary to what happens for the real part, the phase function hardly varies with the changes of the imaginary part of the refractive index as it can be seen in Vermeulen (1996). The main consequence of this fact on the radiance differences is the elimination of the angular dependence since the phase function is the only parameter (in Eq. (2.1)) that depends on the scattering angle. So the radiance differences will be constant and dependent on τ_a and ω_o variations[7]. Opposite to the results of the real part study, the single scattering albedo is more affected by the changes of the imaginary part than the aerosol optical depth in the aerosols selected as we will detail later (Table 2.7 and Table 2.8). And therefore, variations in ω_o will control the sign of the radiance difference in this analysis.

As expected, negative increments of the imaginary part of the refractive index produce positive

[7]Even though the phase function does not vary is still in charge of transferring the effects of τ_a and ω_o on the radiance, and the term constant should be understood in a relative manner.

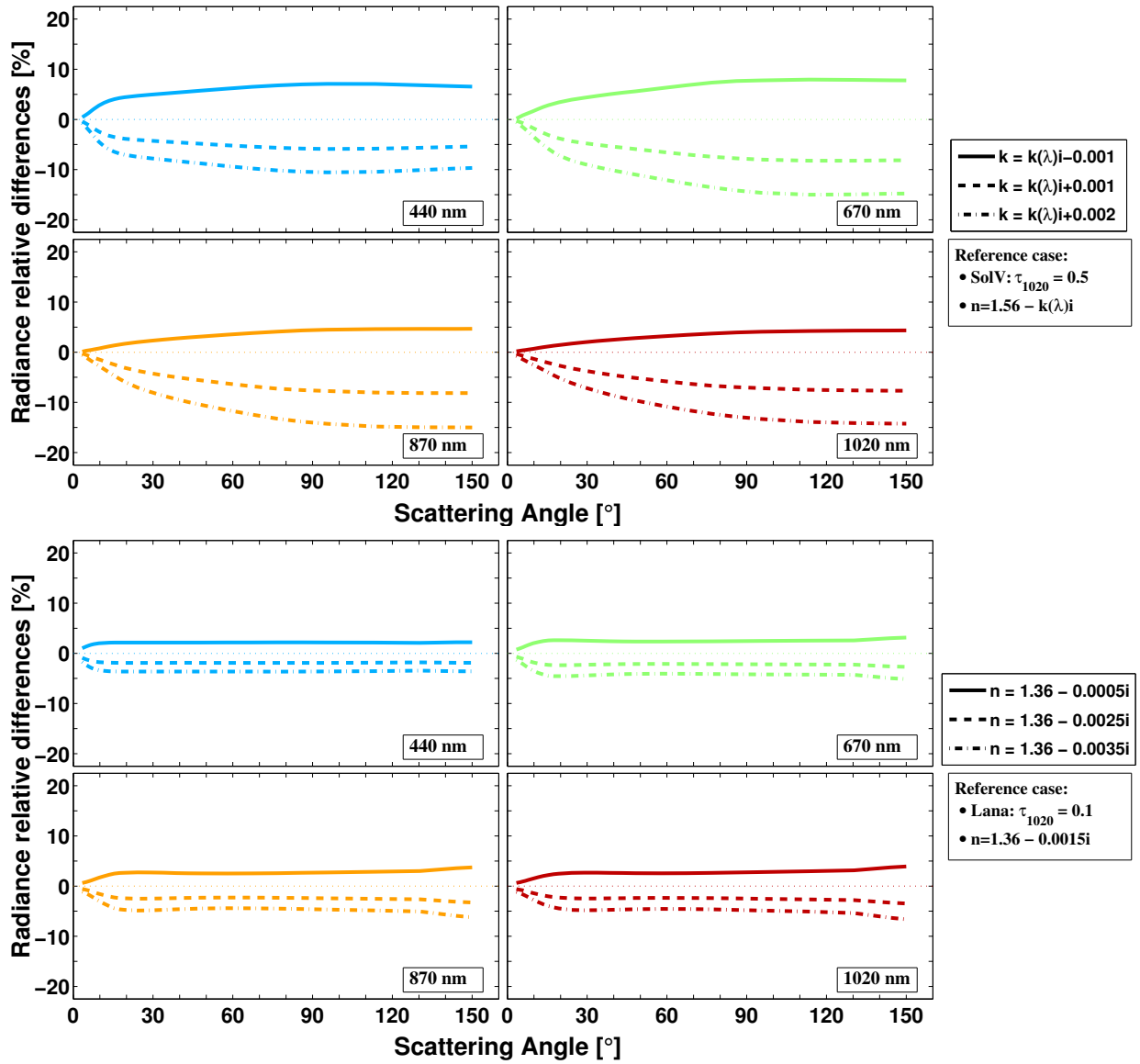

Figure 2.11: Radiance relative differences for desert dust (SolV2 - $\tau_{1020} = 0.5$, at the top) and oceanic (Lana2 - $\tau_{1020} = 0.1$, at the bottom) aerosols between almucantars with and without modifications of the imaginary part of the refractive index. Different wavelengths are represented in different subfigures and with different colors (blue and top left for 440 nm, green and top right for 670 nm, orange and bottom left for 870 nm and red and bottom right for 1020 nm). In every subfigure, solid line is used for radiance relative differences obtained with an increment of -0.001, dashed line is used for $+0.001$ and dashed-dotted for $+0.001$.

variations in ω_o and consequently in the radiance for all the cases in figure 2.11 and figure 2.12. On the other hand increases of k generate negative variations in both ω_o and the radiance. Apart from the biomass burning (with different increments applied), the highest values of relative differences are observed for the desert dust. Indeed, they are obtained for channels 670 nm and 870 nm where the variations of ω_o are the largest as we will see later. On the other hand, the smallest differences were found for the urban aerosol coinciding with the lowest variations in the single scattering albedo.

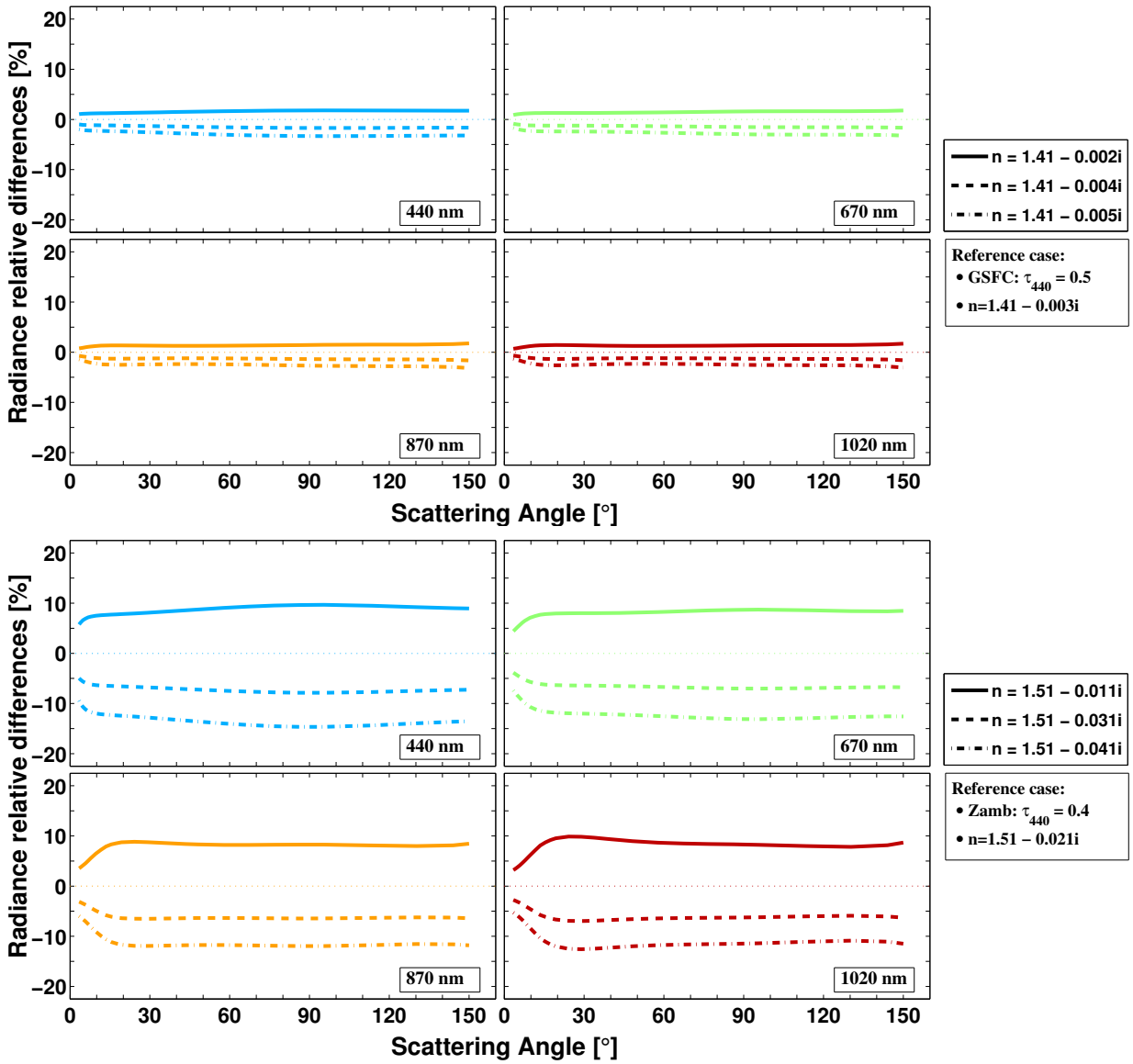

Figure 2.12: Radiance relative differences for urban (GSFC2 - $\tau_{440} = 0.5$, at the top) and biomass burning (Zamb1 - $\tau_{440} = 0.4$, at the bottom) aerosols between almucantars with and without modifications of the imaginary part of the refractive index. Different wavelengths are represented in different subfigures and with different colors (blue and top left for 440 nm, green and top right for 670 nm, orange and bottom left for 870 nm and red and bottom right for 1020 nm). In every subfigure, solid line is used for radiance relative differences obtained with an increment of -0.001 for GSFC and -0.01 for Zamb1, dashed line is used for $+0.001$ for GSFC and $+0.01$ for Zamb1 and dashed-dotted for $+0.002$ for GSFC and $+0.02$ for Zamb1.

Regarding the shape of the differences, all of them are quite similar no matter the aerosol type or the wavelength, and as it was anticipated, they are practically constant for all the scattering angles. The exception are the short scattering angles where relative differences tend to zero. On the other hand, relative differences in the desert dust are not as constant as in the rest of the aerosol types. Doubtless, multiple scattering terms would add more information and a completely detailed analysis would need to contain them.

To study the effects produced by the modifications of the imaginary refractive index in the

aerosol optical depth and in the single scattering albedo, the absolute differences in these magnitudes are presented in table 2.7 and in table 2.8.

Table 2.7: Absolute differences in the **aerosol optical depth** between simulated almucantars with and without modifications of the imaginary part of the refractive index for desert dust (SolV2), oceanic (Lana2), urban (GSFC2) and biomass burning (Zamb1).

	D. Dust (SolV2)			Oceanic (Lanai2)			Urban (GSFC2)			Biom. B. (Zamb1)		
Δk	−0.001	+0.001	+0.002	−0.001	+0.001	+0.002	−0.001	+0.001	+0.002	−0.01	+0.01	+0.02
λ [nm]	$\Delta\tau_a$											
440	0.000	0.000	0.001	−0.001	0.001	0.001	−0.001	0.001	0.001	−0.005	0.005	0.011
670	0.000	0.000	0.000	−0.001	0.001	0.001	−0.001	0.001	0.002	−0.007	0.007	0.014
870	0.000	0.000	0.000	0.000	0.000	0.001	−0.001	0.001	0.002	−0.006	0.006	0.012
1020	0.000	0.000	−0.001	0.000	0.000	0.001	−0.001	0.001	0.002	−0.005	0.005	0.011

Table 2.7 contains absolute differences in aerosol optical depth. The highest differences are observed for biomass burning concluding that the aerosol optical depth is more affected by the absolute value of the increments than radiance relative differences. Actually, the increments for biomass burning were established one order of magnitude higher so as to obtain similar values of radiance differences compared to the other aerosol types. But the effect of this election can be noticed at this point, as absolute differences of the aerosol optical depth are also one order of magnitude larger. The differences in the aerosol optical depth show a linearity with changes in the imaginary refractive index for biomass burning. In the other cases the differences are too small to get any conclusion.

Radiance relative differences are in the same order for the variations in the real part and the imaginary part of the refractive index. However, the effects on the aerosol optical depth were much higher modifying the real part than the imaginary one. But as it was commented the single scattering albedo is more affected and controls the radiance differences in this second case. Table 2.8 shows the variations of ω_o, where differences are positive for negative increments and negative for positive increments as it was previously indicated.

Operating in a similar way as in the study of the real part, if now we consider that changes in the imaginary part are mostly connected with the absorption part of the aerosol extinction, and we derivate the single scattering albedo against the absorption portion of the aerosol extinction we obtain:

$$\frac{\partial \omega_o}{\partial \tau_{a_a}} = \frac{-\tau_{a_s}}{(\tau_{a_a} + \tau_{a_s})^2} \Longrightarrow \Delta\omega_o \simeq \frac{-\tau_{a_s}}{(\tau_a)^2}\Delta\tau_{a_a} \tag{2.6}$$

So the variations of the absorption are multiplied by the scattering part and therefore, much

Table 2.8: Absolute differences in the **single scattering albedo** between simulated almucantars with and without modifications of the imaginary part of the refractive index for desert dust (SolV2), oceanic (Lana2), urban (GSFC2) and biomass burning (Zamb1).

	D. Dust (SolV2)			Oceanic (Lanai2)			Urban (GSFC2)			Biom. B. (Zamb1)		
Δk	−0.001	+0.001	+0.002	−0.001	+0.001	+0.002	−0.001	+0.001	+0.002	−0.01	+0.01	+0.02
λ [nm]	$\Delta\omega_o$											
440	0.023	−0.020	−0.037	0.016	−0.015	−0.028	0.007	−0.007	−0.014	0.049	−0.043	−0.082
670	0.021	−0.023	−0.044	0.019	−0.018	−0.034	0.010	−0.009	−0.018	0.066	−0.054	−0.101
870	0.011	−0.021	−0.040	0.020	−0.018	−0.036	0.013	−0.012	−0.023	0.082	−0.064	−0.117
1020	0.010	−0.019	−0.036	0.020	−0.018	−0.036	0.015	−0.014	−0.027	0.093	−0.070	−0.126

larger than the ones obtained in the real part study. As it has been commented, the scattering portion is very high for desert dust, oceanic and urban aerosols and that is why the effect of small variations in the absorption is strongly amplified in their single scattering albedo. For biomass burning the high values are due to both the high variation of the aerosol optical depth and the scattering part, that even though is the most absorptive, represents still more than 70% of the total extinction.

There is again a symmetry for all the cases, apart from for the desert dust. The highest values are obtained for the largest wavelength except again for the desert dust which has the peak for central wavelengths.

2.4.3 Size distribution

The next point in the sensitivity study is testing the influence of modifications in the size distribution on radiance measurements. Two aerosol types have been chosen to carry out the analysis: biomass burning and desert dust. This election will allow covering both fine and coarse mode predominance and absorbing and non absorbing aerosol.

In order to discuss the incongruence found during the self consistency test of the biomass burning for the fine mode (section 2.2.4), the properties selected will be the ones describing the example with the largest aerosol load (Zamb2 with $\tau_a(440) = 0.8$). On the other hand, for the desert dust aerosol these properties will be the ones obtained with the lowest aerosol load (SolV1 with $\tau_a(1020) = 0.3$).

The working scheme is similar to the one used in the refractive index study: the reference set will be the radiances simulated using almucantar geometry at $SZA = 75°$. Then, these measurements will be compared to those simulated after modifying the size distribution of the selected aerosol

types.

2.4.3.1 Fine mode: Zambia

Figure 2.13 illustrates the modifications done for the size distribution of biomass burning aerosol (Zamb2). Four regions (or study cases) divide the size distribution in order to analyze their influence separately. In each region, three variations of the size distribution are considered: the first of them "a" with less quantity of particles, the second one "b" with more particles and symmetric to the first one, and the third one "c", where the increase is twice as much as for "b". These modifications are not the same for every radius bin and are related to the value of the size distribution.

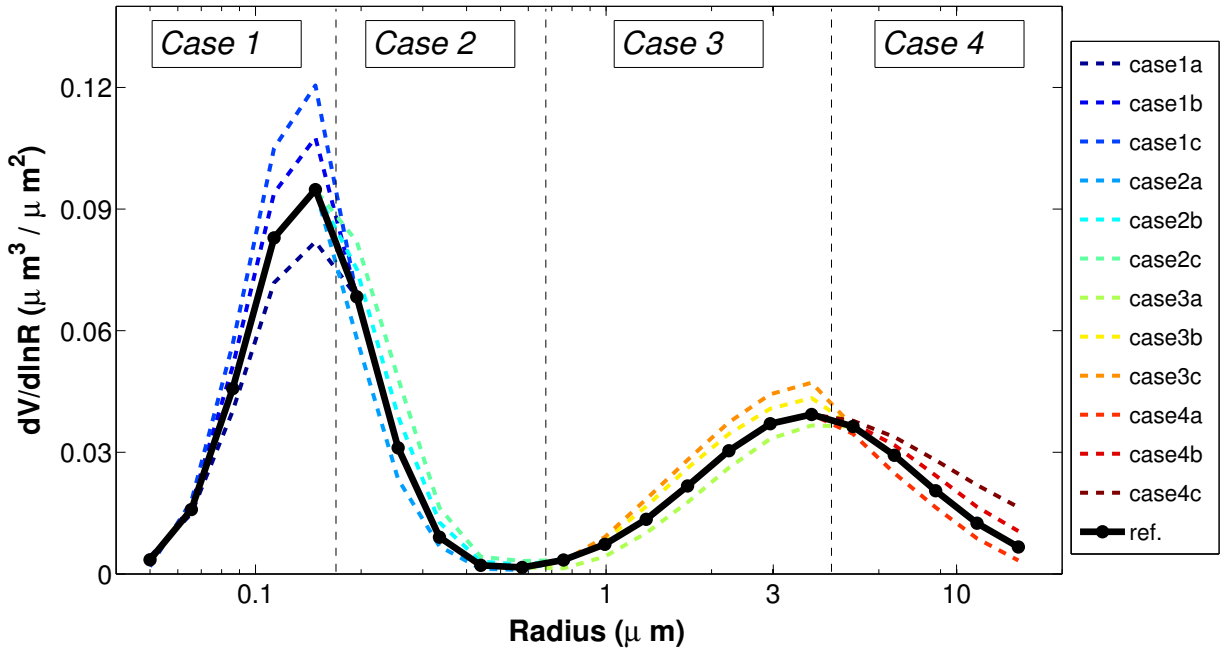

Figure 2.13: Variations in the size distributions of biomass burning (Zamb2 - $\tau_{440} = 0.8$) made in order to analyze their impacts on the radiance measurements. Black line symbolizes the original size distribution and stripped colored lines different variations. Variations are divided in four different regions: two in fine mode and two in the coarse mode. Subindex "a" represents negative variations while "b" and "c" represents positive ones.

In figure 2.14, radiances relative differences for "case 1" (upper part) and "case 2" (bottom part) are plotted. Division represented in figure 2.13 shows that both regions are in the fine mode. The first region corresponds to the radii situated between $0.05\mu m$ and $0.15\mu m$ and the second one between $0.19\mu m$ and $0.58\mu m$.

For the first region, the variations introduced in the size distribution are designed in order to explain the disagreements found while doing the self-consistency test for this example: those variations included in the "case 1b" are similar to the erroneous variations obtained in that study. On the other hand, the variations introduced in the second region are smaller, since the variations are proportional to the height of the size distribution, and this is lower in the second region.

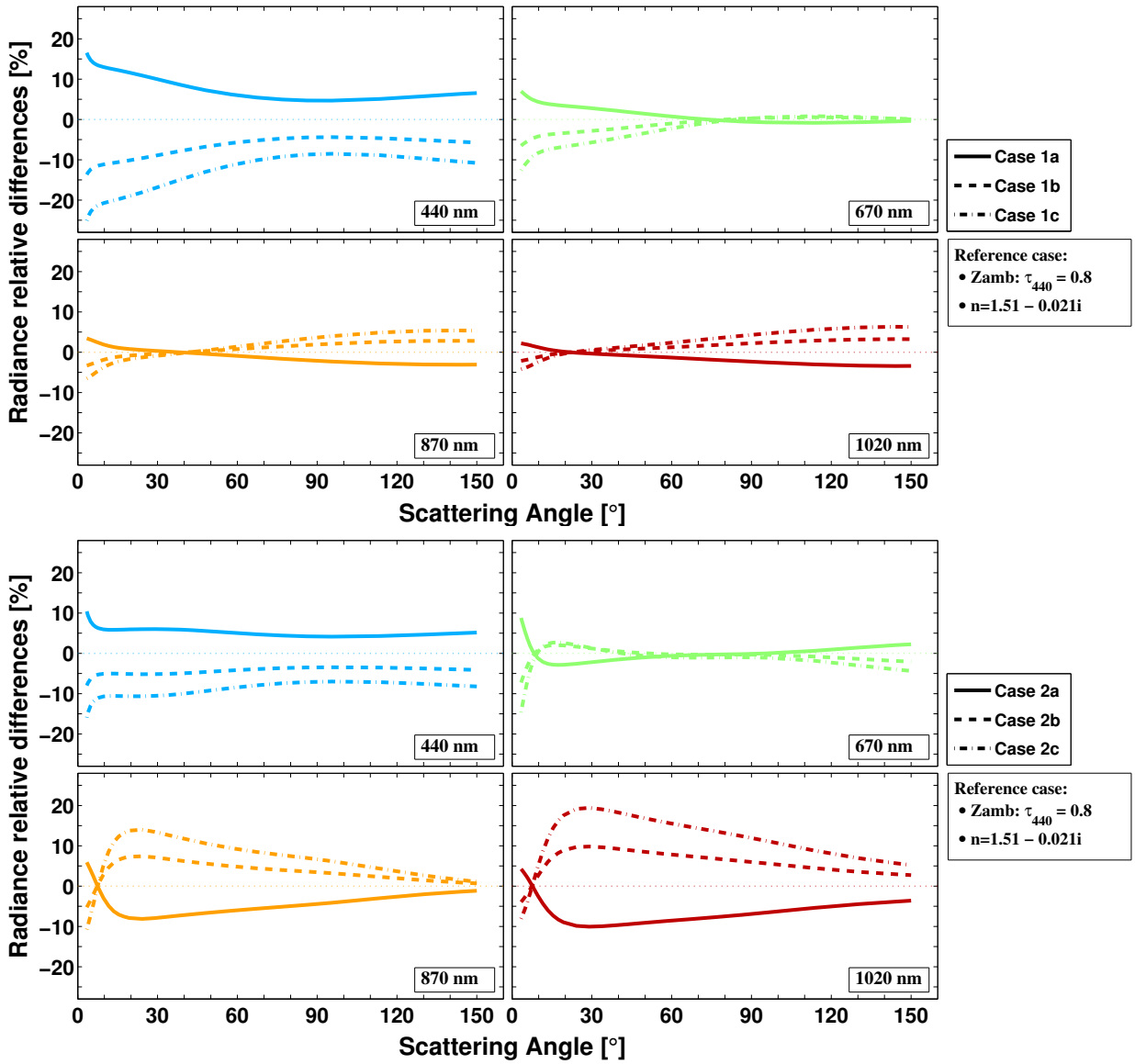

Figure 2.14: Radiance relative differences for biomass burning (Zamb2 - $\tau_{440} = 0.8$) aerosol between almucantars with and without modifications of the size distribution define in figure 2.13 as "case 1" (figure at the top) and as "case 2" (figure at the bottom). Different wavelengths are represented in different subfigures and with different colors (blue and top left for 440 nm, green and top right for 670 nm, orange and bottom left for 870 nm and red and bottom right for 1020 nm). In every subfigure, solid line is used for differences obtained in the "case a", dashed line in the "case b" and dashed-dotted in "case c".

Figure 2.14 shows that the radiance relative differences are stronger for the second region in most of the wavelengths, though the variations in the size distribution were higher for the first one. Thus, apart from the results obtained at 440 nm wavelength, where radiance relative differences for "case 1a" and "case 1b" reach values of $10 - 15\%$ while they are only around $5 - 10\%$ for "case 2a" and "case 2b", differences are much stronger for the second region in the rest of the wavelengths, specially at 870 nm and 1020 nm. Radiance relative differences do not exceed 5% for "case 1a" and "case 1b" while they go beyond 10% for "case 2a" and "case 2b". This fact could explain the discrepancies found in the self-consistency study, as the size distribution variations in "case 1b" only affects radiances at 440 nm.

Results obtained for "case 1c" and "case 2c" do not provide extra information since the relative errors are twice as large as the ones found for "case 1b" and "case 2b".

It is curious to observe how the solid line ("case a" with less particles) is mostly in the positive part of radiance relative differences at 440 nm and 670 nm, for both study regions, while is mostly in the negative part for 870 nm and 1020 nm. For dash and dashed-dotted lines ("case b" and "case c" with more particles) the result are the opposite.

Table 2.9: Absolute differences in the **aerosol optical depth** between the original size distribution (called Zamb2) and its variations (as stated in figure 2.13).

	Case 1 $0.05\mu m \leqslant r \leqslant 0.15\mu m$			Case 2 $0.19\mu m \leqslant r \leqslant 0.58\mu m$			Case 3 $0.76\mu m \leqslant r \leqslant 3.86\mu m$			Case 4 $5.06\mu m \leqslant r \leqslant 15\mu m$		
Δk	a	b	c	a	b	c	a	b	c	a	b	c
λ [nm]	$\Delta\tau_a$											
440	−0.065	0.065	0.129	−0.063	0.056	0.116	−0.007	0.004	0.008	−0.001	0.000	0.001
670	−0.022	0.022	0.044	−0.038	0.036	0.075	−0.007	0.005	0.008	−0.001	0.001	0.001
870	−0.010	0.010	0.021	−0.023	0.023	0.048	−0.008	0.004	0.008	−0.001	0.001	0.001
1020	−0.006	0.006	0.013	−0.016	0.016	0.034	−0.008	0.004	0.008	−0.001	0.001	0.001

Table 2.10: Absolute differences in the **single scattering albedo** between the original size distribution (called Zamb2) and its variations (as stated in figure 2.13).

	Case 1 $0.05\mu m \leqslant r \leqslant 0.15\mu m$			Case 2 $0.19\mu m \leqslant r \leqslant 0.58\mu m$			Case 3 $0.76\mu m \leqslant r \leqslant 3.86\mu m$			Case 4 $5.06\mu m \leqslant r \leqslant 15\mu m$		
Δk	a	b	c	a	b	c	a	b	c	a	b	c
λ [nm]	$\Delta\omega_o$											
440	−0.001	0.001	0.001	−0.002	0.002	−0.001	−0.003	0.000	0.000	−0.001	0	0.001
670	0.001	0.000	−0.001	−0.007	0.003	−0.002	−0.004	0.001	0.000	−0.001	0.001	0.001
870	0.002	−0.002	−0.003	−0.010	0.002	−0.003	−0.004	0.001	−0.001	−0.001	0.001	0.001
1020	0.003	−0.003	−0.005	−0.012	0.000	−0.002	−0.003	0.001	−0.001	−0.002	0.001	0.001

To try to understand what is happening, let us introduce in the discussion the variations obtained for τ_a and ω_o, which are represented in table 2.9 and table **??**. These tables contain information about the four regions even though at this point we are only interested on "case 1" and "case 2". For them, the variations in the aerosol optical depth are much larger than the single

scattering albedo[8], which are practically equal to zero. So if we pretend to reproduce an analysis in terms of single scattering, only τ_a has to be considered. Precisely, variations in this parameter are positive for "case b" and "case c" and negative for "case a", obviously, when the quantity of particles increases the τ_a raises. Therefore, the argument often used in the previous section, if τ_a raises the radiance increases, is only applicable for 870 nm and 1020 nm. For shorter wavelengths, the radiance relative differences can be only explained in terms of multiple scattering[9].

To finish the discussion of the regions 1 and 2, it is interesting to observe how their aerosol optical depth differences at 440 nm are very similar, while for the rest of the wavelengths, the differences observed for the "case 2" are twice as large as the ones obtained for "case 1". This result confirms that the parameters introduced in the inversion are larger affected by the variations in the second region, and therefore, the size distribution bins retrieved for the radii including in the second region are more stable in the retrieval process.

Radiance relative differences due to the size distribution variations in regions 3 and 4 (both in the coarse mode) are plotted in figure 2.15. The upper figure shows the results for the "case 3" (where r fulfills the condition: $0.76\ \mu\ m\ \leqslant\ r\ \leqslant\ 3.86\ \mu\ m$) and the figure at the bottom presents the results for "case 4" (where r satisfies the condition: $5.06\ \mu\ m\ \leqslant\ r\ \leqslant\ 15\ \mu\ m$).

The range in Y-Axe has been modified in order to observe the differences, because they are much shorter than in previous analyzed regions. Relative differences in "case 3" are 13% at the most while they do not exceed 2% in "case 4", reaching these maxima for shortest scattering angles and for the longest wavelength.

In the region 3, radiances differences at 1020 nm are almost insignificant when the scattering angle is greater than 30°, this angle is reduced as the wavelength decreases. In the extreme case at 440 nm, differences are negligible regardless of the scattering angle. On the other hand, differences of τ_a are very small and always below 0.01 (see table 2.9), even for "case 3c". Except at 440 nm where differences are too short to get conclusions, the single scattering theory could be applied to explain the radiance relative differences obtained. For instance, the cases with more particles ("b" and "c" plotted with dashed and dashed-dotted lines) have larger τ_a and the relative differences are also mostly positive, specially for 870 nm and 1020 nm. Needless to say, that the differences in the single scattering albedo are practically insignificant for all the wavelengths.

With differences below 0.5% for almost all angles, we can assure that increases or decreases of the size distribution for radii longer than 5 $\mu\ m$ have almost no consequences on the radiance measurements. Results are similar for τ_a where the maximum variation is 0.001. Therefore, the

[8]Coefficients of scattering and extinction do depend on χ, n and k. So in this study, the only variations that they can suffer, and as a consequence ω_o, are produced by changes in χ. However, the variations in the size distribution are not high enough to drastically change the effective radius of the distribution.

[9]Moreover, this example, Zamb2, has an important aerosol load, and the experiences are done for $SZA = 75°$, so the contribution of multiple scattering is supposed to be very high

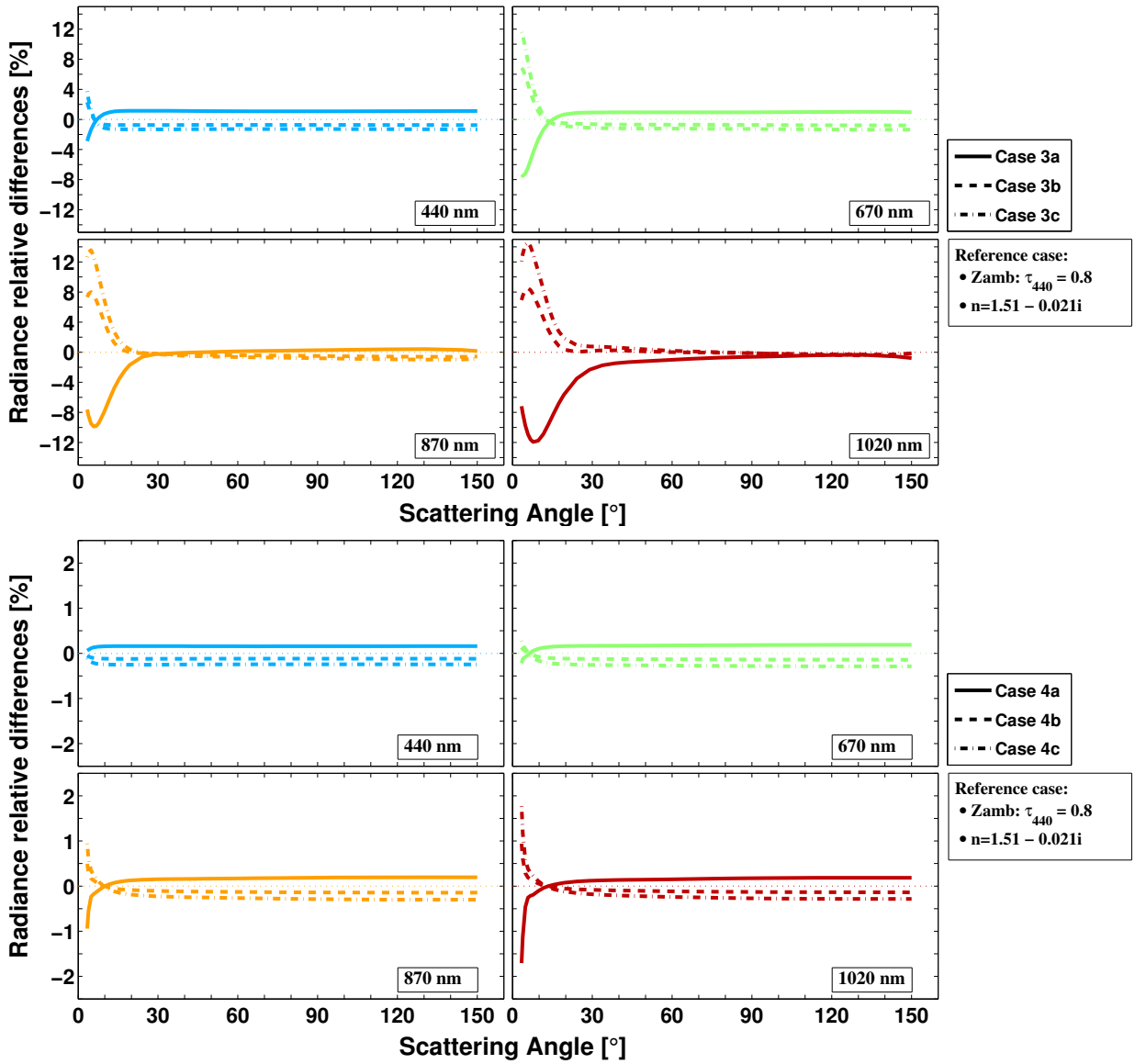

Figure 2.15: Radiance relative differences for biomass burning (Zamb2 - $\tau_{440} = 0.8$) aerosol between almucantars with and without modifications of the size distribution define in figure 2.13 as "case 3" (figure at the top) and as "case 4" (figure at the bottom). Different wavelengths are represented in different subfigures and with different colors (blue and top left for 440 nm, green and top right for 670 nm, orange and bottom left for 870 nm and red and bottom right for 1020 nm). In every subfigure, solid line is used for differences obtained in the "case a", dashed line in the "case b" and dashed-dotted in "case c".

discrepancies observed for this region in figure 2.6 are amply justified.

In conclusion, the variations in "case 1", and especially in "case 4", have less influence in the parameters used in Dubovik's inversion. Therefore, these regions present a higher error when they are characterized. This result is commonly know within AERONET network and it was already shown in Dubovik et al. (2000) (figure 1). Thus, this study only proposes a quantitative way of approaching the same result. Finally, it seems clear that the wavelength range should be extended to improve the retrievals at the extremes of the size distribution: to shorter wavelengths for shorter radii and to longer wavelength in the other end.

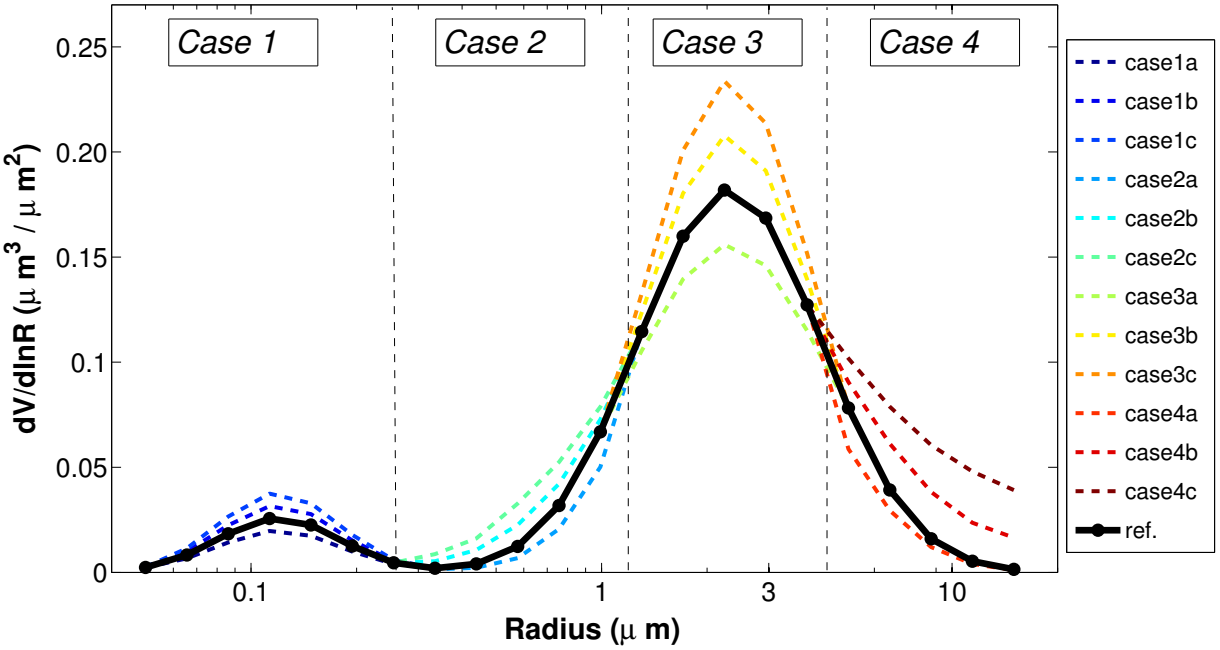

Figure 2.16: Variations in the size distributions of desert dust (SolV1 - $\tau_{1020} = 0.3$) made in order to analyze their impacts on the radiance measurements. Black line symbolizes the original size distribution and stripped colored lines different variations. Variations are classified in four different cases: one in fine mode and three in the coarse mode. Subindex "a" represents negative variations while "b" and "c" represents positive ones.

2.4.3.2 Coarse mode: Solar Village.

The second example of size distribution variations is plotted in figure 2.16. Desert dust aerosol has been chosen in order to analyze the coarse mode more thoroughly. For this purpose, regions have been divided differently from the previous case: 3 areas of variation in the coarse mode and only 1 for the fine mode. Nevertheless, as for the desert dust the volume median radii for both modes are considerably shorter than in the biomass burning, the modification does not change too much the aspect of the divisions. For instance, the last region ("case 4") is the same as in the previous example. Precisely for this last case, we take the liberty of making the variations for "b" and "c" much larger (in proportional terms) than in other areas to see if there is any impact on the radiance measurements; as a consequence, "case 4a" is not symmetrical to "case 4b", because otherwise the size distribution in "case 4a" would be negative.

Figure 2.17 represents the radiance relative differences obtained for the variations in the regions 1 and 2. The fine mode is completely contained in "case 1a" (see figure 2.16) and the variations applied keep the same proportionality as for the biomass burning, being much smaller in absolute terms for this second case. However, the radiance variations are quite similar to the ones obtained for the biomass burning. Therefore, it seems that proportional changes cause similar relative differences in radiance. However, the variations in τ_a are smaller than in the previous case (see table 2.12). Nevertheless, they keep the property of being much larger for 440 nm than for the other

wavelengths. Back to figure 2.17, we can observe how for this wavelength the multiple scattering term seems to have larger influence: the solid line (less particles) is mostly negative for all the wavelengths except for 440 nm where is positive. At this point, it should be also mentioned that the differences in radiance for 440 nm are much more intense than for other wavelengths.

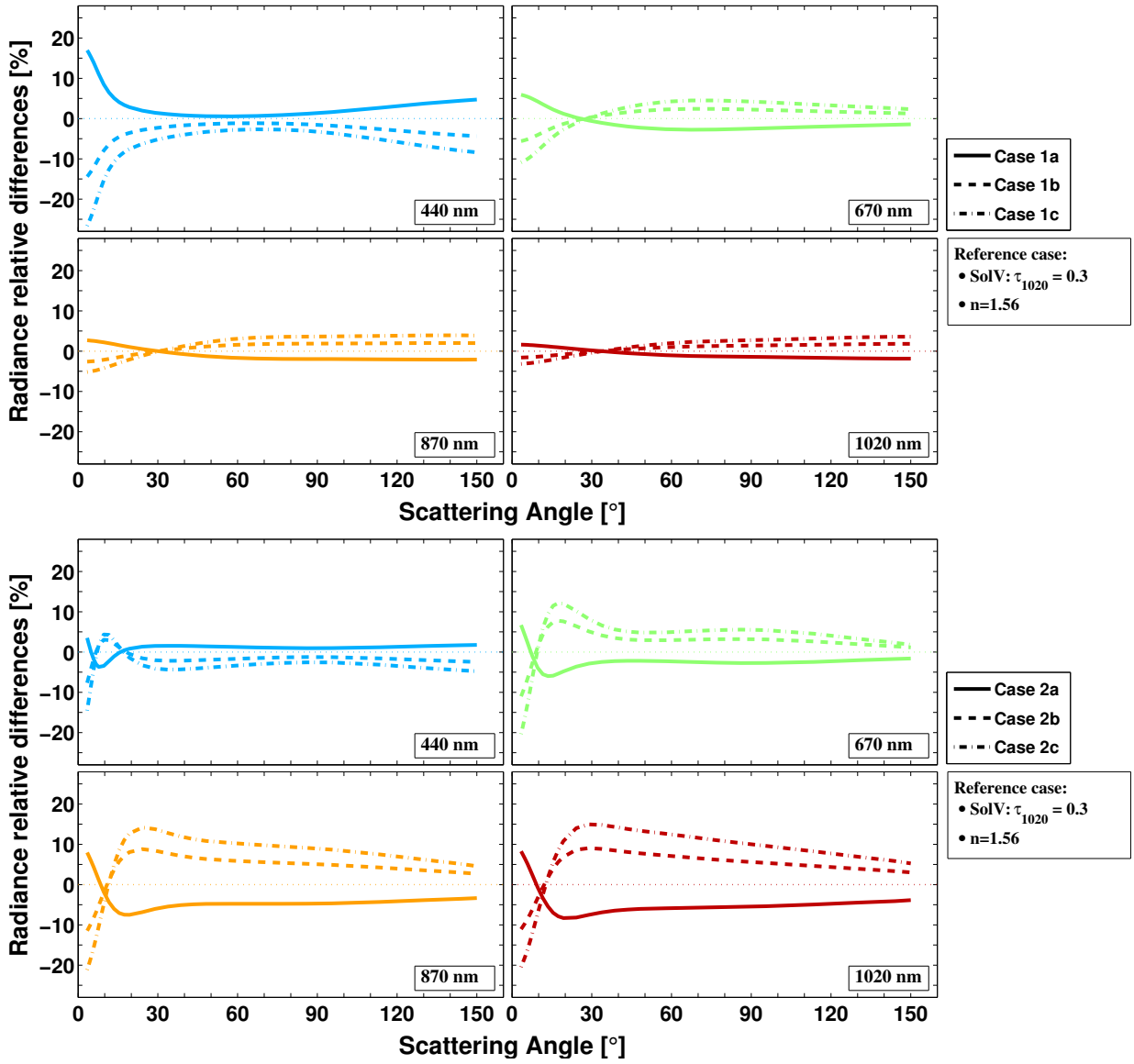

Figure 2.17: Radiance relative differences for biomass burning (SolV1 - $\tau_{1020} = 0.3$) aerosol between almucantars with and without modifications of the size distribution define in figure 2.16 as "case 1" (at the top) and as "case 2" (at the bottom). Different wavelengths are represented in different subfigures and with different colors (blue and top left for 440 nm, green and top right for 670 nm, orange and bottom left for 870 nm and red and bottom right for 1020 nm). In every subfigure, solid line is used for differences obtained in the "case a", dashed line in the "case b" and dashed-dotted in "case c".

However, the differences obtained for the second region (corresponding to the beginning of the coarse mode) are larger for longer wavelengths, even though they are still important at 440 nm. On the other hand, differences in the aerosol optical depth do not depend that much on the wavelength in this second region, similar to what was obtained in the "case 2" during the analysis of the biomass burning. Considering again that decreasing the size distribution provokes a negative increment in

the aerosol optical depth, it can be settled that for long wavelengths the single scattering approach could describe the radiance relative differences in figure 2.17, except at 440 nm, where only the multiple scattering can lead to a good explanation.

Table 2.11: Absolute differences in the **aerosol optical depth** between the original size distribution (called SolV1) and its variations (as stated in figure 2.16).

	Case 1 $0.05\mu m \leqslant r \leqslant 0.26\mu m$			Case 2 $0.33\mu m \leqslant r \leqslant 0.99\mu m$			Case 3 $1.30\mu m \leqslant r \leqslant 3.86\mu m$			Case 4 $5.06\mu m \leqslant r \leqslant 15.0\mu m$		
Δk	a	b	c	a	b	c	a	b	c	a	b	c
λ [nm]	$\Delta\tau_a$											
440	−0.046	0.046	0.092	−0.027	0.039	0.076	−0.021	0.021	0.041	−0.003	0.004	0.008
670	−0.016	0.016	0.033	−0.031	0.046	0.090	−0.022	0.022	0.044	−0.003	0.005	0.009
870	−0.008	0.008	0.015	−0.034	0.046	0.090	−0.023	0.023	0.045	−0.003	0.005	0.010
1020	−0.004	0.005	0.009	−0.035	0.044	0.087	−0.023	0.023	0.045	−0.003	0.005	0.010

Table 2.12: Absolute differences in the **single scattering albedo** between the original size distribution (called SolV1) and its variations (as stated in figure 2.16).

	Case 1 $0.05\mu m \leqslant r \leqslant 0.26\mu m$			Case 2 $0.33\mu m \leqslant r \leqslant 0.99\mu m$			Case 3 $1.30\mu m \leqslant r \leqslant 3.86\mu m$			Case 4 $5.06\mu m \leqslant r \leqslant 15.0\mu m$		
Δk	a	b	c	a	b	c	a	b	c	a	b	c
λ [nm]	$\Delta\omega_o$											
440	−0.006	0.005	0.009	−0.001	0.002	0.004	0.003	−0.003	−0.005	0.001	−0.002	−0.004
670	−0.001	0.001	0.002	−0.002	0.003	0.004	0.001	−0.001	−0.002	0.001	−0.001	−0.003
870	0.000	0.000	0.001	−0.002	0.002	0.003	0.001	0.000	−0.001	0.000	−0.001	−0.002
1020	0.000	0.000	0.000	−0.002	0.002	0.003	0.000	0.000	−0.001	0.000	−0.001	−0.002

As for the biomass burning, differences obtained for the single scattering albedo are practically negligible, as it can be seen in table 2.12

Radiance relative differences for the variations in regions 3 and 4 are illustrated in figure 2.18. Differences for "case 3" are represented at the top of the figure and the range in Y-Axe has been change so as to better observe them. These differences do not exceed 6%, even though region 3 is situated at the peak of the coarse mode and the variations applied are the strongest. In spite of that, the differences in the aerosol optical depth are not so small, and they are halfway between the "case 1" and "case 2" (except for 440 nm where difference in "case 1" are also larger).

Again for this region, a diminution of particle volume concentration provokes an increase in the

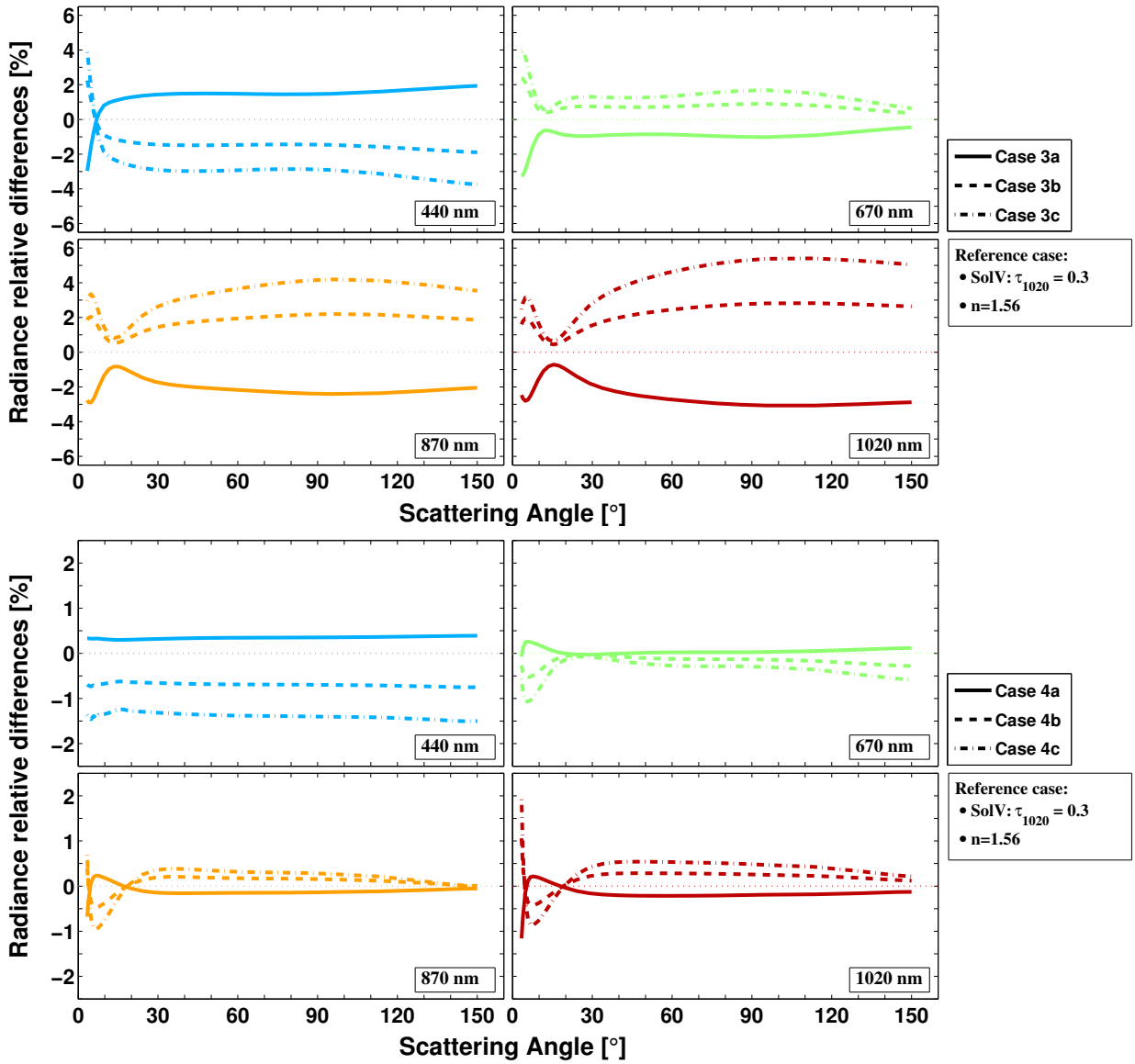

Figure 2.18: Radiance relative differences for biomass burning (SolV1 - $\tau_{1020} = 0.3$) aerosol between almucantars with and without modifications of the size distribution define in figure 2.16 as "case 3" (at the top) and as "case 4" (at the bottom). Different wavelengths are represented in different subfigures and with different colors (blue and top left for 440 nm, green and top right for 670 nm, orange and bottom left for 870 nm and red and bottom right for 1020 nm). In every subfigure, solid line is used for differences obtained in the "case a", dashed line in the "case b" and dashed-dotted in "case c".

radiance relative differences at 440 nm while it is positive for the rest of the wavelengths.

The figure at the bottom in figure 2.18 shows the radiance relative differences for "case 4". The range used in Y-Axe is even shorter than for "case 3", because the maximum of the radiance relative differences is equal to 2% and it is reached at 1020 nm for the shortest scattering angles. Likewise, the variations in the aerosol optical depth (shown in table 2.12) are very short. Only for "case 4c", and at longest wavelengths, they get to 0.01. Thus, the size distribution for radii longer than 5.06μm has little impact on the radiance and the aerosol optical depth in spite of the higher variations. As discussed in the biomass burning type, if we look for have a better accuracy in the

longest radii of the coarse mode, we necessarily need to increase the observation wavelength.

Chapter 3

Error sources in sky radiance measurements

Si quieres ser leído más de una vez, no vaciles en borrar a menudo.

Horacio

Resumen en español del capítulo:

El capítulo 3 está dedicado a la caracterización de las fuentes de error en las medidas de radiancia consideradas en esta tesis. El error de calibración, descrito en la sección 3.2, fue estimado alrededor del 5 % en Holben et al. (1998), valor que utilizaremos para las simulaciones en el capítulo 4.

El error de apuntamiento del fotómetro CIMEL-318 es evaluado por primera vez en este trabajo. Para realizar esta evaluación, contactamos con la empresa CIMEL para así diseñar un procedimiento que comprobara la exactitud en el sistema de apuntamiento en los fotómetros. La empresa nos facilitó dos escenarios ya existentes y que habían sido creados con este mismo fin: "matriz" y "cruz". Analizando las medidas provenientes de estos escenarios, observamos que los datos obtenidos no podían ser utilizados para inferir el apuntamiento de manera directa, debido a la influencia del movimiento del Sol durante la secuencia de medida. Por ello, creamos una herramienta de software encargada de corregir dicho movimiento. La validación de esta corrección, así como, la estimación del apuntamiento de varios fotómetros CIMEL-318 son presentados en la sección 3.3. En los resultados obtenidos para los 6 fotométros de campo analizados, el valor máximo registrado ha sido de $0{,}2^\circ$, en las dos componentes en las que se divide el error de apuntamiento: $\Theta_{\xi_\varphi} = \xi_\varphi \sin(\theta_s)$ (horizontal) y $\Theta_{\xi_\theta} = \xi_\theta$ (vertical). Estos resultados no dependen del ángulo solar cenital y son equivalentes para los dos escenarios "matriz" y "cruz".

Apoyándonos en el escenario matriz y en el procedimiento recogido en Nakajima et al. (1996), hemos calculado el campo de visión de los fotómetros utilizando el Sol, fuente extensa en movimiento, y un haz láser en el laboratorio, fuente puntual y fija. Con ambas fuentes los resultados han sido similares, con diferencias entre ellos por debajo del 5 %, y similares también a las especificaciones de la empresa CIMEL, alrededor de $1{,}2^\circ$ (para fotómetros nuevos).

3.1 Introduction

This chapter contains the characterization of the errors in the sky radiance measurements considered in the thesis. Thus, in section 3.2, the description will start with a short discussion about the errors originated in the calibration process. Afterwards, in section 3.3, the error associated with the pointing system in a sun-photometer CIMEL-318 will be defined and the methodology followed to estimate it will be depicted. To end up with the error sources, section 3.4 will be devoted to the techniques used to calculate the field of view of the sun-photometer.

Finally, in section 3.5, some interesting mathematical relations about radiances and the pointing errors will be commented, as a useful tool to interpret the results in chapter 5.

3.2 Error sources I: Calibration error

During the calibration and the field operation of the Cimel sun-photometer, there are several aspects which introduce uncertainty in the sky radiance measurements. These errors are systematic and, in general terms, they affect differently each spectral channel. In this section we will focus on errors derived from the calibration process or other issues that ultimately can be assimilated as calibration errors (such as bad temperature correction or optical path obstructions).

To estimate the calibration uncertainty in radiance measurements, we need to take into account the mutltiple steps and calibration transfers from the NIST standard to the field photometer. The NIST lamp used to calibrate the SLICK sphere at the GSFC Calibration Facility (`http://cf.gsfc.nasa.gov/`) has an absolute irradiance uncertainty of 0.5%. The SLICK sphere radiance is calibrated within $1-2\%$ accuracy. Repeatability tests may indicate that the traveling master, calibrated by measuring in front of SLICK sphere, is $2-3\%$. The uncertainty in the calibration transfer from the traveling master to the operational spheres in GSFC, Lille and Valladolid, plus the transfer from those spheres to the field photometers, yields to a final estimation of 5% for radiance calibration (Holben et al., 1998). This uncertainty is different (in absolute value and sign) for each channel.

It must be then considered the possibility of aging in the sphere lamps, although the frequent recalibration of the distributed spheres (every 3 months) aims at minimizing such effects. The control of voltage and current in the lamp power supplies allows to monitor possible quick changes in the lamp resistance, therefore indicating that the lamps need to be replaced. This kind of error (aging) would in principle have the same sign for all spectral channels.

To this uncertainty, other sources of uncertainty must be added during deployment. Obstructions in the optical path (dust, humidity, insects, etc.) produce an analogous effect to miscali-

bration. In this case, a reduction in the radiance, although different for each channel, would be observed. In particular, the deposition of dust or other materials produces obstructions that have different transmission depending on wavelength. Furthermore, in standard instruments (aureole and sky acquired through different physical channels) it is possible to have discrepancy between aureole and sky portions of the almucantar or principal plane, since the obstruction may affect only one of both. From the experience of routine monitoring of RIMA-AERONET sites, this kind of error is very frequent. When the magnitude of the obstruction is large it can be easily detected and the data can be blocked so that erroneous retrievals are not available in the real-time database. But issues of small magnitude remain unnoticed, hardly visible as a noise in the A/K ratio time series of the photometer.

We need to remark here that the small aperture of collimators, together with bad sealing by aging of the collimator rubber joints, frequently yields to water leakage into the collimator and on the front windows, which takes long time to dry up. Cimel recently released a new version of collimator that is supposed to solve these problems.

The aging of the interference filters inside the sensor head is another calibration-like error. The interpolation between pre and pos-deployment calibrations minimizes this effect only if the real change was approximately linear. Moreover, if there is a strong change between pre and post calibration coefficients (above 6%/year), the data will hardly be raised to level 2.0 since severe problems in the filter blocking and transmittance may be occurring.

Finally, other effects such as temperature dependency may act as calibration error if they are not properly corrected. In AERONET versions 1 and 2 only generic corrections are applied, based on measurements of temperature dependence in all channels from a set of test photometers. In future version 3, specific temperature corrections for each instrument and channel will be used. For that purpose, GSFC and PHOTONS started several years ago to check temperature dependency in each instrument that is calibrated. A thermal chamber and a stabilized source (integrating sphere) are used for this purpose. Even though these errors are small in magnitude except in 1020 nm and 870 nm channels, they are systematic in nature and may be corrected or at least accounted for in the error estimation.

To summarize, a number of issues can affect the calibration of the radiance channels. The sign and magnitude of the error is generally different for each aureole and sky spectral channel. We attain to the 5% uncertainty described in Holben et al. (1998) although the above description clearly shows that this uncertainty can be eventually exceeded in real field measurements, especially if site managing is not efficient.

3.3 Error sources II: Pointing error

Sun photometer pointing error has an important role in this thesis. This section gives a definition of what should be understood as an error during the pointing process and summarizes the methodology used to calculate its magnitude.

3.3.1 Pointing error: Definition

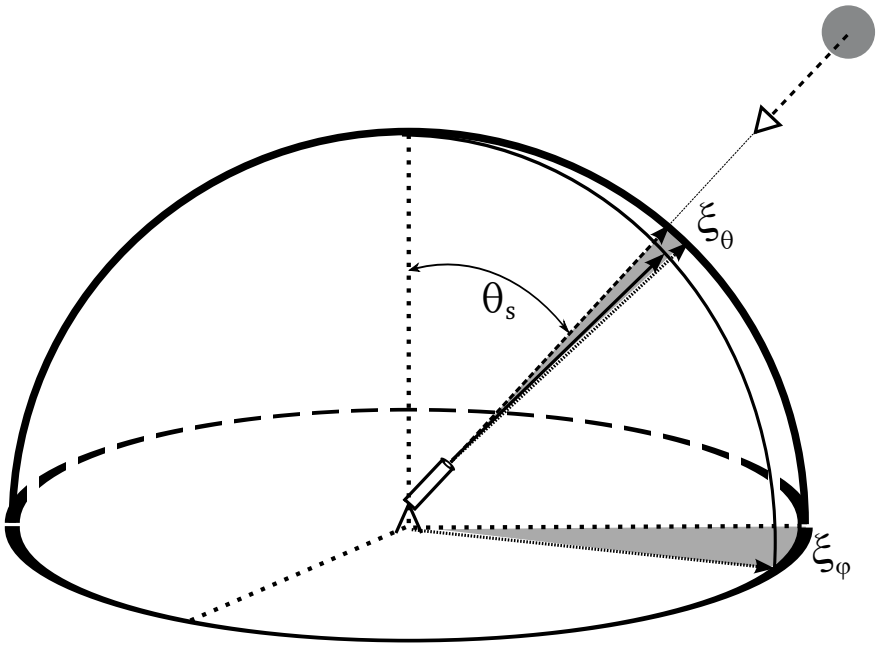

Figure 3.1: Figure used to describe the pointing error. Dashed vector pointing towards the Sun represents the correct pointing while solid line represents a biased pointing. Shading areas are the projection of this error in spherical coordinates: ξ_φ and ξ_θ

Pointing error (see figure 3.1) is defined as the angle between the Sun position (correct pointing) and the erroneous pointing direction. As sun-photometers are moved by two motors, azimuth and zenith axes, the value of the pointing error, Θ_ξ, is normally given in spherical coordinates:

$$\Theta_\xi = \Theta_\xi(\xi_\varphi, \xi_\theta) \tag{3.1}$$

Unfortunately, the scenarios conceived to calculate the pointing error calculate ξ_φ and ξ_θ but not the "total" pointing error Θ_ξ. So, the relation between ξ_φ, ξ_θ and Θ_ξ, should be obtained. Note, here, that if the pointing error is sufficiently small, it can be considered as an infinitesimal displacement (with $dr = 0$) and therefore the relation in Eq. (3.1) could be defined as an infinitesimal

displacement in spherical coordinates:

$$\begin{aligned}\Theta_\xi &= \Theta_{error}(\xi_\varphi, \xi_\theta) = \xi_\theta \hat{\theta} + \sin\theta_s \xi_\varphi \hat{\varphi} \\ \Theta_\xi &= \sqrt{\xi_\theta^2 + \sin\theta_s{}^2 \xi_\varphi^2}\end{aligned} \tag{3.2}$$

To calculate the general relation of Eq. (3.1), the concept of scattering angle needs to be defined.

3.3.1.1 Scattering angle: Definition

In order to obtain a better description of the pointing error, here we define the scattering angle. This concept is very interesting in many fields of physics, playing a fundamental role in the field of atmospheric optics. In this context, the scattering angle is defined as the angle between the forward direction of the Sun beam and a straight line connecting the scattering point observed by a detector. In our particular case, where the detector is a ground based sun-photometer, the Sun can be considered to be in the infinite and the scattering angle is equivalent to the angle formed by the directions of the Sun and the observation from the detector, see figure 3.2.

.

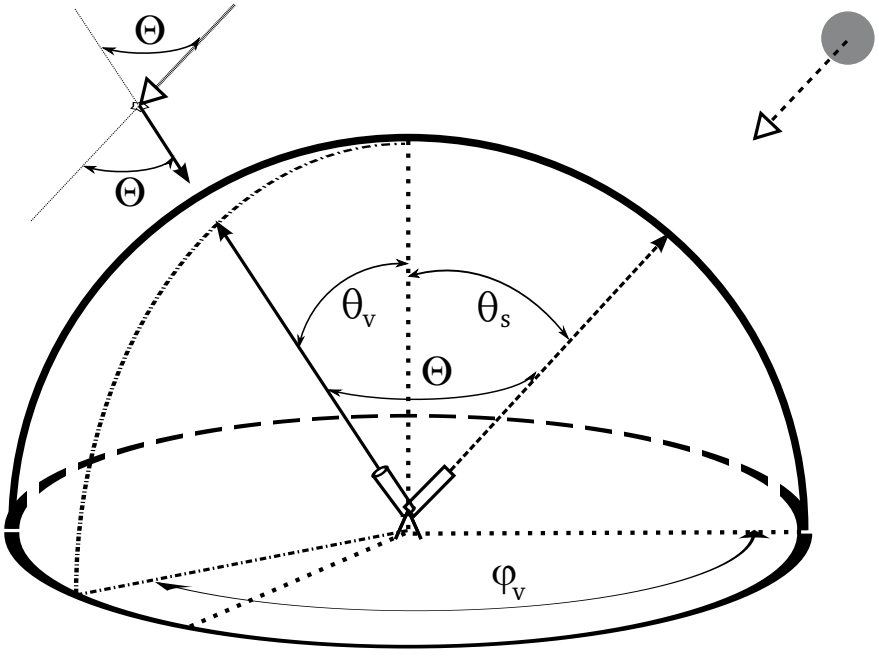

Figure 3.2: Figure used to describe the scattering angle in terms of solar position and the observation angle

Then, the relation between the scattering angle, the solar position and the observation angle can be written as Vermeulen (1996):

$$\cos(\Theta) = \cos(\theta_s)\cos(\theta_v) + \sin(\theta_s)\sin(\theta_v)\cos(\varphi_v - \varphi_s) \tag{3.3}$$

where Θ is the scattering angle, φ_v and θ_v are the observation azimuth and zenith angle, and θ_s the solar zenith angle. In the representation system, the solar azimuth angle (φ_s) can be taken as the azimuth origin and its value set to zero.

3.3.1.2 Pointing errors described in terms of the scattering angle

Revising both definitions, the one given for the pointing error and the one given for the scattering angle, it is easy to observe how the pointing error can be re-defined as the scattering angle of the erroneous pointing direction. If, ξ_φ and ξ_θ are the spherical coordinates of the pointing error, using Eq. (3.3), their relation with the scattering angle can be written as:

$$\cos(\Theta_\xi) = \cos(\theta_s)\cos(\theta_s+\xi_\theta) + \sin(\theta_s)\sin(\theta_s+\xi_\theta)\cos(\xi_\varphi) \tag{3.4}$$

Developing $\cos(\theta_s+\xi_\theta)$ and $\sin(\theta_s+\xi_\theta)$ then

$$\begin{aligned}\cos(\Theta_\xi) =& \cos(\theta_s)[\cos(\theta_s)\cos(\xi_\theta) - \sin(\theta_s)\sin(\xi_\theta)] \\ &+ \sin(\theta_s)\cos(\xi_\varphi)[\cos(\theta_s)\sin(\xi_\theta) + \sin(\theta_s)\cos(\xi_\theta)] \\ =& \cos(\theta_s)^2\cos(\xi_\theta) - \sin(\theta_s)\cos(\theta_s)\sin(\xi_\theta) \\ &+ \sin(\theta_s)\cos(\theta_s)\sin(\xi_\theta)\cos(\xi_\varphi) + \sin^2(\theta_s)\cos(\xi_\varphi)\cos(\xi_\theta)\end{aligned} \tag{3.5}$$

Considering small errors, $\sin(\xi_\theta)$ can be approximated, rejecting terms from third derivative, as ξ_θ; and $\cos(\xi_\theta)$ eliminating terms from forth derivative as $1-\frac{\xi_\theta^2}{2}$. The same is valid for ξ_φ, obtaining:

$$\begin{aligned}\cos(\Theta_\xi) =& \cos^2(\theta_s) - \cos^2(\theta_s)\frac{\xi_\theta^2}{2} - \sin(\theta_s)\cos(\theta_s)\xi_\theta \\ &+ \sin(\theta_s)\cos(\theta_s)\xi_\theta\cos(\xi_\varphi) + \sin^2(\theta_s)(1+\frac{\xi_\theta^2\xi_\varphi^2}{4} - \frac{\xi_\theta^2}{2} - \frac{\xi_\varphi^2}{2})\end{aligned} \tag{3.6}$$

and then

$$\begin{aligned}\cos(\Theta_\xi) =& 1 + \sin(\theta_s)\cos(\theta_s)\sin(\xi_\theta)(\cos(\xi_\varphi)-1) \\ &- (\cos^2(\theta_s)\frac{\xi_\theta^2}{2} + \sin^2(\theta_s)\frac{\xi_\theta^2}{2}) - \sin^2(\theta_s)\frac{\xi_\varphi^2}{2} + \sin^2(\theta_s)\frac{\xi_\theta^2\xi_\varphi^2}{4} \\ \cos(\Theta_\xi) =& 1 - \frac{\xi_\theta^2}{2} - \sin^2(\theta_s)\frac{\xi_\varphi^2}{2} - \sin(\theta_s)\cos(\theta_s)\frac{\xi_\theta\xi_\varphi^2}{2} + \sin^2(\theta_s)\frac{\xi_\theta^2\xi_\varphi^2}{4}\end{aligned} \tag{3.7}$$

and once here, if again, only terms until second order are considered, the last two terms in

Eq. (3.7) can be eliminated. On the other hand, if we also approximate $\cos(\Theta_\xi)$ as $1 - \frac{\Theta_\xi^2}{2}$, then:

$$\begin{aligned} 1 - \frac{\Theta_\xi^2}{2} =& 1 - \frac{\xi_\theta^2}{2} - \sin^2(\theta_s)\frac{\xi_\varphi^2}{2} \\ \Longrightarrow \Theta_\xi^2 =& \xi_\theta^2 + \sin\theta^2 \xi_\varphi^2 \end{aligned} \tag{3.8}$$

Recovering the expression in Eq. (3.2).

Taking into the account that analyzed errors in the present thesis are less than 1°, all the approximations made, which rejected terms from third order, are valid, and therefore, pointing errors can be separated in their azimuth and zenith components.

Even though, first the mathematical approximation is presented here, and then, in the next subsection the pointing error results with the sun-photometer are shown, actually, this subsection is made as a consequence of the next one: One of the first results obtained with the tests made to characterize the sun-photometer pointing was precisely that the zenithal component of the error, ξ_θ, was constant while the azimuthal one, ξ_φ, was constant if it was multiplied by $\sin\theta_s$; this result indicated that the pointing error should be understood as the scattering angle between the Sun bean and the direction where the detector is pointing. Furthermore, this angle was constant in the experiences and now we see that is perfectly in terms of: ξ_θ and $\sin\theta_s\xi_\varphi$.

In order to make the description easier, from now on, the factorization of the total pointing error in spherical coordinates, $\Theta_{\xi_\theta} = \xi_\theta$ and $\Theta_{\xi_\varphi} = \sin\theta_s\xi_\varphi$, will be named as total vertical and horizontal error, respectively. Keeping the names of zenith and azimuth error for ξ_θ and ξ_φ which are related to the two motor movements: zenithal and azimuthal. Needless to say, that zenith and vertical errors are coincident, and sometimes, we will refer to them indistinctly.

3.3.2 Used methods to estimate the pointing error

3.3.2.1 Cimel measurements regarding pointing problem

The GOa-UVA contacted the Cimel company in order to design a process to check the accuracy of the pointing system in CIMEL-318 sun-photometer. The company gave us two existing scenarios previously created for this purpose: “matrix” and “croix”. Analyzing the first measurements, we observed that raw data could not be interpreted directly because of the Sun movement during the measure sequence. Therefore, we created a software tool to correct the fore-mentioned Sun movement. The validation of this correction and the pointing accuracy of several Cimel sun-photometers are analyzed and presented here.

Matrix measurements and correction by solar movement.

Scenario description. The matrix measurement starts with go-sun and track scenarios (pointing to the Sun) and afterwards the Cimel moves towards right $\Delta\varphi = 1°$ and down $\Delta\theta = -1°$ ([1]). From this point it starts scanning the area around the Sun, going from down to up and right to left as plotted in figure 3.3 (on the left). As we can see in the figure, each scenario represents a 0.1° movement to the left from $\Delta\varphi = 1°$ to $\Delta\varphi = -1°$ which results in 21 scenarios. In every scenario the Cimel covers all the zenith angles from $\Delta\theta = -1°$ to $\Delta\theta = 1°$ in steps of 0.1°, while keeping the azimuth angle, and records a total of 21 measurements. An example of a matrix measurement is given in the figure 3.3 (on the right) taken in Lille site on September 22nd 2010 at 12:47:07.

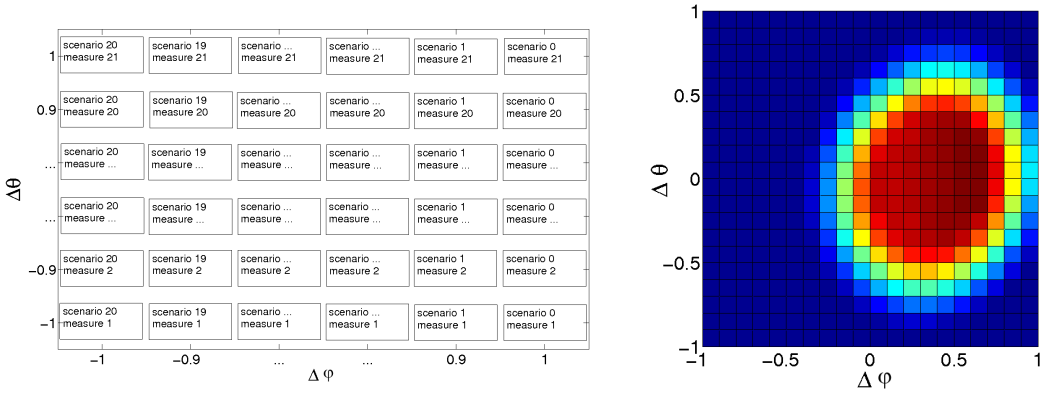

Figure 3.3: Left, explanation of the matrix scenario. Right, a measurement taken in Lille Site on September 22nd 2010 at 12:47:07.

Time is recorded for each scenario, right-left movement. That sequence lasts around 10 seconds, therefore every piece of data is obtained more or less every half a second. The total time used for the whole matrix measurement is 3.5 minutes.

Sun correction. The image produced by the matrix seems to be wrong at first glance. Since the beginning, the responsible of this strange result was the Sun movement during the matrix measurement. In order to check if the Sun movement could be the responsible, we made a brief study of how fast the Sun moves in angular terms in middle latitudes. For this test, we used the algorithm presented by Reda and Andreas (2007), which will be later used to discount the solar movement in the whole pointing error study. Using the mentioned algorithm, in figure 3.4, the zenithal and azimuthal absolute Sun variation per second in Valladolid (middle latitude station) are represented, in the winter, figure 3.4(a), and in the summer, figure 3.4(b).

The zenithal variation never gets higher than $0.003°/s$ reaching this value at sunrise and at sunset, and being its minimum at noon: $0°/s$. Looking at the figures, it does not show a seasonal variability. On the other hand, the azimuthal variation is much higher and season-dependent: the variation reaches its maximum of $0.01°/s$ at noon in the summer. Its minimum of $0.003°/s$ takes

[1] Hereafter the azimuthal displacement of the sun-photometer motor will be call as $\Delta\varphi$, being the zenithal one represented as $\Delta\theta$.

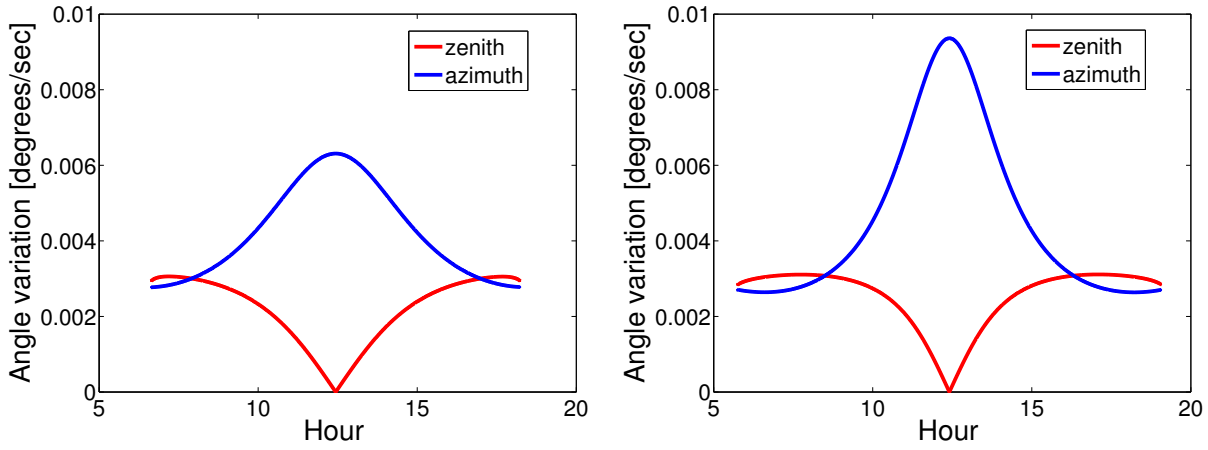

(a) Valladolid in winter

(b) Valladolid in summer

Figure 3.4: Azimuthal and zenithal variation per second in Valladolid site, in the left during the winter and in the right, during the summer.

place at dawn and at sunset (same value than the maximum of solar variation). With these results the bias introduced during the matrix measurement in a middle latitude station can be estimated between 0° and 0.6° in the zenith and between 0° and 2° in the azimuth, and therefore, the Sun movement seems to be a candidate to explain the differences.

Once applied the Sun movement correction to all the matrix data, and re-sizing the matrix, the same matrix as in figure 3.3(b) is plotted in figure 3.5(a). In figure 3.5(b), $\Delta\varphi \sin(\theta_s)$ is put instead of $\Delta\varphi$. The fact that in the first plot appears an ellipse while the second one shows a sphere confirms what we have already settled: even though, the sun-photometer motor does the steps by $\Delta\varphi$ the horizontal sun-photometer pointing error should be evaluated in terms of $\Delta\varphi \sin(\theta_s)$.

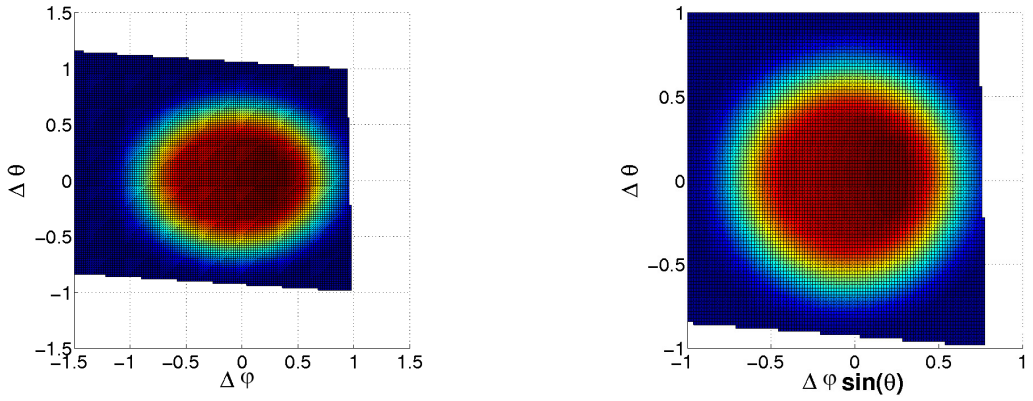

Figure 3.5: Left, matrix measurement taken in Lille Site on September 22nd 2010 at 12:47:07, corrected for the Sun displacement. Right, the same measurement but with the azimuth displacement multiplied by $\sin(\theta_s)$.

Sun croix measurement and correction by solar movement.

Scenario description. The Sun cross measurement, "croix", starts tracking the Sun and then it moves downwards, $\Delta\theta = -4°$. From this point, it moves up recording data for every step of 0.2° (scenario 0). Once it gets $\Delta\theta = 4°$ it repeats the movements but backwards (scenario 1). Afterwards, it points to the Sun again and moves right, $\Delta\varphi = 4°$. From there, it moves left recording data every 0.2°, as well, until $\Delta\varphi = 4°$ (scenario 2), and then it repeats the movement towards right until $\Delta\varphi = 4°$ again (scenario 3). The data obtained between $-2°$ and 2° in both axes are measured with low gain (Sun channel 1) like in the matrix measurement and the rest of the data are recorded with higher gain (aureole) channel. Nevertheless, the relevant part of the measurement is the first set of data.

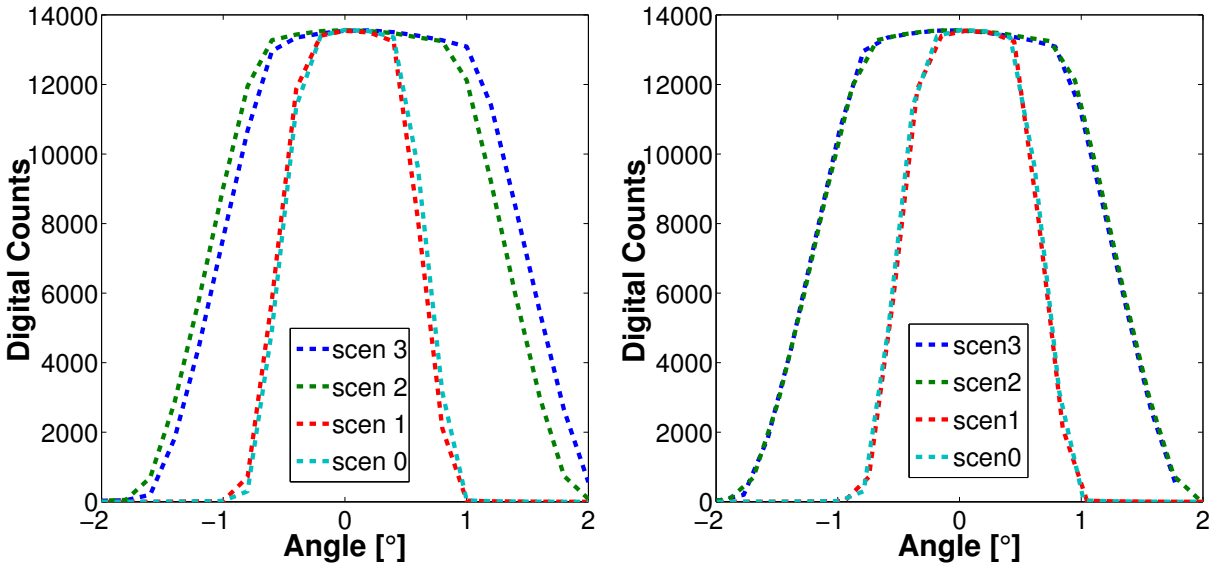

(a) Croix without correction

(b) Croix with correction

Figure 3.6: In the left, croix measurements taken in Valladolid site on August 5th 2010 at 13:41. In the right, shown after applying a Sun movement correction on the data.

Sun correction. The need of correcting the croix measurements by solar displacement during the measurement time was analyzed too. Checking the timing recorded in the data files, from the beginning of the two tracking (considering tracking moment the time recorded in the scenario 0 and 2) until the end of scenario 1 and 3 the Sun photometer uses approximately 40 seconds. The correction is especially critical for azimuth angles during the summer season when a bias of 0.4° would appear otherwise. The cross measurement done at Valladolid site on August 5th 2010 at 13:41 is shown in figure 3.6 with and without the sun correction. It can be clearly seen that the Sun correction is needed, especially for the scenario 3 (green line), which is the second scenario of the azimuthal croix as previously indicated.

Methodology

Center calculations After describing the scenarios and why the Sun movement correction was need, let us describe the methodology used to obtain the pointing bias with the matrix and the croix measurements. The analysis of the matrix measurements consists of obtaining the contour maps for levels between 20% and 80% of the maximum value (with steps of 5%) for the different matrix. Every line level describes an ellipse, as shown in the example in figure 3.7.

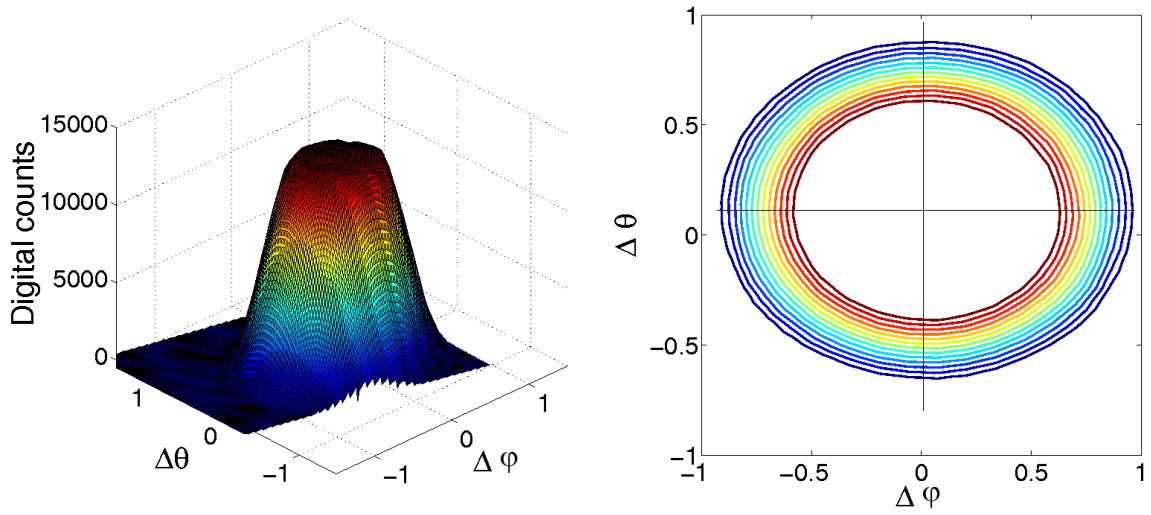

Figure 3.7: Left, matrix measurement done in Valladolid site on August 5th 2010 at 13:41 with a SZA of 54.77, in the right its contour map for levels from 20% to 80% of its maximum value (every 5%).

The value of the pointing error is estimated calculating all the centers and averaging them. A similar procedure is followed for the croix measurements. Using the data from scenarios 0 and 1 (related to $\Delta\theta$) and scenarios 2 and 3 (related to $\Delta\varphi$) the data is interpolated at different heights of its maximum value, in this case from 20% to 80% with steps of 10%. It is important to emphasize again that, the azimuth pointing estimation should be done as $\Delta\varphi \sin(\theta_s)$, consequently after the calculation of the centers (done in terms of $\Delta\varphi$ resulting in ellipses instead of circles in the matrix analysis), every single point is multiplied by $\sin(\theta_s)$ to obtain the pointing error estimation.

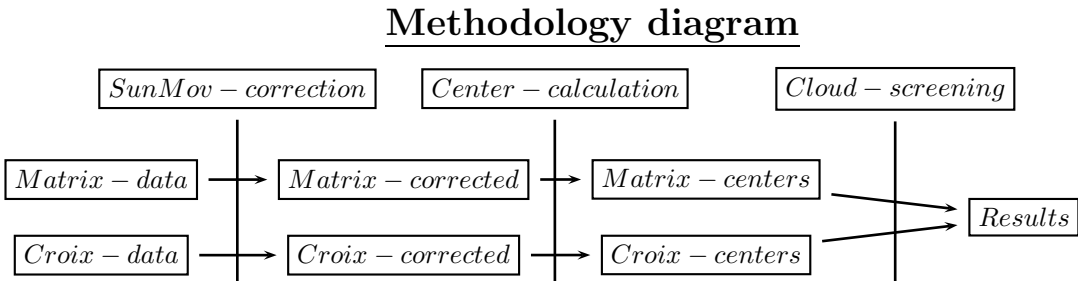

Figure 3.8: Methodology diagram followed to process matrix and croix data

Cloud Screening Croix and matrix measurement are done consecutively and automatically in CIMEL-318 Sun photometer. We only developed a procedure to eliminate those data affected by

clouds in matrix measurements, understanding that the corresponding croix measurement is also contaminated. Experimentally it has been observed that if the matrix measurement is affected by clouds, the standard deviation obtained from the centers of the ellipses described in figure 3.7(b) is higher than 0.2. The process is still under control and every piece of data is visually inspected afterwards. Finally, an acceptable value of the pointing error can be given. A chart of the hole process followed to get the value of the pointing error is illustrated in figure 3.8

3.3.2.2 First tests with observational data

Summary of the collected data

The first tests with the matrix and croix measurements were done in Valladolid during the summer of 2010 with the photometers #353 and #421, and in Lille during the early autumn of 2010 with the photometers #042 and #047. We also did some tests with the photometers #420 and #143 in Valladolid during the autumn. Table 3.1 includes the dates and the description of all the data collected.

Table 3.1: Summary of the croix and matrix measurements done with several sun-photometers.

Station	Photometer	Starting date	Ending date	Valid measurements
Valladolid	#421	29/07/2010	29/07/2010	15
Valladolid	#353	04/08/2010	06/08/2010	19
Lille	#042	22/09/2010	24/09/2010	38
Valladolid	#143	08/10/2010	17/10/2010	110
Lille	#047(1)	09/10/2010	12/10/2010	107
Valladolid	#420(1)	18/10/2010	18/10/2010	34
Lille	#047(2)	21/10/2010	28/10/2010	65
Valladolid	#420(2)	26/10/2010	01/11/2010	65
Valladolid	#420(3)	02/11/2010	08/11/2010	91
Valladolid	#420(4)	09/11/2010	11/11/2010	27

Data were collected using 6 different sun-photometers. The measurements from #047 are split because two different robots were used during the measurement; when it was installed on the first robot, it showed some disagreements which are discussed separately. Once the photometer was set on the second robot, the disagreements disappeared. The problems related to the robot in the measurements of #421, are also studied separately . The photometer number #420 was studied in 4 periods because we deliberately miscalibrated its tracking system: numbers (2) and (3) correspond to those measurements with the biased track system, while numbers (1) and (4) represent the tests when the photometer came to the calibration center and before it was sent back to its field site

once the tracking system was corrected again.

Analysis of the cases with good results.

Table 3.2 and table 3.3 contain the average and the standard deviation of the pointing error for all the data, except for the photometers #421 and #047(1) that due to their fore-mentioned problems are analyzed apart. The test #420(2) and #420(3) where the tracking system was deliberately miscalibrates are also studied later. Table 3.2 shows the results obtained for the horizontal pointing error (azimuthal multiplied by $\sin(\theta_s)$) and table 3.3 for vertical pointing error (or zenithal). The same scheme is used for both tables, the column on the left, presents the results obtained by the matrix, the second column the result obtained by the croix while third and four columns present the results for every croix branch individually.

Table 3.2: Summary of the horizontal pointing error ($\Theta_{\xi_\varphi} = \xi_\varphi \sin(\theta_s)$) of several sun photometers.

Photo.	MATRIX		CROIX		CROIX(1)		CROIX(2)	
	mean	std	mean	std	mean	std	mean	std
#353	0.041	0.021	0.050	0.024	0.044	0.023	0.057	0.023
#042	−0.058	0.018	−0.062	0.016	−0.065	0.016	−0.059	0.016
#143	0.163	0.019	0.156	0.020	0.148	0.029	0.163	0.021
#420(1)	0.115	0.017	0.118	0.019	0.115	0.019	0.120	0.020
#047(2)	−0.110	0.027	−0.108	0.024	−0.109	0.023	−0.107	0.025
#420(4)	−0.082	0.015	−0.069	0.017	−0.093	0.130	−0.067	0.019

Table 3.3: Summary of the vertical pointing error ($\Theta_{\xi_\theta} = \xi_\theta$) of several sun photometers.

Photo.	MATRIX		CROIX		CROIX(1)		CROIX(2)	
	mean	std	mean	std	mean	std	mean	std
#353	0.079	0.020	0.079	0.015	0.084	0.014	0.073	0.016
#042	0.021	0.018	0.020	0.018	0.022	0.018	0.019	0.019
#143	−0.199	0.021	−0.208	0.022	−0.210	0.024	−0.207	0.029
#420(1)	0.025	0.019	0.019	0.015	0.023	0.015	0.016	0.015
#047(2)	−0.046	0.020	−0.049	0.025	−0.034	0.023	−0.064	0.026
#420(4)	0.052	0.019	0.053	0.023	0.065	0.050	0.049	0.023

The two scenarios give practically the same pointing errors with absolute differences under 0.01° between them. This is a very important result as the scenarios are independent and the methodology followed to calculate the pointing error was done separately.

Another important result is that the sun-photometers point the Sun with an error under 0.1° except the photometer #143 whose tracking system seems to be biased 0.2° in both axes.

Using the results of this photometer (with the highest error), the estimated pointing error of every single data is plotted against the date and the SZA in figure 3.9 in order to check if there is any dependence with them. The results do not show any dependence on the date or on the solar zenith angle.

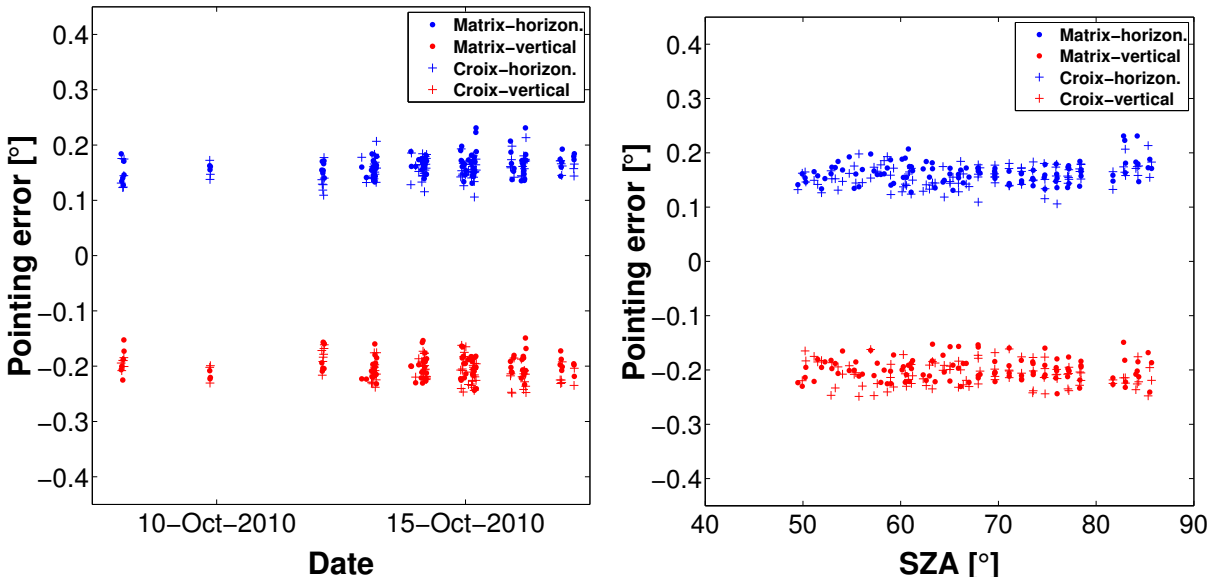

(a) Number #143 - Date

(b) Number #143 - SZA

Figure 3.9: Estimated center for matrix and croix measurements variation with the date (left) and with the sza, (right)

However, the data range for both components of the pointing error is around $0.07 - 0.08$. The result is not surprising as in table 3.2 and table 3.3 the standard deviation was $0.020 - 0.025$ for all the photometers. This high dispersion could be explained by the mechanical characteristic of the CIMEL-318 robot which has a minimum step of 0.05 in azimuth and zenith[1].

Analysis of the cases with bad results.

Among all the test performed with the sun-photometers regarding pointing error evaluation, only two disagreements were found: in the case of photometer #047(1) and photometer #421.

Looking at the values of photometer #047(1) in table 3.4 and table 3.5, there is no agreement between the matrix and croix results and not even between the two branches of the croix measure (croix(1) and croix(2) which refer to scenarios (2) and (3) in table 3.4, and scenarios (0) and (1) in table 3.5). Moreover, standard deviations of both sets are very high, reaching values of 0.1°, as is

[1]Note that the dispersion is also given in horizontal and vertical terms. As the solar zenith angles used for the measurements are very high there is almost no difference between the two components. However, as the dispersion is a function of the azimuthal and zenithal components of the motor it should be understood in these terms, therefore, we would expect the horizontal dispersion to get reduced for short solar zenith angles, which is already noticeable in figure 3.9(b) when $SZA = 50°$.

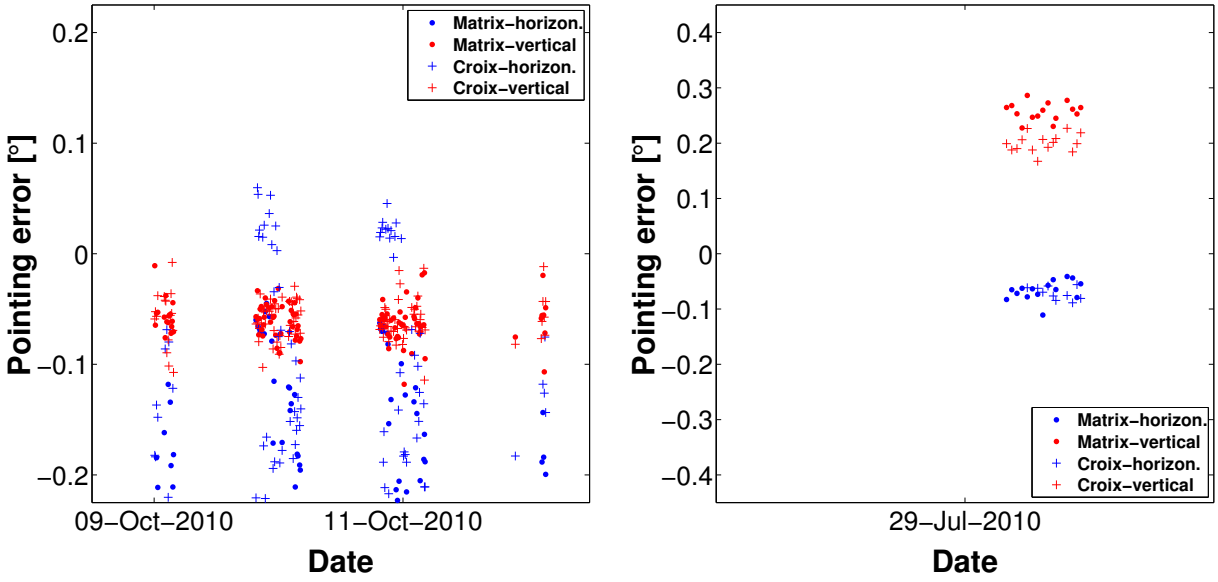

(a) Number #047(1)

(b) Number #421

Figure 3.10: Estimated center for matrix and croix measurements for photometer #047, (left), #421, (right).

also visible from the table 3.4 and table 3.5. and figure 3.10(a) which illustrates the pointing error for the photometer #047(1) as a function of the date. Nevertheless, as soon as the photometer was set on a different robot the error was corrected (re-named to photometer #047(2) and included in table 3.2 and table 3.3), resulting in identifying problems in the robot as the cause of the dispersions.

Table 3.4: Summary of the horizontal pointing error ($\Theta_{\xi_\varphi} = \xi_\varphi \sin(\theta_s)$) of photometers #047 and #421.

Photo.	MATRIX		CROIX		CROIX(1)		CROIX(2)	
	mean	std	mean	std	mean	std	mean	std
#047(1)	−0.220	0.101	−0.125	0.102	−0.233	0.112	−0.020	0.095
#421	−0.066	0.018	−0.071	0.012	−0.166	0.018	0.023	0.014

Table 3.5: Summary of the vertical pointing error ($\Theta_{\xi_\theta} = \xi_\theta$) of photometers #047 and #421.

Photo.	MATRIX		CROIX		CROIX(1)		CROIX(2)	
	mean	std	mean	std	mean	std	mean	std
#047(1)	−0.061	0.017	−0.059	0.019	−0.055	0.019	−0.064	0.020
#421	0.257	0.016	0.200	0.016	0.326	0.018	0.075	0.015

Further on, pointing error results for the photometer #421 are plotted in figure 3.10(b). For this photometer, the data dispersion is normal, showing similar values to the expected results. Even so, there is a disagreement between the pointing errors obtained by the matrix and the croix. The matrix results return expected values, on the other hand, croix calculations present a disagreement between its two branches both for horizontal and vertical error. For instance, in table 3.5 there is a difference between croix(1) and croix(2) (croix scenarios (0) and (1)), of 0.25°. This result

was not found only in the mean but in every single measurement. It seems that the robot skipped some steps when turning back (from scenario (0) to scenario (1)). The same effect is found in the azimuth axes, even though we can not notice it a priori from table 3.4. If, instead of doing the study with $\xi_\varphi \sin(\theta_s)$ (horizontal error), we use just ξ_φ (azimuth error associated with robot movement) there is the same difference of 0.25° between every single data of the scenario (2) and scenario (3). Further tests showed that the cause of the disagreement is the communication between the photometer and the robot, as more cases in other photometers were discovered.

Track test to photometer number #420

Finally, the study of the instrument in which we deliberately miscalibrated its tracking system, number #420, is shown in table 3.1: #420(2) and #420(3). The center estimations for both periods are represented in figure 3.11. Before the sun-photometer was installed, the tracking system was miscalibrated. In order to experiment higher pointing error, it was miscalibrated again during the morning on October 27$^{\text{th}}$ 2010. The pointing error results for this period are illustrated in figure 3.11(a), where the second miscalibration is very noticeable: pointing error values are different in the morning and in the afternoon on October 5$^{\text{th}}$ 2010. To conclude, the figure 3.11(b) shows the evolution of the pointing error the following days. There is a total agreement for matrix and croix center estimations in this case, as well. Therefore, even when the tracking system is highly biased the method is valid.

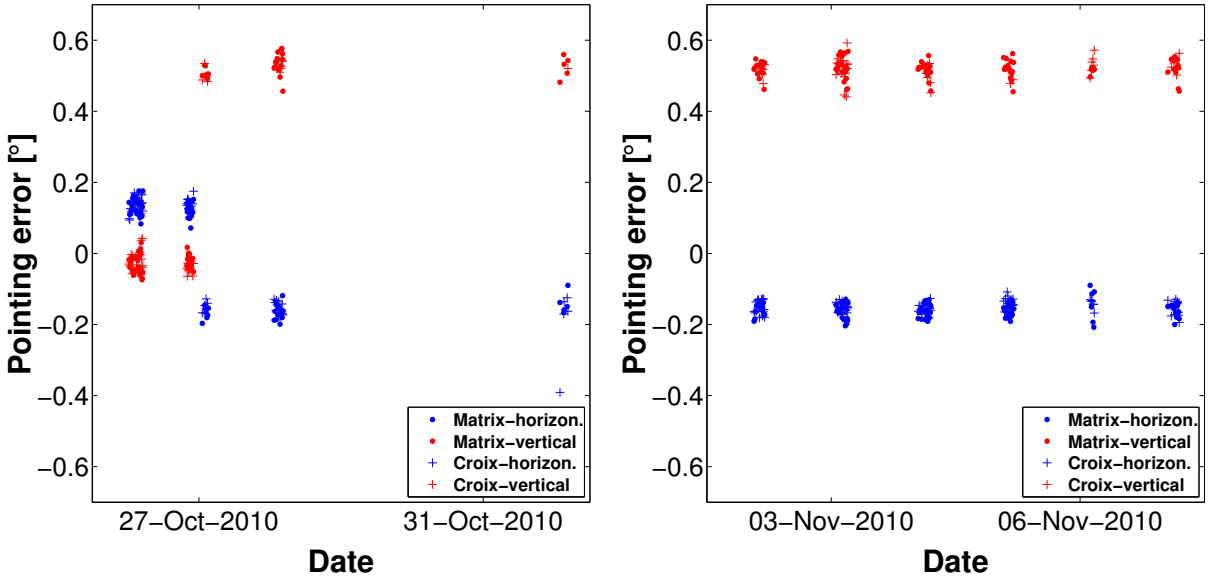

(a) Number #420(2)

(b) Number #420(3)

Figure 3.11: Test with the tracking system of sun-photometer #420.

Implications

The previous analysis was presented in the Lille AERONET workshop in 2011 (annual meetings of the calibration managers in the three AERONET calibration facilities, NASA, LOA and GOA-UVa). The obtained results suggested that matrix and croix measurement are two valid methods to estimate the pointing errors as well as good indicators of different issues as robot problems or dirtiness in the quadrant detector. That is why during this workshop, the croix measurement was proposed to be integrated as a part of the standard automatically measurements within AERONET network. Matrix measurement was discarded due as a lot of memory is needed to record the data.

In order to integrate the croix measurement, the company designed a new E-eprom (5.20h). In the evaluation phase, this E-eprom is currently used only in RIMA network. The new design has already shown to be useful in controlling the pointing error of the network photometers as well as in the early detection of mechanical problems avoiding the data loses.

3.4 Error sources III: Field of view

3.4.1 Field of view of the sun photometers

Ideally, the solid angle in a radiance measurement is supposed to be infinitesimal. However, the sun-photometers have a finite field of view and this could cause some disturbances in the radiance value. According to the company CIMEL, designer of the sun-photometer CIMEL-318, the value of the field of view in the actual sun-photometers is 1.2° while in the old versions it was 2.4°.

Before evaluating if the finite field of view affects the radiance value and the inversion results as a consequence, in the next subsections several methods for calculating the field of view are used in order to check if the company specifications correspond to the values in our instruments. One of the methods will also be used to characterize the form of the field of view with a laser beam in the laboratory.

3.4.2 Matrix measurements and field of view calculations

Nakajima et al. (1996) proposes a method to estimate the field of view from similar measurements to the matrix scenario (described in 3.3.2). In this article, the field of view of the solar radiometer PREDE (standard instrument of the Skynet network) is calculated from a set of measurements similar to the matrix scenarios. Basically, the field of view is obtained as:

$$F.O.V. = \int\int_{\Delta A} \frac{E(x,y)}{E(0,0)} dxdy \tag{3.9}$$

where x and y (in radians) are the polar coordinates that determine the position of the optical

axis with respect to the position of the sun. $E(x, y)$ is the irradiance measurement at any point and $E(0, 0)$ is the irradiance at the center of the sun.

In order to use Eq. (3.9) is necessary to evaluate the measurement $E(0, 0)$ and therefore, to know previously the pointing error. If x_c and y_c are the estimated pointing errors (horizontal and vertical respectively), the Eq. (3.9) can be expressed as:

$$F.O.V. = \sum_{i,j} \frac{E(x_i, x_j)\Delta S(i, j)}{E(x_c, y_c)} \tag{3.10}$$

where i represents the variation in the horizontal (azimuth increment multiplied by $\sin\theta_s$) axes and j in the zenithal one.

Using the names in table 3.1, in table 3.6 calculated values for the field of view are represented. Photometers #421 and #047 in its first part are not represented due to their robot problems. The values for the 5 photometers vary between 1.13° and 1.32°, which means a discrepancy of 10% of Cimel specified value of 1.2°.

Photo.	F.O.V	std
#353	1.302	0.018
#042	1.267	0.029
#143	1.139	0.015
#047(2)	1.297	0.020
#420(1)	1.315	0.015
#420(2)	1.318	0.020
#420(3)	1.320	0.026
#420(4)	1.322	0.026

Table 3.6: Measurements summary for zenithal center (ξ_θ) giving the expected results.

Different values are given for different tracking mis-calibrations in photometer #420. The value obtained keeps almost constant not depending on the pointing accuracy.

3.4.3 Matrix measurements with a laser beam in the laboratory

Here we present a second test for measuring the field of view using the matrix scenario. Instead of taking the Sun as a source, we propose using a laser beam in the laboratory which has been previously expanded and collimated in order to get a punctual source[2] in the infinite (see figure 3.12).

[2]The angular size of any source can be estimated as the quotient between the size of the source, in this case 12 μm, and the focal length of the lens which was around 30 cm in the one used. With these data the angular size was about 0.0023° in our experiments.

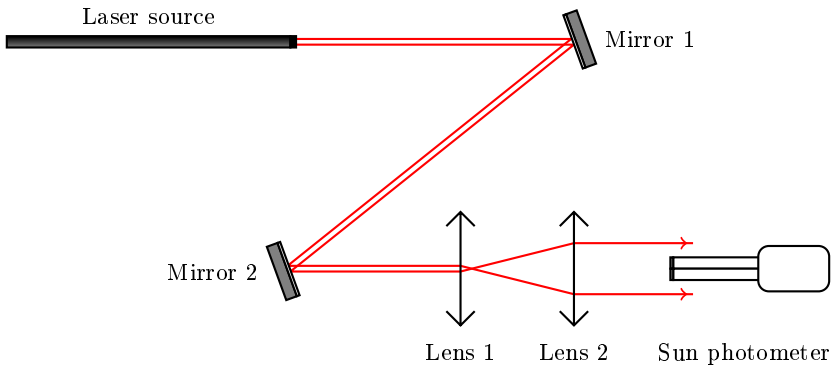

Figure 3.12: Optic design to measure the FOV of sun photometers with a laser beam.

The utilization of a punctual source results not only in the value of the field of view (following the methodology given by Nakajima et al. (1996) and summarized in Eq. (3.9)) but also with the opportunity to estimate the shape of the response of the field of view in the sun-photometer.

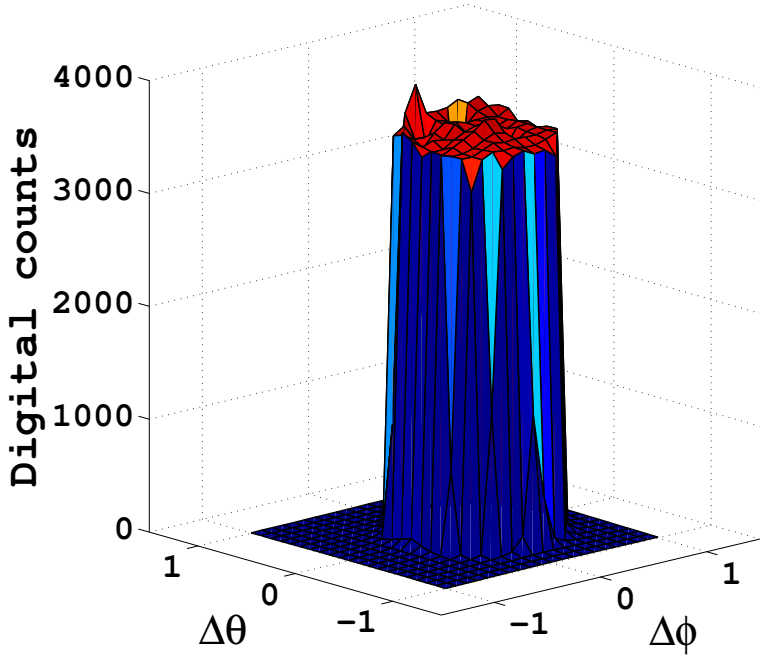

Figure 3.13: Example of a matrix measurement using a laser beam with photometer #143

Figure 3.13 shows an example of a matrix measurement in photometer #143 using the laser beam in the laboratory. We can observe that the response of the field of view is practically cylindric and that the fall is straight, indicating that in the optical system of the sun-photometer the limit illumination and full illumination are the same.

Comparing this representation with the one obtained in figure 3.7 where the Sun was used as the source, we see that in that case the fall was softer due to the angular size of the sun.

The experiences with the laser beam are quite recent and we have only measured the photometer

#143. The result of the test gave a field of view of 1.19° (less than 5% differences compare to the method using the Sun as a source).

3.5 Interesting relations regarding pointing errors and the radiance function

In the subsection 1.1.3 the two set of radiance measurements, which are programmed in the sun-photometer (CIMEL-318), were defined: principal plane and almucantar scenarios.

After pointing the sun, the principal plane varies the zenith angle while the azimuth angle is kept constant. On the other hand, the almucantar keeps constant the zenith angle and covers the different azimuth angles.

Pointing error affects both measurements because, as it was indicated, both scenarios start after pointing the sun. Therefore, the error committed pointing the Sun is dragged to the radiance measurements. A deeper description of this effect is the aim of this subsection as well as a formal analysis of the produced errors in the radiance.

In chapter 5, radiance errors are presented as the fundamental parameter to understand the effects of pointing error over the inversion results. The magnitude used, to quantify radiance errors, is the relative error, defined as:

$$\epsilon_R = \frac{R(\theta', \varphi') - R(\theta, \varphi)}{R(\theta, \varphi)} \tag{3.11}$$

where $R' = R(\theta', \varphi')$ is the radiance with a pointing error and $R = R(\theta, \varphi)$ is the corresponding radiance without error. Next subsections analyze this parameter for all the configurations error-radiance measurement.

3.5.1 Principal plane and vertical error

The first case under study is the simplest one and it will allow us to introduce easily several useful concepts employed in the rest of the cases, as well. In figure 3.14, pointing process with a vertical error is illustrated in the right part: dotted line represents a correct pointing, whereas straight line corresponds to the pointing with a vertical error. This scheme is transfered to a principal plane measurement, shown in the left part of the vault.

Radiance measurement in the principal plane is only function of the zenith angle θ being always zero the azimuth angle. Accordingly, a radiance measurement in the point p belonging to the

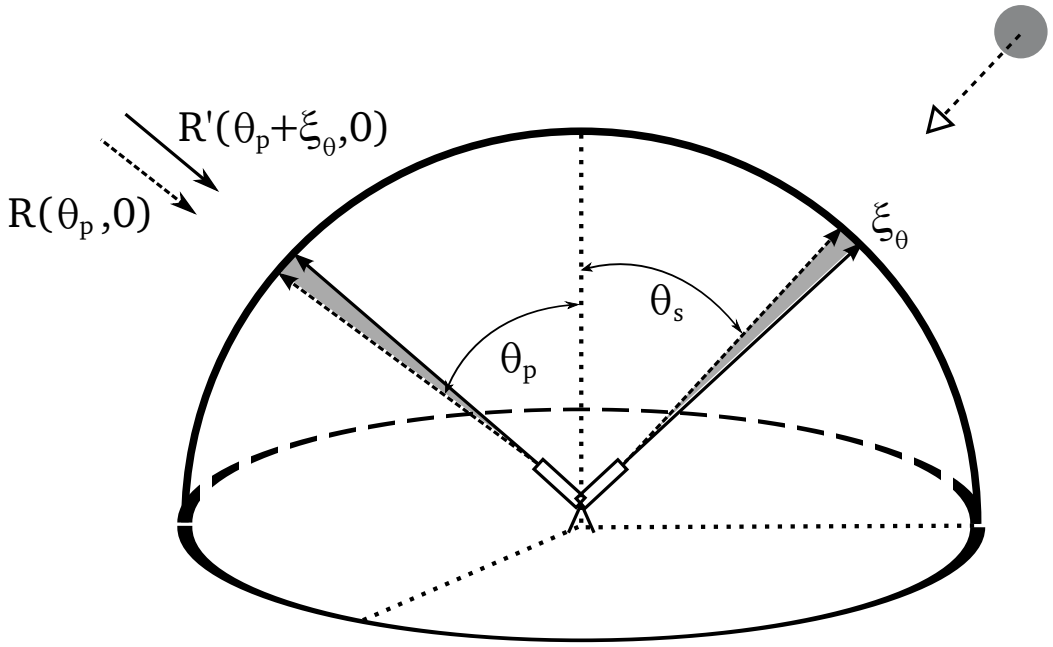

Figure 3.14: Principal plane with vertical error: Straight line represents the measure with the error whereas dotted line represents the corresponding measurement without the error. In the right part of the figure appears the pointing process where a vertical error is committed. In the left. a measurement for a zenith angle of θ_p, belonging to the full principal plane, is represented with and without the vertical error.

principal plane would be given as $R = R(\theta_p, 0)$. A vertical pointing error only modifies the zenith angle adding the error but keeping the azimuth angle as zero, $R' = R(\theta_p + \xi_\theta, 0)$. And thus, the relative error takes the following form:

$$\epsilon_R = \frac{R(\theta_p + \xi_\theta, 0) - R(\theta_p, 0)}{R(\theta_p, 0)} \tag{3.12}$$

If we consider the radiance as a continuous and differentiable function in the point p, its partial derivative with respect θ, at this point, is defined as:

$$\begin{aligned} \left[\frac{\partial R(\theta,\varphi)}{\partial \theta}\right]_{\substack{\theta=\theta_p \\ \varphi=0}} &= \frac{R(\theta_p + d\theta, 0) - R(\theta_p, 0)}{d\theta} \\ R(\theta_p + d\theta, 0) - R(\theta_p, 0) &= \left[\frac{\partial R(\theta,\varphi)}{\partial \theta}\right]_{\substack{\theta=\theta_p \\ \varphi=0}} d\theta \end{aligned} \tag{3.13}$$

If now, the vertical (zenith) error is presupposed to be very small $\xi_\theta \simeq d\theta$, Eq. (3.12) and Eq. (3.13) can be combined as:

$$\epsilon_R = \left[\frac{\partial R(\theta,\varphi)}{\partial \theta}\right]_{\substack{\theta=\theta_p \\ \varphi=0}} \frac{\xi_\theta}{R(\theta_p, 0)} \tag{3.14}$$

Total errors analyzed in this thesis rise up to 1°. Approximation and exact value of the relative error perfectly match almost for all the cases. In fact, an exact expression (Suli and Mayers, 2003) would be given by:

$$R(\theta_p + \xi_\theta, 0) - R(\theta_p, 0) = \left[\frac{\partial R(\theta, \varphi)}{\partial \theta}\right]_{\substack{\theta=\theta_p \\ \varphi=0}} \xi_\theta + \frac{1}{2}\left[\frac{\partial^2 R(\theta, \varphi)}{\partial \theta^2}\right]_{\substack{\theta=\theta_c \\ \varphi=0}} \xi_\theta^2 \tag{3.15}$$

with $\theta_c \in (\theta_p, \theta_p + \xi_\theta)$.

The smaller ξ_θ is the better the approximation, because the second order term in the right part of the equation will be much smaller than the first order term. Still, the approximation was though to summarize the error analysis so as not to repeat comments and graphics when talking about relative errors, for those cases which share all the conditions but the absolute value of the pointing error. Then, anomalies between approximation and exact value of the relative error will be indicated. These anomalies will take place for largest error, and shortest scattering angles, when radiance function varies more rapidly.

Finally, it should be indicated that the vertical error, in the case of principal plane, can be positive or negative and both are subject to analysis. The Eq. (3.14) is valid for both cases just giving ξ_θ the correct sign.

3.5.2 Principal plane and horizontal error

In a second step, a horizontal error instead of a vertical mispointing is considered. In figure 3.15, there is a graphical description of the situation. The pointing process is represented in the right part of the figure. The azimuth error, ξ_φ, varies for different solar zenith angle, being constant the horizontal error Θ_{ξ_φ}. Nevertheless, to carry out an analog study to the one in the previous subsection, we just need to remark that the azimuth error, ξ_φ, is fixed and constant during the principal plane measurement, once the horizontal error is set during the pointing process.

The relative error, in the point p, is defined now as:

$$\epsilon_R = \frac{R(\theta_p, \xi_\varphi) - R(\theta_p, 0)}{R(\theta_p, 0)} \tag{3.16}$$

And then again, considering the radiance as a continuous and differentiable function in the

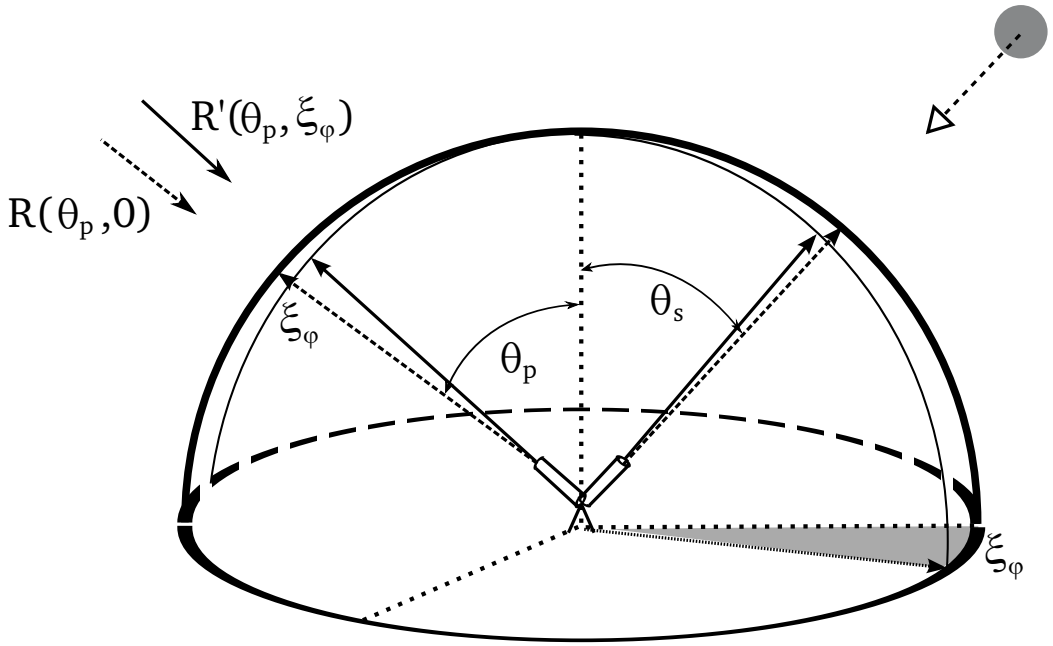

Figure 3.15: Principal plane with horizontal error: Straight line represents the measure with the error whereas dotted line represents the corresponding measurement without the error. In the right part of the figure appears the pointing process where a horizontal error is committed. In the left. a measurement for a zenith angle of θ_p, belonging to the full principal plane, is represented with and without the horizontal error.

point p, its partial derivative with respect φ in p is defined as:

$$\begin{aligned} \left[\frac{\partial R(\theta,\varphi)}{\partial \varphi}\right]_{\substack{\theta=\theta_p \\ \varphi=0}} &= \frac{R(\theta_p, d\varphi) - R(\theta_p, 0)}{d\varphi} \\ R(\theta_p, d\varphi) - R(\theta_p, 0) &= \left[\frac{\partial R(\theta,\varphi)}{\partial \varphi}\right]_{\substack{\theta=\theta_p \\ \varphi=0}} d\varphi \end{aligned} \tag{3.17}$$

Assuming ξ_φ to be very small, then $\xi_\varphi \simeq d\varphi$, and Eq. (3.16) and Eq. (3.17) can be rewritten as:

$$\epsilon_R = \left[\frac{\partial R(\theta,\varphi)}{\partial \varphi}\right]_{\substack{\theta=\theta_p \\ \varphi=0}} \frac{\xi_\varphi}{R(\theta_p, 0)} \tag{3.18}$$

Using the same construction as in Eq. (3.15), $\xi_\varphi \simeq d\varphi$ means to reject second order terms by comparison with the first order one:

$$\left[\frac{\partial R(\theta,\varphi)}{\partial \theta}\right]_{\substack{\theta=\theta_p \\ \varphi=0}} \xi_\varphi \gg \frac{1}{2}\left[\frac{\partial^2 R(\theta,\varphi)}{\partial \theta^2}\right]_{\substack{\theta=\theta_p \\ \varphi=\varphi_c}} \xi_\varphi^2 \tag{3.19}$$

with $\varphi_c \in (0, \xi_\varphi)$.

But this case presents the controversy of rising ξ_φ when the solar zenith angle decreases. Following Eq. (3.8), horizontal and azimuth error are related in an excellent approximation as $\Theta_{\xi_\varphi} = \sin\theta_s \xi_\varphi$. The maximum horizontal pointing error (Θ_{ξ_φ}) considered has been 1°, as for the vertical one. The minimum solar zenith angle taken for the pointing analysis was 15°, which means that the value of ξ_φ is 3.86° in these extreme conditions. Anew, we should insist that substituting the real errors for their derivative approximations has been designed to summarize the results. Therefore, those cases showing differences between radiance derivatives and errors will be commented.

Positive and negative horizontal errors in the principal plane measurement are symmetrically equivalents. So, only positive errors will be analyzed, being the results extensible to the negative case.

3.5.3 Almucantar and vertical error

For an almucantar measurement, the azimuth angle φ varies while the zenith angle keeps constant and equal to θ_s. Almucantar is subdivided by its right and left movement, and afterwards, the mean value is taken as the valid measurement.

If only a vertical error ξ_θ is considered, the symmetry in φ of radiance function will be still valid, and therefore, taking right or left set of measurements is equivalent so only one of the two branches needs to be analyzed here. In this case, right branch is chosen with φ varying from 0 to 180. This property will not be valid for horizontal errors, as we will discuss subsequently.

So, after the preliminary considerations, we deal with an almucantar (with φ varying from 0 to 180) which pointing process suffers a vertical error, as it is represented in figure 3.16.

In the point a, belonging to the almucantar, the radiance relative error due to the vertical pointing error will be given by:

$$\epsilon_R = \frac{R(\theta_s + \xi_\theta, \varphi_a) - R(\theta_s, \varphi_a)}{R(\theta_s, \varphi_a)} \tag{3.20}$$

If we suppose the radiance to be a continuous and differentiable function in the point a, its partial derivative with respect θ, in this point, is defined as:

$$\begin{aligned} \left[\frac{\partial R(\theta,\varphi)}{\partial\theta}\right]_{\substack{\theta=\theta_s \\ \varphi=\varphi_a}} &= \frac{R(\theta_s + d\theta, \varphi_a) - R(\theta_s, \varphi_a)}{d\theta} \\ R(\theta_s + d\theta, \varphi_a) - R(\theta_s, \varphi_a) &= \left[\frac{\partial R(\theta,\varphi)}{\partial\theta}\right]_{\substack{\theta=\theta_s \\ \varphi=\varphi_a}} d\theta \end{aligned} \tag{3.21}$$

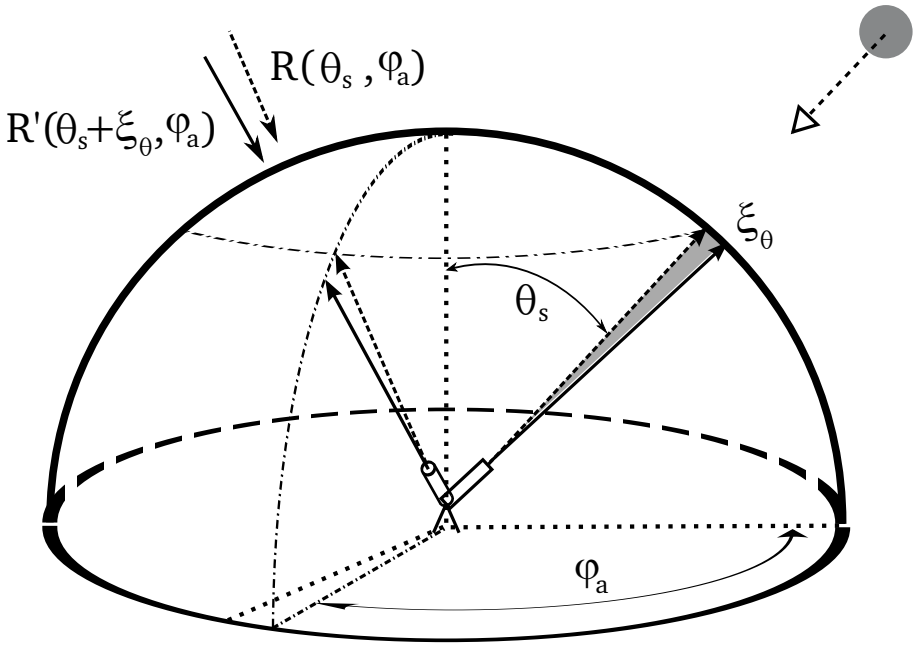

Figure 3.16: Almucantar with vertical error: Straight line represents the measure with the error whereas dotted line represents the corresponding measurement without the error. In the right part of the figure appears the pointing process where a vertical error is committed. In the left. a measurement for a azimuth angle of φ_a, belonging to the full almucantar, is represented with and without the vertical error.

Using the same approximation as in the previous subsections, $\xi_\theta \simeq d\theta$, Eq. (3.20) and Eq. (3.21) can be combined as:

$$\epsilon_R = \left[\frac{\partial R(\theta,\varphi)}{\partial\theta}\right]_{\substack{\theta=\theta_s \\ \varphi=\varphi_a}} \frac{\xi_\theta}{R(\theta_s,\varphi_a)} \tag{3.22}$$

To end up, vertical error, also for an almucantar measurement, can be positive or negative and both are analyzed. To fulfill both analysis, ξ_θ needs to get the correct sign in Eq. (3.22). For very short scattering angles, in an almucantar configuration, radiance presents a maximum. For these cases, second derivative term will not be discarded compared to the first derivative term and the analysis should be made more careful.

3.5.4 Almucantar and horizontal error

Last case is the most complex for all the configurations error-radiance measurement. In figure 3.17, an almucantar with a horizontal pointing error is represented.

The symmetric approximation used for vertical error is not valid in this case and the horizontal error should be introduced, separately, in left and right measurements. If the azimuth error,ξ_φ, is positive (towards right); the radiance measurement in the right branch will take the form $R'_r =$

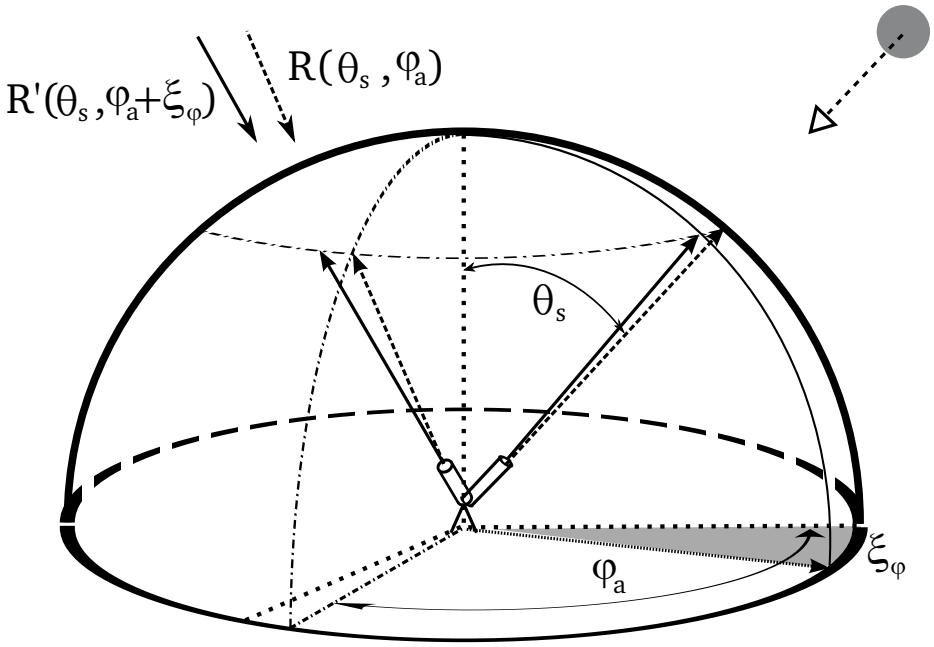

Figure 3.17: Almucantar with horizontal error: Straight line represents the measure with the error whereas dotted line represents the corresponding measurement without the error. In the right part of the figure appears the pointing process where a horizontal error is committed. In the left. a measurement for a azimuth angle of φ_a, belonging to the full almucantar, is represented with and without the horizontal error.

$R(\theta_s, \varphi_a + \xi_\varphi)$, while in the left branch will be $R'_l = R(\theta_s, -\varphi_a + \xi_\varphi)$. Using the symmetry of radiance error in φ, the expression for the left branch can be rewritten as $R'_l = R(\theta_s, \varphi_a - \xi_\varphi)$. Then, radiance relative error will be expressed as:

$$\begin{aligned} \epsilon_R &= \frac{\frac{R'_r(\theta,\varphi))+R'_l(\theta,\varphi)}{2} - R(\theta,\varphi)}{R(\theta,\varphi)} \\ \epsilon_R &= \frac{\frac{R(\theta_s,\varphi_a+\xi_\varphi)+R(\theta_s,\varphi_a-\xi_\varphi)}{2} - R(\theta_s,\varphi_a)}{R(\theta_s,\varphi_a)} \end{aligned} \tag{3.23}$$

or multiplied by two:

$$\epsilon_R = \frac{R(\theta_s, \varphi_a + \xi_\varphi) + R(\theta_s, \varphi_a - \xi_\varphi) - 2R(\theta_s, \varphi_a)}{2R(\theta_s, \varphi_a)} \tag{3.24}$$

On the other hand, if the function radiance, R, has a second derivative in the point a, the partial derivative of R with respect to φ can be written approximated as:

$$\left[\frac{\partial^2 R(\theta,\varphi)}{\partial\varphi^2}\right]_{\substack{\theta=\theta_s \\ \varphi=\varphi_a}} = \frac{R(\theta_s, \varphi_a + \xi_\varphi) + R(\theta_s, \varphi_a - \xi_\varphi) - 2R(\theta_s, \varphi_a)}{d\varphi^2} \tag{3.25}$$

And then again, if ξ_φ is very small, then we can approach $\xi_\varphi \simeq d\varphi$ and combine Eq. (3.23) and

Eq. (3.25), obtaining:

$$\epsilon_R = \left[\frac{\partial^2 R(\theta,\varphi)}{\partial\varphi^2}\right]_{\substack{\theta=\theta_s \\ \varphi=\varphi_a}} \frac{\xi_\varphi^2}{2R(\theta_s,\varphi_a)} \tag{3.26}$$

Due to the symmetry on measurements, here, the approximation $\xi_\varphi \simeq d\varphi$ is better than in previous cases. In fact, exact expression of Eq. (3.26) would be given by (Suli and Mayers, 2003):

$$\left[\frac{\partial^2 R(\theta,\varphi)}{\partial\varphi^2}\right]_{\substack{\theta=\theta_s \\ \varphi=\varphi_a}} = \frac{R(\theta_s,\varphi_a+\xi_\varphi)+R(\theta_s,\varphi_a-\xi_\varphi)-2R(\theta_s,\varphi_a)}{\xi_\varphi} - \frac{\xi_\varphi^2}{12}\left[\frac{\partial^4 R(\theta,\varphi)}{\partial\varphi^4}\right]_{\substack{\theta=\theta_s \\ \varphi=\varphi_c}} \tag{3.27}$$

with $\varphi_c \in (\varphi_a, \varphi_a+\xi_\varphi)$. So, forth order terms are rejected by doing the approximation.

Actually Eq. (3.14), Eq. (3.18) and Eq. (3.22) are just the basic equations to transfer errors from one parameter to other which depend on the it, but Eq. (3.27) is something different due to the way that the almucantar is processed. The result is that the radiance measurement in an almucantar configuration is affected by the second derivative term in a horizontal pointing error.

These properties will be used along the chapter 5 in order to study the radiance differences obtained introducing pointing errors.

Chapter 4

Error influence on the inversion of sky radiances I: Calibration error

La buena es la que dice que sí

Carlos Cuesta Rueda (Positivista)

Resumen en español del capítulo:

En el capítulo 4 se exponen los resultados obtenidos simulando los errores de calibración. La metodología seguida ha consistido en simular para las cuatro longitudes de onda y para los dos canales de "aureola" y "sky", todas las posibles combinanciones, suponiendo errores de $-5\,\%$, $0\,\%$ y $+5\,\%$. El análisis se ha realizado para cinco diferentes SZA, para todos los tipos de aerosoles considerados y para las dos geometrías: almucantar y plano principal, haciendo un total 524880 inversiones.

El análisis muestra una menor incidencia de los errores en la calibración de los distintos canales espectrales para los casos con mayor espesor óptico de aerosoles o mayor ángulo cenital solar, en claro acuerdo con los criterios aplicados en AERONET a los datos de calidad asegurada (nivel 2.0). Este estudio presenta ciertas novedades respecto al trabajo de Dubovik et al. (2000), ya que éste no consideró la posibilidad de errores diferentes para distintos canales y longitudes de onda, tratando sólamente los casos extremos, donde todos eran o $-5\,\%$ o $+5\,\%$. Se ha demostrado que esta consideración es necesaria para estimar de forma correcta la influencia de la calibración en la obtención de la distribución de tamaños tanto en las medidas de almucantar como de plano principal, sobre todo en el modo grueso.

Los errores en los productos derivados de la inversión son grandes en parámetros como el índice de refracción si la radiancia tiene una precisión del $5\,\%$. Esto es especialmente crítico en el caso de los aerosoles poco absorbentes, donde los errores de la parte real superan el $10\,\%$ y en la parte imaginaria llegan a ser superiores al $100\,\%$.

Estos datos ponen de manifiesto la necesidad de hacer un mayor esfuerzo en la precisión de la calibración. También debe existir un buen control de la coherencia entre las medidas de los canales de "sky" y "aureola", lo que está muy relacionado con un control rutinario de las medidas en coordinación con los responsables de la estación.

4.1 Introduction

After describing the errors and the methodology used to calculate them, this is the first of three chapters dealing with the study of the error influence on the inversion of sky radiances. The general strategy in the three chapters will be simulating radiances using the forward module of Dubovik's code with the properties of the selected aerosols (described in chapter 2), introducing the type of error specific for each case. In a first step, these radiances are contrasted to those without errors. Afterwards the erroneous radiances will be inverted and the aerosol products retrieved will be compared to the original properties.

4.2 Methodology used to analyze the calibration influence

Following the idea laid out in the introduction, this section explains the methodology used to study the calibration errors. Although the analysis in itself is theoretical, the input data used to simulate radiances correspond to real observations of the key aerosol types from Dubovik et al. (2002), as it was described in detail in chapter 2. As mentioned, the aerosol types used are desert dust, oceanic, urban and biomass burning aerosol. For each case we have considered two aerosol loads: one with lower and another with higher aerosol optical depth, which makes a total of 8 different cases.

As discussed in subsection 1.1.3, the radiance calibration is done determining 8 calibration coefficients: four wavelengths multiplied by the two radiance channels (aureole and sky). These coefficients have an absolute error of 5% (established by AERONET, Holben et al. (1998)) and originated in the calibration procedure.

In this study, we simulate the radiances using the properties of the 8 aerosol examples (4 types with two aerosol load), for 5 different solar zenith angles: 15°, 30°, 45°, 60° and 75° and with the two geometries used to measure the sky radiance within AERONET Network (principal plane and almucantar) and explained in subsection 1.1.3, resulting in 80 reference cases.

Then, for every simulated case, the radiances measurements are divided in 8 different sets regarding their calibrations coefficient. Afterwards every set is multiplied by either 105% (simulating an error of +5% in the calibration coefficient), 100% (supposing that the calibration coefficient is correctly calibrated) or 95% (simulating an error of −5% in the calibration coefficient).

In the study all the possible combinations were taken into account resulting in $3^8 = 6561$ inversions for every of the 80 reference cases (524880 inversions in total).

Figure 4.1. shows the flow-chart of the study. As commented in the introduction, here we only compare the retrievals obtained from inversions with and without the introduced error. As the calibration error is directly transmitted into the radiance value, a radiance comparison is not

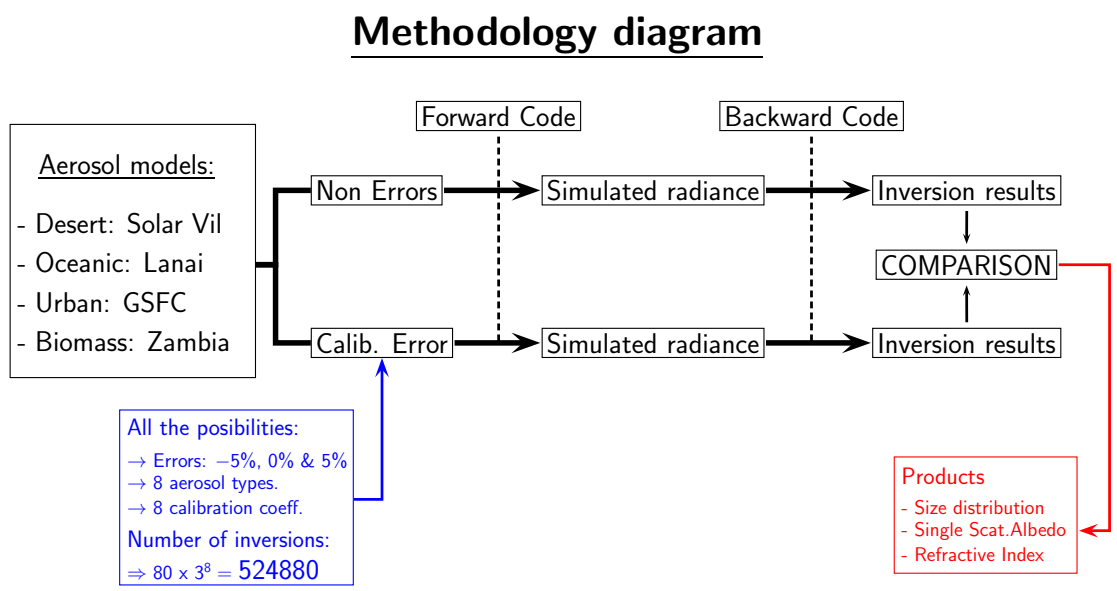

Figure 4.1: Methodology diagram followed to carry out the simulations in order to check the effects of the calibration error on Dubovik's inversion

needed in this case. Obviously the radiance differences will have the value of 0% or ±5%, depending on the calibration error that was considered.

In the next two chapters (chapter 5 regarding pointing errors and chapter 6 influence of the finite field of view), radiances differences will not be so straight forward and they will need to be separately calculated and analyzed.

As a final remark, it should be mentioned that radiance and irradiance calibrations are independent from each other, thus, the aerosol optical depth is not affected by the radiance error considered in this study. That is why the non error values of the aerosol optical depth are kept constant through all the simulations.

4.3 Calibration error consequences on inversion results

4.3.1 Desert dust (Solar Village)

Following the same order as in subsection 2.2.1, the first case studied is the desert dust aerosol registered in Solar Village. The two examples of this aerosol type described in that subsection are also the ones considered here: $\tau_{1020} = 0.3$ (SolV1) and $\tau_{1020} = 0.5$ (SolV2).

The most important characteristics of this aerosol can be summarized in its prominent coarse mode in the size distribution and the dependency of the imaginary refractive index on the wavelength being more absorbing for shorter wavelengths. The values found in Solar Village site are not

particularly large. As commented in section 2.2.1 they are smaller than the ones found in other studies at AERONET wavelengths and they could be considered as non absorbing (see table 2.1). The inversion results generated from simulated radiance measurements were consistent with the inputs: the size distribution did not present major differences with the input for every SZA in both almucantar and principal plane simulations. For principal plane retrievals, the rest of the parameters had a normal behavior too. However, as commented in subsection 2.2.1.2, the refractive index and the single scattering albedo suffered instability problems for short SZA in almucantar simulations due to the lack of information about large scattering angles.

After recalling briefly the main characteristics of desert aerosol and its inversion results, derived with simulated radiance data without error, let us analyze the results obtained with simulated radiances including calibration errors.

Before proceeding with the results analysis on the desert dust, we will describe the layout of the figures 4.2 and 4.3 which summarize the consequence of the calibration errors on the retrievals for the example with less aerosol load (figure 4.2) and with more aerosol load (figure 4.3) respectively. The same scheme will be used for the rest of the aerosol types further on. The two main figures are divided into 3 plots: showing the values for size distribution, single scattering albedo and the refractive index. Every single plot is further divided into 6 subplots, with the results at $SZA = 15°$, $SZA = 45°$ and $SZA = 75°$: the 3 subplots at the top for the almucantar, and the bottom 3 for the principal plane. The X-scale for the size distribution represents the radius while for single scattering albedo and the refractive index it denotes the wavelength. The refractive index subplots contain at the same time both the real part (left part) and the imaginary part (right part). The Y-scale on the left (of the whole plot) refers to the values of the real part while the Y-scale on the right expresses the values of the imaginary part.

Within the subplots, a black solid line is used to illustrate the inversion with no calibration error, the gray area contains all the 6561 simulations done following the methodology in section 4.2, red dotted lines delimit the cases where sky and aureole calibration are the same for each wavelength[1], the green dotted line represents the case where an error of -5% was introduced into all the calibration coefficients, while the blue dotted line represents the case with an error of $+5\%$ introduced into all the calibration coefficients. Evidently, the gray area contains the area delimited by the red lines as these cases are a subset of the first one; at the same time, blue and green lines are within the area delimited by the red lines as they fulfill the condition of having identical errors for the aureole and sky calibration coefficient at the same wavelength.

Some general characteristics extensible to all the aerosol types analyzed are visible already in this particular case. In most of the retrieved parameters, the errors are reduced by two causes: when

[1]Even though the calibrations are independent, the measurement is repeated at 6° with both aureole and sky channel, which is a mode of controlling that the two channels have a similar calibration.

the solar zenith angle increases (specially in the almucantar) and when the aerosol optical depth increases (in our study for the example analyzed with the highest aerosol load). This result is known within AERONET scope (Dubovik et al., 2000) and taken into the account in version 2.0 where the level 2.0 is only given to the optical parameters retrievals if $SZA > 50^\circ$ and $\tau_a(440) > 0.4$. Thus, the maximum errors are normally obtained for the almucantar at $SZA = 15^\circ$ in the example with the lowest aerosol load. However, the coarse mode of the size distribution is the only parameter which does not seem to follow these rules, and it shows the highest errors for almucantar and principal plane with $SZA = 75^\circ$.

Another common feature is that the single scattering albedo and the imaginary part of the refractive index are limited by the green and blue line (extreme error cases for all the wavelengths). This result was expected as both parameters are strongly connected to the total amount of radiance measured (note that, the aerosol optical depth is fixed, as commented in section 4.2). The single exception is the almucantar at 15°, reoccurring throughout this thesis as a particular case due to the lack of information associated with it. The green line, representing the case with all the calibration coefficients with an error of -5%, provides the minimum value obtained for the single scattering albedo and the maximum of the imaginary part of the refractive index. The blue line, which stands for the case with all the calibration coefficients with an error of $+5\%$, is just the opposite: maximum value for the single scattering albedo and the minimum value for the imaginary part of the refractive index. The accuracy study presented in Dubovik et al. (2000) only considers these two cases, where all the errors in the calibration coefficients are equal to $+5\%$ or -5% [2]. As mentioned, both lines delimit the errors for the single scattering albedo and the imaginary part of the refractive index in our study, and therefore, they are representative of the maximum error obtained due to calibration uncertainties.

The effects of the calibration errors on the size distribution are also studied just with the two cases where all the calibration coefficients have an error of $+5\%$ or -5% in the work by Dubovik et al. (2000). However, in our approach, the results for the size distribution are not delimited by the blue and green lines. The retrieval of the size distribution is generally more connected to the form of the radiance, which converts the green line and the blue line in just two regular cases. Thus, the study by Dubovik et al. (2000) is improved here depicting all those cases where the errors of each channel are treated independently.

The same is true for the real refractive index: Even though in the desert dust case the green and the blue lines seem to be the extreme cases, this is an effect single to this aerosol type and it does not reappear in the next examples. Therefore, the possibility of different errors for different calibration coefficients should be admitted in order to properly account for the maximum error in the real part of the refractive index and the refractive index due to the calibration uncertainty.

[2] In the paper named as $\Delta I = 5\%$ and $\Delta I = -5\%$.

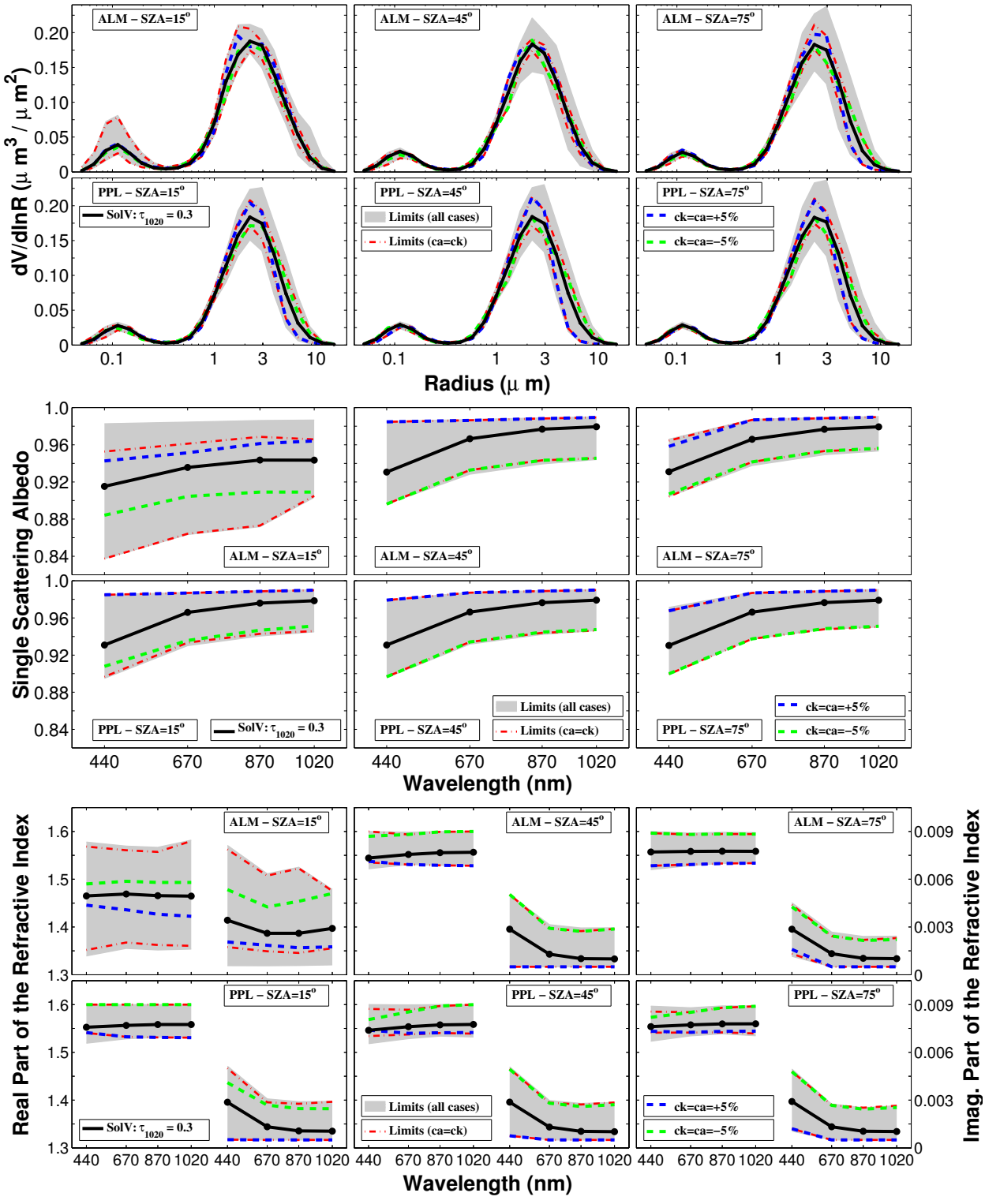

Figure 4.2: Influence of the calibration error on the products (size distribution (top), single scattering albedo (middle) and refractive index (bottom)) retrieved with Dubovik's inversion for Solar Village example with $\tau_{1020} = 0.3$. Black solid line represents the inversion with no calibration error, the gray area contains all the simulations done following the methodology in section 4.2, red dotted lines delimit the area for those case where sky and aureole calibration coefficients are the same for each wavelength, the green dotted line represents the case with an error of -5% in all the calibration coefficients and blue dotted line the case with $+5\%$ error in all the calibration coefficients

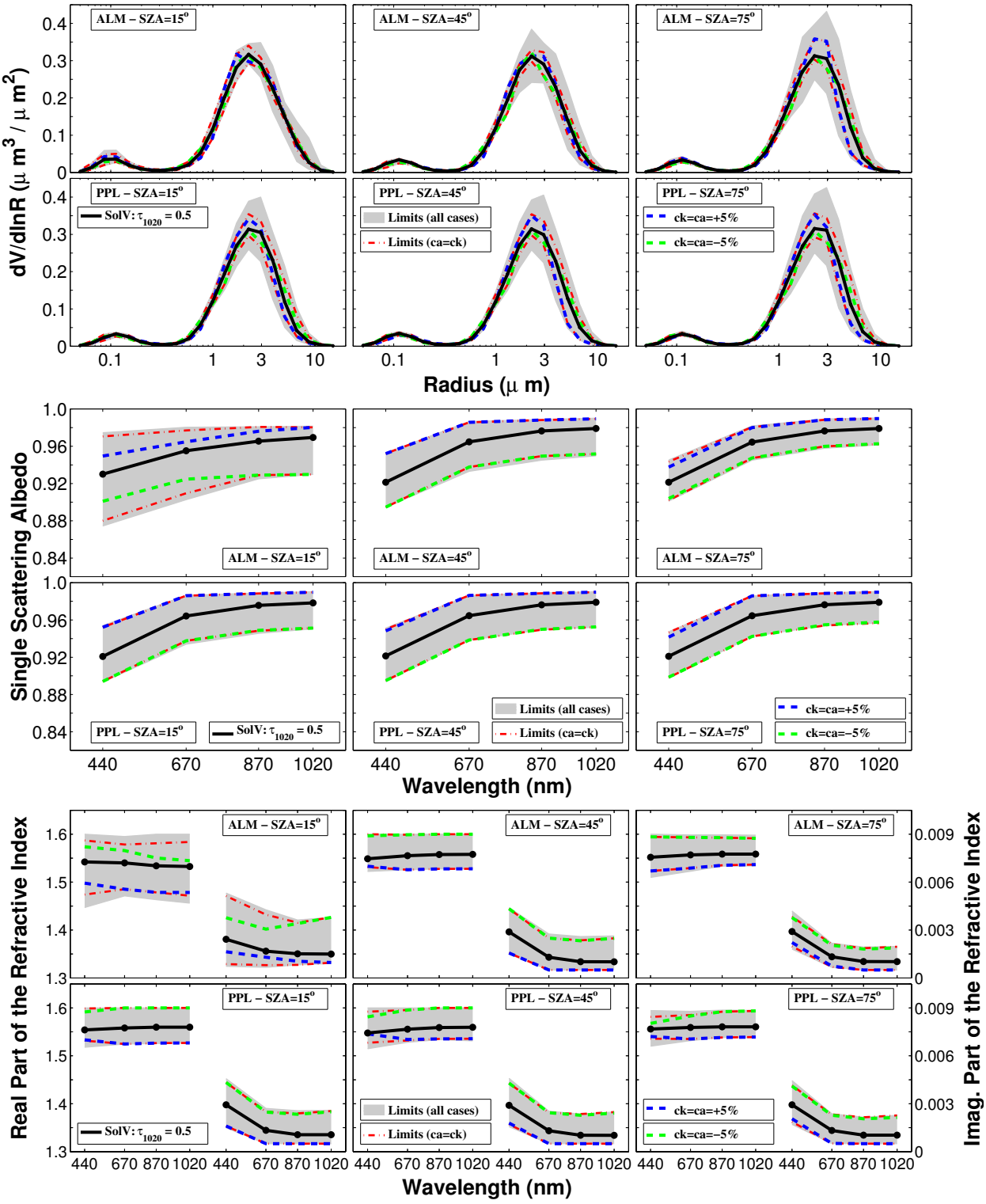

Figure 4.3: Influence of the calibration error on the products (size distribution (top), single scattering albedo (middle) and refractive index (bottom)) retrieved with Dubovik's inversion for Solar Village example with $\tau_{1020} = 0.5$. Black solid line represents the inversion with no calibration error, the gray area contains all the simulations done following the methodology in section 4.2, red dotted lines delimit the area for those case where sky and aureole calibration coefficients are the same for each wavelength, the green dotted line represents the case with an error of -5% in all the calibration coefficients and blue dotted line the case with $+5\%$ error in all the calibration coefficients

Moving on to the analysis of this specific case, the maximum error found in the fine mode of the size distribution goes beyond 100%, for the coarse mode up to 30%. For the optical parameters, the maximum error is around 8% for the single scattering albedo, up to 10% for the real part of the refractive index, and more than 150% for the imaginary part of the refractive index.

Nevertheless, these maximum errors were always found for the case of the almucantar at 15°, except for the coarse mode of the size distribution, as commented. If this case is excluded from the analysis, the errors show a drastic reduction to the levels of 5% for the single scattering albedo, 4% for the real part of the refractive index and around 100% in the imaginary part. Another more restrictive analysis would be to consider only those results fulfilling the level 2.0 criteria in AERONET which would limit our results to the case of almucantar at 75°; for the desert dust, the two examples would be included as their aerosol optical depth at 440 nm is higher than 0.4 (see table 2.1). This restriction would obtain the shortest errors in the optical parameters, for instance, the errors in the single scattering albedo would be reduced to the values of 3%.

However and as previously commented, for the size distribution the best results regarding errors are not retrieved with this restriction: while the fine mode has the same behavior as the optical parameters, and level 2.0 conditions give the lowest errors, the coarse mode shows an opposite trend and the minimum dispersion is found for the almucantar at 15°, rising as the solar zenith angle increases.

Due to its importance, this result should be analyzed in more detail in order to better understand the reasons behind it. Having a second look at the errors obtained for the size distributions in the three almucantar retrievals, one singular aspect is notable. While the gray area in the coarse mode increases with the SZA, the area limited by the red lines is practically constant, or in other words, the error in the coarse mode grows with the SZA because of those cases which have different error in the sky and aureole calibration coefficients for the same wavelength. Two important concepts should be clarified to gain the insight of what is happening. The first one is that the radiance form of short scattering angles contains most of the information of the coarse mode (up to $10-15°$, see case 3 in figure 2.15 and figure 2.18) so differences in the calibration errors between aureole and sky channels produce extra jumps in this part of the radiance and change its form. The second concept is that the switch between measuring with the aureole and the sky channels occurs at 6° in terms of almucantar (azimuth) angle, but in terms of the scattering angle it depends on the SZA. In this way, when $SZA = 15°$ the change aureole-sky takes place at a scattering angle of 1.55°, for $SZA = 45°$ at a scattering angle of 4.24° and for $SZA = 75°$ at a scattering angle of 5.80°. Therefore, the information regarding the coarse mode is divided (more or less) $10\% - 90\%$ between aureole and sky for $SZA = 15°$, while the percentages are $40\% - 60\%$ for $SZA = 75°$. As a consequence, it is not strange that different calibration errors between aureole and sky generate more instabilities for large solar zenith angles.

The results in the principal plane, which show constant errors in the coarse mode regardless of the SZA, support this theory: in this geometry, the scattering angle where the switch between measuring with the aureole and the sky channels is produced does not depend on the SZA, happening always at 6°.

This discussion will be continued in the next section with the oceanic aerosol which is the second case study including the coarse mode.

4.3.2 Oceanic (Lanai)

The second case under analysis is the aerosol of Lanai site with oceanic characteristics. As commented in chapter 2 the examples taken for this aerosol used as a reference the aerosol optical depth at 1020 nm with two possibilities: $\tau_{1020} = 0.05$ and $\tau_{1020} = 0.1$.

In section 2.2.2, the main characteristics of this aerosol were described. As it was commented there, its coarse mode is smaller than for the desert dust ($C_{V_c}/C_{V_f} \sim 2$) but still higher than in the next cases. It is not absorbing with very low values of the imaginary part of the refractive index (see table table 2.2).

In the self-consistency study, the inversion retrievals generated from simulated radiance measurements did not show significant differences with respect to the inputs. The discrepancies for small solar zenith angles were much lower than for the desert dust examples.

In field observations, the main difficulty in the retrieval of the oceanic aerosol properties is the low aerosol optical depth[3]. As the aerosol properties are taken in the examples with the aim of being realistic, neither of the two examples could obtain level 2.0 (as discussed in section 2.2.2).

Getting back to the analysis of the calibration error simulations, figure 4.4 and figure 4.5 illustrate the consequences on the examples $\tau_{1020} = 0.05$ and $\tau_{1020} = 0.1$, respectively using the same scheme described in the desert dust discussion.

The errors in the oceanic aerosol are higher than for desert dust in general terms, as it can be seen in the retrievals. The only exceptional case is the result obtained for the almucantar at $SZA = 15°$. As it was indicated, the errors reported for the imaginary part of the refractive index and for the single scattering albedo in the desert dust were much higher in the almucantar at $SZA = 15°$ than in the other situations. Now in the oceanic aerosol, the almucantar at $SZA = 15°$ presents errors in these two parameters comparable to the other situations (as represented in figure 4.4 and figure 4.5).

Analyzing the values in figure 4.4 which contains the retrievals for the lowest aerosol load, we

[3]Typically below 0.15 at 440 nm, Smirnov et al. (2002b). In the variability study, Dubovik et al. (2002), the average for Lanai was $< \tau_{1020} >= 0.04$ which means $< \tau_{440} > \ 0.13$ approximately.

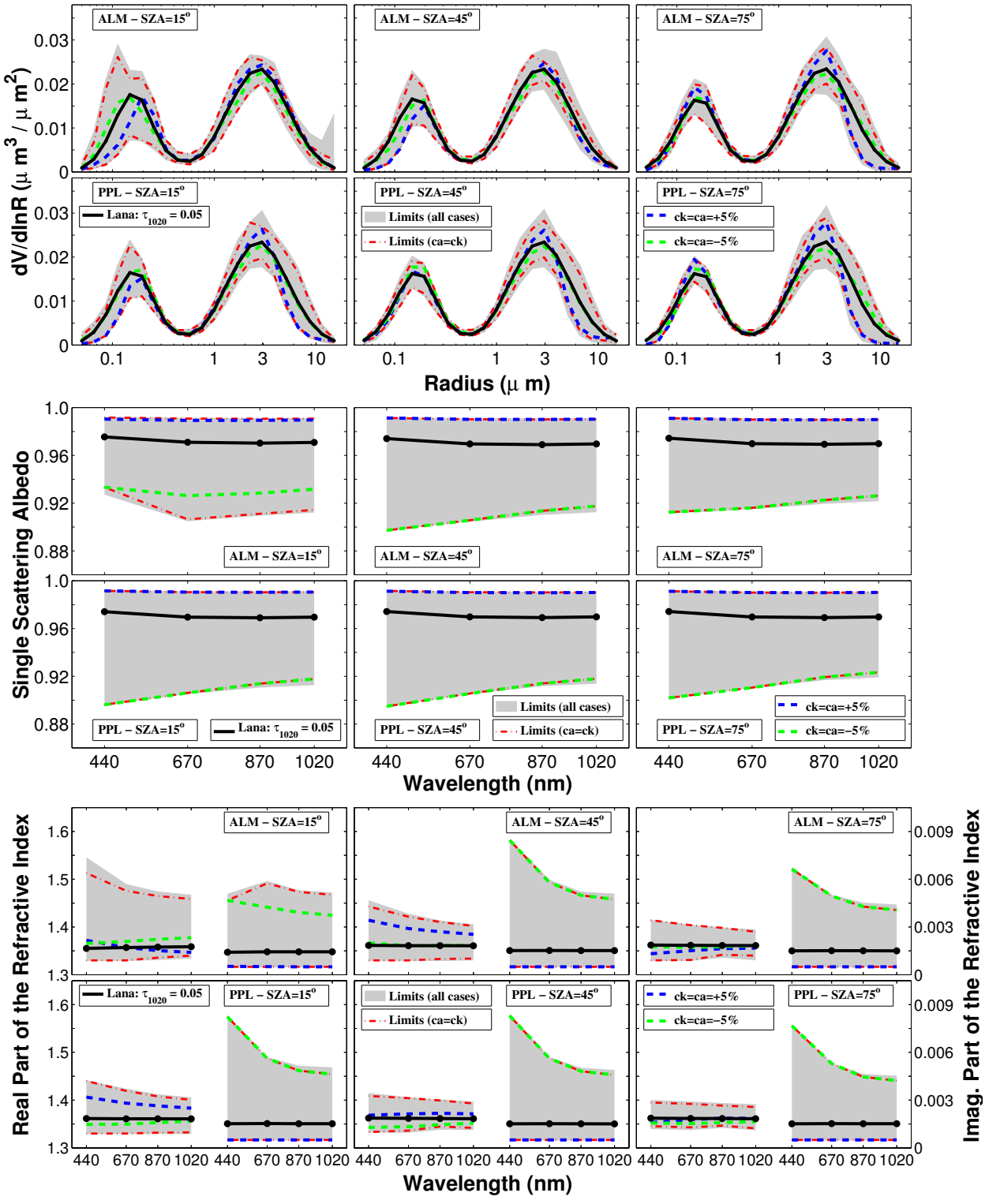

Figure 4.4: Influence of the calibration error on the products (size distribution (top), single scattering albedo (middle) and refractive index (bottom)) retrieved with Dubovik's inversion for Lanai example with $\tau_{1020} = 0.05$. Black solid line represents the inversion with no calibration error, the gray area contains all the simulations done following the methodology in section 4.2, red dotted lines delimit the area for those case where sky and aureole calibration coefficients are the same for each wavelength, the green dotted line represents the case with an error of -5% in all the calibration coefficients and blue dotted line the case with $+5\%$ error in all the calibration coefficients

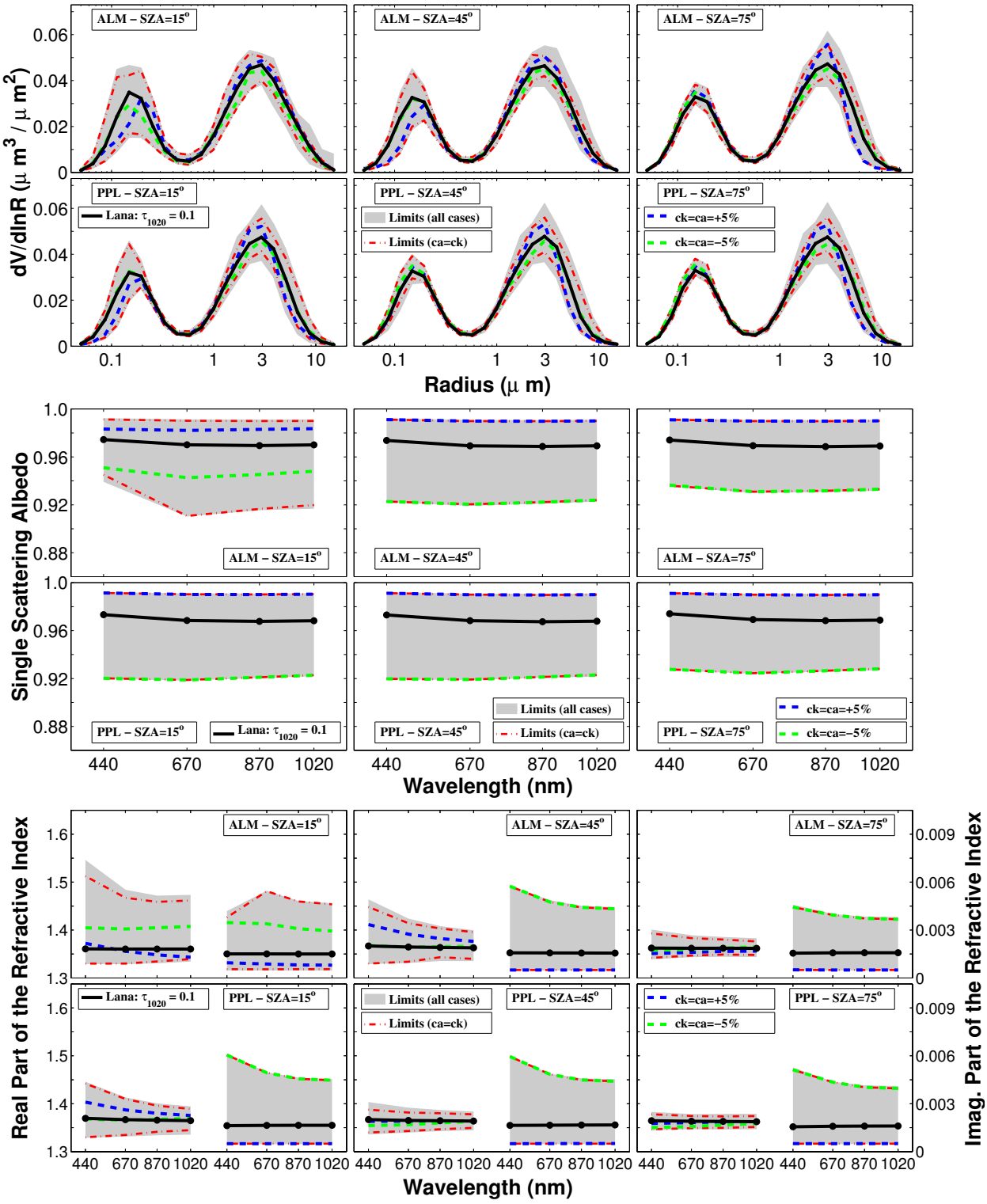

Figure 4.5: Influence of the calibration error on the products (size distribution (top), single scattering albedo (middle) and refractive index (bottom)) retrieved with Dubovik's inversion for Lanai example with $\tau_{1020} = 0.1$. Black solid line represents the inversion with no calibration error, the gray area contains all the simulations done following the methodology in section 4.2, red dotted lines delimit the area for those case where sky and aureole calibration coefficients are the same for each wavelength, the green dotted line represents the case with an error of -5% in all the calibration coefficients and blue dotted line the case with $+5\%$ error in all the calibration coefficients

see that the error in the single scattering albedo goes beyond 7% and in the imaginary part of the refractive index exceeds 400%.The case with the highest aerosol load shows a notable improvement in these two retrievals, as it can be observed in figure 4.5, confirming that the errors decreases with the aerosol load. Thus, the single scattering albedo error is reduced to 5% and the error in the imaginary part of the refractive index to 300%, in this second case.

The error in these parameters show a certain dependence on the wavelength which indicates lower errors for larger wavelengths, especially the imaginary part of the refractive index. Thus, for instance, if the wavelength at 440 nm is not considered, the errors for the imaginary part of the refractive index are 250% for the first example (figure 4.4) and 150% for the second one (figure 4.5). This relation was not so evident in the desert dust even though the error is slightly lower for longer wavelengths as well.

Once again, the maximum errors for the single scattering albedo and for the imaginary refractive index are obtained when all the calibration coefficients have an error of $+5\%$ or -5%. However, this case clearly shows that the maximum errors for the real part of the refractive index do not show this behavior, which is a feature characteristic for all the aerosol types analyzed except the desert dust.

Another property of the real refractive index as opposed to the imaginary refractive index and the single scattering albedo is the strong dependency of the error on the solar zenith angle, or in other words, on the maximum scattering angle in the radiance measurement set. For both aerosol load examples, the error in the real refractive index goes beyond 10% at $SZA = 15^\circ$ in the almucantar while it decreases to 5% at $SZA = 75^\circ$ both in almucantar and principal plane geometry.

The oceanic aerosol is a better study case of the fine mode concentration than the desert dust where the fine mode is scarce. The principal characteristic of its error is that it gets drastically reduced as the solar zenith angle increases. For the first example (Lana1), the error is reduced from the 100% at $SZA = 15^\circ$ to 40% at $SZA = 75^\circ$. For the second one (Lana2) where the errors in the fine mode of the size distribution are lower, the reduction goes from the 60% obtained at $SZA = 15^\circ$ to the 30% at $SZA = 75^\circ$.

On the other hand, the error in the coarse mode has a similar behavior as in the desert dust case: although at a lower rate, the error still grows with solar zenith angle in the almucantar, and remains constant in the principal plane. The area between the two red lines keeps constant and the gray area is the one getting increased with the growth of the solar zenith angle like in the desert dust. The reasons behind this are the same as exposed in the previous aerosol type.

As commented before, none of the retrievals from the two examples selected in the oceanic aerosol could get the level 2.0. The second example with $\tau_{440} = 0.274$ (table 2.2) showed evident

improvement in the results compared to the first example which has $\tau_{440} = 0.137$. This seems to indicate that if the aerosol optical depth grew up to the required 0.4, the errors would decrease. Nevertheless, following the variability study by Dubovik et al. (2002) this increase does not seem very realistic for this aerosol type and it is in consequence not considered here.

4.3.3 Urban (GSFC)

This section deals with the urban aerosol. As commented in chapter 2 and contrary to the two previous cases, its fine mode is more important than the coarse one which is hardly present so the calibration error consequences on a near pure fine mode case can be examined here.

Still, the absorption coefficients are very low like in previous cases. Actually, the urban aerosol found in the Goddard Space Flight Center site was chosen because it has the lowest absorption value from all the examples presented in Dubovik et al. (2002). Nevertheless, high absorption and fine mode predominance will be discussed in the next example of biomass burning.

Two cases were selected taken as a reference the aerosol optical depth at 440 nm: $\tau_{440} = 0.2$ and $\tau_{440} = 0.5$.

The retrievals obtained from the self-consistency study made in subsection 2.2.3.2 for the two selected examples (taking as a reference: $\tau_{440} = 0.2$ and $\tau_{440} = 0.5$) show a general agreement with the inputs except for the instability problems in the refractive index and single scattering albedo calculated from almucantar retrievals with short SZA, as it was the case for the desert dust.

Moving on to the calibration error consequences, which are represented in figure 4.6 and figure 4.7, let us start with the size distribution results where we observed that the absolute error in the coarse mode is very low regardless of the scattering angle due to the scarce number of large particles. On the other hand, in the fine mode, the error strongly depends on the solar zenith angle. Thus, in the first example (figure 4.6) the fine mode has an error of 100% (in volume median radius of the fine mode) at $SZA = 15°$ which is reduced to 50% at $SZA = 75°$. The second example (figure 4.7)which presents lower error rates shows a reduction from 60% at $SZA = 15°$ to only 15% at $SZA = 75°$.

If we limited the analysis to the AERONET level 2.0 criteria then only this last case with the highest aerosol load and the largest solar zenith angle would be included. As we just saw, the errors in this case are very small. This result show that in the case of aerosol with a dominant fine mode the implementation of level 2.0 is very useful for excluding the consequences of the errors originating in the calibration procedure on the retrieved size distribution. This was already expected as, resulting from the analysis of the other two aerosol types, the fine mode was known to have an important error reduction when the aerosol load and the solar zenith angle were large and the "problematic" coarse mode is almost absent in this example.

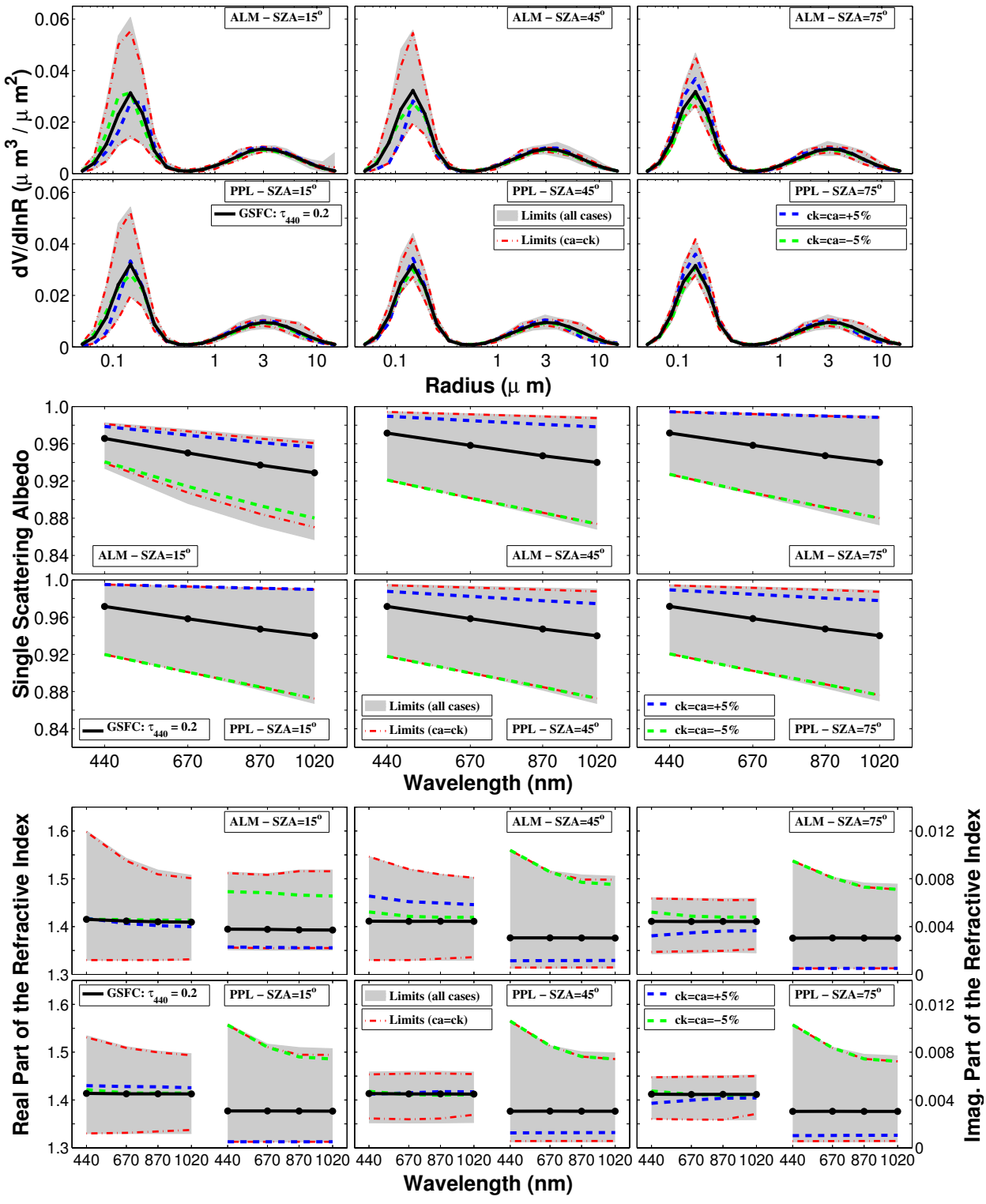

Figure 4.6: Influence of the calibration error on the products (size distribution (top), single scattering albedo (middle) and refractive index (bottom)) retrieved with Dubovik's inversion for GSFC example with $\tau_{440} = 0.2$. Black solid line represents the inversion with no calibration error, the gray area contains all the simulations done following the methodology in section 4.2, red dotted lines delimit the area for those case where sky and aureole calibration coefficients are the same for each wavelength, the green dotted line represents the case with an error of -5% in all the calibration coefficients and blue dotted line the case with $+5\%$ error in all the calibration coefficients

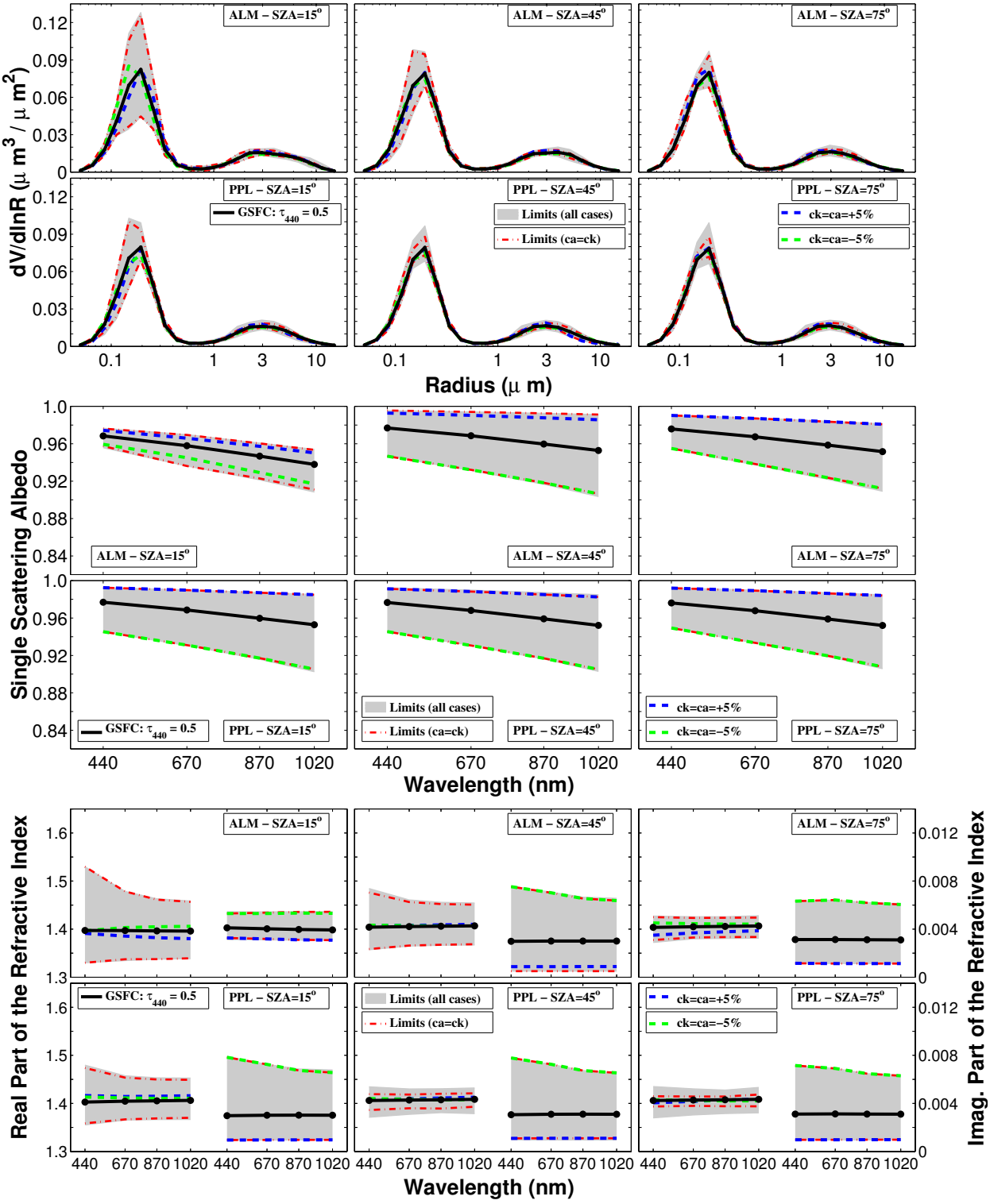

Figure 4.7: Influence of the calibration error on the products (size distribution (top), single scattering albedo (middle) and refractive index (bottom)) retrieved with Dubovik's inversion for GSFC example with $\tau_{440} = 0.5$. Black solid line represents the inversion with no calibration error, the gray area contains all the simulations done following the methodology in section 4.2, red dotted lines delimit the area for those case where sky and aureole calibration coefficients are the same for each wavelength, the green dotted line represents the case with an error of -5% in all the calibration coefficients and blue dotted line the case with $+5\%$ error in all the calibration coefficients

Once again, paying attention to the blue and green lines, the importance of considering all the calibration coefficients independently in order to properly account for the errors is evident. While both lines are quite close to the black line, driving us to the conclusion that the errors are low, a complete analysis represented by the gray area clearly shows that the errors are quite large, specially for short solar zenith angles.

Continuing the study with the optical parameters, the errors in the retrievals are much lower in the second example for the single scattering albedo and for the two refractive indexes. The single scattering albedo shows that the error goes up to 6% in the first example while for the second one it decreases to just 3%. In the imaginary part of the refractive index, the error is 250% in the first example and it is reduced to 100% in the second one.

The error study for the real part of the refractive index also exhibits one peculiarity. Although the other two parameters were constant with the changes in the solar zenith angle, the real part of the refractive index, same as the fine mode in the size distribution, is very sensitive to its variation. So the error reduction is achieved as the aerosol load and the solar zenith angle increase. The case with the highest error is, therefore, the example with lowest aerosol load at 15° in the almucantar, where it reaches 15%. Just by increasing the solar zenith angle, the error already drops to 6% (almucantar at $SZA = 75°$), and considering the highest aerosol load example the error is as low as 3%.

Taking all of this into consideration, we can conclude that the quality assurance procedure (level 2.0 criteria) implemented by AERONET indeed rules out the cases most susceptible to calibration errors in urban aerosol. However, the high value of the relative error of the imaginary part of the refractive index still persists as a problem; nevertheless the values of its magnitude are very low and the biomass burning appears as a good chance to see what happens with this error when the absolute value of absorption rises.

4.3.4 Biomass burning (Mongu)

As in the chapter 2, the biomass burning aerosol is the last case studied. The features selected are the ones given by the climatology study (Dubovik et al. (2002)) in Mongu site. The two examples were obtained using as reference: $\tau_{440} = 0.4$ and $\tau_{440} = 0.8$ in subsection 2.2.4, both passing the aerosol optical depth criteria of AERONET level 2.0.

Its size distribution is dominated by the fine mode, as in the urban aerosol case. The novelty in this case is its large absorption values which are one order of magnitude higher than in the other examples taken (in terms of the imaginary part of the refractive index).

As we noted in the chapter 2, this aerosol type presented visible differences between the original inputs and all the inversion-retrieved parameters from the simulated radiance measurements for

both the almucantar and the principal plane in the self-consistency study (see figure 2.6). The instabilities found in the size distribution, refractive index and size distribution were the largest at short solar zenith angles.

Proceeding with the calibration error study, figures 4.8 and 4.9 show the results obtained for this aerosol. Starting the analysis with the size distribution, we can observe that the blue and green line are very close to the black line with differences always bellow 10%, without any variation regarding the SZA and the measurement geometry used in the simulation. Then, if only the cases with all the calibration errors equal to $\pm 5\%$ had been considered here, the results would have indicated that the size distribution retrieved for the biomass burning aerosol would present a very low influence due to radiance calibration errors.

However, letting the calibration errors have different values the results vary significantly. Thus, for instance, in the almucantar at $SZA = 15^{\circ}$ errors are beyond 100% for the first example (figure 4.8) and around 50% for the second one (figure 4.9) indicating, as in previous examples, the error reduction as the aerosol load increases. We can also observe that the gray area is much smaller for larger SZA: errors are diminished to 20% at $SZA = 75^{\circ}$ for the first example and to 10% in the second one.

As in the GSFC case, the concentration of the coarse mode is so small that the absolute errors are very low and they do not seem to grow with the SZA. Therefore, for the biomass burning, the size distribution is more accurately retrieved with the condition of large SZA regarding calibration errors, supporting once again the conditions established in AERONET criteria level 2.0.

The next step in the analysis is the single scattering albedo retrievals illustrated in figure 4.8 and figure 4.9. In the first example (figure 4.8), the errors are around 3% for all the cases except the almucantar at $SZA = 15^{\circ}$, where they are a bit higher. In the second example (figure 4.9), the errors are only about 2% if again we take out the study for the almucantar at $SZA = 15^{\circ}$. The errors in this parameter are the lowest observed in the radiance calibration error simulations leading us to the conclusion that the higher the absorption is, the lower the errors in the single scattering albedo.

In the study of the imaginary part of the refractive index, the assumption that the higher the absorption the lower the error in the retrieved parameters is even more evident. Thus, in the first example (figure 4.8), the error in this parameter is just 50% excluding the almucantar at $SZA = 15^{\circ}$ where it is around 70%. In the second example (figure 4.9), the errors are even smaller with values of 50% for the almucantar at $SZA = 15^{\circ}$ and 40% for the rest of the cases. Compared to the other aerosol types, the relative errors in this parameter show the smallest values here for the biomass burning. Even though the value in the imaginary part of the refractive index is one order of magnitude larger than in the other cases, the absolute error generated by the calibration error does not increase proportionally.

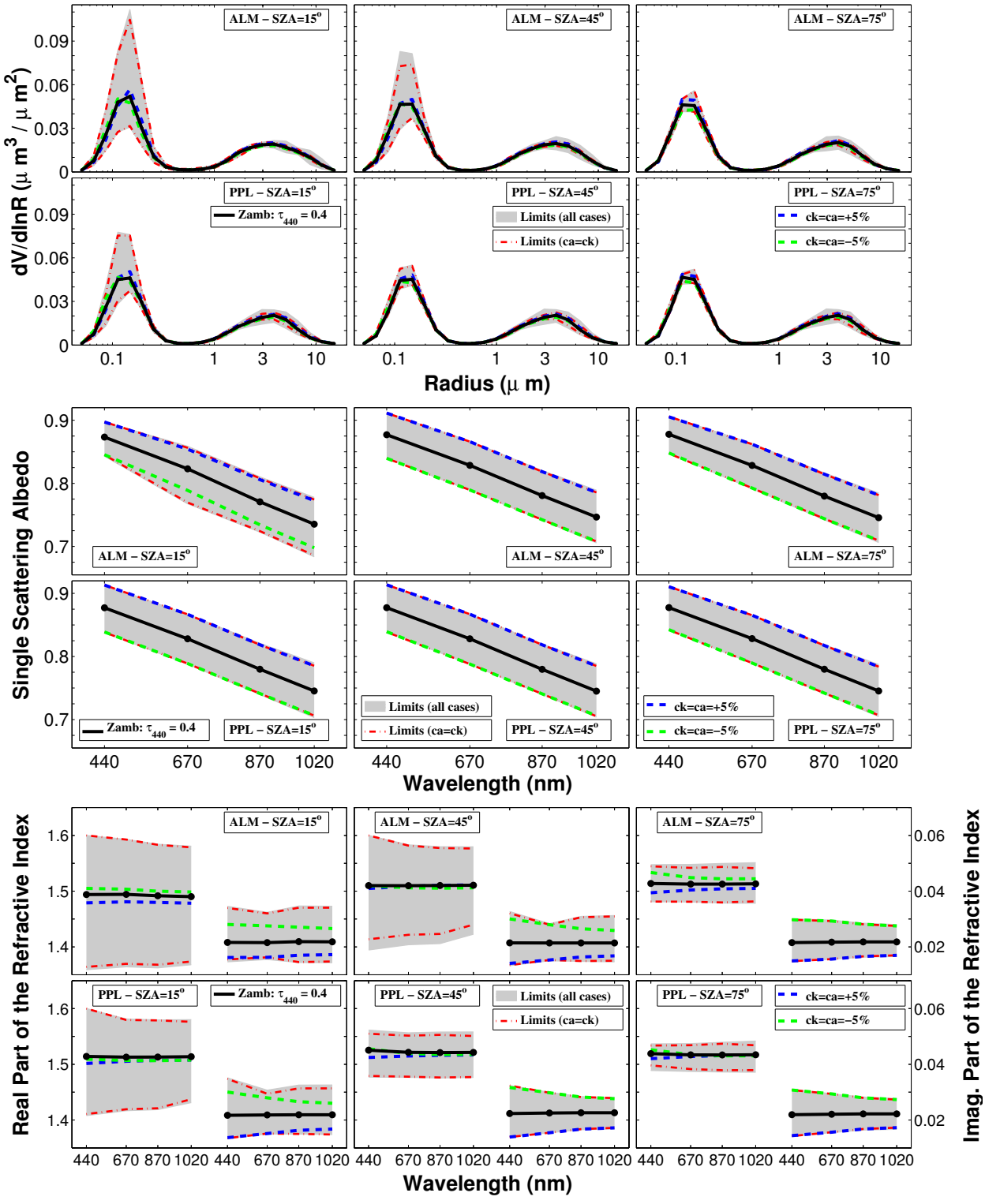

Figure 4.8: Influence of the calibration error on the products (size distribution (top), single scattering albedo (middle) and refractive index (bottom)) retrieved with Dubovik's inversion for Mongu example with $\tau_{440} = 0.4$. Black solid line represents the inversion with no calibration error, the gray area contains all the simulations done following the methodology in section 4.2, red dotted lines delimit the area for those case where sky and aureole calibration coefficients are the same for each wavelength, the green dotted line represents the case with an error of -5% in all the calibration coefficients and blue dotted line the case with $+5\%$ error in all the calibration coefficients

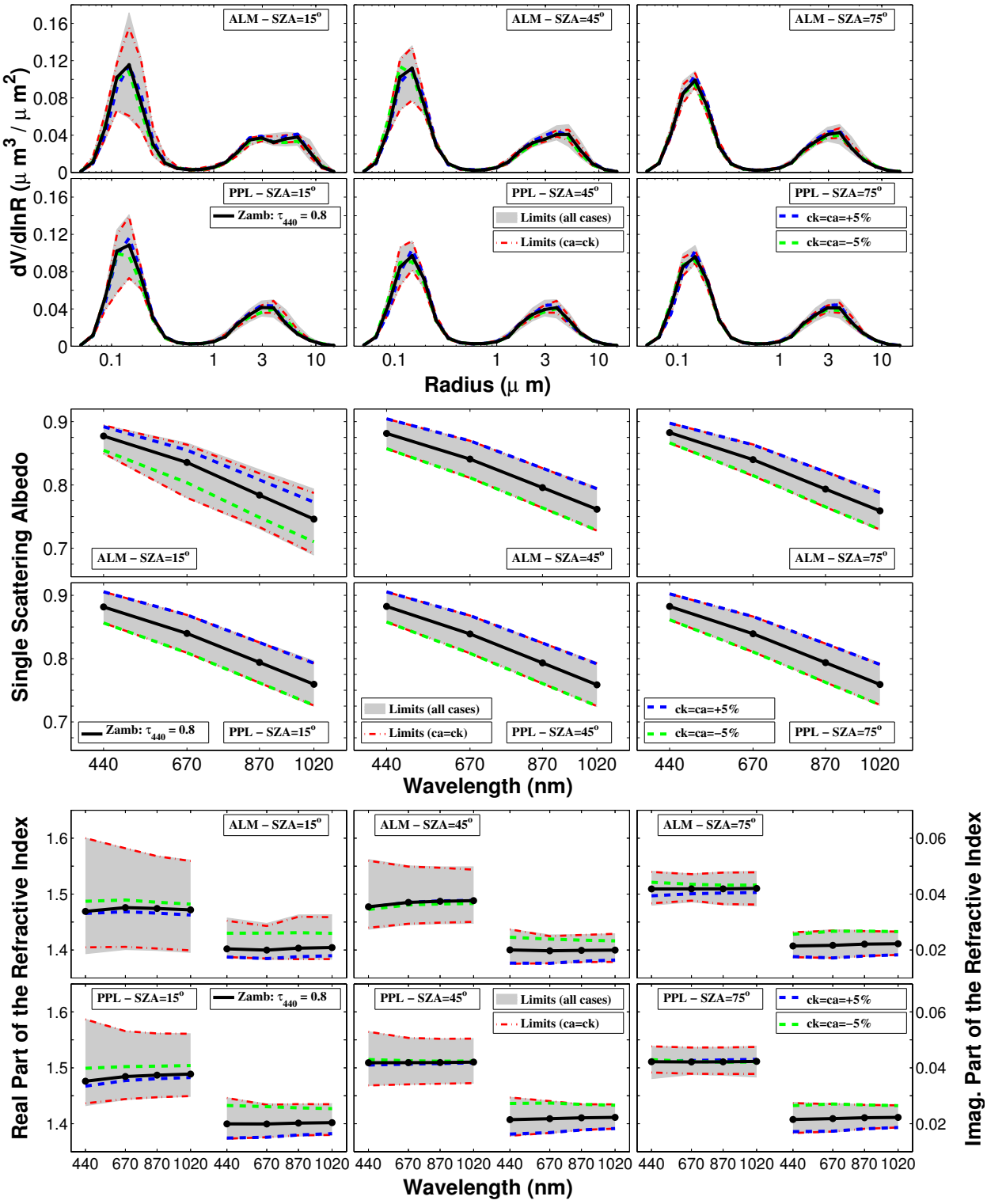

Figure 4.9: Influence of the calibration error on the products (size distribution (top), single scattering albedo (middle) and refractive index (bottom)) retrieved with Dubovik's inversion for Mongu example with $\tau_{440} = 0.8$. Black solid line represents the inversion with no calibration error, the gray area contains all the simulations done following the methodology in section 4.2, red dotted lines delimit the area for those case where sky and aureole calibration coefficients are the same for each wavelength, the green dotted line represents the case with an error of -5% in all the calibration coefficients and blue dotted line the case with $+5\%$ error in all the calibration coefficients

The real part of the refractive index shows a similar behavior as in GSFC case with a strong reduction for larger solar zenith angles. Thus for the almucantar case at 15°, the differences with the retrieved value for the non-calibration error cases[4] are around 10% for both examples selected in the biomass burning aerosol (Figures 4.8 and 4.9). When the solar zenith angle grows to 75°, the differences diminish to 4% in the case with the lowest aerosol load (figure 4.8) and to 3% in the case with the highest aerosol load (figure 4.9).

[4]We emphasize here that the values are compare with the results for the non-calibration error retrievals because as commented, the self-consistency study gave high differences between the inputs and the values retrieved.

Chapter 5

Error influence on the inversion of sky radiances II: Pointing error

Every man's life ends the same way. It is only the details of how he lived and how he died that distinguish one man from another.

Ernest Hemingway

Resumen en español del capítulo:

En el capítulo 5 se muestran los resultados obtenidos simulando los errores de apuntamiento. En este caso, el estudio se divide en dos partes: una primera analiza la influencia de los errores de apuntamiento en las medidas de radiancia. En una segunda parte, se estudia cómo estos errores afectan a los resultados de la inversión.

Siguiéndo el estudio de los errores de apuntamiento en los fotómetros de campo desarrollado en el capítulo 3, se han simulado medidas introduciendo errores de $0{,}2^\circ$ (observado en los test) y $0{,}4^\circ$ (considerado como máximo posible ya que está al límite de no ser observado por las medidas de irradiancia Solar directa para los actuales fotómetros) para las dos componentes en las que se divide el error de apuntamiento: $\Theta_{\xi_\varphi} = \xi_\varphi \sin(\theta_s)$ (horizontal) y $\Theta_{\xi_\theta} = \xi_\theta$ (vertical). También se ha incluido el caso de error de apuntamiento de 1°, ya que este fue considerado en el trabajo Dubovik et al. (2000), aunque este valor no representa un caso realista.

La consideración que se hace en este trabajo acerca de que el almucantar está formado por dos ramas (izquierda y derecha) y que los datos de radiancia deben ser promediados para obtener el valor introducido en el procedimiento de inversión representa una sustancial mejora respecto al análisis en Dubovik et al. (2000). Esto hecho tiene una especial trascendencia, ya que de esta forma el almucantar no se ve casi afectado por los errores de apuntamiento.

Ciñéndonos a los resultados de casos realistas (errores de apuntamiento por debajo de $0{,}4^\circ$). El caso más relevante es el error vertical en el plano principal. El error de apuntamiento afecta de forma diferente al almucantar y al plano principal, lo cual puede explicar que haya diferencias entre los productos derivados. Este error cambia la forma de la radiancia observada en función del ángulo de scattering y podría, junto con el efecto de reducción de información a bajo SZA, producir artificios en los resultados de la inversión.

5.1 Introduction

This chapter has been designed to analyze the importance of the correct pointing in the acquisition of the sky radiance measurements.

Similarly as in the previous chapter, using the properties of the aerosol examples described in chapter 2 principal plane and almucantar measurements are simulated with and without pointing errors. Afterwards, these simulated radiances are inverted.

The pointing error, as shown in section 3.3, can be split in vertical and horizontal error. Even though both components of the error are manifested together, in this study, they will be considered separately in order to obtain more specific information from the two different effects.

Apart from the comparison of the inversion retrievals, this chapter also brings the comparison of the simulated radiances with and without pointing errors (contrary to the situation in the previous chapter) because there is no simple relation between pointing error and the radiance differences. As we will show, these difference depend on the scattering angle, the solar zenith angle and the geometry

5.2 Methodology used to analyze the pointing error influence

Figure 5.1 shows the work-flow of the study, where in a first step, the simulated radiance with and without error are compared, followed by a second comparison, of the products retrieved by Dubovik's inversion from both simulations. As seen from the scheme, the vertical errors considered are positive or negative while horizontal errors are only positive.

The vertical error is made departing from the Sun towards the zenith or towards the Earth surface, which results with different consequences in almucantar and principal plane measurements, and therefore, both possibilities should be considered. The sign of the error was established as positive in the case of variation towards the zenith, and negative in the case of variation towards the Earth surface. In the principal plane, the vertical error is transmitted directly to the scattering angle with the relation of $1:1$, while in the almucantar, the consequence on the scattering angle is lower and depends on the SZA. The exact value of this relation can be obtained according to the expression in Eq. (3.3).

The horizontal error is either to the left or the right of the Sun. In the principal plane, regardless of the direction of the error the consequences are symmetric. In the almucantar, the errors are initially not symmetric but due to the calculation process followed in AERONET which averages the left and the right branches of the almucantar, they become symmetric. As a consequence, for both geometries, there is no need to consider the sign of the horizontal error and only the

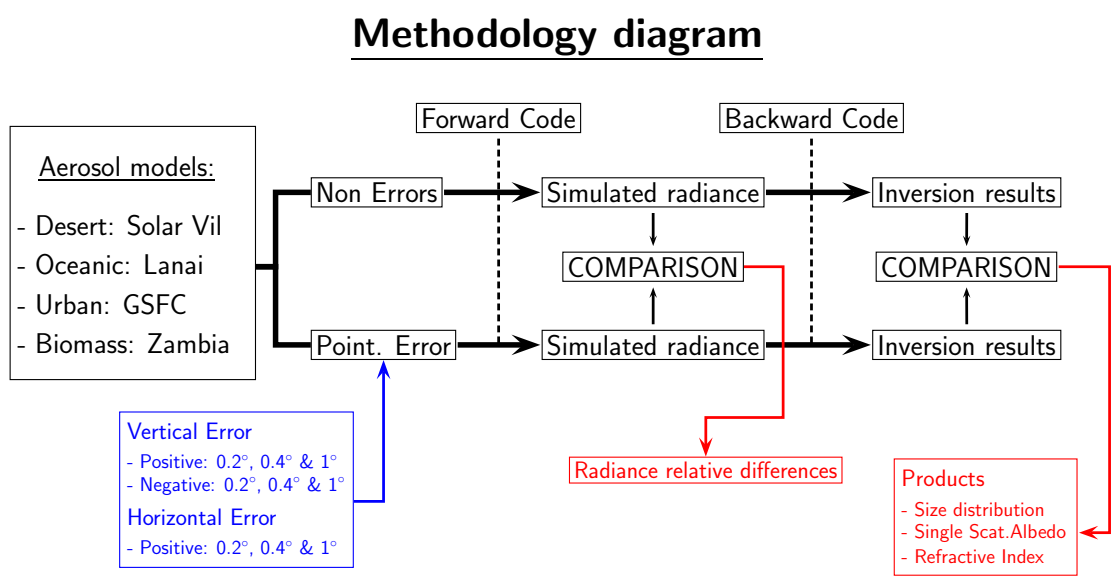

Figure 5.1: Methodology diagram followed to carry out the simulations in order to check the effects of the pointing error on Dubovik's inversion

absolute value is relevant. Similarly to the case of the vertical error and principal plane geometry, the horizontal error should be transmitted directly on the scattering angle in the almucantar but due to the averaging process, the effect is weaker and not straightforward. This effect was already commented in subsection 3.5.4. In the principal plane, the consequences of the horizontal error on the scattering angle are calculated following Eq. (3.3) (with $\Theta_{\xi_\varphi} = \sin\theta_s \xi_\varphi$).

The values of the pointing errors introduced in the simulations are 0.2°, 0.4° and 1°. The first two errors are possible in the actual field photometers: the value of 0.2° was obtained for both components of the error in photometer 143# and the value of 0.4° is admitted as realistic because due to the value of the field of view (around 1.2° in new photometers) the measurements of the aerosol optical depth would not be affected by this error and therefore not noticeable during the standard operation of the CIMEL-318 sun-photometer in AERONET network.

The last error considered (1°) would be visible, if happening in the actual photometers, while analyzing the aerosol optical depth measurements. However, in the case of the old photometers, it would be in the limit of the detectability. Therefore, here it is taken into account as it is an extreme case (for old photometers) and as an extension of the study described in Dubovik et al. (2000) (dealing with the accuracy of Dubovik's inversion), as the analysis of pointing error in the fore-mentioned work did not include principal plane simulations and the average of the two almucantar branches neither.

As in the previous chapter, the study is done with the same 80 reference cases obtained as the combination of the 8 aerosol examples described in chapter 2, the 5 different solar zenith angles (15°, 30°, 45°, 60° and 75°) and the two geometries used to measure the sky radiance (almucantar and

principal plane). This makes a total number of 800 simulations: the 80 reference cases combined with the 10 pointing errors considered (non error plus six vertical and three horizontal error cases).

Similarly to the case of the radiance calibration errors, the aerosol optical depth values used in all the simulations will be the ones of the non-error set as this magnitude is considered to be not affected by the pointing errors.

5.3 Pointing error consequences on radiance measurements

Even though the analysis of the pointing error on the inversion results will be done by aerosol type as the one of the calibration error, the consequences on the radiance measurements will be done considering the possible combinations given by the two geometries and the two components of the error, vertical and horizontal. Thus, the four possible scenarios are principal plane with vertical error, almucantar with vertical error, principal plane with horizontal error and almucantar with horizontal error.

5.3.1 Principal plane with vertical pointing error

In the same way than in section 3.5, the relative difference study will start with those obtained from principal plane measurements with vertical pointing errors. In that subsection, the relative difference in principal plane due to a vertical pointing error was approximated as (Eq. (3.14)):

$$\epsilon_R = \left\| \frac{\partial R(\theta,\varphi)}{\partial \theta} \right\|_{\substack{\theta=\theta_p \\ \varphi=0}} \frac{\xi_\theta}{R(\theta_p,0)} \tag{5.1}$$

The considered values for the pointing errors have been $\xi_\theta = \pm 0.2^\circ, \pm 0.4^\circ$ and $\pm 1^\circ$ Even though we remarked that the approximation in Eq. (5.1) is not always valid, all the cases under study for the different aerosol types and pointing vertical errors are perfectly represented by this equation. In other words, relative differences in radiance are linearly dependent on the vertical pointing error for the principal plane case. Therefore, the six studies corresponding to the six pointing errors considered can be summarized in only one plot representing the variation rate in relative differences. The presented plots are calculated for the 0.2° case, and then converted to differences per degree of pointing error. From figure 5.2 to figure 5.5, radiance relative errors (per degree) caused by a vertical pointing error are represented for the 4 different studied aerosol types. Every figure is subdivided in three parts with different values of SZA ($SZA = 15^\circ, 45^\circ$ and 75°). We will skip here the representation of the SZA=30° and SZA=60° cases for simplicity.

Among all the investigated cases, the largest relative differences in radiance were found for vertical pointing errors in principal plane measurements, since pointing errors in this case directly

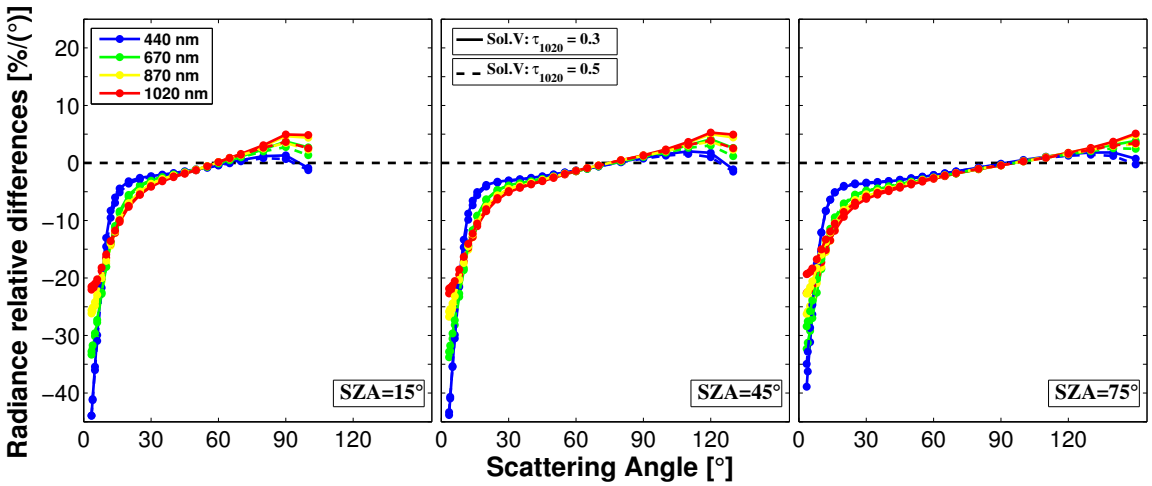

Figure 5.2: Radiance relative error (per degree) caused by a vertical pointing error in principal plane simulated measurements. Solar Village aerosol climatic model was taken for the tests using two different AOD: $\tau_{1020} = 0.3$ (solid line) and $\tau_{1020} = 0.5$ (dashed line). From left to right, SZA increases for the different figures.

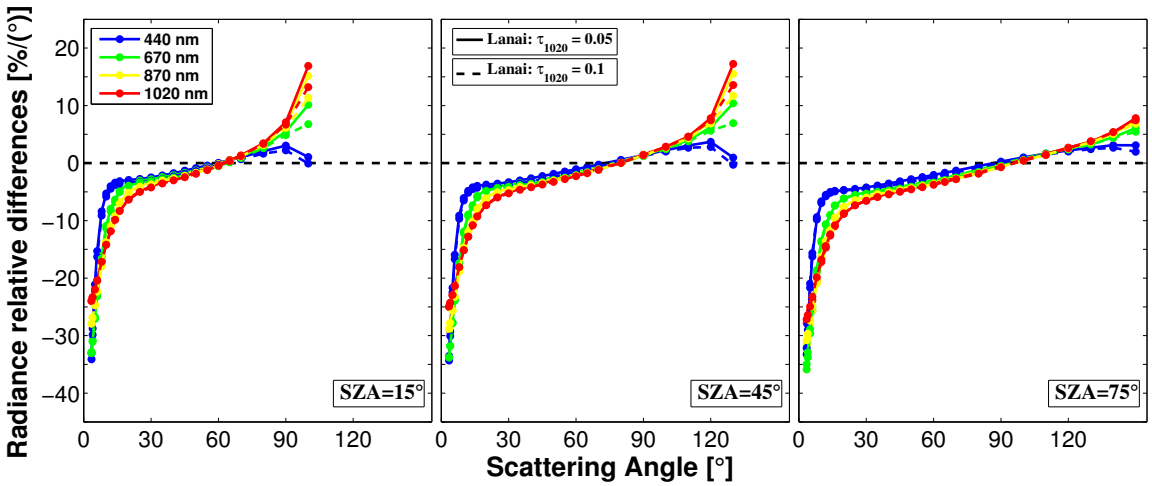

Figure 5.3: Radiance relative error (per degree) caused by a vertical pointing error in principal plane simulated measurements. Lanai aerosol climatic model was taken for the tests using two different AOD: $\tau_{1020} = 0.05$ (solid line) and $\tau_{1020} = 0.1$ (dashed line). From left to right, SZA increases for the different figures.

transfer the error to the observed scattering angle.

The positive sign in vertical error was established for variation toward the zenith in the pointing process (see subsection 5.2), i.e. for a regular observation in the principal plane it will always mean to be further from the Sun. Therefore, radiance relative differences are expected to be negative for short scattering angles.

Analyzing the figures 5.2, 5.3, 5.4 and 5.5, the maximum value in the radiance relative difference per degree of pointing error was found in the case of desert dust aerosol (Solar Village site), reaching values over 40% for 440 nm at short scattering angles (as expected). The rest of the cases also present large values for short scattering angles, exceeding always 30% at the maximum values (2° scattering angle). For the oceanic aerosol (Lanai site), the maximum differences are obtained at

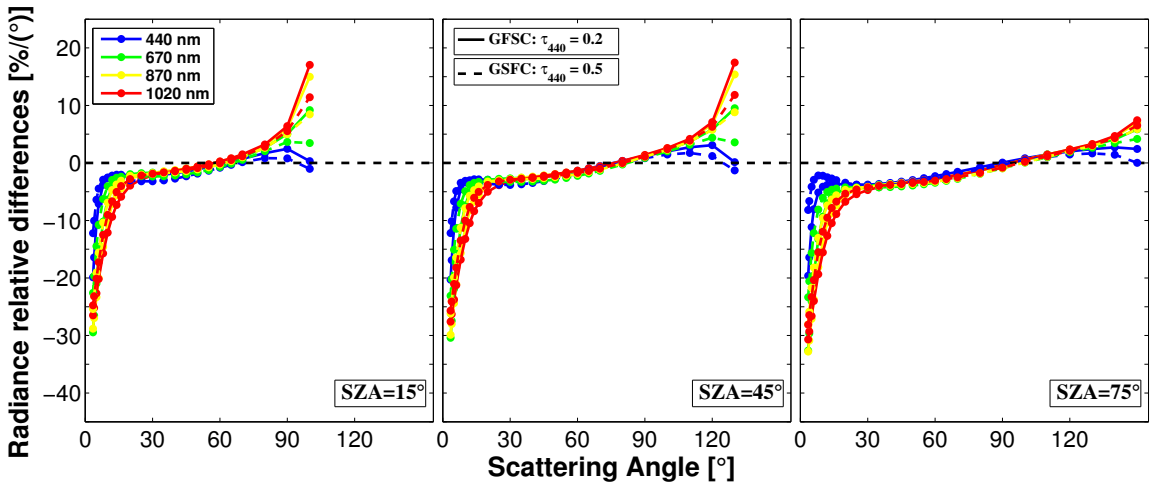

Figure 5.4: Radiance relative error (per degree) caused by a vertical pointing error in principal plane simulated measurements. GSFC aerosol climatic model was taken for the tests using two different AOD: $\tau_{440} = 0.2$ (solid line) and $\tau_{440} = 0.5$ (dashed line). From left to right, SZA increases for the different figures.

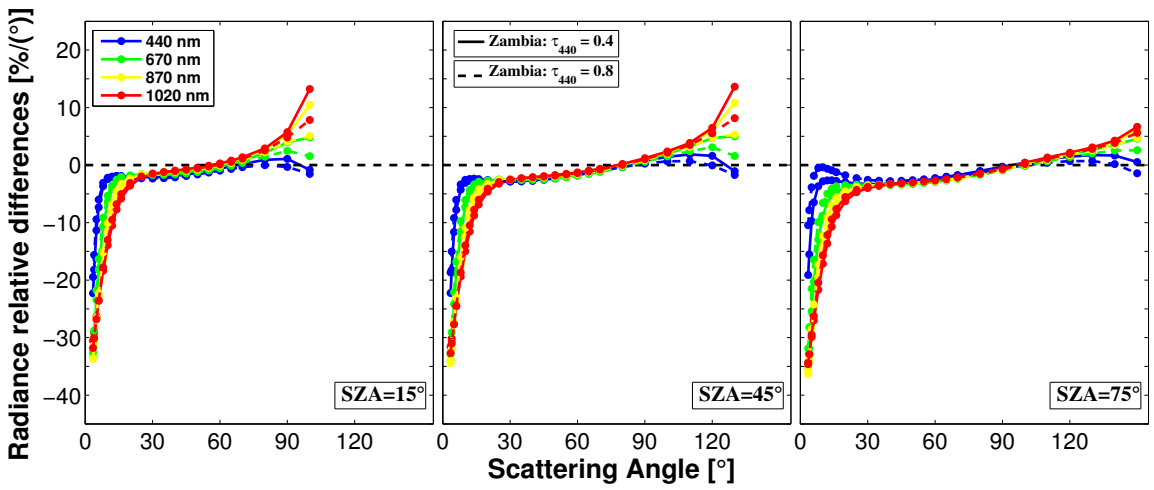

Figure 5.5: Radiance relative error (per degree) caused by a vertical pointing error in principal plane simulated measurements. Mongu aerosol climatic model was taken for the tests using two different AOD: $\tau_{440} = 0.4$ (solid line) and $\tau_{440} = 0.8$ (dashed line). From left to right, SZA increases for the different figures.

440 nm wavelength too, though the 670 nm channel presents strong differences as well. On the other hand, urban (GSFC site) and biomass burning aerosols (Mongu site) reach the maximum errors at longer wavelengths (870 nm and 1020 nm). As the scattering angle grows relative differences get suddenly reduced for all aerosol types. After this strong reduction, there is a transition zone where the differences are small, but still tending to zero until they become positive. The scattering angle where the difference are zero depends more on the SZA than on the aerosol type. The angle is about $60° - 70°$ for $SZA = 15°$, around $80° - 90°$ for $SZA = 45°$ and over $100°$ for $SZA = 75°$.

Remembering now the figure 2.8 where the radiance from the principal plane were represented, it can be observed that the angles presenting a minimum in radiance are the ones showing zero differences in figures 5.2, 5.3, 5.4 and 5.5.

Then, in the positive differences zone, there are different behaviors for different aerosol types and SZA. In this way, high errors about 15% are reached for oceanic and urban aerosols at 1020 nm with $SZA = 15°, 45°$. High errors are also obtained for biomass burning aerosol while differences remain below 5% for desert dust aerosol. This fact is related to the shape of the aerosol phase function at large scattering angles, which clearly differs from spherical (marine, smoke) and non-spherical (dust) aerosol particles.

Finally, following equation 5.1, if the errors were negative the sign of the differences would be opposite: very high positive errors for short scattering angles, going to a transition zone afterwards, ending up in negative values for large scattering angles (plots not shown).

5.3.2 Almucantar with vertical pointing error

Continuing the description of vertical errors, in this subsection the effects over almucantar measurements are analyzed. Back again to section 3.5, the radiance relative error for this particular case can be approximated by Eq. (3.22) as:

$$\epsilon_R = \left\| \frac{\partial R(\theta,\varphi)}{\partial \theta} \right\|_{\substack{\theta=\theta_S \\ \varphi=\varphi_a}} \frac{\xi_\theta}{R(\theta_S,\varphi_a)} \tag{5.2}$$

However, the approximation presents a difficulty in this second case. Basically, radiance relative differences have different behavior for positive and negative pointing errors when the scattering angles are short. As we commented in section 3.5, for short scattering angles, almucantar's angle are a maximum in the radiance function for a vertical displacement, and that is why Eq. (5.2) is not anymore valid; since $R(\theta,\varphi_a)$ is a maximum in a vertical range, $\left\| \frac{\partial R(\theta,\varphi)}{\partial \theta} \right\|_{\substack{\theta=\theta_S \\ \varphi=\varphi_a}}$ is equal to zero and the second derivative term cannot be neglected. Nevertheless, once the sign of the error is set, the relative difference plot calculated for 0.2° of pointing error (and used to estimate the error per degree, as it was done in the previous section) was observed to be a good representation of the other two errors (0.4° and 1°). Thus, this pseudo-linear dependency of radiance relative differences for positive vertical errors ($\xi_\theta = 0.2°, 0.4°$ and 1°), and separately, for negative vertical errors ($\xi_\theta = -0.2°, -0.4°$ and $-1°$) will let us reduce the number of figures.

Relative radiance errors (per degree) caused by a vertical pointing error are represented for the different aerosol models from figure 5.6 to figure 5.9. There are two representations for each aerosol type: one respect to positive vertical error and the other one respect to negative vertical error. It is easy to see that both representations are not symmetrical for short scattering angles, due to the influence of the second derivative term; however, as the scattering angle grows ($> 10°$ aprox.) the symmetry is recovered in both representations for every aerosol type, obviously when the first derivative term recuperates its importance against the second derivative term.

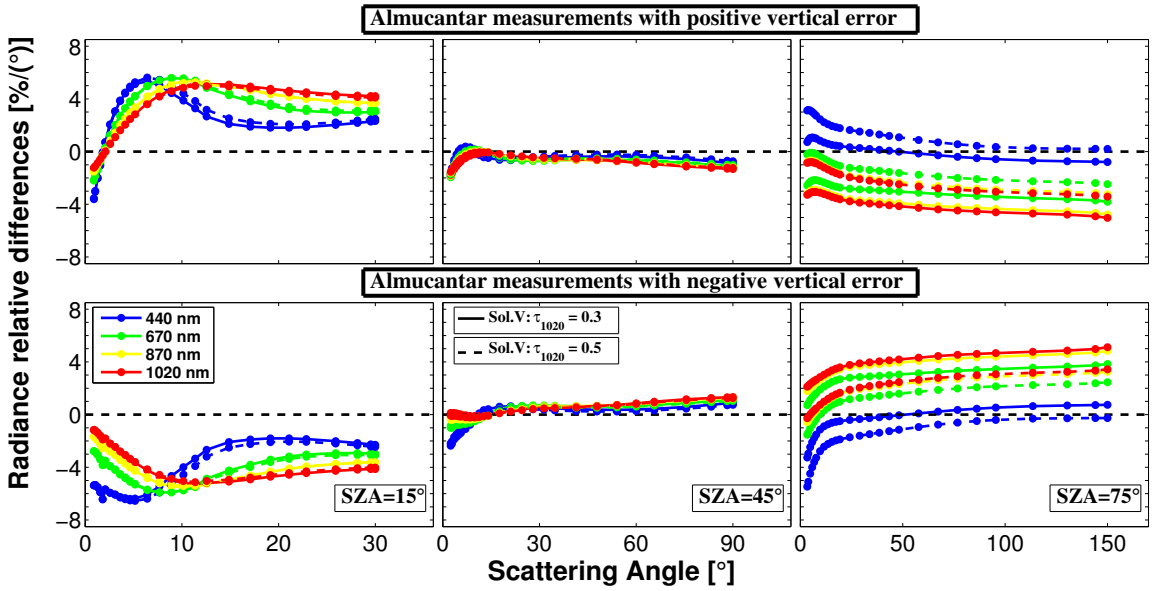

Figure 5.6: Radiance relative error (per degree) caused by a vertical pointing error in almucantar simulated measurements. Solar Village (desert dust) aerosol was taken for the tests using two different AOD: $\tau_{1020} = 0.3$ (solid line) and $\tau_{1020} = 0.5$ (dashed line). From left to right, SZA increases for the different figures (note the different range in scattering angle as SZA increases). In the upper part, the radiance error is represented for positive pointing error whereas the pointing error is negative in the bottom part.

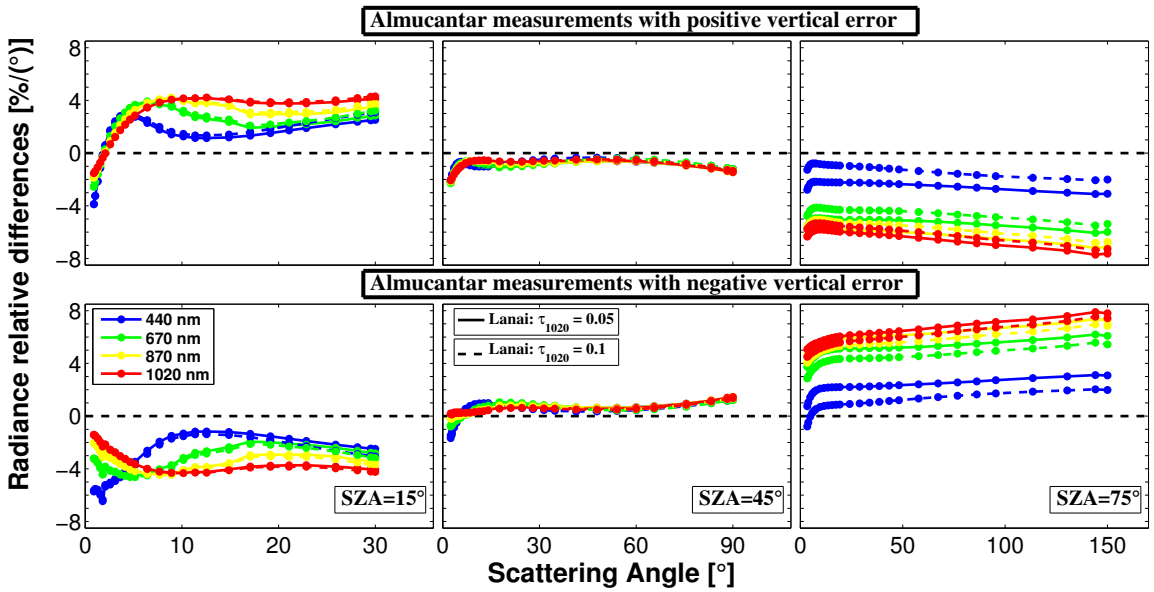

Figure 5.7: Radiance relative error (per degree) caused by a vertical pointing error in almucantar simulated measurements. Lanai (oceanic) aerosol was taken for the tests using two different AOD: $\tau_{1020} = 0.05$ (solid line) and $\tau_{1020} = 0.1$ (dashed line). From left to right, SZA increases for the different figures (note the different range in scattering angle as SZA increases). In the upper part, the radiance error is represented for positive pointing error whereas the pointing error is negative in the bottom part.

In opposition to the previous case (vertical errors in principal plane), differences depend strongly on the SZA. For example, at $SZA = 45°$, differences can be almost neglected for all aerosol types. At $SZA = 15°$, differences for short scattering angles are also small and negative for both positive and negative vertical errors (non-symmetry), and then differences grow towards positive values for

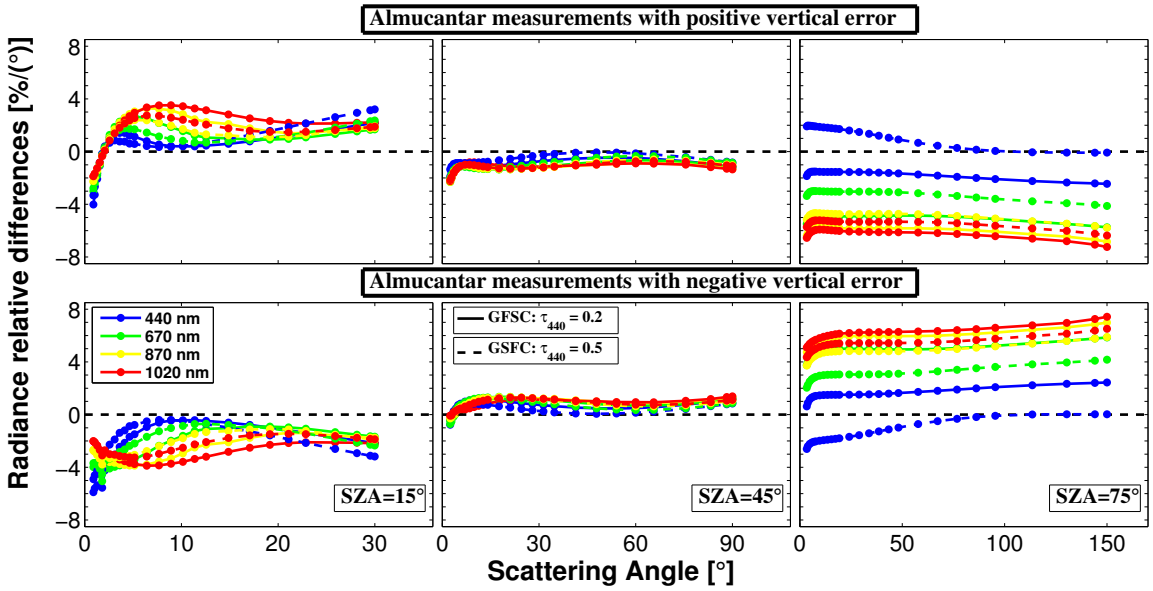

Figure 5.8: Radiance relative error (per degree) caused by a vertical pointing error in almucantar simulated measurements. GSFC (urban) aerosol was taken for the tests using two different AOD: $\tau_{440} = 0.2$ (solid line) and $\tau_{440} = 0.5$ (dashed line). From left to right, SZA increases for the different figures (note the different range in scattering angle as SZA increases). In the upper part, the radiance error is represented for positive pointing error whereas the pointing error is negative in the bottom part.

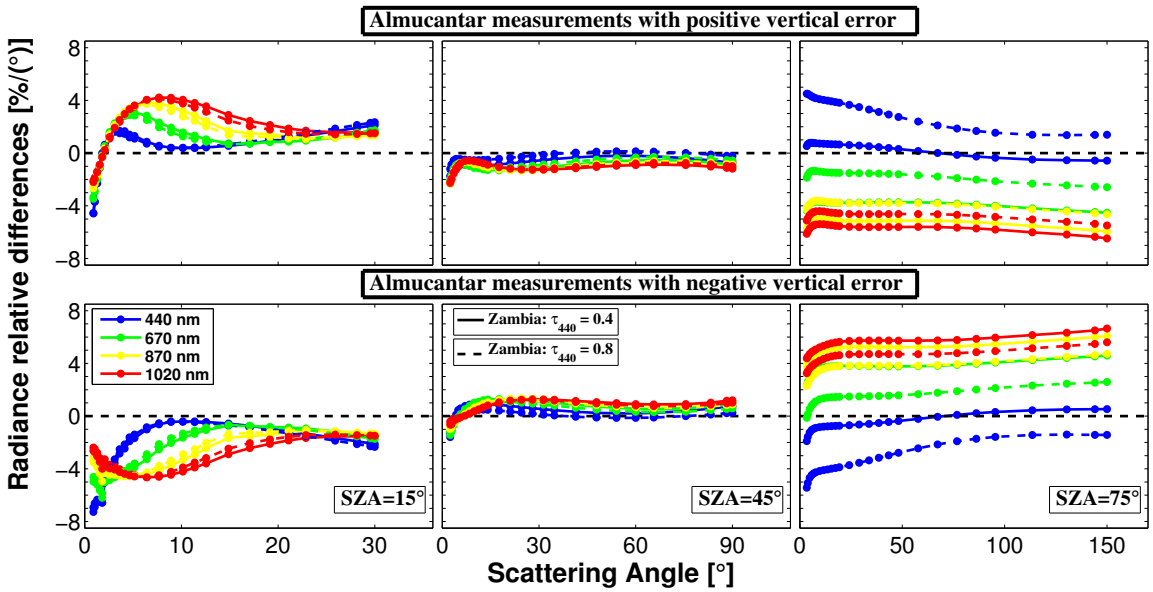

Figure 5.9: Radiance relative error (per degree) caused by a vertical pointing error in almucantar simulated measurements. Mongu (biomass burning) aerosol was taken for the tests using two different AOD: $\tau_{440} = 0.4$ (solid line) and $\tau_{440} = 0.8$ (dashed line). From left to right, SZA increases for the different figures (note the different range in scattering angle as SZA increases). In the upper part, the radiance error is represented for positive pointing error whereas the pointing error is negative in the bottom part.

positive pointing errors while keeping negative values for negative pointing errors. The observed differences are more important for desert dust (Solar Village) than for the other cases, reaching values of about $7 - 8\%$ at maximum. Nonetheless, looking at $SZA = 75°$, differences are more significant for oceanic (Lanai), urban (GSFC) and biomass burning (Mongu) than for desert dust;

also, for this case ($SZA = 75°$), differences are strongly wavelength dependent and the highest differences are reached for 1020 nm whereas differences at 440 nm are almost zero. To end up, it should be noticed that for large scattering angles differences have opposite sign with respect to the case with $SZA = 15°$: Negative differences are obtained for positive vertical pointing errors whilst positive differences are obtained for negative pointing errors.

5.3.3 Horizontal pointing error for almucantar and principal plane

Last subsection about radiance errors summarizes horizontal errors for both almucantar and principal plane. The main reason to put them together is that the differences obtained are quite small compared to the previous cases. On the other hand, as commented in section 5.2, both present the feature of being independent from the error sign.

In the same way that vertical errors have a large influence on principal plane measurements, significant differences could be expected for horizontal pointing error in almucantar measurements. But as we already described, the almucantar measurement is the average of the two branches (right and left from the sun). This makes horizontal errors and the related effect on the radiance to be related with the second derivative term of the radiance function instead of the first one, as it was commented in section 3.5:

$$\epsilon_R = \left\| \frac{\partial^2 R(\theta,\varphi)}{\partial \varphi^2} \right\|_{\substack{\theta=\theta_S \\ \varphi=\varphi_a}} \frac{\xi_\varphi^2}{2R(\theta_S,\varphi_a)} \tag{5.3}$$

Errors are drastically reduced with this simple strategy and differences in radiance are only noticeable for short scattering angles, as it can be seen from figure 5.10 to figure 5.13, where in the upper panels of the figures, relative radiance errors in almucantar measurements (per degree) caused by horizontal pointing error are represented for the selected aerosol types. For $SZA = 45°$ and $SZA = 75°$, relative errors are always positive with the largest values under 3%. Errors have more relevance only in the case of $SZA = 15°$. For all the aerosol types, relative differences at $SZA = 15°$ follow the same pattern: small and negative differences for short scattering angles up to 3°. Afterwards, they rapidly grow toward positive values reaching their maxima at 5°; the value of the maximum is larger for biomass burning aerosol 9% (440 nm) than for the rest of the cases ($6-7\%$). After the maxima, values decrease fast towards 0, being already all the values under 1% for scattering angles larger than 10°.

The last step of the whole study will be to analyze the influence of horizontal pointing error on principal plane measurements. In section 3.5, relative radiance errors were also related to the

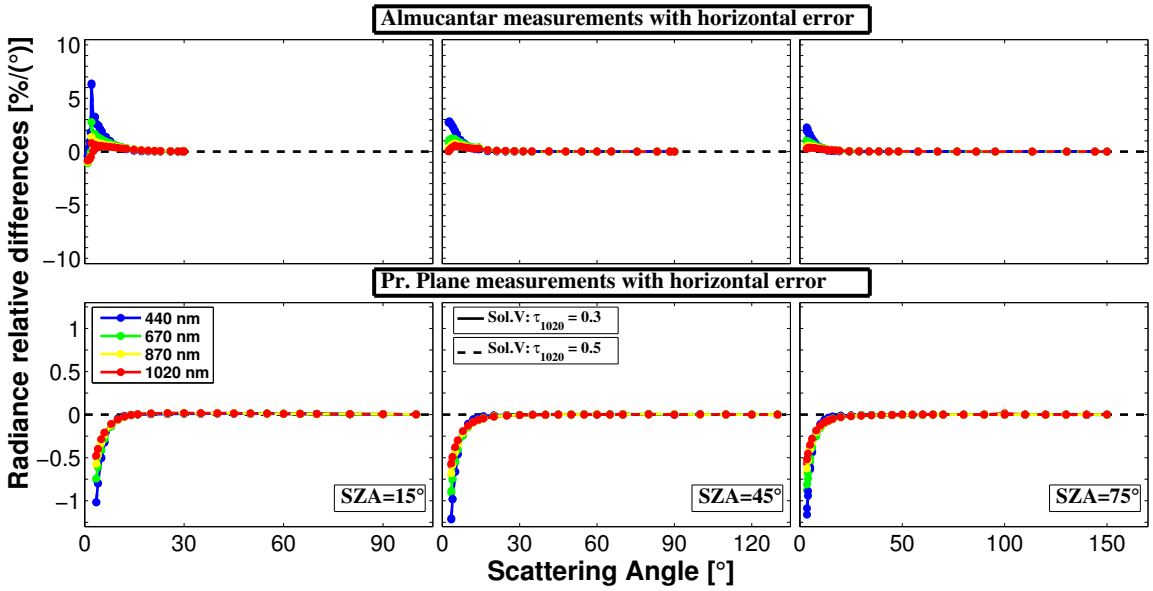

Figure 5.10: Radiance relative error (per degree) caused by a horizontal pointing error in almucantar (upper part) and principal plane (bottom part) simulated measurements. Solar Village (desert dust) aerosol was taken for the tests using two different AOD: $\tau_{1020} = 0.3$ (solid line) and $\tau_{1020} = 0.5$ (dashed line). From left to right, SZA increases for the different figures (note the different range in scattering angle as SZA increases). In the upper part, the radiance error is represented for positive pointing error whereas the pointing error is negative in the bottom part.

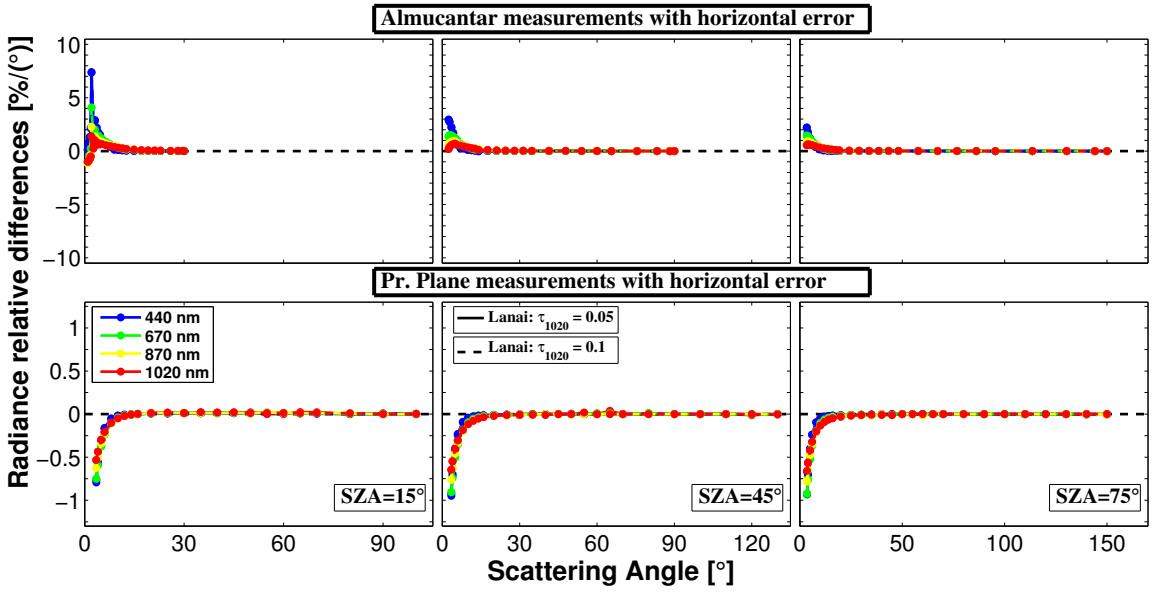

Figure 5.11: Radiance relative error (per degree) caused by a horizontal pointing error in almucantar (upper part) and principal plane (bottom part) simulated measurements. Lanai (oceanic) aerosol was taken for the tests using two different AOD: $\tau_{1020} = 0.05$ (solid line) and $\tau_{1020} = 0.1$ (dashed line). From left to right, SZA increases for the different figures (note the different range in scattering angle as SZA increases). In the upper part, the radiance error is represented for positive pointing error whereas the pointing error is negative in the bottom part.

horizontal error as a function of the its first derivative (Eq. (3.18)):

$$\epsilon_R = \left\| \frac{\partial R(\theta,\varphi)}{\partial \varphi} \right\|_{\substack{\theta=\theta_p \\ \varphi=0}} \frac{\xi_\varphi}{R(\theta_p, 0)} \tag{5.4}$$

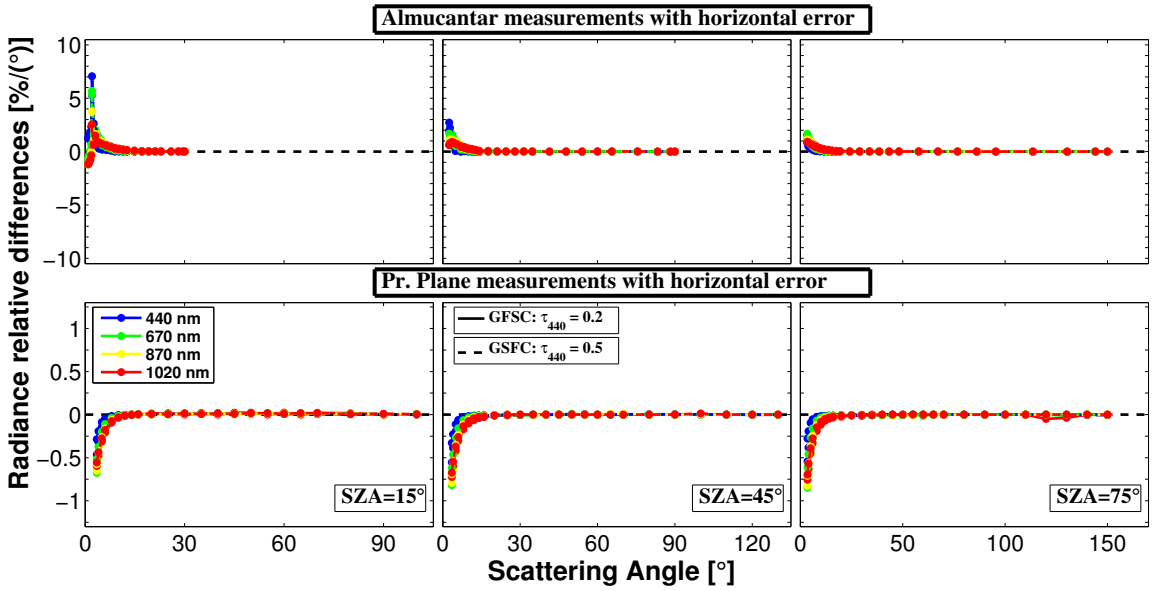

Figure 5.12: Radiance relative error (per degree) caused by a horizontal pointing error in almucantar (upper part) and principal plane (bottom part) simulated measurements. GSFC (urban) aerosol was taken for the tests using two different AOD: $\tau_{440} = 0.2$ (solid line) and $\tau_{440} = 0.5$ (dashed line). From left to right, SZA increases for the different figures (note the different range in scattering angle as SZA increases).

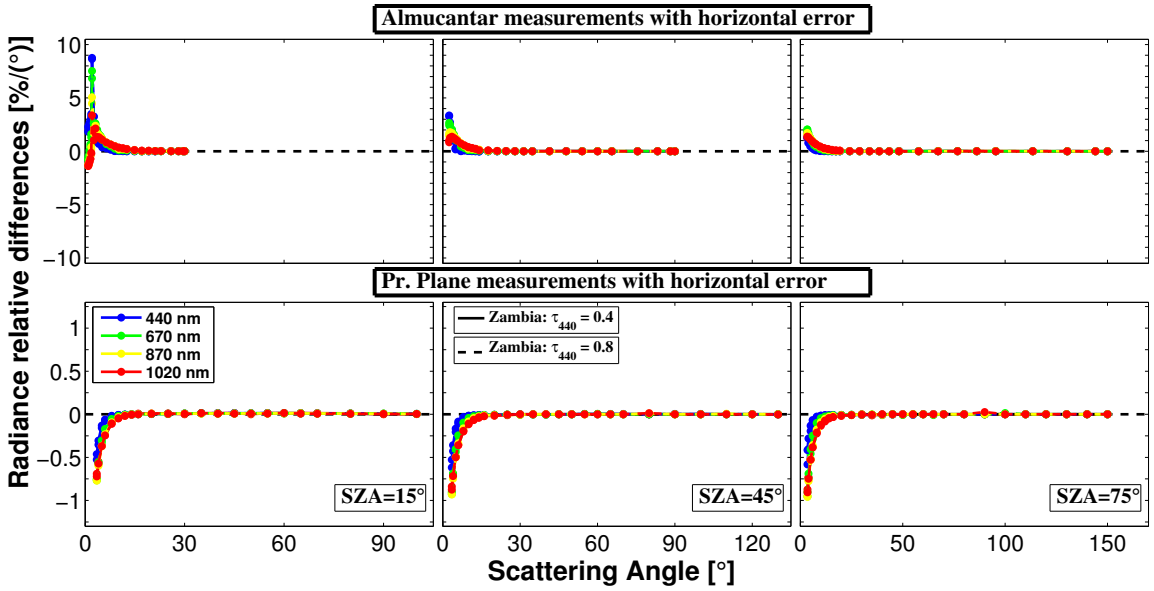

Figure 5.13: Radiance relative error (per degree) caused by a horizontal pointing error in almucantar (upper part) and principal plane (bottom part) simulated measurements. Mongu (biomass burning) aerosol was taken for the tests using two different AOD: $\tau_{440} = 0.4$ (solid line) and $\tau_{440} = 0.8$ (dashed line). From left to right, SZA increases for the different figures (note the different range in scattering angle as SZA increases).

As in the case of vertical errors in almucantar measurements, the radiance errors in principal plane caused by horizontal pointing errors are expected to be small. Actually these errors are not only small but they are the smallest found during the study. All the differences are negative, and the highest value, 1.25%, was found for desert dust aerosol at $SZA = 45°$, for 440 nm channel and at 3.5° of scattering angle. The shape of the differences does not depend on SZA, having a similar

behavior also for all the aerosol types: difference about 1% for the shortest scattering angles and from there on these differences get reduced, being almost unnoticed at 10° of scattering angle.

5.4 Pointing error consequences on inversion results

After the analysis on the radiance simulations with pointing errors, the consequences of these errors on the inversion results are the next subject here. The section is sub-divided again according to the aerosol type instead of the type of pointing errors as in the previous section, because the physical magnitudes to compare (aerosol derived properties) are different for each aerosol type.

5.4.1 Desert dust (Solar Village)

As in chapter 2 and chapter 4, the first aerosol type analyzed is the desert dust (Solar Village) with the the two possibilities commented for its aerosol load, $\tau_{1020} = 0.3$ and $\tau_{1020} = 0.5$ (see discussion in subsection 2.2.1 about the characteristics of dust).

Figure 5.14 presents the size distributions derived from radiance measurements with pointing errors The figure is subdivided into three plots, one for each value of the simulated pointing errors: 0.2°, 0.4° and 1°. Then, each of the plots is divided, in turn, in another six subplots. In the upper part, the three subplots correspond to almucantar inversion results from simulations with positive vertical error, negative vertical error and horizontal error, from left to right, respectively. Same configuration is used for the bottom part but with principal plane simulations. And, finally, in all of these eighteen subplots, size distributions are illustrated. In black color, original size distributions are represented, with solid line for $\tau_{1020} = 0.3$ and dashed line for $\tau_{1020} = 0.5$. Then different colors are used for different solar zenith angles: dark blue for $SZA = 15°$, light blue for $SZA = 30°$, green for $SZA = 45°$, orange for $SZA = 60°$ and brown for $SZA = 75°$.

The consequences of a 0.2° pointing error on size distributions can be observed in the first plot. There are not significant differences with respect to the original size distributions for almucantar results, neither for vertical nor horizontal errors. However, slight differences can be seen for the principal plane, although only for vertical pointing errors. These differences seem to be mainly negative when the vertical error is positive and positive when the vertical error is negative. But it is in the next figure, for 0.4° pointing error, where differences start to be more noticeable. For this pointing error, principal planes with a positive vertical error present a 10% decrease in the size distributions between $1\mu m$ and $3\mu m$ and a little increment around $4 - 5\%$ for larger radii. With negative vertical error, the situation is opposite: there is a big increase up to $15 - 20\%$ for radii between $1\mu m$ and $3\mu m$ accompanied by a significant reduction for larger radii. In the rest of the cases, principal plane with horizontal error and almucantar with horizontal and vertical errors,

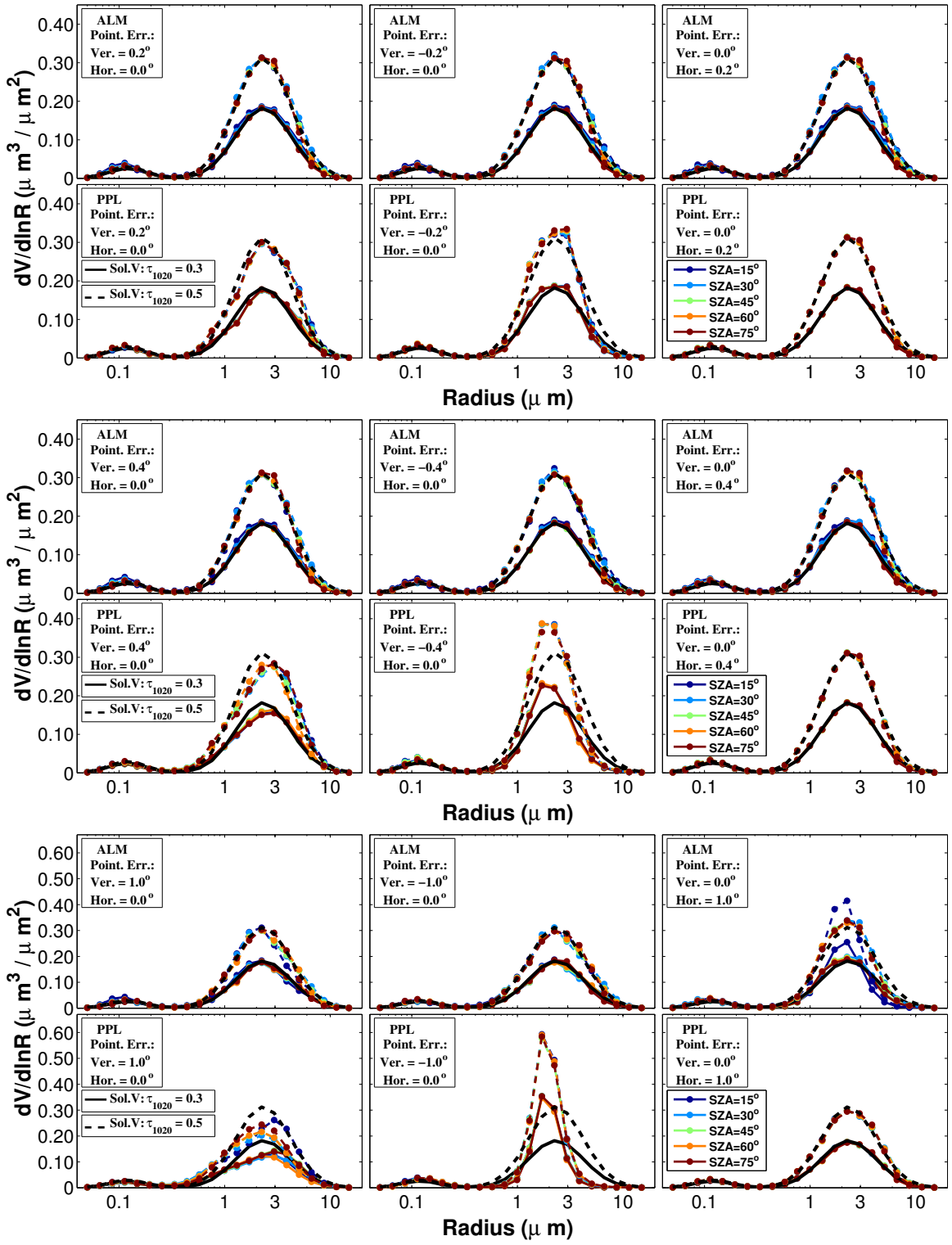

Figure 5.14: Retrieved size distributions for Solar Village case after introducing different pointing errors: 0.2° in the figure at the top, 0.4° in the figure in the middle and 1° in the figure at the bottom. In each of the figures, subfigures on top show results from almucantars and at the bottom from principal planes. Subfigures on the left correspond to retrievals with vertical errors, and on the right, to horizontal errors. Solid line is used for the case of $\tau_{1020} = 0.3$ and dashed line for $\tau_{1020} = 0.5$. Colors indicate the solar zenith angle: dark blue for $SZA = 15°$, light blue for $SZA = 30°$, green for $SZA = 45°$, orange for $SZA = 60°$ and brown for $SZA = 75°$ while black is used for the original size distributions.

there are no remarkable differences. This situation was reasonably expected during the analysis of radiances in the previous section, where differences in radiance measurements with vertical pointing errors were at least ten times larger than for the rest of the cases.

In the figure for 1° error, Y-axes have been modified in order to represent the results, as for negative vertical errors the maximum of the size distribution is twice as larger as the one on the original size distribution. Therefore, differences are up to 100% in the range from $1\mu m$ and $3\mu m$. The decrease part in the size distribution after $3\mu m$ is so strong that size distribution is zero above $5\mu m$. For positive errors, there is a significant decrease up to 30% for radii between $1\mu m$ and $3\mu m$, also, and opposite to previous cases of negative pointing error, there is a diminution from $3\mu m$. Even for 1° of horizontal pointing error in principal plane, no effects are observed in the size distributions.

Almucantar simulations show some differences for the 1° case. With vertical pointing error, the size distribution decreases softly (up to 10%) for radii between $2\mu m$ and $7\mu m$. These differences are more noticeable for positive errors and short SZA, corresponding to the largest differences observed for Solar Village in subsection 5.3.2.

For horizontal errors, differences in general are a little bit higher than in the last case. The size distribution rises before $3\mu m$ and diminishes above this radius. The result for $SZA = 15°$ needs to be commented apart because its increase before $3\mu m$ is about 30% and its decrease is strong too, being the size distribution practically 0 at $5\mu m$, for both $\tau_{1020} = 0.3$ and for $\tau_{1020} = 0.5$.

Analyzing the differences in the ω_o and in the refractive index is the next step. The results obtained here together with the errors in radiances will be useful for a better understanding of the differences in size distributions. Figure 5.15 and Figure 5.16 show the results obtained with the tests for the $\omega_o$and refractive index respectively. The basic scheme in both representations is the same as in figure 5.14: the two illustrations are composed of three figures representing each of the three considered pointing errors. Then every figure contains six subfigures: three in the upper part for almucantar simulations and another three at the bottom reproducing the results for the principal plane. From left to right, they correspond to positive vertical errors, negative vertical errors and horizontal errors, respectively. All figures, in both schemes, have solar zenith angle as the X-Axis. On the other hand, the Y-Axis in figure 5.15 represents the $omega_o$, whilst in figure 5.16 it expresses the real part of the refractive index (left Y-axis) and the imaginary part (right Y-axis). Different color lines distinguish the results for each wavelength: blue for 440 nm wavelength, green for 670 nm, yellow for 870 nm and red for 1020 nm. The solid line was used to illustrate the results with $\tau_{1020} = 0.3$ and the dashed line for the ones with $\tau_{1020} = 0.5$. The results of the non-error inversion are not represented in order to not oversaturate the figure but they can be seen in figure 2.3.

Before starting the discussion, there are several questions that should be brought up. First,

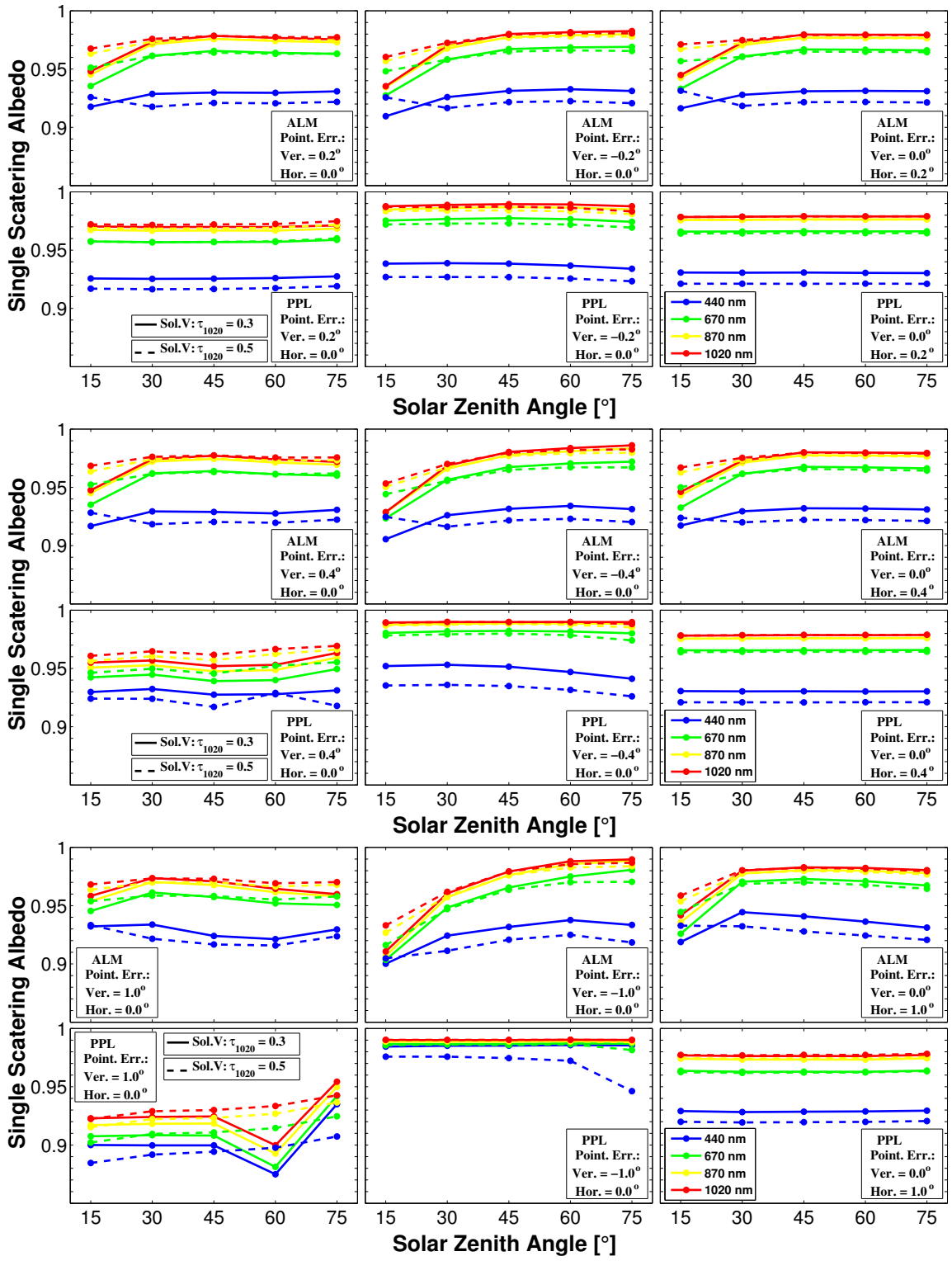

Figure 5.15: Retrieved single scattering albedo for Solar Village case after introducing different pointing errors: 0.2° in the figure at the top, 0.4° in the figure in the middle and 1° in the figure at the bottom. In each of the figures, subfigures on top show results from almucantars and at the bottom from principal planes. Subfigures on the left correspond to retrievals with vertical errors, and on the right, to horizontal errors. Solid line is used for the case of $\tau_{1020} = 0.3$ and dashed line for $\tau_{1020} = 0.5$. Colors indicate the wavelength: blue for 440 nm, green for 670 nm, yellow for 870 nm and red for 1020 nm.

as showed in subsection 2.4.3, the coarse mode of the size distribution is more connected to short scattering angles, while the information about fine particles is more equally distributed.

On the other hand, the optical properties also affect all the scattering angles. Single scattering albedo and imaginary refractive index are closely related. Moreover, since our simulations keep constant the aerosol optical depth, an increase of radiance will mean more scattering compared to the absorption and therefore, ω_o will rise while the imaginary part of refractive index will fall. The opposite situation will occur for less radiance: ω_o will decrease due to the reduction of the scattered light and the imaginary refractive index will raise because of a larger absorption. Finally as shown in subsection 2.4.1, the real part of the refractive index is more connected with the shape of the radiance. High values of radiance for short scattering angles and low values for large angles are related to low values of the real refractive index. The opposite situation will mean high values in the real refractive index.

Revising figure 5.6 (radiance relative differences in almucantar measurements with vertical errors), differences are always negative for very short scattering angles, no matter the SZA and the sign of the error. This caused a decrease in the coarse mode of all size distributions in figure 5.14. But the differences have a dissimilar behavior for larger scattering angles: positive errors cause positive differences for $SZA = 15°$, negative differences for $SZA = 75°$ and no differences at $SZA = 45°$. As a consequence, ω_o will increase at short scattering angles and decrease at large scattering angles. This tendency is found in figure 5.15 for 0.2°, 0.4° and 1° values of vertical error in almucantar simulations. This drift is opposite to the fictitious almucantar cycle presented in subsection 2.2.1.2. It is interesting to observe that for 1° error, ω_o is more constant along the day that for non-error simulations.

When errors are negative, there are negative differences for $SZA = 15°$ and positive differences for $SZA = 75°$, finding no differences again at $SZA = 45°$. Thus, ω_o would have the opposite behavior: reduction for short SZA and increment for large SZA. Therefore, negative vertical pointing errors will enlarge the fictitious daily cycle of ω_o in almucantar retrievals. This is confirm in figure 5.15 where for the example $\tau_{1020} = 0.3$ differences are more visible: around 5% at 440 nm (non-error case was 2%) and 8% for the rest of the channels (4% in the non-error case).

The imaginary part of the refractive index responds in the same way as the $omega_o$, but its variations have the opposite sign. In figure 5.16, the imaginary part is represented on the right part of the figures. Looking at the almucantar simulations with vertical errors, it can be seen that the values of the imaginary part of the refractive index diminish for short SZA and increase for large SZA. Again, this acts against the fictitious cycle discussed in subsection 2.2.1.2. For negative errors, the effect is opposite and it magnifies the fictitious cycle; for example, imaginary refractive index at 1020 nm gets 10 times higher at 15° than at 75° (for $\tau_{1020} = 0.3$). The real part, represented on the left, does not follow the tendency of the other two parameters. For large SZA,

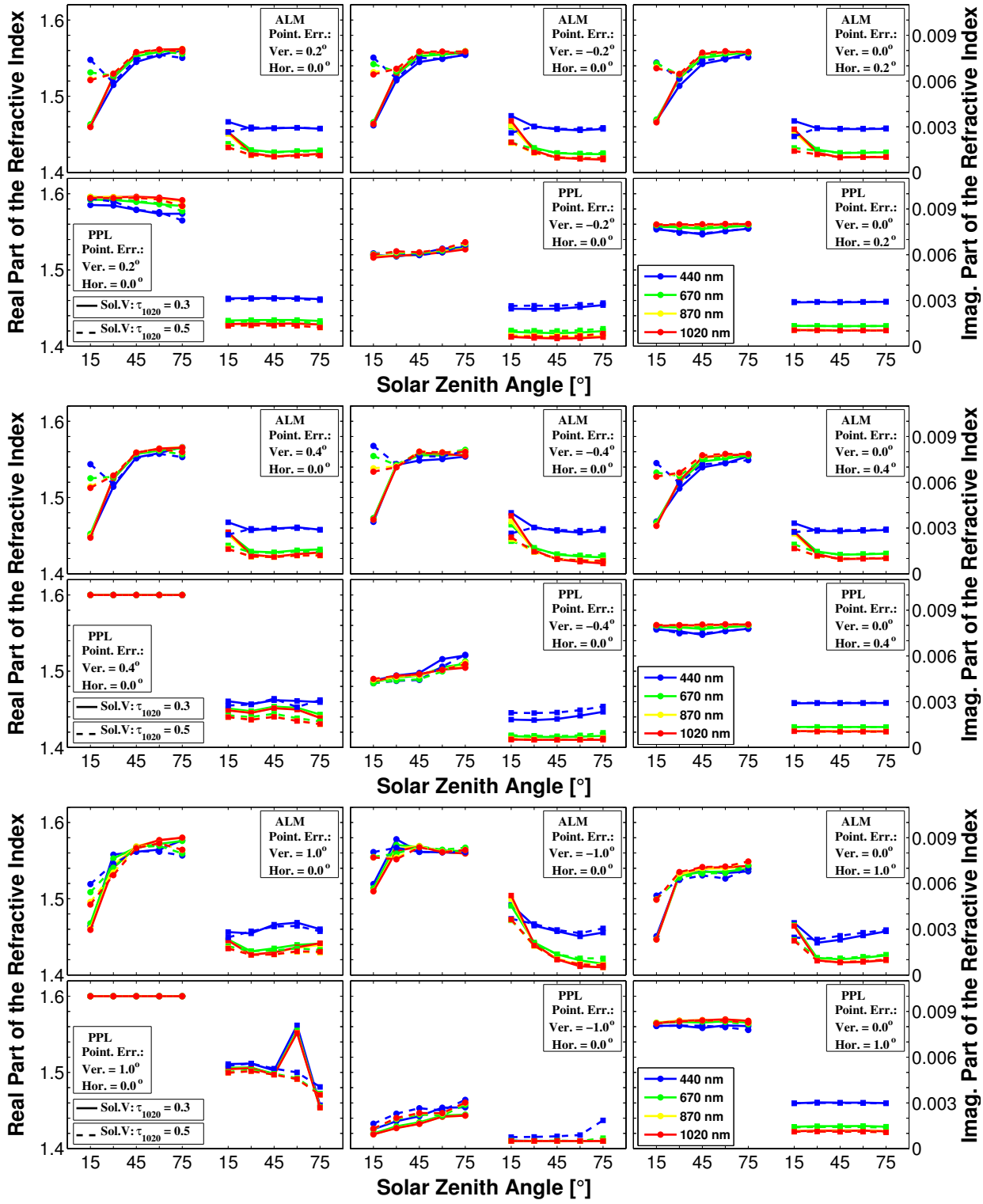

Figure 5.16: Retrieved refractive index for Solar Village case after introducing different pointing errors: 0.2° in the figure at the top, 0.4° in the figure in the middle and 1° in the figure at the bottom. In each of the figures, subfigures on top show results from almucantars and at the bottom from principal planes. Subfigures on the left correspond to retrievals with vertical errors, and on the right, to horizontal errors. Solid line is used for the case of $\tau_{1020} = 0.3$ and dashed line for $\tau_{1020} = 0.5$. Colors indicate the wavelength: blue for 440 nm, green for 670 nm, yellow for 870 nm and red for 1020 nm. Y-Axes express the real refractive index (on the left) and the imaginary refractive index (on the right)

it hardly varies. On the other hand, the effects in short SZA are seen only from 0.4° of pointing error, decreasing for positive vertical errors and increasing for negative ones. The explanation can be found in figure 5.2: differences for $SZA = 15°$ depend on the scattering angle, whereas they are almost constant for $SZA = 75°$. Thus, radiance form does not change at $SZA = 75°$ and consequently the real refractive index remains constant. But, at $SZA = 15°$, positive errors transfer more light to large scattering angles, enlarging the real refractive index, and negative errors attenuate the light at large scattering angles, reducing, as a result, the real refractive index.

Let us now analyze the influence of vertical pointing errors on the principal plane retrievals. At this point, it should be noted that principal plane non-error inversion results do not present any problems such as the fictitious cycle found in non-error almucantar retrievals. However, radiance differences due to pointing errors are higher for principal plane than for almucantar measurements, and consequently, the effect on the inversion results may be more visible. It was already seen with the size distributions and it will be a constant in the chapter: principal plane results are more stable respect to SZA variations, but they are conversely more sensitive to pointing errors.

Back to figure 5.2, radiance differences in the principal plane produced by positive vertical pointing errors are mostly negative, specially for short scattering angles. Based on this, we can expect the single scattering albedo to decrease, imaginary part of refractive index to increase and real part of refractive index to enlarge to a great extent, due to the high differences at short scattering angles compared to the rest. Expectancies for the consequences of negative errors are just the opposite. Taking a quick look at figures Figure 5.15 and figure 5.16 we see that our expectations were correct: Figure 5.15 shows that ω_o drops for positive errors and grows for negative errors. These variations are stronger than for almucantar simulations and they do not have a marked dependency with the SZA. Examining figure 5.16, the real part of the refractive index suffers larger variations than in almucantar tests. For positive vertical errors, the real part was thought to grow significantly and it actually raises in such a way that gets the highest value allowed by the code at 0.4° of pointing error in all the channels. For negative errors, this parameter decreases gradually as the pointing error increases: without error, values for different wavelengths were about 1.56 (same as the input figure 2.3 and table 2.1); with 0.2° error it falls to about 1.52; with 0.4° error, it gets down to 1.50 and with 1° error, it decreases to 1.44. Values are slightly shorter for small SZA, as well as differences in radiance were more pronounced for small SZA in figure 5.2. The imaginary part of the refractive index varies less than the real part. It shows a smooth increment for positive vertical pointing errors of 0.2° and 0.4°, being stronger for 1°. For negative errors, the same variations are observed but with opposite sign: soft decrease for 0.2° and 0.4° while values for 1.0° error are under 0.001 at all wavelengths.

Horizontal errors do not change the retrievals of ω_o and refractive index, neither for almucantar nor for principal plane simulations for 0.2° and 0.4° pointing error. For 1°, principal plane retrievals are kept constant while almucantar results for 15° and 30° of SZA change lightly.

5.4.2 Oceanic (Lanai)

As in previous descriptions the next step is the analysis of the test made with the Oceanic aerosol using Lanai examples. First we analyzed the size distributions which are presented in figure 5.17. The scheme of this figure is the same as in figure 5.14. Again, significant results are only obtained for principal plane with vertical errors where differences are already noticeable for 0.2°. The coarse mode, as in the desert dust case, presents lower values for positive errors, and it increases for negative errors. As the pointing error rises, the tendency in the results seems clearer. For positive errors, the coarse mode between $1\mu m$ and $5\mu m$ radii, decreases up to 10% for 0.4° and up to 50% for 1°, without differences for longer radii. With negative errors, the increment is about 10% and 100% respectively for 0.4° and 1°, in the interval $1 - 4\mu m$. As in the desert dust case, the size distribution declines for longer radii, softly for 0.4° and rather more steeply for 1° error. However, the novelty of the oceanic aerosol lies in the appearance of the fine mode. The behavior of the fine mode is opposite to that of the coarse mode: it grows for positive errors and decreases for negative errors. To be more precise, the perturbations are only observed for radii smaller than $0.15\mu m$. The explanation is given by figure 5.3, i.e. radiance differences in principal plane for positive vertical errors. If for small scattering angles differences were negative, these differences were positive for scattering angles larger than 90°. Therefore positive vertical errors provoke an increase in the backscattered radiation, interpreted by the code as an enlargement of the fine mode[1].

Horizontal errors do not create any variations in the size distribution for principal plane, as it could be expected from the differences in radiance introduced by these errors, figure 5.11.

Almucantars show differences only when the pointing error is 1° and among the investigated cases, the highest differences are reached when $SZA = 15°$ in horizontal errors, as it was seen in the desert dust case.

However, the single scattering albedo suffers deviations even for small errors. In figure 5.18 it can be seen that for vertical errors, positive values increase the single scattering albedo when the SZA is smaller than 45°, whereas for larger SZA the single scattering albedo gets reduced. The effects are opposite for negative errors. Therefore, the single scattering albedo shows a cycle, with differences between $SZA = 15°$ and $SZA = 75°$ up to 0.02 for vertical errors of 0.2°, up to 0.04 when errors are 0.4° and up to 0.08 for 1.0° error. The same cycle is observed for the imaginary part of refractive index in figure 5.19, but with the opposite trend. The explanation of both cycles is the same as the one given in the desert dust case: the differences in radiance (figure 5.7) have opposite sign for short and large SZA. For positive errors and short SZA, the differences in radiance are

[1] Even though the study was done for biomass burning, these ideas can be easier interpreted remembering figures 2.14 and 2.15. A decrease of particles in the region called "case 4" provoked there a fall in radiance but only for the first scattering angles, while an increase of the particles in the region called "case 4" produced a rise in the radiance but mostly at the large scattering angles.

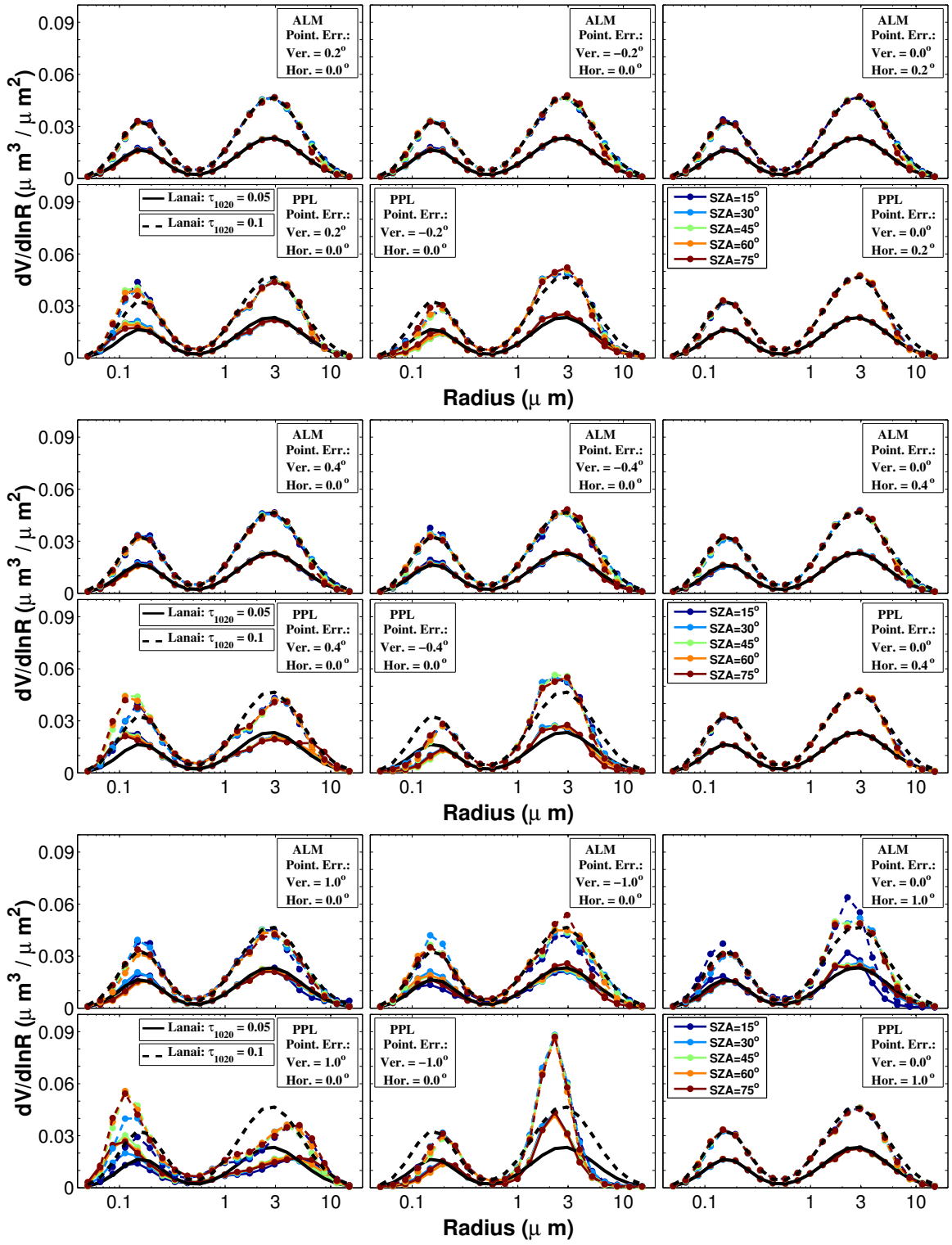

Figure 5.17: Retrieved size distributions for Lanai case after introducing different pointing errors: 0.2° in the figure at the top, 0.4° in the figure in the middle and 1° in the figure at the bottom. In each of the figures, subfigures on top show results from almucantars and at the bottom from principal planes. Subfigures on the left correspond to retrievals with vertical errors, and on the right, to horizontal errors. Solid line is used for the case of $\tau_{1020} = 0.05$ and dashed line for $\tau_{1020} = 0.1$. Colors indicate the solar zenith angle: dark blue for $SZA = 15°$, light blue for $SZA = 30°$, green for $SZA = 45°$, orange for $SZA = 60°$ and brown for $SZA = 75°$ while black is used for the original size distributions.

mostly positive, what means that there is more radiance with the same absorption, resulting in an enlargement of the single scattering albedo and a decrease in the imaginary part of refractive index; for large SZA radiance differences are negative, leading to the opposite consequences. Horizontal errors do not have a significant impact, except maybe a slight increase in the radiance, that resulted in a small increase of ω_o (and small decrease of imaginary part of refractive index).

The retrievals from principal plane simulations do not present a cycle for the single scattering albedo and for the imaginary part of refractive index neither. Radiance differences do not change the sign when varying the SZA (figure 5.3). For positive errors these differences are mostly negative, what generates a decrease in the ω_o (about 0.1 for errors of 0.2°, about 0.2 when errors are 0.4° and about 0.4 for 1.0° error case) and an increase in the imaginary part of refractive index (0.0005, 0.001 and 0.003 for 0.2°, 0.4° and 1° errors respectively). For negative errors these differences are positive, causing the opposite effects. It should be noticed that as Lanai aerosol is not very absorptive, and negative vertical errors can be interpreted in principal plane as a reduction of the absorption, the extreme values for the outputs are obtained concerning non-absorption already for 0.4°: single scattering albedo rises up to 0.99 while the refractive index falls to 0.001 at all wavelengths. Horizontal errors do not produce any changes.

The last part of this section focuses on the study of the real part of refractive index. Starting with vertical errors and principal plane retrievals, the separation of real part of the refractive index for different wavelengths is the first thing that attracts attention in figure 5.19. Due to the fact that in the Solar Village case the limit of the real refractive index was reached ($n = 1.6$), this effect was not so notorious. The reason again can be found in the analysis of the radiance relative differences (figure 5.3), in which the shortest wavelength experiences greater changes as the scattering angle varies. For positive vertical errors, the relative differences in radiance for 3° scattering angle are about -35% for 440 nm and 670 nm whereas they do not exceed -30% for the other two wavelengths. Already at 15° these differences drop to -5% for 440 nm and 670 nm while the variation is smaller for the largest wavelengths. In all cases, the trend is to have more light for longer scattering angles, what suggests an increase in the real refractive index, as in the case of desert dust, and therefore, these wavelengths with more variation should show a larger increase.

However, the results say that only for 1020 nm the refractive index increases, which is in disagreement with the previous argument. It should be remembered that this idea was used successfully in the desert dust case and if radiance differences in both cases present the same behavior, apparently there is no immediate explanation for the different behavior of the real refractive index in the Lanai case. A possible explanation could be obtained analyzing size distributions: In the desert dust case for positive vertical errors, the retrievals from principal planes gave a decrease of the coarse mode and no variations in the fine mode. More light for longer scattering angle with less particles could be only explained with a strong increase in the real refractive index. But in the Lanai case, the fine mode increases for vertical pointing errors. In this second scenario, if the

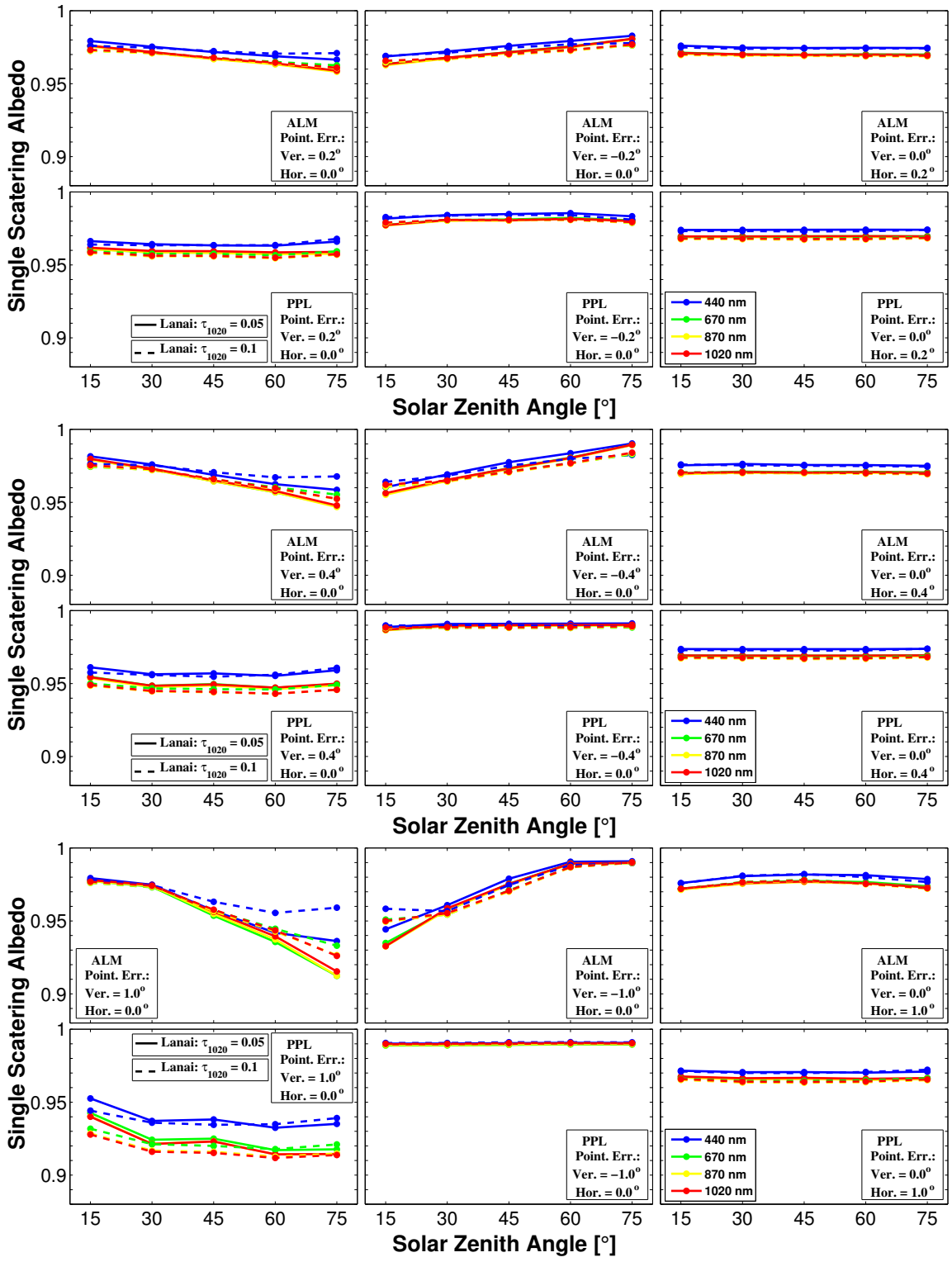

Figure 5.18: Retrieved single scattering albedo for Lanai case after introducing different pointing errors: 0.2° in the figure at the top, 0.4° in the figure in the middle and 1° in the figure at the bottom. In each of the figures, subfigures on top show results from almucantars and at the bottom from principal planes. Subfigures on the left correspond to retrievals with vertical errors, and on the right, to horizontal errors. Solid line is used for the case of $\tau_{1020} = 0.05$ and dashed line for $\tau_{1020} = 0.1$. Colors indicate the wavelength: blue for 440 nm, green for 670 nm, yellow for 870 nm and red for 1020 nm.

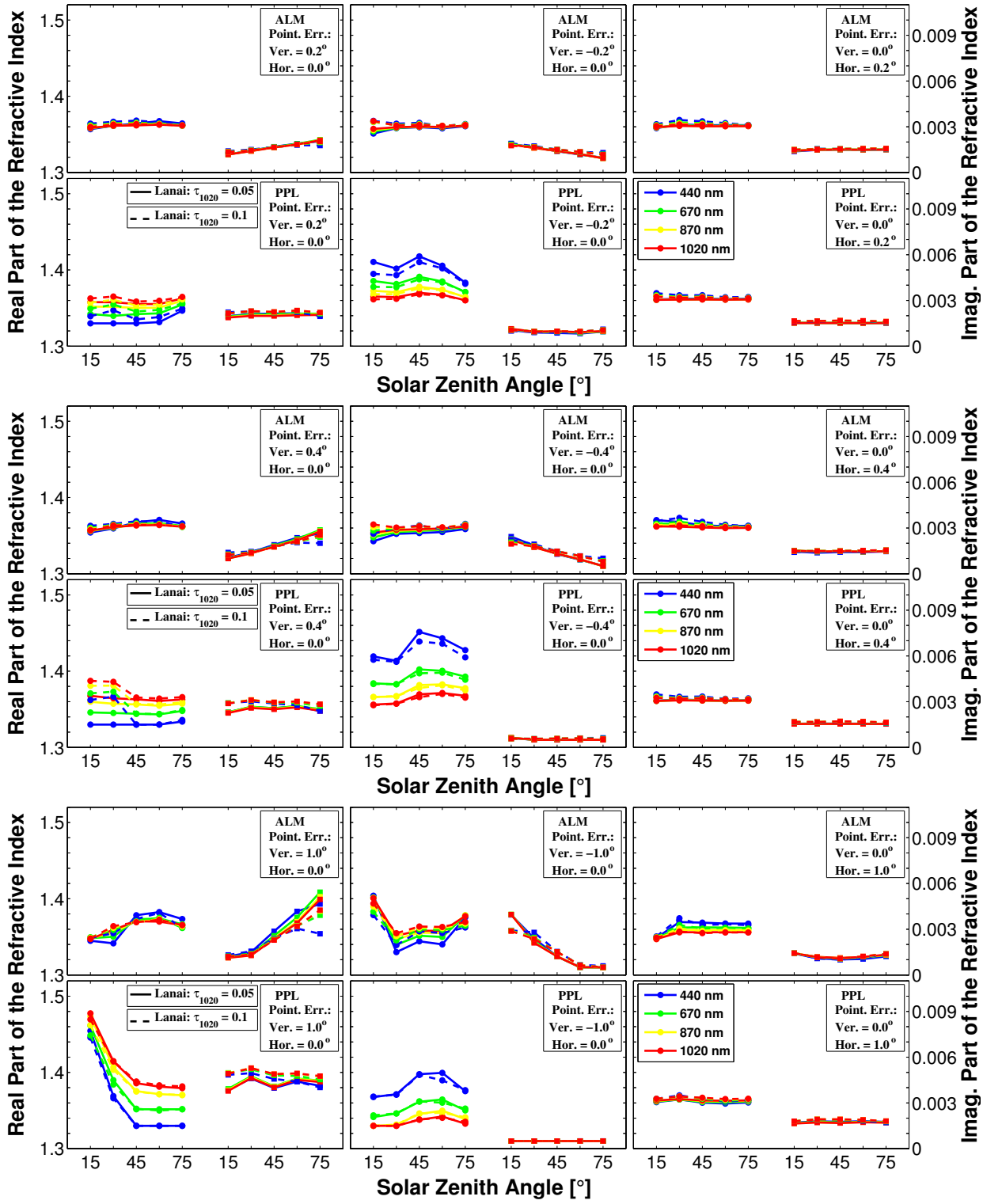

Figure 5.19: Retrieved refractive index for Lanai case after introducing different pointing errors: 0.2° in the figure at the top, 0.4° in the figure in the middle and 1° in the figure at the bottom. In each of the figures, subfigures on top show results from almucantars and at the bottom from principal planes. Subfigures on the left correspond to retrievals with vertical errors, and on the right, to horizontal errors. Solid line is used for the case of $\tau_{1020} = 0.05$ and dashed line for $\tau_{1020} = 0.1$. Colors indicate the wavelength: blue for 440 nm, green for 670 nm, yellow for 870 nm and red for 1020 nm. Y-Axes express the real refractive index (on the left) and the imaginary refractive index (on the right)

increment of the particles is very strong, even in the case of more light, the real refractive index can drop.

There are two ideas supporting this argument. First, the real refractive index at 1020 nm was commented to be the only one showing an increase, this wavelength could be though less affected by the fine mode, and accordingly, to have similar behavior as in the desert dust case. On the other hand, for 1° pointing error the fine mode did not grow for $SZA = 15°$ and only grew slightly for $SZA = 30°$. If we check again the results for real refractive index, we find that for these two particular cases the real refractive index undergoes a large increase.

For negative vertical errors, the study is a little bit more complicated. For the 440 nm channel, there is an increase in all the simulations but the highest values are reached at 0.4° of error. 670 nm channel raises for 0.2° and 0.4° but decreases for 1° error. The other two wavelengths present a small variation for 0.2° and 0.4°, but they drop considerably for 1° error. Once again, the explanation could be found in the size distribution: as it was commented the fine mode decreases for negative vertical errors, but there is no variation between the results at 0.4° and 1° of pointing error. While the decrease in the number of particles justifies the decrease in radiance for large scattering angles (0.2° and 0.4°) the real part of the refractive index does not vary or even rises; however, in the last case, where the number of particles are kept, the real part of the refractive index drops to adjust to the absence of light.

Continuing with the vertical errors, almucantar simulations do not present meaningful differences except for the case of 1°. With this error, the real part of the refractive index does not vary for large SZA as it occurred in the desert dust case. The effects are only visible for short SZA, decreasing the value for positive vertical errors and increasing for negative ones. There are no important fluctuations in the size distributions for almucantar retrievals and the change of radiance shape, commented in figure 5.3, at $SZA = 15°$, is reflected in a variation on the real part of the refractive index.

To end up, it should be mentioned that there is no variation in the retrieved real part of the refractive index neither for principal plane nor for almucantar simulations with horizontal pointing errors.

5.4.3 Urban (GSFC)

As in chapter 4, the last two examples will provide us a better scenario to understand the effects on size distributions dominated by the fine mode. We start here again with the two examples of the urban aerosol with the features given by the variability study in GSFC (non-absorbing aerosol) keeping the biomass burning examples from Mongu site for the last subsection.

Concerning pointing error influence on urban aerosol, figure 5.20 presents the size distributions

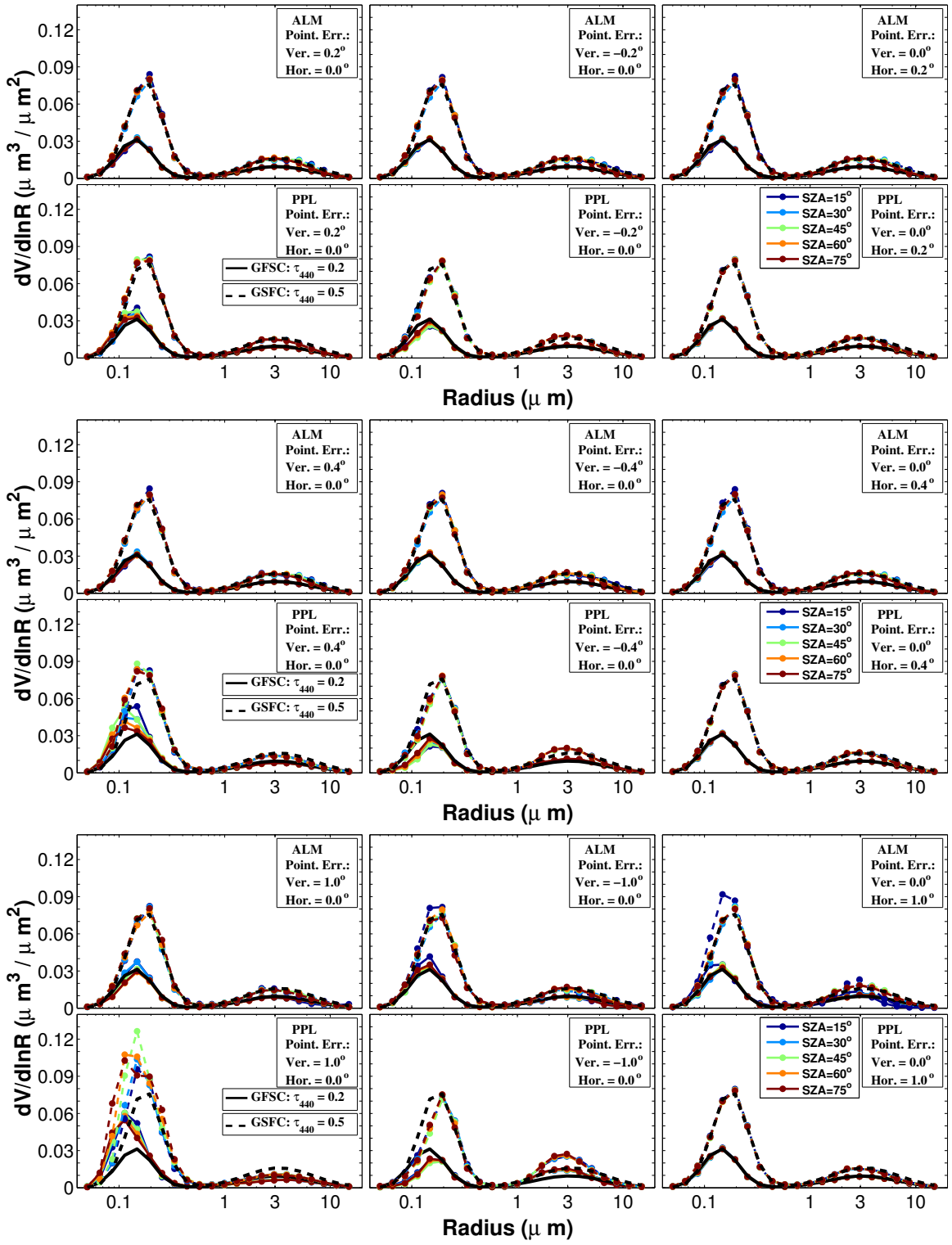

Figure 5.20: Retrieved size distributions for GSFC case after introducing different pointing errors: 0.2° in the figure at the top, 0.4° in the figure in the middle and 1° in the figure at the bottom. In each of the figures, subfigures on top show results from almucantars and at the bottom from principal planes. Subfigures on the left correspond to retrievals with vertical errors, and on the right, to horizontal errors. Solid line is used for the case of $\tau_{440} = 0.2$ and dashed line for $\tau_{440} = 0.5$. Colors indicate the solar zenith angle: dark blue for $SZA = 15°$, light blue for $SZA = 30°$, green for $SZA = 45°$, orange for $SZA = 60°$ and brown for $SZA = 75°$ while black is used for the original size distributions.

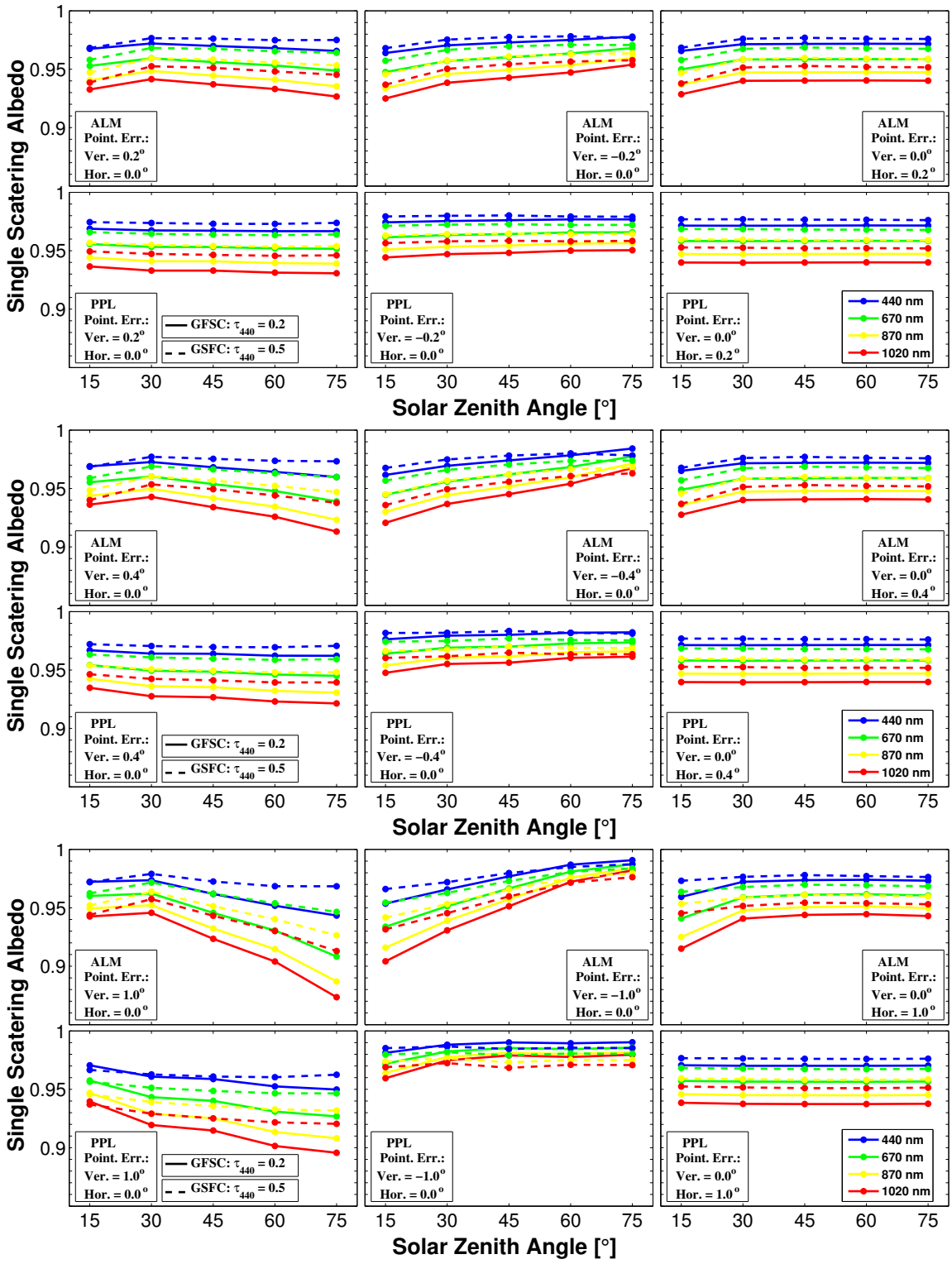

Figure 5.21: Retrieved single scattering albedo for GSFC case after introducing different pointing errors: 0.2° in the figure at the top, 0.4° in the figure in the middle and 1° in the figure at the bottom. In each of the figures, subfigures on top show results from almucantars and at the bottom from principal planes. Subfigures on the left correspond to retrievals with vertical errors, and on the right, to horizontal errors. Solid line is used for the case of $\tau_{440} = 0.2$ and dashed line for $\tau_{440} = 0.5$. Colors indicate the wavelength: blue for 440 nm, green for 670 nm, yellow for 870 nm and red for 1020 nm.

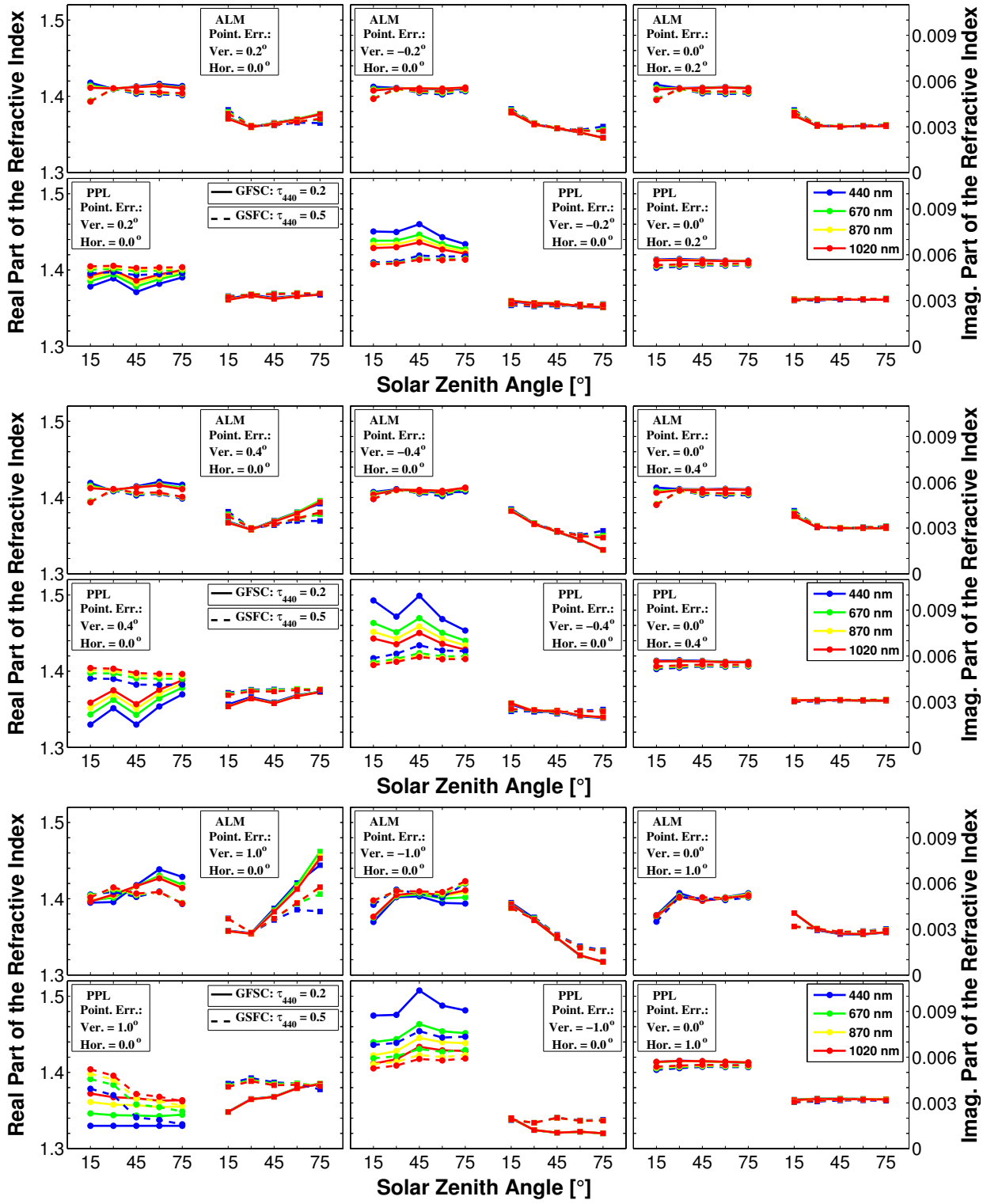

Figure 5.22: Retrieved refractive index for GSFC case after introducing different pointing errors: 0.2° in the figure at the top, 0.4° in the figure in the middle and 1° in the figure at the bottom. In each of the figures, subfigures on top show results from almucantars and at the bottom from principal planes. Subfigures on the left correspond to retrievals with vertical errors, and on the right, to horizontal errors. Solid line is used for the case of $\tau_{440} = 0.2$ and dashed line for $\tau_{440} = 0.5$. Colors indicate the wavelength: blue for 440 nm, green for 670 nm, yellow for 870 nm and red for 1020 nm. Y-Axes express the real refractive index (on the left) and the imaginary refractive index (on the right)

in the same format as the previous cases. Subfigure for 0.2° pointing error does not show differences between the reference value and the retrieved size distributions. However, once the errors rise up to 0.4°, differences show up and, as it could be expected, are largest for vertical errors in principal plane retrievals. However, these differences are not as strong as for desert dust or oceanic aerosol, specially for $\tau_{440} = 0.5$ case (dashed lines). These differences are concentrated in the fine mode and only up to $0.2\mu m$. They are positive for vertical positive errors and negative when errors are negative. Again, the backscattering plays the important role in the analysis, and as we pointed out for Lanai aerosol: There is an increase of light with the same sign as the pointing error, which also makes the change in particle concentration to take the same sign. When errors go up to 1°, differences in the principal plane retrieval grow too. For positive errors, values up to $0.1\mu m$ of radius, are double than their references, and from this point until $0.2\mu m$, they are considerately higher, being practically identical after it. A little reduction of the coarse mode concentration can be observed as well. Negative errors provoke a decrease in the fine mode and an increase in the coarse mode, even though the differences are not as relevant as in the previous cases. Almucantar inversions exhibit slight differences, mainly in the fine mode concentration. There are positive increments for both positive and negative vertical errors, while values drop for horizontal errors.

The single scattering albedo presents the same behavior as in the other aerosol types. Variations in this parameter, in figure 5.21, are easier to understand following the principle that: the more the light is scattered, the higher the ω_o is. Vertical positive pointing errors in almucantars produce positive increments for short solar zenith angles and negative increments for large solar zenith angles, since in the first situation, radiance differences were mostly positive, figure 5.8, and mostly negative in the second one. Both give rise to a ω_o daily cycle opposite to the fictitious cycle in almucantar measurements obtained for urban aerosol (minimum ω_o at noon, see subsection 2.2.3.2). The fictitious circle is canceled already for 0.2°. From 0.4°, the new cycle, with a maximum in ω_o at noon, predominates.

Negative vertical errors enhance the fictitious cycle since ω_o at large solar zenith angles is increased while it is reduced at short solar zenith angles. Differences between short and large zenith angles in ω_o are around: $0.02 - 0.03$ (depending on the wavelength) for 0.2° of pointing error, $0.04 - 0.05$ for 0.4° and up to 0.08 for 1°. On the other hand, the imaginary part of the refractive index, represented in figure 5.22, has the same pattern, but with opposite variations than the single scattering albedo for vertical errors in almucantar retrievals. Differences between short and large solar zenith angles have similar values than for Lanai and Solar Village case: up to 0.002 for 0.2°, up to 0.003 for 0.4° and up to 0.005 for 1°. It is interesting to observe that differences in both cycles, single scattering albedo and imaginary part of refractive index, are more pronounced for lower aerosol load.

Continuing with the vertical error analysis, let us consider now their effects on the principal plane for single scattering albedo and imaginary refractive index retrievals. Positive errors produced

negative differences in radiance, figure 5.4, therefore, it is not surprising that the single scattering albedo diminishes, and the imaginary part of refractive index becomes higher. As negative errors induced positive differences in radiance, the effects are opposite in this second case for both parameters. For the single scattering albedo, increases and decreases are almost identical and are about 0.01 for 0.2° of vertical pointing error, 0.02 for 0.4° and up to 0.04 for 1°, being always maximum at the 1020 nm wavelength. For the imaginary part of the refractive index, variations are almost non visible for 0.2°, smaller than 0.001 for 0.4°, and up to 0.0015 for 1°, though they create some instability in the latter case.

Again, the horizontal errors go practically unnoticed in the products obtained by both almucantar and principal plane retrievals.

As usual, the real part of the refractive index is reserved for analysis in the last part of the section. Results of the simulations can be seen in figure 5.22. Differences in this parameter are insignificant for almucantar simulations for both horizontal and vertical errors. Only when the vertical error is equal to 1°, some fluctuations appear, even though they are considerably smaller than for the previously analyzed aerosols. About the simulations with the principal plane, to see whether variations for vertical errors are like those found for dust (Solar Village) or like those found for oceanic aerosol (Lanai) arouses curiosity. This curiosity is clarified already in the first subfigure, for 0.2° error, in which the decrease of the refractive index for positive errors indicates that it will follow the same pattern as in Lanai analysis. Again, the high increase of particles (and fixed optical depth) makes the real part of the refractive index to descend, even though a more simply analysis with only radiances would indicate the opposite result.

For the 1020 nm channel, this influence is minor, but becomes greater as the wavelength is shorter, or on other words, is larger at wavelengths more affected by the fine mode. Needless to say, that for negative errors the explanation above is valid but changing the sign of the variations. Once again the differences are more pronounced for low aerosol load. For the $\tau_{440} = 0.5$ case (dashed lines), the real part of the refractive index is more stable when facing vertical pointing errors, being its differences under 0.2, even for the case of 0.4° error. For 1° error, its differences become more pronounced except at short solar zenith angles; if we look back to figure 5.20, it can be seen that for short solar zenith angles differences in the size distribution were the smallest. But the conclusive proof of the relation between the real refractive index and the fine mode can be seen from the low aerosol optical depth case. For a positive error of magnitude 0.4°, differences in the real part of the refractive index are larger for short solar zenith angles, coinciding with the largest differences in the size distribution. For 1° the differences in the size distribution almost have the same value regardless of the solar zenith angle, and the differences in real refractive index present are also independent of the SZA. Finally, we want to indicate that the real refractive index does not present variations due to horizontal errors in the case of the principal plane retrievals.

5.4.4 Biomass burning (Mongu)

The study of the size distributions of the biomass burning aerosol is not supposed, in theory, to bring interesting novelties, once the behavior of the fine mode was analyzed in the previous case and the differences in radiance between both aerosol types looked quite similar. However, the analysis of the behavior of the single scattering albedo and refractive index could be considered motivating, taking into the account that the absorption of this aerosol is very high, about one order of magnitude larger than for the other aerosol types.

Starting first with the almucantar results, the size distribution does not suffer almost variations in the retrievals obtained with pointing error simulations, as in previous cases. Only for 1° horizontal error the variations in the coarse mode deserve to be mentioned: size distribution rises before $3\mu m$ and decreases after this radius. This is even more visible for $SZA = 15°$ as it was commented in Solar Village and Lanai cases.

Continuing only with the almucantar, the retrievals for vertical and positive pointing errors, the single scattering albedo presents positive increments for short solar zenith angles and negative increments for large solar zenith angles, due to the sign of the radiance differences (positive or negative, respectively figure 5.9), as in all the previously analyzed cases This provokes a daily cycle with a descend of the single scattering albedo at noon.

For negative errors, effects are the opposite and the cycle shows an increase in ω_o at noon. Compared to the previous cases, both cycles and differences for the single scattering albedo, in general, show smaller values than for the other aerosol types. Therefore it can be stated that highly absorbing aerosols give greater stability to the single scattering albedo against pointing errors in almucantar measurements.

Moving on the analysis for the refractive index, in the other three analyzed cases, the real part of refractive index had a similar behavior for vertical errors in almucantar simulated measurements: this parameter hardly varied and the effects were only visible for the case of 1° and short SZA, decreasing the value for positive errors and increasing for negative ones. For the biomass burning the study needs to be separated between the two AOD cases. For the first one $\tau_{440} = 0.4$, the real part of the refractive index has no variations, confirming the idea that for high absorption the behavior of the aerosol properties is more stable regarding pointing issues. However, there are some fluctuations, without a clear pattern, for the case with $\tau_{440} = 0.8$, although these variations are less important than in the previous aerosol types. Looking now at the imaginary part, its variations follow the same pattern as the SZA but with opposite sign as for the other three aerosol cases; the maximum variation of this parameter is 0.005, found for 1° of pointing error (as could be expected). The curious thing is that this variation coincides with those of the other aerosol types; but, given that the absorption is one order of magnitude higher, the relative variation is one order

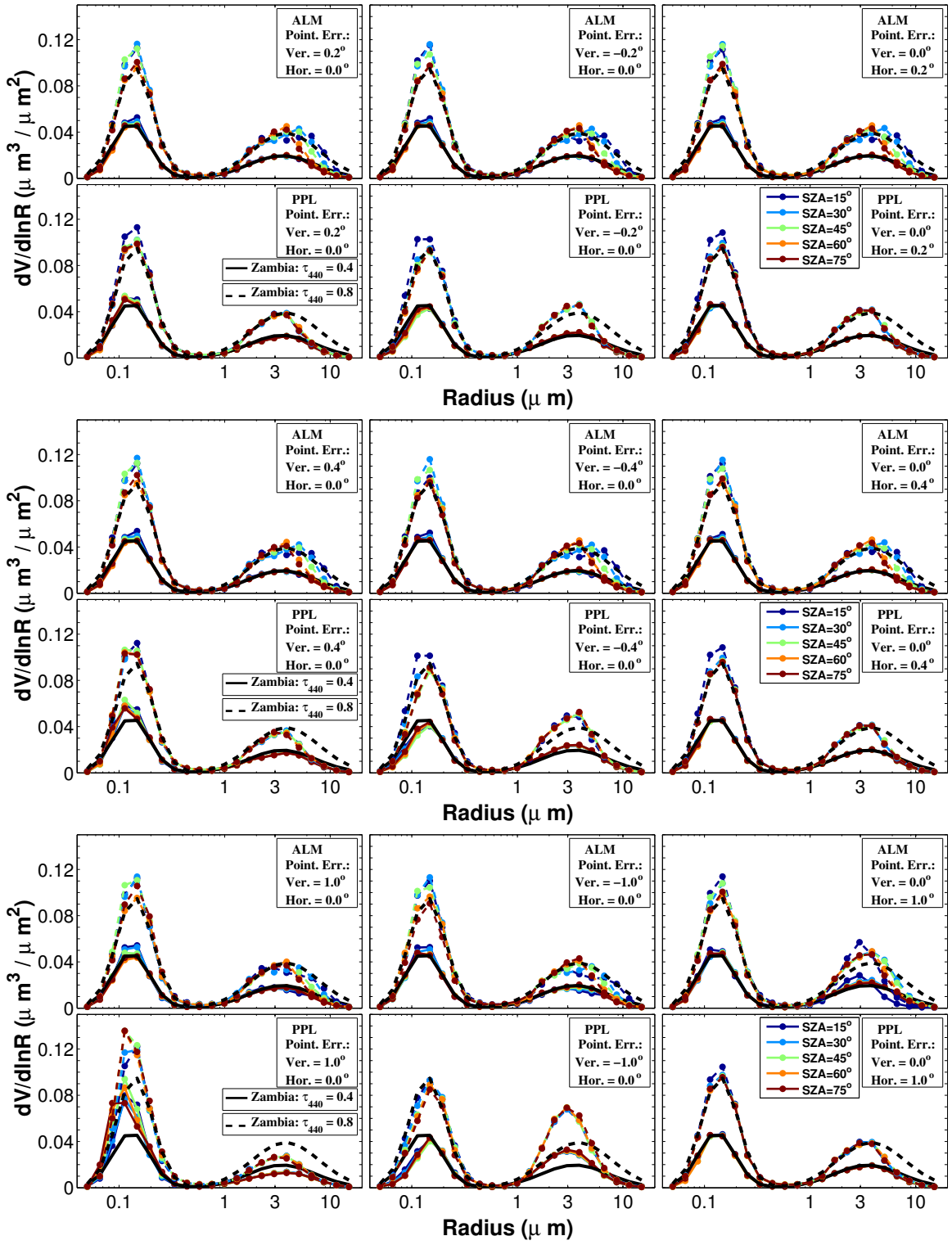

Figure 5.23: Retrieved size distributions for Mongu case after introducing different pointing errors: 0.2° in the figure at the top, 0.4° in the figure in the middle and 1° in the figure at the bottom. In each of the figures, subfigures on top show results from almucantars and at the bottom from principal planes. Subfigures on the left correspond to retrievals with vertical errors, and on the right, to horizontal errors. Solid line is used for the case of $\tau_{440} = 0.4$ and dashed line for $\tau_{440} = 0.8$. Colors indicate the solar zenith angle: dark blue for $SZA = 15°$, light blue for $SZA = 30°$, green for $SZA = 45°$, orange for $SZA = 60°$ and brown for $SZA = 75°$ while black is used for the original size distributions.

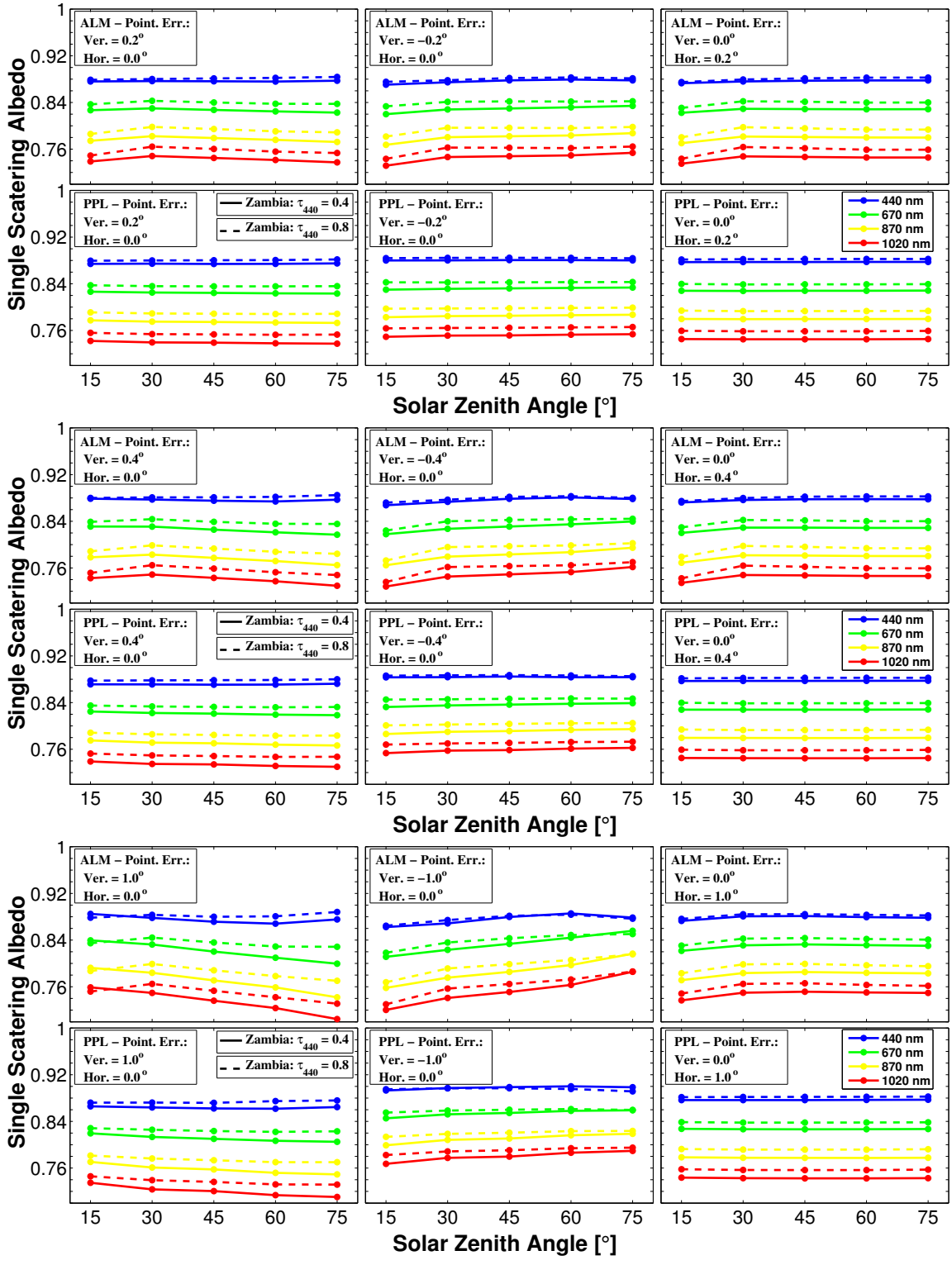

Figure 5.24: Retrieved single scattering albedo for Mongu case after introducing different pointing errors: 0.2° in the figure at the top, 0.4° in the figure in the middle and 1° in the figure at the bottom. In each of the figures, subfigures on top show results from almucantars and at the bottom from principal planes. Subfigures on the left correspond to retrievals with vertical errors, and on the right, to horizontal errors. Solid line is used for the case of $\tau_{440} = 0.4$ and dashed line for $\tau_{440} = 0.8$. Colors indicate the wavelength: blue for 440 nm, green for 670 nm, yellow for 870 nm and red for 1020 nm.

smaller, confirming again the better stability of biomass burning aerosol against pointing errors. For horizontal errors, both parts of the refractive index have the same trend than in the previously analyzed cases, no presenting noticeable changes.

Following the same scheme, now with the principal plane retrievals, let us starting commenting that positive vertical errors have shown well defined implications on the size distribution for the previous cases: the coarse mode has decreased, due to the negative values in radiance relative differences for short scattering angles. More concretely, the decrease has taken place for radii between 1 and $3\mu m$ for desert dust aerosol and between 1 and $4\mu m$ for oceanic aerosol. For biomass burning aerosol, the descend is less pronounced and also for radii between 1 and $4\mu m$. Actually, for larger radii there is not enough information on the implications because the inversion code drastically has reduced the concentration for radii larger than $4\mu m$, as it was commented. On the other hand, the fine mode has raised due to the increase of the backscattering in the other aerosol types. The rise was found for the smallest radii, up to $0.15\mu m$ in oceanic aerosol case and up to $0.2\mu m$ for the urban aerosol case. For the biomass burning, the increment is only visible when the pointing error is 1°, and when the radius is smaller than $0.2\mu m$, as it can be seen in figure 5.23.

For negative vertical pointing errors, the radiance differences and their implications have the opposite sign. Thus, the fine mode was reduced for oceanic and clean urban aerosol for short radii. For the biomass burning aerosol, there is also a reduction, although it is somewhat hidden because error-free simulations also produced fine mode higher than the input. The coarse mode concentration, as in the desert dust and the oceanic case, has a reduction for radii smaller than $4\mu m$, slightly for a 0.4° pointing error value and doubling the input size distribution values when the pointing error rises to 1°.

No significant differences were observed for horizontal errors.

Going on with the single scattering albedo, this had a common pattern in the previous cases: it decreased with positive errors as differences were mostly negative; and with negative vertical errors the situation was the opposite. In the previous cases, increases and decreases were practically symmetrical, with values up to 0.01 for 0.2° of vertical pointing error, 0.02 for 0.4° and up to 0.04 for 1°. In this case, differences are not even visible for 0.2°, smaller than 0.01 for 0.4° and around 0.02 for 1°, showing again that the higher absorption provides greater stability.

Horizontal errors do not introduce any changes for the biomass burning in the single scattering albedo as in the cases studied until.

The result for the imaginary part of the refractive index has followed the same behavior as the single scattering albedo but with the opposite sign in all the aerosol types analyzed until now, and the biomass burning is not an exception. The absolute variations introduced by the pointing errors

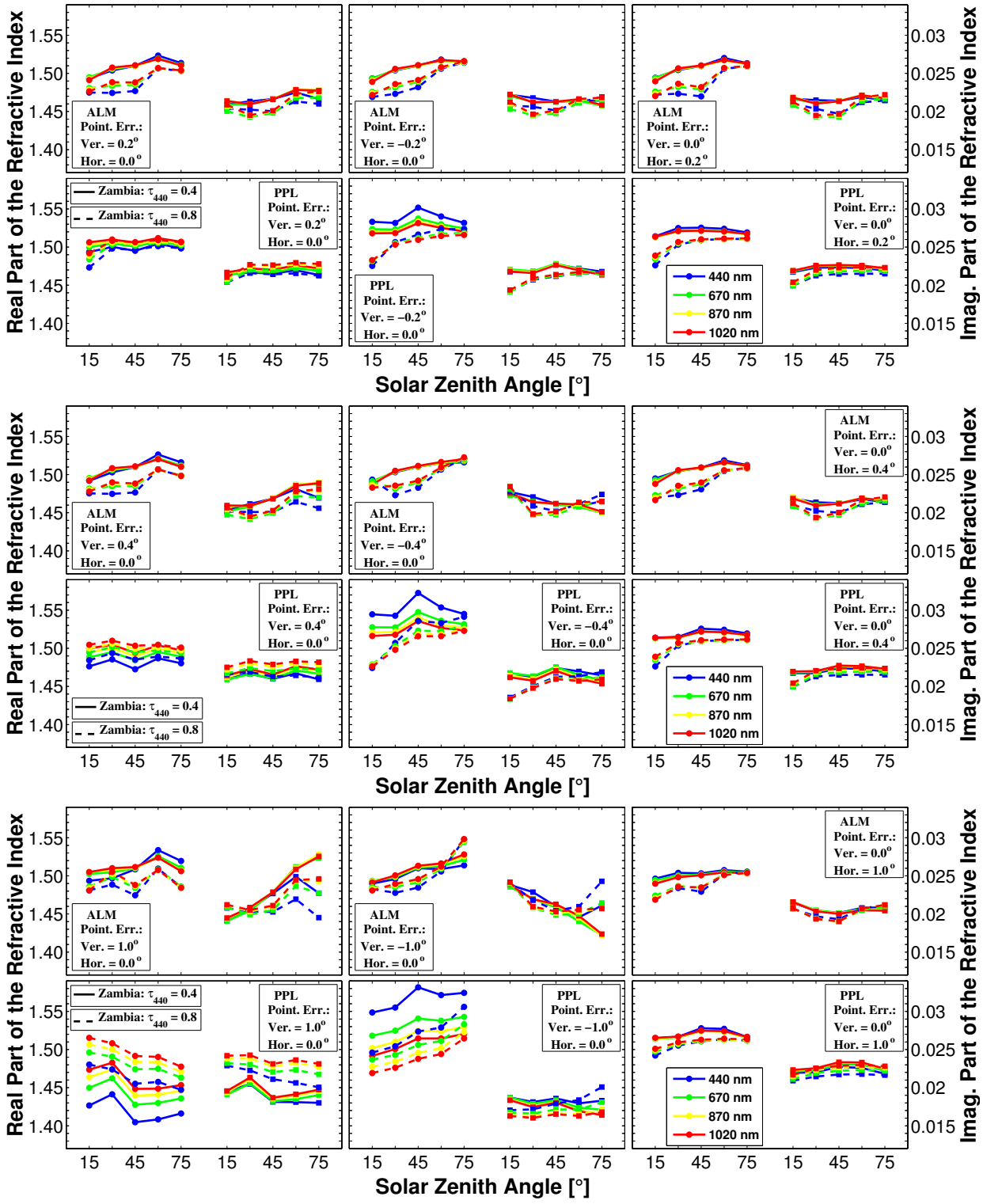

Figure 5.25: Retrieved refractive index for Mongu case after introducing different pointing errors: 0.2° in the figure at the top, 0.4° in the figure in the middle and 1° in the figure at the bottom. In each of the figures, subfigures on top show results from almucantars and at the bottom from principal planes. Subfigures on the left correspond to retrievals with vertical errors, and on the right, to horizontal errors. Solid line is used for the case of $\tau_{440} = 0.4$ and dashed line for $\tau_{440} = 0.8$. Colors indicate the wavelength: blue for 440 nm, green for 670 nm, yellow for 870 nm and red for 1020 nm. Y-Axes express the real refractive index (on the left) and the imaginary refractive index (on the right)

observed in this case are similar to the ones in the previous cases. However, as the the imaginary part of the refractive index is one magnitude order larger for the biomass burning, the relative differences are much less important, as it was fore-mentioned.

The real part of refractive index has presented two different behaviors depending on the aerosol type until now: for desert dust, positive errors provoked positive increments and negative errors negative ones. This fact was perfectly explained by the shape of the radiance differences as a function of the scattering angle. However, for the cases where the fine mode had more importance (oceanic and urban aerosol) the effects were reversed: the strong increment of particles in the fine mode needed a decrease in the real refractive index. Obviously, as it can be seen in figure 5.25, the behavior of the real part of refractive index in the biomass burning aerosol follows the last pattern, because of the importance of its fine mode.

None of the two parts of the refractive index suffers variations due to vertical errors in principal plane simulations.

Chapter 6

Error influence on the inversion of sky radiances III: Finite field of view

Like a plucked and skinny goose.
And as I prepared for bed,
I Asked myself with voice unsteady,
If of all the stuff I read,
I Ever made the slightest use.

James Clerk Maxwell
"A Vision of a wrangler,
of a University, of Pedantry
and of Philosophy."

Resumen en español del capítulo:

En este capítulo se ha desarrollado una metodología para analizar el efecto en las medidas y en los resultados de la inversión al considerar un campo de visión finito. La manera teórica de comprobar dicho efecto viene descrito mediante una convolución de la función respuesta del campo de visión con los valores angulares de la radiancia de cielo. Como en la subsección 3.4.3, se mostró que la respuesta del campo de visión se puede aproximar a un cilindro, la convolución puede ser simplificada en una integral de superficie dentro de la región del campo de visión. En nuestro procedimiento esta integral es sustituida por un suma discreta dividiendo el campo de visión en 17 *areas distribuidas de manera simétrica. Posteriormente se calculan las radiancias para estos* 17 *puntos y se promedia el valor de los mismos.*

Una vez aplicado esta metodología para los campos de visión $1{,}2^\circ$ *(actualmente en la mayor parte de los fótometros en AERONET) y de* $2{,}4^\circ$ *(valor correspondiente a equipos antiguos) se ha demostrado que la influencia de esta limitación instrumental en la medida es pequeña o nula para los tipos de aerosoles considerados, siendo en la práctica despreciable el efecto sobre los productos de inversión.*

6.1 Introduction

The concept of sky radiance can be defined as the radiant flux per unit projected area and per unit solid angle coming from a specified point in the sky (McCluney, 1994). That is why, ideally, the observational solid angle should be infinitesimal. The AERONET inversion code developed by Dubovik and King (2000), which uses radiance measurements as input, assumes this approximation considering the sun-photometer field of view as punctual.

However, as commented in chapter 3 the company CIMEL-Electronique, designer of the sun-photometer CIMEL-318, specifies that the value of the field of view in the actual instruments is 1.2° while in old versions it was 2.4°. The tests made in subsections 3.4.2 and 3.4.3 show that the actual field of view of the sun-photometer is between 1.1°-1.3° in agreement with the company specifications. Unfortunately, non test has been developed yet for old instruments and it remains as a future work.

In this last chapter of the thesis, the errors introduced due to the utilization of a finite field of view in new and old photometers are estimated, and their consequences in the inversion procedure studied.

6.2 Methodology used to analyze the field of view influence

The effect of the finite field of view on the radiance measurement in every observation point is obtained by the convolution of the viewing geometry and the angular values of the sky radiance. In subsection 3.4.3, the tests made with the sun-photometer CIMEL-318 showed that the response of its field of view can be approximated as a cylinder. Using this result, the convolution is simplified as a surface integral of the radiance function within the field of view region. In our approach, the integral will be substituted by a discrete sum considering 17 points in the field of view range around the observation point, see figure 6.1.

These 17 points corresponds to the centers of 17 identical areas arranged in a symmetric distribution: a central circle plus 2 annuli divided in 8 portions. In order to obtain a correct division of the field of view in every observation point of the sky, firstly, this scheme is plotted in the zenith, where the representation is straightforward, and secondly, the scheme is transported to the required point through two rotations: one in θ_v and the other one in φ_v, corresponding to the observation angles.

In figure 6.1, the areas and the coordinates of these 17 points are represented considering a field of view of 2.4° and $\theta_v = 10°$ (left) or $\theta_v = 80°$ (right). As a curiosity, observe that for $\theta_v = 10°$, the field of view in the azimuth-axis covers 15° while the in the zenith-axis covers 2.4°. On the other

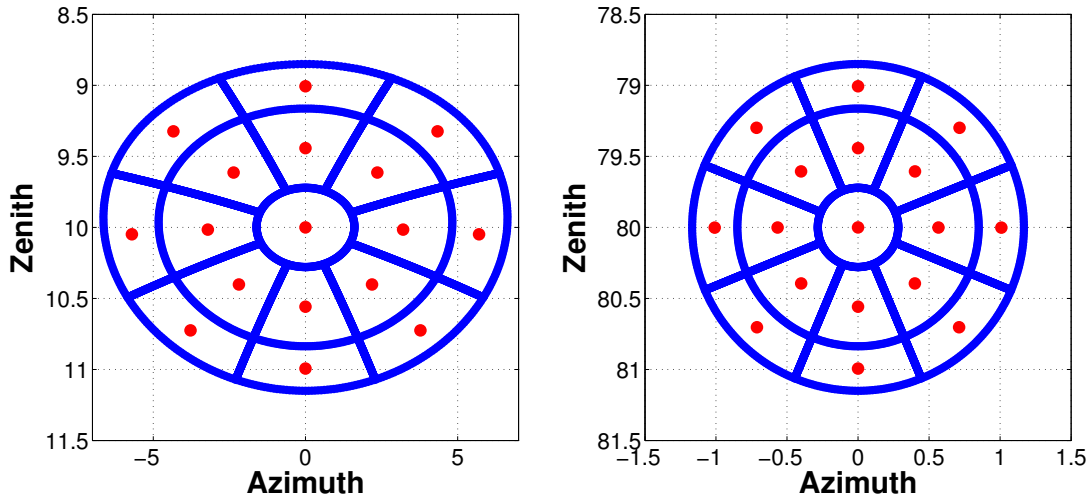

Figure 6.1: Representation of the 17 point-scheme followed to simulate the effects of a finite field of view on the radiance measurements. In both figures the field of view is 2.4°, on the left, $\theta_v = 10°$, and on the right $\theta_v = 80°$. For both cases $\varphi_v = 0°$, even though the representation does not depend on $varphi_v$ (it is just a translation).

hand, in the plot with $\theta_v = 80°$ the field of view covers around 2.4° in both axes.

As the areas are chosen in order to be equal, the fore-mentioned surface integral (needed to estimate the radiance value of every point in the sky considering that the sun-photometer has a finite field of view) is approximated by averaging the sky radiance values obtained in the 17 selected points.

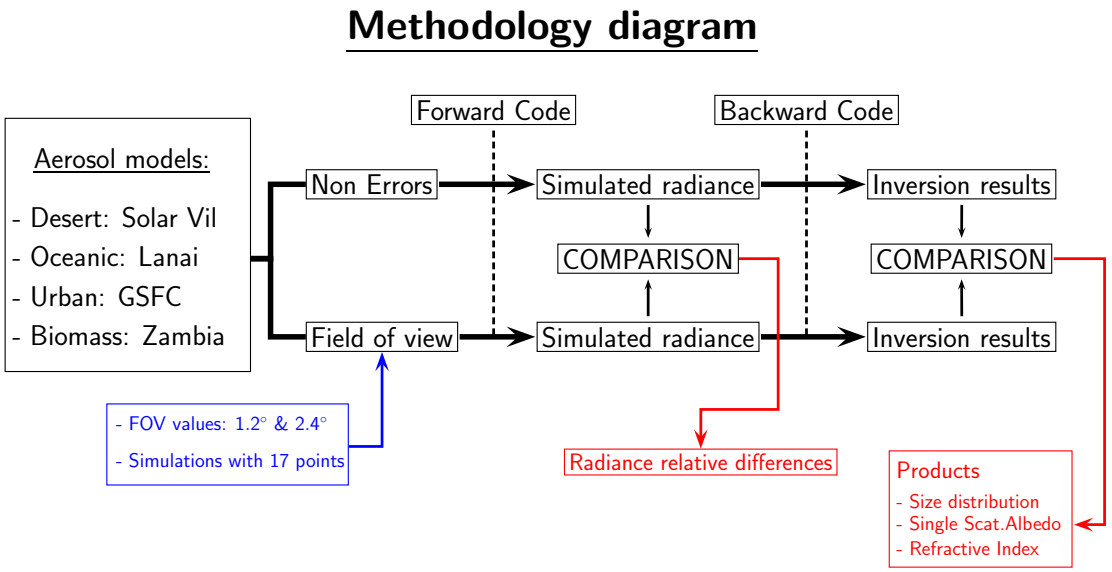

Figure 6.2: Methodology diagram followed to carry out the simulations in order to check the effects of a finite field of view on Dubovik's inversion

Figure 6.2 shows the work-flow followed in the study. The test are done considering values of

the field of view of 1.2° or 2.4° in every measurement point for the almucantar and for the principal plane geometries. As in previous chapters, the study is done using the 8 aerosol examples described in chapter 2 and for the same 5 solar zenith angles (15°, 30°, 45°, 60° and 75°).

The radiance value in the central point of the 17 points-scheme is the same as the one the in non-error data set used in previous sections and it is used as the reference value to calculate the relative differences introduced by the finite field of view, in a first step. Then, the averaged radiances are introduced in the backward module of Dubovik's code and the retrievals compared to the ones obtained without accounting the effects of a finite field of view.

6.3 Consequences on radiance measurements

The Laplacian in a point of a surface can be understood as the difference between the value of the surface in that point and the average of the values in the surrounding points. The scheme followed here in order to simulate the effects of the field of view does the average of the values around the observation point. If now, in order to obtain the relative difference, we compare the average radiance value with the value in the point, this could be considered as the proxy of the Laplacian of the radiance function in the observation point[1].

In one dimension the analogy term of the Laplacian is the second derivative which gives the character, concave or convex, of the function in a certain point. The Laplacian offers a similar information but considering a surface instead of a line. As a consequence, the relative differences obtained in this analysis will give us an idea if the radiance (as a surface) has a concave or convex form, or simply, if the sky point under analysis is higher or lower that the average of the points around. Note that the relative differences in the almucantar due to the horizontal errors were expressed in terms of the second derivative, and considering that the zenith variations have a much lower importance in the almucantar, we should expect a certain resemblance between the relative differences produced by the horizontal pointing error and the one obtained from the field of view study given here.

Figure 6.3 represents the radiance relative difference between the test made simulating the effect of the field of view and the so-called non error data set for the aerosol type GSFC and using both geometries: almucantar (figure at the top) and principal plane (figure at the bottom). Equivalent to the figures in chapter 5, every figure is subdivided in three parts with different values of SZA ($SZA = 15°, 45°$ and 75°). The cases SZA=30° and SZA=60° are skipped for simplicity.

As it was expected, differences represented at the top of figure 6.3 show a certain resemblance with the ones plotted at the top of figure 5.12. This fact confirms that for the almucantar, the

[1] Observe that the center point is included in the average, and among other things, it does not allow a mathematical description, contrary to the case of pointing error in subsection 3.5

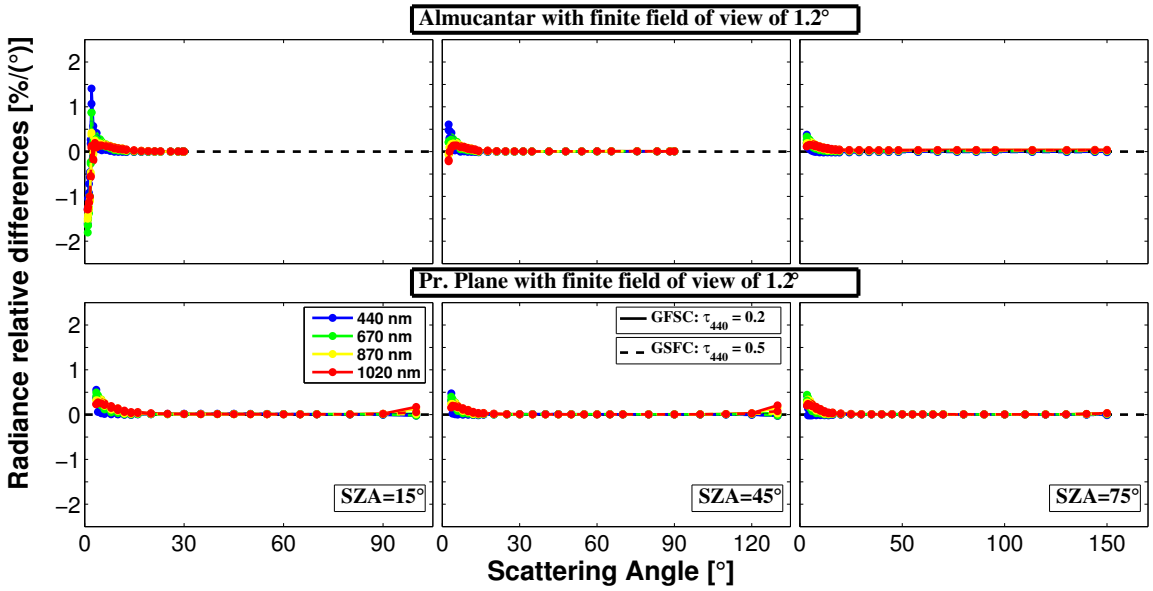

Figure 6.3: Radiance relative error obtained simulating the effects of a finite field of view of 1.2° in almucantar (upper part) and principal plane (bottom part). GSFC (urban) aerosol was taken for the tests using two different AOD: $\tau_{440} = 0.2$ (solid line) and $\tau_{440} = 0.5$ (dashed line). From left to right, SZA increases for the different figures (note the different range in scattering angle as SZA increases).

differences obtained in the study of the field of view look quite similar to the ones obtained in the study of the horizontal pointing error. The discrepancies between them appear for very short scattering angles where the zenithal variations acquire larger importance. Indeed, the zenithal variations are relevant in the almucantar geometry only for short scattering angles, where the radiance present in this coordinate a strong maximum[2] which results in negative values of the radiance relative differences in the field of view simulations. Continuing with the analogies presented in the beginning of the section, here it is obvious that these negative values are caused by the negative value in the second derivative partial of the radiance respect to the zenith angle.

Once the scattering angles become larger than 3°, the two figures (the two at the top in figure 5.12 and figure 6.3) are very similar and the unique discrepancy between them is the total value of the differences. We should remember here, that the differences represented in figure 5.12 were per degree of pointing error. Comparing them with the values in figure 6.3, we could conclude that the differences in figure 6.3 would correspond to a horizontal pointing error around 0.3°.

The maximum absolute value of the differences for the almucantar analysis is around 2% and is obtained at $SZA = 15°$ when the scattering angle is very short coinciding with the region where the zenith angle variations have a greater importance. There is a second peak when the scattering angle becomes larger, in this case with a positive value and around 1.5%. For scattering angles higher than 15°, the differences are practically negligible. For the other SZA represented in the figure, the differences are always smaller than 0.6%.

[2]Note that this maximum was already mentioned in subsection 5.3.2 causing the need of dividing the vertical pointing error analysis on the almucantar in positive and negative pointing errors.

The field of view study for the principal plane, represented at the bottom in figure 6.3, does not show any similarities with any of the pointing errors analysis. The differences obtained are always positive and only noticeable for short scattering angles. Nevertheless the values are always under 0.6%.

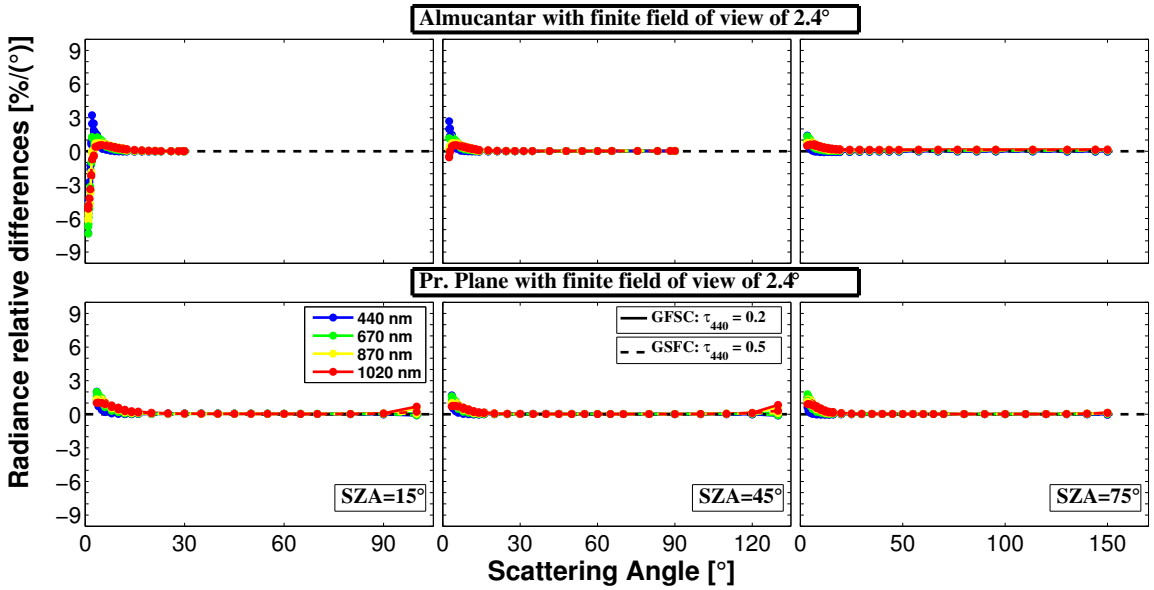

Figure 6.4: Radiance relative error obtained simulating the effects of a finite field of view of 2.4° in almucantar (upper part) and principal plane (bottom part). GSFC (urban) aerosol was taken for the tests using two different AOD: $\tau_{440} = 0.2$ (solid line) and $\tau_{440} = 0.5$ (dashed line). From left to right, SZA increases for the different figures (note the different range in scattering angle as SZA increases).

The second analysis, illustrated in figure 6.4, corresponds to the simulations made considering a field of view of 2.4°. The figure has the same scheme as the one in figure 6.3 and the differences obtained using the almucantar geometry are represented at the top while for the principal plane are plotted at the bottom.

Similarly to the previous case, the differences in the almucantar are more significant when $SZA = 15°$. Again for this case, the differences can be separated in two regions: the first one for very short scattering angles where the variations in the zenith angle are relevant which make the relative differences to be negative and also the highest in absolute value. When the scattering angle is larger than 3°, the differences have the same aspect as the differences derived in the analysis of horizontal pointing errors in the almucantar; the values are positive and noticeable for short scattering angles and negligible once the scattering angle becomes higher than 15°. Observe that in this second region the differences present a certain linearity with the size of the field of view considered, being the maximum value for this region around 3%. On the other hand, the maximum value obtained when the scattering angle is smaller than 3° is much higher than twice as the one obtained in the analysis for a field of view of 1.2°: in figure 6.4, the differences reach almost 8% while in figure 6.3 they were just around 2%.

Radiance relative differences for the principal plane accounting the effects of a field of view

of 2.4° look quite similar to the ones achieved in the previous analysis. The values are always positive and only significant when the scattering angle is relatively small; in this case, the maximum difference are around 2%.

The idea that the relative differences produced by the field of view are not important underlies in all the results presented until here. In fact, only the differences obtained for the simulations made using the almucantar geometry and for very short scattering angles were said to be significant. We are not going to present here the differences for the rest of the aerosol cases because are quite similar to the ones obtain for GSFC and they would not add anything distinct. The reason why we have selected the case with the urban aerosol (GSFC) is because it presents the highest differences, even though, as we commented, they are similar to the rest.

6.4 Consequences on inversion results

In the previous section, we concluded that the differences obtained considering the finite field of view were quite small in general terms. Therefore, we should not expect here to get important consequences on the inversion results. In fact, radiance relative differences for almucantar simulating a field of view of 1.2° were said to be similar to the ones that we would achieved simulating a horizontal pointing error of 0.3° and we already saw in chapter 5 that a horizontal error of 0.4° did not have any perceptible changes in the inversion retrievals so the consequences here should not be noticeable. For the principal plane where the differences were even lower, the result is expected to be the same.

In the same format that the inversion retrievals were presented for the self-consistency analysis in chapter 2, the retrievals for the field of view simulations for urban aerosol are plotted in figure 6.5. From left to the right are represented the results obtained for the size distribution, the single scattering albedo and the refractive index. Results obtained with almucantar geometry are shown in the upper part while results from simulations with principal plane are placed at the bottom.

Comparing the retrievals illustrated in figure 6.5 and the ones achieved in the self-consistency study in chapter 2 (figure 2.5), we do not observe any differences. It can be concluded, therefore, that the actual field of view of 1.2° do not include any variations respect to the non-error case.

On the other hand, the results for a field of view of 2.4° are plotted in figure 6.6. In this second case, the variations respect to the non error data set are only relevant for the real part of the refractive index. Thus, in the almucantar, the results obtained for $SZA = 15°$ are around 3% lower than in the self-consistency analysis, for the rest of the SZA the differences are negligible. For the principal plane, the real part show small oscillations, under 3%, but they appear for all the SZA.

The results for the other aerosol types are not illustrated. As in the case of the radiance

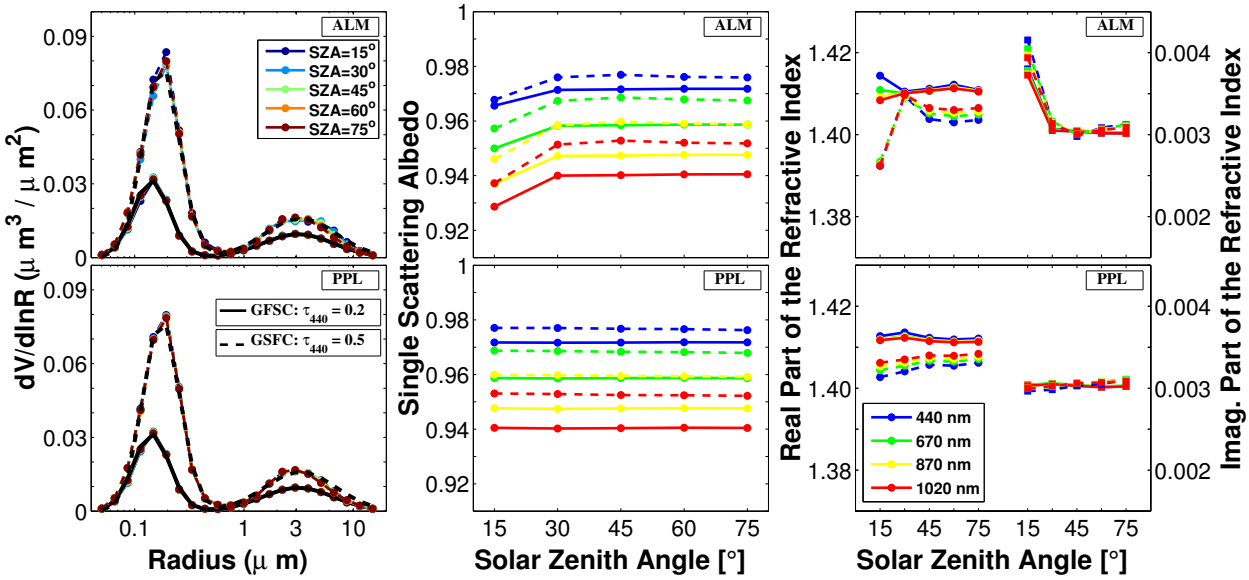

Figure 6.5: Summary of aerosol products obtained for the study of the effects of a field of view of 1.2°, using urban aerosol type (GSFC site) with two different AOD: $\tau_a(440) = 0.2$ (solid line) and $\tau_a(440) = 0.5$ (dashed line): in the upper part almucantar results are shown whereas principal plane results are presented in the bottom part. Figures on the left correspond to size distribution results. Figures in the center illustrate the results for the single scattering albedo, and figures on the right describe the results for the refractive index.

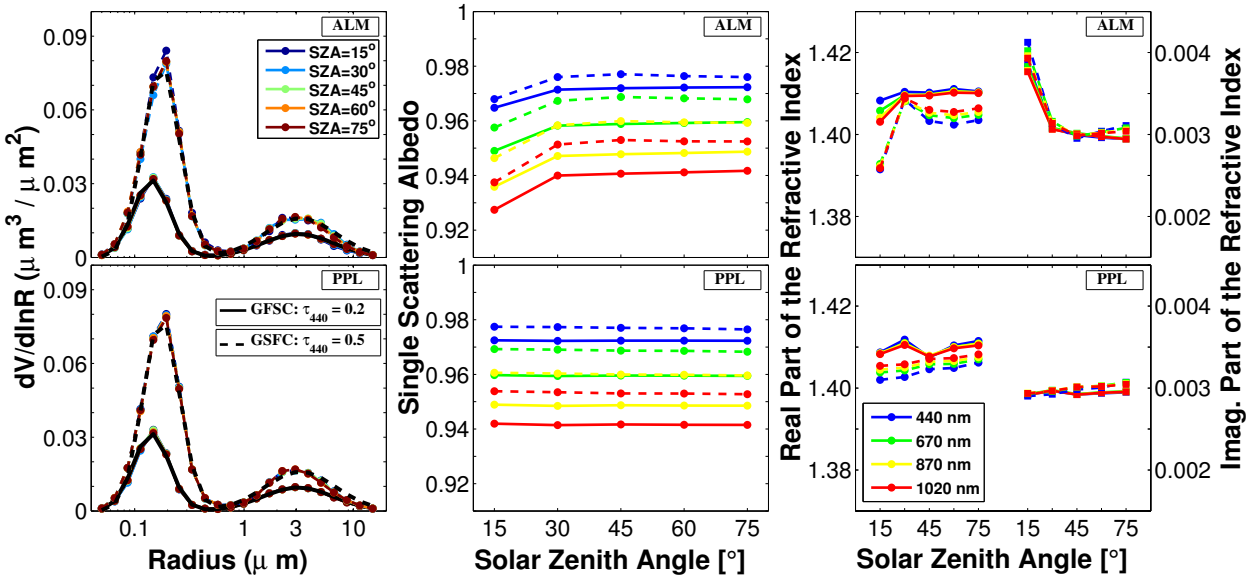

Figure 6.6: Summary of aerosol products obtained for the study of the effects of a field of view of 2.4°, using urban aerosol type (GSFC site) with two different AOD: $\tau_a(440) = 0.2$ (solid line) and $\tau_a(440) = 0.5$ (dashed line): in the upper part almucantar results are shown whereas principal plane results are presented in the bottom part. Figures on the left correspond to size distribution results. Figures in the center illustrate the results for the single scattering albedo, and figures on the right describe the results for the refractive index.

differences, they do not provide anything new and the results gotten in the GSFC can be extended for them: there are no differences for the field of view of 1.2° and only small variations in the real part of the refractive index are observed for the case with a field of view of 2.4°.

Conclusions (English)

To believe is very dull. To doubt is intensely engrossing. To be on the alert is to live. To be lulled into security is to die.

Oscar Wilde

Conclusions

As explained in the Introduction, two main objectives were in the scope of this PhD work. First, we intended to find the reason behind the observed discrepancies between almucantar and principal plane retrievals, investigating whether they could be caused by errors in the radiance measurements. After the analyses in chapters 4, 5 and 6, the only error that could cause the discrepancy is the pointing error, since it affects more the principal plane (especially the vertical error), whereas the almucantar is less affected, at least for the typical errors that were considered in our analysis (0.2° y 0.4°).

The second objective was to find out the reason why the retrievals at low solar zenith angles are different than those at large SZA. The self-consistency test performed in chapter 2 demonstrated that, even for simulated measurements without error, aerosol retrievals at low SZA are distorted due to the lack of information of scattering angles larger than 2·SZA in the almucantar measurements. The analysis in chapter 4 also shows that calibration errors have more influence on the retrievals at low SZA, therefore they can amplify the differences between retrievals al low and large SZA.

In chapter 2 it was also described the influence on the sky radiance of particle properties such as the complex refractive index and the size distribution. Our study shows that certain parameters, like the real part of the refractive index, change the shape of the radiance as a function of the scattering angle, whereas the imaginary part affects the value of the radiance but not its angular distribution. Same as it is considered in AERONET, the particles sizes that have larger influence on the radiance are those in the range 0.2-0.6 μm. Outside that range, especially for radii below

0.2 or above 5 μm, the radiance is less affected and the inversion procedure is less sensitive. The spectral channel at 440 nm wavelength shows in general the largest variations due to changes in the investigated aerosol properties, therefore the accuracy in the measurement of this channel, therefore its calibration, has especial relevance.

In chapter 3 the sun photometer pointing error was defined and described for the different geometries. Furthermore, a procedure to evaluate the pointing error was developed, based on the matrix and cross measurements. Both types of measurements yield to equivalent results, therefore the cross measurements were added to the routine operation of Cimel photometers within RIMA network, in order to provide monitoring of the pointing accuracy during field deployment. These measurements also allow detecting operation issues in the robot or the quadrant detector. The field of view of one instrument was evaluated with two methods: matrix measurements using the Sun as a source and a laser source in the laboratory. Both procedures agree within 5%.

Calibration errors were investigated in chapter 4. The analysis showed that calibration errors have less influence with increasing solar zenith angle and aerosol optical thickness, in clear agreement with the AERONET level 2.0 criteria for data quality assurance. The study by Dubovik et al. (2000) about calibration error did not consider the possibility of having different errors in the different channels and wavelgths. It only considered the extreme cases in which all channels would have -5% o $+5\%$ error. It has been demonstrated that the consideration of independent errors for each channel is necessary for the correct estimation of the uncertainty in the size distribution retrieval both for almucantar and principal planes, especially regarding the coarse mode. Actually the aureole/sky discrepancies generate more instability in the retrieval at larger solar zenith angles.

The uncertainty in the inversion retrieved properties are really large for parameters such as the complex refractive index if a 5% accuracy in the radiance is considered. This fact shows the necessity of increasing the calibration accuracy. There must also exist exhaustive monitoring of the coherence between aureole and sky channels, in a close collaboration between network and site managers.

The pointing error study in chapter 5 has simulated the effect of horizontal and vertical (positive and negative) pointing errors on almucantar and principal plane measurements. The most relevant case is the vertical error in principal plane measurements. The pointing error affects differently almucantars and principal planes, what can be an explanation for discrepancies in the derived products. This error changes the shape of the observed radiance as a function of the scattering angle and could explain, together with the undesired effects at low SZA, the artefacts in the retrievals such as that shown for the Hamim site.

In chapter 6 we developed a methodology to investigate the effect of the finite field of view on the radiance measurements. This instrumental limitation in the radiance measurement has been shown to be small or negligible for the investigated cases, which means that in practice it does not

affect the retrieved aerosol products.

Finally we want to remark that most of the investigated errors are more relevant for the desert dust aerosol type: the coarse mode has the worst behaviour in the self-consistency test; the least sensitive to the inversion procedure; and the most affected by calibration errors. These facts, together with the particle non-sphericity, can explain why this aerosol type presents the largest complications in the retrieval of properties from sky radiances.

Outlook

- Extend the analysis to other parameters such as the phase function, asymmetry parameter, etc.
- Apply the knowledge to real observations: to compare radiances from co-located instruments and inversion results depending on observed pointing errors, etc.
- Study the differences between radiances simulated with the forward module and those retrieved by the inversion module. Next step would be comparing the measured radiances with those retrieved by the inversion module.
- Implement in CAELIS the use of cross measurements to monitor and correct pointing errors, as well as detect operation issues in the instruments.
- Develop a procedure to estimate the horizontal and vertical error on the basis of the almucantar and principal plane data. It could be verified by means of the cross scenarios. This point is of great interest because it would allow correcting data from the past.
- Apply the vicarious method to estimate the field of view and enhance the study with the three methods (matrix with sun, laser and vicarious) using several instruments.
- Investigate with simulations whether the use of other spectral channels, such as the 1640 nm or ultraviolet channels, could enhance the retrieval of the coarse or the fine mode regions of the size distribution. Comparisons with other sources of data, such as in situ observations, could be accomplished.

Conclusiones y líneas futuras (Spanish)

Y así, del mucho leer y del poco dormir, se le secó el celebro de manera que vino a perder el juicio.

Miguel de Cervantes Saavedra

Conclusiones

Como se explica en la introducción, la tesis partía con dos objetivos principales. El primero era intentar justificar las discrepancias encontradas entre las propiedades de los aerosoles derivadas de las inversiones de plano principal y almucantar, analizando si estas se pueden atribuir a errores en la medida de la radiancia. Después del análisis realizado en los capítulos 4, 5 y 6, el único error que podría justificar estas diferencias es el error de apuntamiento, puesto que afecta de manera más acusada al plano principal (que es más susceptible a dicho error, especialmente en el caso del error vertical), mientras que el almucantar no se ve afectado, al menos para el análisis teórico de los errores típicos (0.2° y 0.4°).

El segundo de los objetivos era encontrar la razón que justificase las diferencias entre las propiedades ópticas de los aerosoles obtenidas en condiciones de bajo SZA, frente a aquellas derivadas en condiciones de SZA grandes. El análisis de auto-consistencia realizado para los distintos tipos de aerosol en el capítulo 2 permite concluir que, incluso utilizando medidas simuladas sin error, las propiedades ópticas de los aerosoles obtenidas a bajos SZA se ven adulteradas debido principalmente a la falta de información proveniente de ángulos de scattering superiores a 2·SZA en las medidas de almucantar. El análisis del capítulo 4 añade además que cuando existen errores en la calibración, estos se manifiestan en mayor medida cuando el SZA es menor, pudiendo acrecentar así, las diferencias entre las inversiones realizadas a bajos y altos SZA.

En el capítulo 2 también se ha descrito la influencia sobre la radiancia del índice de refracción real e imaginario y la distribución de tamaños. Este estudio muestra cómo cambios en ciertos parámetros, como el índice de refracción real, cambian la forma de la radiancia en función del ángulo de scattering,

mientras que la parte imaginaria afecta básicamente al valor de la radiancia, pero no a su distribución angular. Tal y como se considera en AERONET, los tamaños que más influyen en la radiancia (y por tanto los que se obtienen de forma más estable en la inversión) son los comprendidos entre 0.2 y 0.6 μm. Fuera de ese rango, en especial por debajo de 0.2 μm y por encima de 5, la radiancia se ve poco afectada y el procedimiento de inversión es poco sensible. El canal espectral de 440 nm es el que presenta en general mayores variaciones con los distintos parámetros, por lo que la precisión en la medida de esta longitud de onda, y por tanto su calibración, es de especial relevancia.

En el capítulo 3 se ha definido y descrito el error de apuntamiento de los fotómetros en función de la geometría de observación. Así mismo se ha desarrollado un procedimiento para evaluar el error de apuntamiento a partir de las medidas al sol de los escenarios matriz y cruz. Ambas medidas producen resultados equivalentes, lo cual ha llevado a instalar en los fotómetros de RIMA medidas rutinarias de cruz para monitorizar el apuntamiento durante su período de medidas en estación. Este escenario permite además detectar problemas de funcionamiento en el robot seguidor o el detector de cuadrante que apunta al sol. Además se ha evaluado para un fotómetro el campo de visión mediante dos métodos: medidas del escenario matriz usando como fuentes el sol y un laser en el laboratorio, encontrándose un acuerdo mejor del 5% entre ambos procedimientos.

Los errores de calibración han sido analizados en el capítulo 4. El análisis muestra una menor incidencia de los errores en la calibración de los distintos canales espectrales si aumentan el espesor óptico de aerosoles o el ángulo cenital solar, en claro acuerdo con los criterios aplicados en AERONET a los datos de calidad asegurada (nivel 2.0). Los errores de calibración han sido analizados en el capítulo 4. El análisis muestra una menor incidencia de los errores en la calibración de los distintos canales espectrales si aumentan el espesor óptico de aerosoles o el ángulo cenital solar, en claro acuerdo con los criterios aplicados en AERONET a los datos de calidad asegurada (nivel 2.0). El estudio de Dubovik et al. (2000) sobre este error no consideró la posibilidad de la posibilidad de errores diferentes para distintos canales y longitudes de onda, tratando sólamente los casos extremos, donde todos eran o $-5\,\%$ o $+5\,\%$. Se ha demostrado que esta consideración es necesaria para estimar de forma correcta la influencia de la calibración en la obtención de la distribución de tamaños en medidas tanto de almucantar como de plano principal, sobre todo el modo grueso.

Los errores en los productos derivados de la inversión son realmente grandes en parámetros como el índice de refracción si la radiancia tiene una precisión del 5%. Esto pone de manifiesto la necesidad de hacer un mayor esfuerzo en la precisión de la calibración. También debe existir un buen control de la coherencia entre las medidas de los canales de "sky" y "aureola", lo que está muy relacionado con un control rutinario de las medidas en coordinación con los responsables de la estación.

El estudio sobre el error de apuntamiento en el capítulo 5 ha simulado el efecto de errores horizontales y verticales (positivos y negativos) para las geometrías de almucantar y plano principal. El caso más relevante es el error vertical en el plano principal. El error de apuntamiento afecta de forma diferente al

almucantar y al plano principal, lo cual puede explicar que haya diferencias entre los productos derivados. Este error cambia la forma de la radiancia observada en función del ángulo de scattering y podría, junto con el efecto de reducción de información a bajo SZA, producir artificios en los resultados de la inversión como los mostrados para la estación de Hamim.

En el capítulo 6 se ha desarrollado una metodología para analizar el error de las medidas debido al campo de visión finito. La influencia de esta limitación instrumental en la medida de la radiancia se ha demostrado pequeña o nula para los casos considerados, siendo en la práctica despreciable el efecto sobre los productos de inversión.

Por último, hemos de destacar que la mayoría de factores analizados muestran su peor comportamiento en el caso del aerosol desértico: el modo grueso es el que peor responde al test de auto-consistencia; el que muestra menos sensibilidad en la inversión; y el más afectado por errores de calibración. Todo esto, añadido a la no-esfericidad de las partículas, explica por qué este tipo de aerosol es el más complicado para extraer propiedades mediante la inversión de radiancias.

Líneas futuras

- *Extender el análisis teórico a otros parámetros como la función de fase, parámetro de asimetría, etc.*
- *Aplicar los conocimientos adquiridos a casos reales: comparar radiancias entre distintos fotómetros que midan en la misma estación; comparar los resultados de las inversiones en función de error de apuntamiento que se observe, etc.*
- *Estudiar las diferencias entre radiancias simuladas (provenientes del módulo forward) y las que se obtienen tras la inversión (provenientes del módulo backward). Así mismo, comparar las radiancias observadas en casos reales con las que se obtienen como producto de la inversión, en particular en función del ángulo de scattering y del tipo de aerosol.*
- *Usar las medidas de las "cruces" en CAELIS para controlar y corregir errores de apuntamiento, así como detectar problemas en el funcionamiento de los fotómetros.*
- *Desarrollar un procedimiento que obtenga error apuntamiento horizontal y vertical a partir de las medidas de almucantar y plano principal, verificándolo con los escenarios "cruz". Esto es de gran interés porque permitiría corregir errores de apuntamiento en series pasadas.*
- *Utilizar el método vicarious para sacar el FOV y completar el estudio con los tres métodos (matrix al sol, laser y vicarious) y más fotómetros.*
- *Investigar si mejoran las inversiones de aerosol desértico con la utilización del canal de 1640 nm, así como posibles medidas de radiancia en el ultravioleta (sobre todo para el modo fino) mediante*

simulaciones. También se podrían realizar comparaciones con otras fuentes de información, como medidas in situ.

Bibliography

Mas sabe el diablo por Google que por diablo.

Jesús de la Fuente

Angstrom, A. Techniques of determining the turbidity of the atmosphere. *TELLUS*, vol. 13(2), pages 214–223, 1961. ISSN 0040-2826.

Berjon, A. Determinacion de parametros biofisicos de la cubierta vegetal mediante inversion de modelos de transferencia radiativa. 2007.

Bohren, C. and Huffman, D. *Absorption and Scattering of Light by Small Particles*. John Wiley & Sons Inc, 1983. ISBN 0-471-05772-X.

Cachorro, V. E., Toledano, C., Berjon, A., de Frutos, A. M., Torres, B., Sorribas, M. and Laulainen, N. S. An "in situ" calibration correction procedure (KCICLO) based on AOD diurnal cycle: Application to AERONET - El Arenosillo (Spain) AOD data series. *JOURNAL OF GEOPHYSICAL RESEARCH-ATMOSPHERES*, vol. 113(D12), 2008. ISSN 0148-0227.

Claquin, T., Schulz, M., Balkanski, Y. and Boucher, O. Uncertainties in assessing radiative forcing by mineral dust. *TELLUS SERIES B-CHEMICAL AND PHYSICAL METEOROLOGY*, vol. 50(5), pages 491–505, 1998. ISSN 0280-6509.

Coulson, K. *Polarization and intensity of light in the atmosphere*. A. DEEPAK Publishing, 1988. ISBN 0-937194-12-3.

D'Almeida, G., Koepke, P. and Shettle, E. *Atmospheric Aerosols: Global Climatology and Radiative Characteristics*. A.Deepak Publishing, 1991. ISBN 0-937194-22-0.

Dubovik, O. Aerosol retrievals from AERONET sun/sky-radiometers: Overview of inversion principles, products and advances. The Second International Conference of Aerosol Science and Global Change, Hangzhou, China, 2009.

DUBOVIK, O., HOLBEN, B., ECK, T., SMIRNOV, A., KAUFMAN, Y., KING, M., TANRE, D. and SLUTSKER, I. Variability of absorption and optical properties of key aerosol types observed in worldwide locations. *JOURNAL OF THE ATMOSPHERIC SCIENCES*, vol. 59(3), pages 590–608, 2002. ISSN 0022-4928.

DUBOVIK, O. and KING, M. A flexible inversion algorithm for retrieval of aerosol optical properties from Sun and sky radiance measurements. *JOURNAL OF GEOPHYSICAL RESEARCH-ATMOSPHERES*, vol. 105(D16), pages 20673–20696, 2000. ISSN 0747-7309.

DUBOVIK, O., LAPYONOK, T. and OSHCHEPKOV, S. Improved technique for data inversion: Optical sizing of multicomponent aerosols. *APPLIED OPTICS*, vol. 34(36), pages 8422–8436, 1995. ISSN 0003-6935.

DUBOVIK, O., SINYUK, A., LAPYONOK, T., HOLBEN, B. N., MISHCHENKO, M., YANG, P., ECK, T., VOLTEN, H., MUNOZ, O., VEIHELMANN, B., VAN DER ZANDE, W. J., LEON, J., SOROKIN, M. and SLUTSKER, I. Application of spheroid models to account for aerosol particle nonsphericity in remote sensing of desert dust. *JOURNAL OF GEOPHYSICAL RESEARCH-ATMOSPHERES*, vol. 111(D11), 2006. ISSN 0148-0227.

DUBOVIK, O., SMIRNOV, A., HOLBEN, B., KING, M., KAUFMAN, Y., ECK, T. and SLUTSKER, I. Accuracy assessments of aerosol optical properties retrieved from Aerosol Robotic Network (AERONET) Sun and sky radiance measurements. *JOURNAL OF GEOPHYSICAL RESEARCH-ATMOSPHERES*, vol. 105(D8), pages 9791–9806, 2000. ISSN 0747-7309.

DUBOVIK, O., YOKOTA, T. and SASANO, Y. Improved technique for data inversion and its application to the retrieval algorithm for ADEOS/ILAS. In *REMOTE SENSING: INVERSION PROBLEMS AND NATURAL HAZARDS* (edited by Susskind, J and Singhroy, V and Tanaka, S), vol. 21 of *ADVANCES IN SPACE RESEARCH*, pages 397–403. Comm Space Res; World Climate Res Programme; European Space Agcy; NOAA, Natl Environm Satellite Data & Informat Sci; Sci Comm Ocean Res; Int Union Geol Sci; Int Astronaut Federat; Int Decade Nat Disaster Reduct; UNESCO; UN, Off Outer Space Affairs, 1998. ISBN 0-08-043311-1. ISSN 0273-1177. 31st COSPAR Scientific Assembly, BIRMINGHAM, ENGLAND, JUL 14-21, 1996.

ECK, T., HOLBEN, B., REID, J., DUBOVIK, O., SMIRNOV, A., O'NEILL, N., SLUTSKER, I. and KINNE, S. Wavelength dependence of the optical depth of biomass burning, urban, and desert dust aerosols. *JOURNAL OF GEOPHYSICAL RESEARCH-ATMOSPHERES*, vol. 104(D24), pages 31333–31349, 1999. ISSN 0747-7309.

GASTEIGER, J., GROSS, S., FREUDENTHALER, V. and WIEGNER, M. Volcanic ash from Iceland over Munich: mass concentration retrieved from ground-based remote sensing measurements. *ATMOSPHERIC CHEMISTRY AND PHYSICS*, vol. 11(5), pages 2209–2223, 2011. ISSN 1680-7316.

GATHMAN, S. Optical properties of the marine aerosol as predicted by the Navy aerosol model. *OPTICAL ENGINEERING*, vol. 22(1), pages 57–62, 1983. ISSN 0091-3286.

HARTLEY, W., HOBBS, P., ROSS, J., RUSSELL, P. and LIVINGSTON, J. Properties of aerosols aloft relevant to direct radiative forcing off the mid-Atlantic coast of the United States. *JOURNAL OF GEOPHYSICAL RESEARCH-ATMOSPHERES*, vol. 105(D8), pages 9859–9885, 2000. ISSN 0747-7309.

HERMAN, B., BROWNING, S. and REAGAN, J. Determination of aerosol size distributions from lidar measurements. *JOURNAL OF THE ATMOSPHERIC SCIENCES*, vol. 28(5), pages 763–&, 1971. ISSN 0022-4928.

HESS, M., KOEPKE, P. and SCHULT, I. Optical properties of aerosols and clouds: The software package OPAC. *BULLETIN OF THE AMERICAN METEOROLOGICAL SOCIETY*, vol. 79(5), pages 831–844, 1998. ISSN 0003-0007.

HITZENBERGER, R. and RIZZI, R. Retrieved and measured aerosol mass size distributions - a comparison. *APPLIED OPTICS*, vol. 25(4), pages 546–553, 1986. ISSN 0003-6935.

HOLBEN, B., ECK, T., SLUTSKER, I., TANRE, D., BUIS, J., SETZER, A., VERMOTE, E., REAGAN, J., KAUFMAN, Y., NAKAJIMA, T., LAVENU, F., JANKOWIAK, I. and SMIRNOV, A. AERONET - A federated instrument network and data archive for aerosol characterization. *REMOTE SENSING OF ENVIRONMENT*, vol. 66(1), pages 1–16, 1998. ISSN 0034-4257.

HOLBEN, B., TANRE, D., SMIRNOV, A., ECK, T., SLUTSKER, I., ABUHASSAN, N., NEWCOMB, W., SCHAFER, J., CHATENET, B., LAVENU, F., KAUFMAN, Y., CASTLE, J., SETZER, A., MARKHAM, B., CLARK, D., FROUIN, R., HALTHORE, R., KARNELI, A., O'NEILL, N., PIETRAS, C., PINKER, R., VOSS, K. and ZIBORDI, G. An emerging ground-based aerosol climatology: Aerosol optical depth from AERONET. *JOURNAL OF GEOPHYSICAL RESEARCH-ATMOSPHERES*, vol. 106(D11), pages 12067–12097, 2001. ISSN 0747-7309.

HOLBEN, B. N., ECK, T. F., SLUTSKER, I., SMIRNOV, A., SINYUK, A., SCHAFER, J., GILES, D. and DUBOVIK, O. AERONET's Version 2.0 quality assurance criteria - art. no. 64080Q. In *Remote Sensing of the Atmosphere and Clouds* (edited by Tsay, SC and Nakajima, T and Singh, RP and Sridharan, R), vol. 6408 of *PROCEEDINGS OF THE SOCIETY OF PHOTO-OPTICAL INSTRUMENTATION ENGINEERS (SPIE)*, page Q4080. 2006. ISBN 978-0-8194-6515-3. ISSN 0277-786X. Conference on Remote Sensing of the Atmosphere and Clouds, Goa, INDIA, NOV 13-16, 2006.

JUNGE, C. The size distribution and aging of natural aerosols as determined from electrical and optical data on the atmosphere. *JOURNAL OF METEOROLOGY*, vol. 12(1), pages 13–25, 1955.

KANDLER, K., BENKER, N., BUNDKE, U., CUEVAS, E., EBERT, M., KNIPPERTZ, P., RODRIGUEZ, S., SCHUETZ, L. and WEINBRUCH, S. Chemical composition and complex refractive index of Saharan Mineral Dust at Izana, Tenerife (Spain) derived by electron microscopy. *ATMOSPHERIC ENVIRONMENT*, vol. 41(37), pages 8058–8074, 2007. ISSN 1352-2310.

KASTEN, F. and YOUNG, A. Revised optical air-mass tables and approximation formula. *APPLIED OPTICS*, vol. 28(22), pages 4735–4738, 1989. ISSN 0740-3224.

KAUFMAN, Y., TANRE, D., DUBOVIK, O., KARNIELI, A. and REMER, L. Absorption of sunlight by dust as inferred from satellite and ground-based remote sensing. *GEOPHYSICAL RESEARCH LETTERS*, vol. 28(8), pages 1479–1482, 2001. ISSN 0094-8276.

KING, M. and BYRNE, D. Method for inferring total ozonde content from spectral variation of total optical depth obtained with a solar radiomenter. *JOURNAL OF THE ATMOSPHERIC SCIENCES*, vol. 33(11), pages 2242–2251, 1976. ISSN 0022-4928.

KING, M., BYRNE, D., HERMAN, B. and REAGAN, J. Aerosol size distributions obtained by the inversion of spectral optical depth measurements. *JOURNAL OF THE ATMOSPHERIC SCIENCES*, vol. 35(11), pages 2153–2167, 1978. ISSN 0022-4928.

KOEPKE, P., HESS, M., SCHULT, I. and SHETTLE, E. Global aerosol data set. *MPI Meteorologie Hamburg, Report No. 243*, (), page 44, 1997. ISSN 0937-1060.

KOKHANOVSKY, A. A., BUDAK, V. P., CORNET, C., DUAN, M., EMDE, C., KATSEV, I. L., KLYUKOV, D. A., KORKIN, S. V., C-LABONNOTE, L., MAYER, B., MIN, Q., NAKAJIMA, T., OTA, Y., PRIKHACH, A. S., ROZANOV, V., YOKOTA, T. and ZEGE, E. P. Benchmark results in vector atmospheric radiative transfer. *JOURNAL OF QUANTITATIVE SPECTROSCOPY & RADIATIVE TRANSFER*, vol. 111(12-13), pages 1931–1946, 2010. ISSN 0022-4073.

LEVIN, Z., JOSEPH, J. and MEKLER, Y. Properties of Sharav (Khamsin) dust - Comparison of optical and direct sampling data. *JOURNAL OF THE ATMOSPHERIC SCIENCES*, vol. 37(4), pages 882–891, 1980. ISSN 0022-4928.

LIOU, K. N. *An introduction to atmospheric radiation*. Academic Press Inc, 1980. ISBN 0-12-451451-0.

MCCLUNEY, R. *Introduction to Radiometry and Photometry*. ARTECH HOUSE INC , 1994. ISBN 0-89006-678-7.

MICHALSKY, J., LILJEGREN, J. and HARRISON, L. A comparison of sun photometer derivations of total column water vapor and ozone to standard measures of same at the Southern Great Plains Atmospheric Radiation Measurement site. *JOURNAL OF GEOPHYSICAL RESEARCH-ATMOSPHERES*, vol. 100(D12), pages 25995–26003, 1995. ISSN 0148-0227.

MISHCHENKO, M., TRAVIS, L., KAHN, R. and WEST, R. Modeling phase functions for dustlike tropospheric aerosols using a shape mixture of randomly oriented polydisperse spheroids. *JOURNAL OF GEOPHYSICAL RESEARCH-ATMOSPHERES*, vol. 102(D14), pages 16831–16847, 1997. ISSN 0148-0227.

MUELLER, D., ANSMANN, A., FREUDENTHALER, V., KANDLER, K., TOLEDANO, C., HIEBSCH, A., GASTEIGER, J., ESSELBORN, M., TESCHE, M., HEESE, B., ALTHAUSEN, D., WEINZIERL, B., PETZOLD, A. and VON HOYNINGEN-HUENE, W. Mineral dust observed with AERONET Sun photometer, Raman lidar, and in situ instruments during SAMUM 2006: Shape-dependent particle properties. *JOURNAL OF GEOPHYSICAL RESEARCH-ATMOSPHERES*, vol. 115, 2010a. ISSN 0148-0227.

MUELLER, D., WEINZIERL, B., PETZOLD, A., KANDLER, K., ANSMANN, A., MUELLER, T., TESCHE, M., FREUDENTHALER, V., ESSELBORN, M., HEESE, B., ALTHAUSEN, D., SCHLADITZ, A., OTTO, S. and KNIPPERTZ, P. Mineral dust observed with AERONET Sun photometer, Raman lidar, and in situ instruments during SAMUM 2006: Shape-independent particle properties. *JOURNAL OF GEOPHYSICAL RESEARCH-ATMOSPHERES*, vol. 115, 2010b. ISSN 0148-0227.

NAKAJIMA, T., TONNA, G., RAO, R., BOI, P., KAUFMAN, Y. and HOLBEN, B. Use of sky brightness measurements from ground for remote sensing of particulate polydispersions. *APPLIED OPTICS*, vol. 35(15), pages 2672–2686, 1996. ISSN 0003-6935.

OLMO, F., QUIRANTES, A., LARA, V., LYAMANI, H. and ALADOS-ARBOLEDAS, L. Aerosol optical properties assessed by an inversion method using the solar principal plane for non-spherical particles. *JOURNAL OF QUANTITATIVE SPECTROSCOPY AND RADIATIVE TRANSFER*, vol. 109, pages 1504–1516, 2008.

O'NEILL, N., ECK, T., SMIRNOV, A., HOLBEN, B. and THULASIRAMAN, S. Spectral discrimination of coarse and fine mode optical depth. *JOURNAL OF GEOPHYSICAL RESEARCH-ATMOSPHERES*, vol. 108(D17), 2003. ISSN 0148-0227.

PATTERSON, E. and GILLETTE, D. Commonalities in measured size distributions for aerosols having a soil-derived component. *JOURNAL OF GEOPHYSICAL RESEARCH-OCEANS AND ATMOSPHERES*, vol. 82(15), pages 2074–2082, 1977. ISSN 0148-0227.

PHILLIPS, D. A technique for numerical solution of certain integral equations of first kind. *JOURNAL OF THE ACM*, vol. 9(1), pages 84–&, 1962. ISSN 0004-5411.

PRATS, N., CACHORRO, V. E., SORRIBAS, M., MOGO, S., BERJON, A., TOLEDANO, C., DE FRUTOS, A. M., DE LA ROSA, J., LAULAINEN, N. and DE LA MORENA, B. A. Columnar aerosol optical properties during "El Arenosillo 2004 summer campaign". *ATMOSPHERIC ENVIRON-*

MENT, vol. 42(11), pages 2643–2653, 2008. ISSN 1352-2310. Conference on Visibility, Aerosols, and Atmospheric Optics, Vienna, AUSTRIA, SEP 03-06, 2006.

REDA, I. and ANDREAS, A. Solar position algorithm for solar radiation applications (vol 76, pg 577, 2004). *SOLAR ENERGY*, vol. 81(6), page 838, 2007. ISSN 0038-092X.

REID, E., REID, J., MEIER, M., DUNLAP, M., CLIFF, S., BROUMAS, A., PERRY, K. and MARING, H. Characterization of African dust transported to Puerto Rico by individual particle and size segregated bulk analysis. *JOURNAL OF GEOPHYSICAL RESEARCH-ATMOSPHERES*, vol. 108(D19), 2003. ISSN 0148-0227.

REID, J., HOBBS, P., RANGNO, A. and HEGG, D. Relationships between cloud droplet effective radius, liquid water content, and droplet concentration for warm clouds in Brazil embedded in biomass smoke. *JOURNAL OF GEOPHYSICAL RESEARCH-ATMOSPHERES*, vol. 104(D6), pages 6145–6153, 1999. ISSN 0747-7309.

REMER, L., GASSO, S., HEGG, D., KAUFMAN, Y. and HOLBEN, B. Urban/industrial aerosol: Ground-based Sun/sky radiometer and airborne in situ measurements. *JOURNAL OF GEOPHYSICAL RESEARCH-ATMOSPHERES*, vol. 102(D14), pages 16849–16859, 1997.

RUSSELL, P., HOBBS, P. and STOWE, L. Aerosol properties and radiative effects in the United States East Coast haze plume: An overview of the Tropospheric Aerosol Radiative Forcing Observational Experiment (TARFOX). *JOURNAL OF GEOPHYSICAL RESEARCH-ATMOSPHERES*, vol. 104(D2), pages 2213–2222, 1999. ISSN 0148-0227.

SALTELLI, A. Sensitivity analysis for importance assessment. *RISK ANALYSIS*, vol. 22(3), pages 579–590, 2002. ISSN 0272-4332.

SHAW, G. E. Sun photometry. *BULLETIN OF THE AMERICAN METEOROLOGICAL SOCIETY*, vol. 64, pages 4–10, 1983.

SHETTLE, E. and FENN, R. Models of aerosols of lower troposphere and the effect of humidity variations on their optical propoerties. *AFCRL, Technical Report 79 0241*, vol. (), page 100, 1979. ISSN 72-0241.

SMIRNOV, A., HOLBEN, B., ECK, T., DUBOVIK, O. and SLUTSKER, I. Cloud-screening and quality control algorithms for the AERONET database. *REMOTE SENSING OF ENVIRONMENT*, vol. 73(3), pages 337–349, 2000. ISSN 0034-4257.

SMIRNOV, A., HOLBEN, B., ECK, T., SLUTSKER, I., CHATENET, B. and PINKER, R. Diurnal variability of aerosol optical depth observed at AERONET (Aerosol Robotic Network) sites. *GEOPHYSICAL RESEARCH LETTERS*, vol. 29(23), 2002a. ISSN 0094-8276.

SMIRNOV, A., HOLBEN, B., KAUFMAN, Y., DUBOVIK, O., ECK, T., SLUTSKER, I., PIETRAS, C. and HALTHORE, R. Optical properties of atmospheric aerosol in maritime environments. *JOURNAL OF THE ATMOSPHERIC SCIENCES*, vol. 59(3), pages 501–523, 2002b. ISSN 0022-4928.

SOKOLIK, I. and TOON, O. Incorporation of mineralogical composition into models of the radiative properties of mineral aerosol from UV to IR wavelengths. *JOURNAL OF GEOPHYSICAL RESEARCH-ATMOSPHERES*, vol. 104(D8), pages 9423–9444, 1999. ISSN 0148-0227.

SOLOMON, S., QIN, D., MANNING, M., CHEN, Z., MARQUIS, M., AVERYT, K., M., T. and H.L., M. *Technical Summary. In: Climate Change 2007: The Physical Science Basis Contribution of Working Group I to the Fourth Assessment Report of the Intergovernmental Panel on Climate Change.* . Cambridge University Press, 2007. ISBN 9780521705967.

STAMNES, K. and DALE, H. A new look at the discrete ordinate method for radiative-transfer calcultaions in anisotropically scattering armospheres. II: intensity computations. *JOURNAL OF THE ATMOSPHERIC SCIENCES*, vol. 38(12), pages 2696–2706, 1981. ISSN 0022-4928.

SULI, E. and MAYERS, D. *An Introduction to Numerical Analysis*. Cambridge University Press, 2003. ISBN 0521007948.

TAKAMURA, T. and NAKAJIMA, T. Overview of SKYNET and its activities. *OPTICA PURA Y APLICADA*, vol. 37, pages 3303–3308, 2004.

TANAKA, M., SHIOBARA, M., NAKAJIMA, T. and YAMANO, M. Aerosol optical characteristics in the yellow sand events observed in may, 1982 at nagasaki .1. observations. *JOURNAL OF THE METEOROLOGICAL SOCIETY OF JAPAN*, vol. 67(2), pages 267–278, 1989. ISSN 0026-1165.

TANRE, D., KAUFMAN, Y., HOLBEN, B., CHATENET, B., KARNIELI, A., LAVENU, F., BLAREL, L., DUBOVIK, O., REMER, L. and SMIRNOV, A. Climatology of dust aerosol size distribution and optical properties derived from remotely sensed data in the solar spectrum. *JOURNAL OF GEOPHYSICAL RESEARCH-ATMOSPHERES*, vol. 106(D16), pages 18205–18217, 2001. ISSN 0148-0227.

TANRE, D., REMER, L., KAUFMAN, Y., MATTOO, S., HOBBS, P., LIVINGSTON, J., RUSSELL, P. and SMIRNOV, A. Retrieval of aerosol optical thickness and size distribution over ocean from the MODIS airborne simulator during TARFOX. *JOURNAL OF GEOPHYSICAL RESEARCH-ATMOSPHERES*, vol. 104(D2), pages 2261–2278, 1999. ISSN 0747-7309.

TEGEN, I. and LACIS, A. Modeling of particle size distribution and its influence on the radiative properties of mineral dust aerosol. *JOURNAL OF GEOPHYSICAL RESEARCH-ATMOSPHERES*, vol. 101(D14), pages 19237–19244, 1996. ISSN 0148-0227. International Specialty Conference on Aerosols and Atmospheric Optics - Radiative Balance and Visual Air Quality, SNOWBIRD, UT, SEP 26-30, 1994.

TOLEDANO, C., CACHORRO, V., BERJON, A., DE FRUTOS, A., FUERTES, D., GONZALEZ, R., TORRES, B., RODRIGO, R., BENNOUNA, Y. and L., M. RIMA-AERONET network: longterm monitoring of aerosol properties. Optica Pura y Aplicada. *OPTICA PURA Y APLICADA*, vol. 44(4), pages 629–633, 2011. ISSN .

TORRES, B., BERJON, A., TOLEDANO, C., CACHORRO, V., FUERTES, D., GONZALEZ, R., BENNOUNA, Y., RODRIGO, R. and DE FRUTOS, A. AERONET-RIMA calibration facility: Accuracy assessment of sky radiances in Autilla del Pino (Palencia-Spain). *OPTICA PURA Y APLICADA*, vol. 44(4), pages 665–669, 2011. ISSN .

TRAKHOVSKY, E. and SHETTLE, E. Improved inversion procedure for the retrieval of aerosol size distributions using aureole measurements. *JOURNAL OF THE OPTICAL SOCIETY OF AMERICA A-OPTICS IMAGE SCIENCE AND VISION*, vol. 2(11), pages 2054–2061, 1985. ISSN 0740-3232.

TWOMEY, S. On numerical solution of Fredholm integral equations of first kind by inversion of linear system produced by quadrature. *JOURNAL OF THE ACM*, vol. 10(1), pages 97–&, 1963. ISSN 0004-5411.

TWOMEY, S. Application of numerical filtering to solution of integral equiations encountered in indirect sensing measurements. *JOURNAL OF THE FRANKLIN INSTITUTE-ENGINEERING AND APPLIED MATHEMATICS*, vol. 279(2), pages 95–&, 1965. ISSN 0016-0032.

TWOMEY, S. *Introduction to the mathematics of inversion in remote sensing and indirect measurements*. Elsevier, New York, 1977. ISBN 0486694518.

VERMEULEN, A. Caractérisation des aérosols á partir de mesures optiques passives au sol: apport des luminances totale et polarisée mesurées dans le plan principal. 1996.

VIDEEN, Y. Y. M. M., G. *Photopolarimetry in Remote Sensing: Proceedings of the NATO Advanced Study Institute, held in Yalta, Ukraine, 20 September - 4 October 2003 (NATO Science Series II: Mathematics, Physics and Chemistry)*. Springer, 2004. ISBN 1402023669.

WARD, D., HAO, W., SUSOTT, R., BABBITT, R., SHEA, R., KAUFFMAN, J. and JUSTICE, C. Effect of fuel composition on combustion efficiency and emission factors for African savanna ecosystems. *JOURNAL OF GEOPHYSICAL RESEARCH-ATMOSPHERES*, vol. 101(D19), pages 23569–23576, 1996. ISSN 0148-0227.

WARD, D., SUSOTT, R., KAUFFMAN, J., BABBITT, R., CUMMINGS, D., DIAS, B., HOLBEN, B., KAUFMAN, Y., RASMUSSEN, R. and SETZER, A. Smoke and fire characteristics for Cerrado and deforestation burns in Brazil: Base-B experiment. *JOURNAL OF GEOPHYSICAL RESEARCH-ATMOSPHERES*, vol. 97(D13), pages 14601–14619, 1992. ISSN 0148-0227.

WEHRLI, C. GAW–PFR: A network of Aerosol Optical Depth observations with Precision Filter Radiometers. In: WMO/GAW Experts workshop on a global surface based network for long term observations of column aerosol optical properties. Informe técnico, GAW Report No. 162, WMO TD No. 1287, 2005.

WILLEKE, K. and BARON, P. *Aerosol measurement: principles, techniques, and applications* . New York: Van Nostrand Reinhold, 1993. ISBN 0442004869.

WISCOMBE, W. Delta-M Method - Rapid yet accurate radiative flux calculations for strongly asymmetric phase functions. *JOURNAL OF THE ATMOSPHERIC SCIENCES*, vol. 34(9), pages 1408–1422, 1977. ISSN 0022-4928.

–¿Qué te parece desto, Sancho? – Dijo Don Quijote –

Bien podrán los encantadores quitarme la ventura,

pero el esfuerzo y el ánimo, será imposible.

Segunda parte del Ingenioso Caballero

Don Quijote de la Mancha

Miguel de Cervantes

–Buena está – dijo Sancho –; fírmela vuestra merced.

–No es menester firmarla – dijo Don Quijote–,

sino solamente poner mi rúbrica.

Primera parte del Ingenioso Caballero

Don Quijote de la Mancha

Miguel de Cervantes